UNIVERSITA' DEGLI STUDI DI PADOVA

FACOLTA' DI SCIENZE MM.FF.NN.

Dipartimento di Scienze Chimiche - Sede Amministrativa: Università di Padova

SCUOLA DI DOTTORATO DI RICERCA IN

SCIENZA ED INGEGNERIA DEI MATERIALI

CICLO XX

Coordinatore: Prof. Gaetano Granozzi

SYNTHESIS OF GOLD AND SILVER NANOPARTICLES FOR PHOTONIC APPLICATIONS

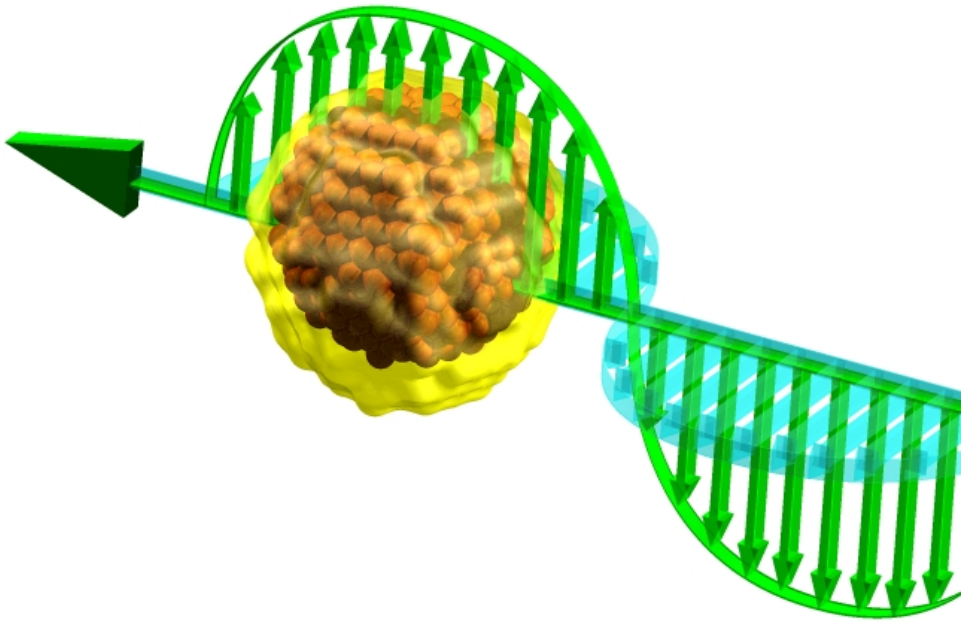

Dottorando: Dott. Vincenzo Amendola

Supervisore: Prof. Moreno Meneghetti

15 Gennaio 2008

UNIVERSITA' DEGLI STUDI DI PADOVA

FACOLTA' DI SCIENZE MM.FF.NN.

Dipartimento di Scienze Chimiche

Sede Amministrativa: Università di Padova

SCUOLA DI DOTTORATO DI RICERCA IN
SCIENZA ED INGEGNERIA DEI MATERIALI
CICLO XX

Coordinatore: Prof. Gaetano Granozzi

SYNTHESIS OF GOLD AND SILVER NANOPARTICLES FOR PHOTONIC APPLICATIONS

Dottorando: Dott. Vincenzo Amendola

Supervisore: Prof. Moreno Meneghetti

15 Gennaio 2008

Doubt

is one of the names of intelligence

Jorge Luis Borges

Contents

Riassunto ***1***

Abstract and outline ***9***

Section 1: Gold and silver nanoparticles

Chapter 1 - Overview on gold and silver nanoparticles ***15***

1.1 Historical background *17*

1.2 Synthesis *18*

1.3 Characterization *20*

1.4 Physical and chemical properties *21*

Chapter 2 - Photonics of gold and silver nanoparticles ***27***

2.1 Origin of the surface plasmon absorption *29*

2.2 Mie model *31*

2.3 Dielectric constant of metal nanoparticles *34*

2.4 Specific phenomena influencing the surface plasmon absorption *35*

2.5 Sensing by surface plasmon absorption *37*

2.6 Analytical models for SPA of core@shell spheres and non spherical particles *39*

2.7 Discrete dipole approximation *42*

2.8 Finite difference time domain method *44*

2.9 Local electric field enhancement and plasmons mutual interactions *45*

2.10 Aggregated metal nanoparticles *47*

2.11 Surface enhanced Raman scattering *49*

2.12 Surface plasmon excitation dynamics *50*

2.13 Surface plasmon radiative dynamics *52*

2.14 Plasmonic modulation of molecular fluorescence *55*

2.15 Plasmonic transmission and waveguiding *57*

2.16 Non linear optics of metal nanoparticles *59*

Section 2: Synthesis

Chapter 3 - LASiS and characterization of metal nanoparticles ***67***
3.1 Laser ablation synthesis in solution *69*
3.2 Colloidal systems *72*
3.3 UV-Vis characterization of AuNP and AgNP using Mie theory *73*
3.4 LASiS set up and nanoparticles characterization *76*
3.5 LASiS of gold nanoparticles *77*
3.6 Processing gold nanoparticles: size reduction, reshaping and ageing *80*
3.7 LASiS of gold nanoparticles in toluene *83*
3.8 LASiS of silver nanoparticles *87*
3.9 Insight of the Mie – Gans fitting *93*
3.10 LASiS of copper nanoparticles *98*
3.11 Sequential laser ablation synthesis of gold and silver nanoparticles. *99*
3.12 Controlled aggregation of gold nanoparticles for SPA engineering *100*
3.13 Chemical free size manipulation of AuNP by laser irradiation *102*
3.14 AuNP bioconjugation *110*

Chapter 4 - Chemical reduction of silver thiolated complexes ***117***
4.1 Silver thiolated complexes *119*
4.2 Chemical reduction procedure *120*
4.3 Synthesis of spherical Ag:4-FTP nanoparticles *121*
4.4 Synthesis of Ag:4-FTP nanoparticles with exotic absorption properties *122*
4.5 Synthesis of Ag:4-FTP nanowires embedding AgNP *127*

Section 3: Photonic applications

Chapter 5 - Multiphoton absorption properties of organic molecules and AuNP ***131***
5.1 Concepts of nonlinear optics *133*
5.2 Overview of the principal nonlinear optical phenomena *140*
5.3 Model for the dynamics of excited states *143*
5.4 Experimental set up for nonlinear optical measurements *146*
5.5 Multiphoton absorption properties of organic molecules *150*

5.6 Optical limiting properties of AuNP:Zinc phthalocyanines blend *183*

Chapter 6 - Optical doping and optical switching of AuNP infiltrated opals ***203***

6.1 Overview on photonic crystals *204*

6.2 Synthesis of opals infiltrated with gold nanoparticles *207*

6.3 Linear optical properties of opals doped with gold nanoparticles *208*

6.4 Light localization effects in opals doped with gold nanoparticles *213*

6.5 Optical switching properties of opals doped with gold nanoparticles *216*

Chapter 7 - Controlled cell uptake of AuNP for photothermal therapy ***223***

7.1 Photothermal therapy *225*

7.2 Conjugation of gold nanoparticles with PNIPAm *227*

7.3 Temperature controlled cell uptake of gold nanoparticles *233*

7.4 Laser induced cell thermolysis *237*

Conclusions ***241***

Appendix

A - Extinction cross sections of metal nanostructures calculated by DDSCAT 6.1 ***I***

B - List of scientific publications ***XI***

Table of abbreviations

AgNP	Silver nanoparticle / nanoparticles	**MNP**	Metal nanoparticle / nanoparticles
AN	Acetonitrile	**MPA**	Multiphoton absoprtion
AuNP	Gold nanoparticle / nanoparticles	**MS**	Mass spectrometry
BSA	Bovine serum albumin	**Nc**	Naphthalocyanine
CID	Chemical interface damping	**NIR**	Near infrared
DDA	Discrete dipole approximation	**NL**	Nonlinear
DLS	Dynamic light scattering	**NLO**	Nonlinear optical
DMF	Dimethylformamide	**NLT**	Nonlinear transmittance
DMSO	Dimethylsulphoxide	**NMR**	Nuclear magnetic resonance
DSB	Distyrylbenzene	**NSET**	Nanomaterial surface energy transfer
EA	Exotic absorption	**OD**	Optical density
EDS	Energy dispersion spectroscopy	**OL**	Optical limiting
EELS	Electron energy loss spectroscopy	**Pc**	Phthalocyanine
ELISA	Enzyme linked immunosorbent assay	**PCR**	Polymerase chain reactions
ESA	Excited state absorption	**PCS**	Photon correlation spectroscopy
ES-TPA	Excited state – two photons absorption	**P&P**	Pump and probe
ET	Energy / electron transfer	**PL**	Photoluminescence
EtOH	Ethanol	**pNIPAm**	poly(N-isopropylacrylamide)
FDTD	Finite difference time domain	**PS**	Polystyrene
FRET	Forster resonance energy transfer	**PVP**	Polyvinylpirrolidone
FTIR	Fourier transformed infrared	**RSA**	Reverse saturable absorption
4-FTP	4-Fluorothiophenol	**SA**	Saturable absorption
FWHM	Full width half maximum	**SDS**	Sodium dodecyl sulfate
HL	High loading	**SEM**	Scanning electron microscopy
HM	Hybridization model	**SERS**	Surface enhanced Raman scattering
HOMO	Highest occupied molecular orbital	**SHG**	Second harmonic generation
Hp	Hemiporphyrazine	**SPA**	Surface plasmon absorption
HRTEM	High resolution TEM	**SubPc**	Subphthalocyanine
ICP-AES	Inductively coupled plasma - atomic emission spectroscopy	**SVPB**	Styryl(vinylpyridyl)benzene
ISC	Intersystem corssing	**TEM**	Transmission electron microscopy
LASiS	Laser ablation synthesis in solution	**THF**	Tetrahydrofuran
LCST	Lower critical solution temperature	**THG**	Third harmonic generation
LL	Low loading	**TPA**	Two photons absorption
LNMG	Log Normal Mie Gans	**TPMA**	Tris(2-pyridylmethyl)amine
LUMO	Lowest unoccupied molecular orbital	**XPS**	X ray photoelectron spectroscopy
MG	Mie - Gans	**XRD**	X ray diffraction
ML	Medium loading	**UV-Vis**	Ultraviolet - visible

Riassunto

Il presente progetto di ricerca ha riguardato la sintesi di nanoparticelle metalliche con strutture e proprietà innovative e lo studio di alcune loro applicazioni in fotonica, mediante spettroscopia non lineare con impulsi laser a nanosecondi e lunghezza d'onda di 532 nm. In particolare il progetto di ricerca si e' articolato nelle seguenti fasi: la sintesi di nanoparticelle metalliche con proprietà plasmoniche o proprietà ottiche significative a 532 nm, la manipolazione mediante irraggiamento laser delle nanostrutture, la loro funzionalizzazione o bioconiugazione, l'utilizzo di nanoparticelle di oro per applicazioni fotoniche o biofotoniche, lo studio delle proprietà di assorbimento multifotonico di particelle di oro in presenza di molecole organiche e lo studio approfondito delle proprietà e dei meccanismi di assorbimento multifotonico di una serie di molecole organiche dalla struttura innovativa.

L'interesse nello studio di materiali con dimensioni nanometriche sorge dalle nuove proprietà chimico fisiche che derivano dall'alto rapporto superficie/volume, dall'elevato numero di atomi di superficie rispetto ai solidi macroscopici e dagli effetti quantistici di confinamento in strutture cosi' piccole. In particolare le nanotecnologie sembrano prossime a rivoluzionare due settori fondamentali della nostra civiltà, quali le tecnologie dell'informazione e le tecnologie mediche. In questo panorama le nanostrutture metalliche di oro e argento rivestono un ruolo fondamentale per una combinazione fortunata di proprietà peculiari, quali l'intensa banda di assorbimento dovuta all'oscillazione collettiva degli elettroni di conduzione (denominata plasmone di superficie), la facilità di funzionalizzare la loro superficie con una serie innumerevole di molecole con funzioni specifiche e, molto importante, l'assenza di citotossicità delle particelle di oro in organismi viventi. Inoltre l'elevata stabilità fisico – chimica e la possibilità di ingegnerizzare in diversi modi le proprietà ottiche lineari delle nanostrutture di oro e argento ne hanno decretato la larga diffusione nell'ambito delle nanoscienze.

Solitamente le nanoparticelle di oro (AuNP) o di argento (AgNP) sono ottenute mediante riduzione chimica dei rispettivi sali con un buon controllo di dimensioni e forma finale dei prodotti. Tuttavia tale approccio presenta alcuni svantaggi, tra cui la difficoltà e la necessità pressoché assoluta di purificare le particelle dai reagenti chimici in eccesso ed il fatto che la purificazione trova comunque un limite nella presenza costante di molecole di stabilizzanti sulla superficie delle particelle, le quali a loro volta rendono difficile la funzionalizzazione con qualsivoglia molecola esterna alla procedura di sintesi. Inoltre gli stabilizzanti possono interferire con le proprietà chimico fisiche delle particelle e spesso inducono effetti di tossicità non contemplati dal metallo in se'.

Per aggirare questi inconvenienti e' stato ottimizzato un metodo di sintesi di nanoparticelle di oro e argento mediante l'ablazione laser a 1064 nm di un target di metallo massivo immerso in una soluzione liquida, chiamato LASiS dall'acronimo di *Laser Ablation Synthesis in Liquid Solution*. La LASiS e' una tecnica molto veloce ed ha costi di produzione molto bassi. Inoltre non richiede nessun reagente chimico, pertanto la purificazione del prodotto non e' necessaria e la funzionalizzazione delle particelle puo' avvenire direttamente aggiungendo le molecole desiderate alla soluzione colloidale, senza ricorrere alle reazioni di place exchange necessarie con le particelle ottenute per riduzione chimica. La LASiS puo' essere estesa a diversi solventi, offrendo

la possibilità di scegliere quello piu' adatto alla solubilizzazione della molecola che contiene la funzione che si desidera agganciare alla superficie delle particelle metalliche. Un risultato di particolare interesse e' stato trovato nel caso di LASiS di AuNP in toluene, in quanto la SPA e' completamente assente nello spettro UV-Vis perche' le particelle di oro sono inglobate in una matrice di carbonio parzialmente grafitico. La SPA delle particelle puo' essere ripristinata mediante un trattamento ossidante chimico oppure in aria ad alta temperatura per rimuovere la matrice grafitica.

Per ottenere informazioni sulle particelle metalliche senza la necessità di ricorrere a misure TEM, e' stato messo a punto un modello di fitting degli spettri UV – Vis molto semplice sfruttando il modello di Mie per il calcolo della sezione d'urto di estinzione di nanoparticelle metalliche sferiche ed il modello di Gans per l'analogo calcolo su particelle sferoidali.

Solitamente le dimensioni delle particelle ottenute mediante LASiS in un dato solvente non possono essere modificate agendo solo sui parametri dell'ablazione laser. D'altra parte ottenere dimensioni ben controllate mediante l'utilizzo di reagenti chimici implica una serie di svantaggi, come discusso in precedenza. Pertanto e' stata ideata una tecnica basata sulla manipolazione per irraggiamento laser a 532 nm delle dimensioni medie di particelle di oro ottenute per LASiS in acqua. Tale tecnica non necessita di alcun reagente chimico, pertanto si presta eccezionalmente bene alla successiva funzionalizzazione o bioconiugazione delle particelle o al loro utilizzo in campioni biologici vivi senza timore di effetti collaterali come la tossicità. La manipolazione delle dimensioni iniziali delle AuNP si basa su due approcci, uno top down per ottenere raggi piu' piccoli ed uno bottom up per ottenere dimensioni maggiori. Le particelle cosi' ottenute in acqua sono state funzionalizzate con una biomolecola "modello", l'albumina da siero bovino (BSA), per dimostrare l'elevata disponibilità della superficie alla bioconiugazione. I risultati ottenuti sono molto positivi, in quanto e' stato possibile monitorare la coordinazione della BSA con le AuNP gia' per un rapporto di 1 molecola di albumina ogni 10 nanoparticelle di oro. Tale rapporto e' molto piu' basso rispetto a quelli solitamente utilizzati per la funzionalizzazione di particelle ottenute per riduzione chimica, in quanto le reazioni di place exchange richiedono che la funzione sia presente in alta concentrazione e, se possibile, ad alta temperatura. Inoltre sono rari i casi in cui e' possibile monitorare la funzionalizzazione di nanoparticelle ottenute mediante riduzione chimica attraverso l'evoluzione della SPA. Pertanto il presente metodo appare

estremamente utile nel caso in cui i leganti siano preziosi o disponibili solo in piccole quantità.

Le particelle di argento ottenute mediante LASiS hanno un picco di assorbimento plasmonico intorno ai 400 nm. Questo rende difficile studiarne le proprietà ottiche non lineari mediante un laser a Nd:YAG con output a 1064 nm, a 532 nm (2° armonica) e a 355 nm (3° armonica). D'altra parte e' noto che la banda di assorbimento plasmonico può cambiare sensibilmente agendo sulla forma delle nanoparticelle di oro ed argento. Questo perche' cambiando la simmetria della particella si originano nuove risonanze plasmoniche a diverse energie. Il metodo piu' diffuso per ottenere AgNP con forme complesse consiste nella riduzione chimica di sali di argento in presenza di molecole che inducano una crescita anisotropa. Nel presente caso si e' studiata la possibilità di ottenere nanostrutture di argento con proprietà plasmoniche innovative mediante riduzione chimica di complessi tiolati di argento, in particolare utilizzando tiofenoli. In questo caso e' stato possibile ottenere particelle di argento con proprietà di assorbimento nel visibile non compatibili con le ordinarie bande di assorbimento plasmonico. Contrariamente alle particelle di argento ordinarie, tali particelle hanno dimostrato di possedere anche proprietà di fluorescenza nel vicino infrarosso, in corrispondenza della finestra utile per le telecomunicazioni e per applicazioni di labelling in tessuti biologici. L'origine di tali proprietà, tuttora in corso di studio, sembra legato alle dimensioni delle particelle di argento ed alla natura aromatica dei leganti.

In generale, materiali che mostrano intense proprietà di assorbimento nel visibile possono essere ottimi candidati anche per lo studio di fenomeni ottici non lineari, dal momento che la suscettività dielettrica agli ordini successivi al primo diventa molto grande quando la radiazione elettromagnetica e' in risonanza con le transizioni elettroniche del sistema investigato. Le particelle di oro e argento si prestano a due tipi principali di fenomeni ottici non lineari: come sistemi per il light harvesting grazie alla loro enorme sezione d'urto di assorbimento lineare, e come sistemi per l'amplificazione degli effetti ottici non lineari in materiali circostanti, grazie agli altrettanto enormi effetti di amplificazione del campo locale in prossimità della loro superficie dovuti all'oscillazione collettiva degli elettroni di conduzione. Molecole organiche con proprietà di assorbitori saturabili inversi (RSA) che coinvolgano stati di tripletto a vita relativamente lunga (centinaia di nanosecondi per lo meno) si prestano particolarmente

bene ad esplorare i fenomeni del tipo sopra descritto mediante spettroscopie nonlineari con impulsi laser a 9 nanosecondi come la trasmittanza nonlineare o il pump & probe. Nel presente caso, diverse molecole organiche dalla struttura innovativa sono state investigate mediante spettroscopie nonlineari a 532 nm, ma solo alcune di esse hanno evidenziato un comportamento da RSA con stati di tripletto (derivati fullerenici, ftalocianine, subftalocianine ed alcune emiporfirazine). In altri casi le elevate energie depositate dal fascio laser incidente hanno favorito processi fotochimici che modificano la struttura e le proprietà delle molecole oggetto di investigazione. Nel caso di una porfirazina di Mg in DMSO il classico meccanismo RSA e' presente solo a basse fluenze, mentre ad alte fluenze si ha la formazione di una specie molecolare carica con elevato assorbimento a due fotoni da stato eccitato. L'assorbimento a due fotoni da stato eccitato, un processo ancora poco studiato in letteratura, si e' rivelato un meccanismo importante per i sistemi studiati, essendo caratteristico anche di alcune emiporfirazine. Inoltre si è verificato come la variazione delle proprietà ottiche non lineari in seguito a piccole differenze nella struttura delle molecole investigate puo' essere utilizzata in sensoristica, come e' stato possibile dimostrare nel caso di derivati bistirilbenzenici funzionalizzati con dei sensori specifici per lo ione Zn^{2+}.

L'interazione di nanoparticelle di oro con molecole dotate di proprietà di RSA come le ftalocianine di zinco sono interessanti per lo studio di nuovi meccanismi per il trasferimento di energia o di elettroni. Effettivamente e' stato misurato un netto miglioramento delle proprietà di limitazione ottica nel caso di AuNP ottenute per LASiS e miscelate ad una soluzione di ftalocianine di zinco. Il meccanismo che e' stato dedotto a giustificazione dell'efficiente e durevole limitazione ottica si basa, da un lato, sul trasferimento di carica dalle ftalocianine alle particelle di oro e, dall'altro, sulla frammentazione fotoindotta delle particelle di oro, che restano le protagoniste della limitazione ottica. I due processi agiscono in sinergia con l'irraggiamento laser per produrre la rigenerazione delle particelle di oro e la stabilizzazione dell'effetto di trasmittanza nonlineare.

Data l'elevata polarizzabilità delle nanoparticelle metalliche, conferita loro dall'elevato numero di elettroni di conduzione, si sono utilizzate le particelle di oro per il "doping ottico" di cristalli fotonici. Inserire AuNP negli interstizi tra le sfere di polistirene ha consentito di modulare la posizione del band gap fotonico, in modo tanto maggiore quanto piu' alta e' la frazione di oro negli interstizi, e di misurare effetti di

localizzazione del campo elettromagnetico della radiazione incidente per lunghezze d'onda prossime al band gap. E' stato inoltre possibile ottenere un effetto di switching ottico del gap fotonico in misura del 150% mediante misure di pump & probe a bassa fluenza (32 mJ/cm^2), sfruttando il forte assorbimento delle AuNP in prossimità dei 532 nm. Tale valore e' superiore a tutti gli altri sinora riportati in letteratura.

L'elevata sezione d'urto di assorbimento delle AuNP (pari a circa 10^5 volte quello dei comuni cromofori organici), unita alla bassissima efficienza di decadimento radiativo dell'eccitazione plasmonica (inferiore all'1% per particelle al di sotto dei 10 nm di raggio), rende le nanoparticelle di oro degli efficienti convertitori di radiazione elettromagnetica in calore. Questa peculiarità puo' essere sfruttata per la terapia fototermica, una volta indirizzate le nanoparticelle verso cellule cancerose, distruggendole mediante il semplice irraggiamento con radiazione laser. In quest'ottica e' di estrema importanza la selettività con la quale e' possibile inserire le particelle solo nelle cellule che si desidera eliminare. Piu' in generale il problema del targeting cellulare selettivo puo' aprire nuove prospettive nel drug delivery, nella terapia genica e nell'imaging cellulare oltre che servire per la terapia fototermica. In questo quadro si e' studiato un nanomateriale composto da particelle di oro ottenute mediante LASiS in acqua, funzionalizzate con un polimero termosensibile, il poli-n-isopropilacrilammide (PNIPAm). Le particelle modificate con PNIPAm hanno consentito di controllare l'uptake delle particelle di oro nelle cellule agendo soltanto sulla temperatura. Infatti, si ritiene che le particelle ricoperte da PNIPAm non siano in grado di entrare nelle cellule quando la temperatura e' di 34°C per un effetto sterico dovuto all'estensione delle catene polimeriche, oppure perche' la distensione del polimero impedisce l'adsorbimento di proteine del terreno di coltura che favoriscono il passaggio attraverso la membrana cellulare. Questo risultato rende teoricamente possibile sfruttare la temperatura per il targeting selettivo dei tessuti cancerosi, in quanto essi solitamente hanno una temperatura di alcuni gradi superiore a quella dei tessuti sani. Quindi sono stati svolti degli esperimenti di irraggiamento a 532 nm con una fluenza di 19 mJ/cm^2 per verificare la possibilità di distruggere selettivamente solo le cellule che contenevano le AuNP in quantità maggiore. I risultati di tale irraggiamento sono incoraggianti e indicano un nuovo approccio per il targeting selettivo e la terapia fototermica dei tessuti tumorali.

La natura delle ricerche contenute in questa tesi di Dottorato, le quali disegnano un percorso trasversale attraverso la sintesi e le applicazioni delle particelle metalliche in nanofotonica ed in biofotonica, e' quella di un lavoro seminale per mettere in luce nuovi approcci alle suddette discipline. Di conseguenza ciascuno degli argomenti affrontati dalle ricerche qui descritte si presta agevolmente ad ulteriori sviluppi ed investigazioni.

Abstract and outline

The importance of nanomaterials for science and technology is highly increased in last years. Gold and silver nanoparticles had a significant role in this process, due to their many peculiarities, first of all the surface plasmon absorption and the surface accessibility for further functionalization.

This PhD thesis pass through the synthesis of gold and silver nanoparticles, with the final aim of studying linear and nonlinear photonic applications of these nanostructures. A particular interest regarded the synthesis of gold and silver particles having optical features compatible with nonlinear optical spectroscopy performed with 532 nm - 9 ns laser pulses. Two unconventional pathways were exploited for this purposes, the first one consists of laser ablation synthesis in solution (LASiS) and the second one consists of chemical reduction synthesis of silver particles stabilized by thiophenols. Both cases originated gold and silver particles with strong absorption bands around 532 nm and other features not accounted by conventional synthesis techniques.

Primarily, metal nanoparticles obtained by LASiS do not need any stabilizing agents or chemical reagents, hence purification procedures are not necessary and the surface is highly available for surface functionalization.

In case of chemical reduction synthesis of silver particles stabilized by thiophenol molecules, an exotic absorption spectra with a number of peaks in the whole visible window and luminescence properties in the near infrared have been found. The origin is currently object of investigation, since such optical behaviours are not conceived by ordinary plasmonic structures.

The combination of nanometric size effects, like the surface plasmon absorption close to 532 nm, with solid state properties, like the large number of higly polarizable conduction electrons, prompted to the study of gold nanoparticles for various photonic applications.

The huge linear absorption cross section of gold nanoparticles suggests the investigation of energy or charge transfer process with other organic molecules possessing multiphoton absorption properties of interest for photovoltaics, optical limiting or photodynamic therapy. Multiphoton absorption properties of several innovative compounds have been investigated and are discussed in this thesis, like fullerene derivatives, bistirilbenezene derivatives and the family of phthalocyanine and porphyrin derivatives. For monitoring the occurrence of charge or energy transfer by nanosecond nonlinear optical spectroscopy, gold nanoparticles have been coupled to molecules that behave as reverse saturable absorbers involving long life triplet states. Hence the case of gold nanoparticles in presence of zinc phthalocyanines was investigated, and charge transfer process from the molecule to the particles was evidenced, which originated an enhancement of optical limiting performances of gold nanoparticles by a self healing mechanism.

The large polarizability of gold nanoparticles and their small size allowed also the manipulation of the photonic pseudo gap in a polystyrene opal. The band gap energy was modulated by increasing the load of gold in the opal, while pump & probe measurements at 532 nm and 9 ns allowed the optical switch of the photonic bandgap when in presence of gold nanoparticles.

The large absorption cross section of nanometric size gold nanoparticles, coupled to the fast nonradiative decay rate and the very low radiative decay efficiency makes them perfect converter of light into heat. This concept is at the basis of photothermal cancer

therapy, provided that gold particles can be efficiently addressed to cancerous cells. This has been done by the conjugation of gold particles with a thermo responsive polymer based on poly(N-isopropylacrylamide). An increase of the particles uptake in cells was achieved just by switching the bath temperature and the subsequent irradiation at 532 nm of cells allowed the selective death only where a large uptake of gold particles occurred. This approach paved the way to a new therapy based on the combination of photonic properties of gold particles and temperature responsive properties of poly(N-isopropylacrylamide).

For the illustration of the above work, this PhD thesis has been divided in three sections. Section I provides a survey of the main chemical – physical features of gold and silver nanostructures, with particular care in their photonic and plasmonic properties. Section II describes the two synthetic approaches for obtaining gold and silver nanoparticles, namely LASiS for gold and silver and chemical reduction for silver particles stabilized by thiophenols. Section III deals with photonic applications of gold nanoparticles, comprising the multiphoton absorption properties in presence of organic molecules, the modulation of linear and nonlinear optical properties of photonic crystals and the temperature controlled cell uptake for photothermal therapy of cancerous tissues.

Section I:

Gold and silver nanoparticles

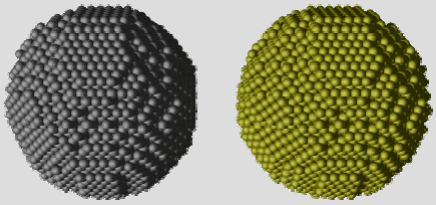

Chapter 1

Overview on gold and silver nanoparticles

In the last fifteen years we assisted to the massive advance of nanomaterials in material science. Every object possessing at least one characteristic dimension between 1 and 100 nm can be defined as a "nanomaterial". When dealing with such small structures, the ratio between surface (or interface) and inner atoms became significant. This means that quantistic effects and surface atoms with partial coordination strongly influence physical and chemical behaviour of the nanomaterials, originating properties different from both molecules and bulk solids, sometimes complementary with them.

The spread of nanotechnology in the last years is strictly due to the improvement of characterization and synthesis techniques on the nanometer scale. This allowed the release of scientists innate curiosity toward a field generous of new physical phenomena and synthetic opportunities. From this point of view, Feynman's prophecy of looking at

nanotechnology "just for fun" has been fulfilled,[1] but the massive amount of money attracted by nanotechnology has also a more concrete basement. In fact microtechnology and molecular chemistry shaped the last century by enormous advancements in information science and medicine. Now, nanomaterials, laying for size and properties in between molecules and micromaterials, promise to further revolutionize human life. For instance one can look at nanoparticles like at small building blocks to create new materials,[2] in an analogous way to what happen with bare atoms, or one can consider that nanomaterials have a size similar to several important biomolecules, making them the natural choice for hybrid systems.[3]

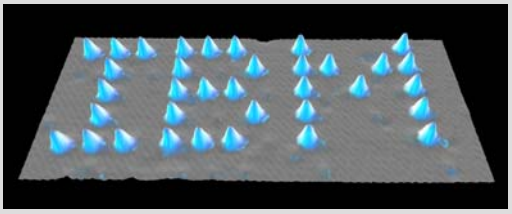

Figure 1.1 *Scanning tunnelling microscopy (STM) image of Xenon atoms on Nickel (110). Many scientists assume that nanotechnology began with the discovery of STM, that also allows single atom manipulation.*

In this panorama gold and silver nanoparticles (AuNP and AgNP hereafter) are playing a protagonist role. The reason for AuNP and AgNP success lies in a favourable combination of physical – chemical properties and advances in chemical synthesis. The main characteristic of AuNP and AgNP is the surface plasmon absorption (SPA), which has $10^5 – 10^6$ larger extinction cross section than ordinary molecular chromophores and is also more intense than that of other metals particles, due to the weak coupling to interband transitions. The frequency of gold and silver SPA can also be tuned from visible to near infrared acting on shape, size or nanoparticles assembly.

Furthermore AuNP and AgNP have high chemical stability and photostability and especially AuNP are non toxic for living organisms. Their physicochemical stability, bright colours and biocompatibility explain why traces of AuNP and AgNP utilization are dated back to the 5th century B.C. in China and Egypt.

Since the surface chemistry of AuNP and AgNP particles is very simple and is mainly based on the sulphur – metal bond, one often deals with nanoparticles covered by a shell of ligands with sulphur based functionalities. Due to the 'simple' surface chemistry, recent years also faced sensible progress in AuNP and AgNP synthesis with tailored shape or size and this provided a gamut of tools with engineered properties, opening the access of nanotechnology to manifold applications.

1.1 Historical background

Solutions of liquid gold have been first mentioned by Egyptian and Chinese authors around 5th century BC. In fact Ancients believed in their metaphysical and healing powers. [4]

Colloidal gold and silver have been used since Ancient Roman times to colour glass of intense shades of yellow, red, or mauve, depending on the concentration of the two metals. A fine example is the famous Lycurgus Cup in the British Museum, dated 4th century AD.[5] For all the middle ages Au colloids have also been used in medicine believing in their curative properties for various disease.[4]

In 15th century Italian artisans in Gubbio and Deruta were able to prepare brightly coloured porcelain, called luster, containing silver and silver - copper alloy nanoparticles. The technique was developed in the Islamic world during the 9th century and exploited the reducing atmosphere obtained heating dried genista up to 600°C to obtain nanoparticles by reducing metal oxides or metal salts previously deposed on the ceramic piece from a vinegar solution.[4, 6] In the 17th century the glass-colouring process was further refined by Andreus Cassius and Johann Kunchel by contriving "*Purple of Cassius*", a precipitate of colloidal gold and stannic hydroxide they added to the base glass.[4]

Figure 1.2 *Luster dated 1525 from the Workshop of "Maestro" Giorgio Andreoli in Gubbio, representing Hercules and the centaur Nessus.*

The first "scientific" study of metal nanoparticles is dated back to the seminal work of Michael Faraday around 1850.[7] Faraday was the first to recognise that the red colour of gold colloid was due to the minute size of the Au particles and that one could turn the preparation blue by adding salt to the solution. He obtained gold colloids reducing $AuCl_4^-$ by phosphorus, following a procedure already reported by Paracelsus in 16th century about the preparation of "*Aurum Potabile*" and based on a two phase water / CS_2 reaction. Some of Michael Faraday's preparations are still preserved today in the Faraday Museum in London.[8]

Other synthetic methods for colloidal metal particles have been developed in the early 20th century, both physical or chemical, until the fundamental work of Turkevitch in 1951.[9] He started a systematic study of AuNP synthesis with various methods by using

transmission electron microscopy (TEM) analysis to optimise the preparative conditions until obtaining what is commonly known as the Turkevitch method.

1.2 Synthesis

The approaches to metal nanoparticles synthesis can be divided in physical and chemical methods. Physical methods, as ion implantation and all the sputtering techniques, are used to obtain metal nanoparticles supported on substrates or embedded in solid matrices. Condensation of metal vapours by adiabatic expansion was successfully exploited in the synthesis of metal particles as well as of oligoatomic metal clusters.[10]

The most widely used methods are based on chemical reduction in solution (wet chemistry) to yield nanoparticles colloids.[11] All these wet chemical approaches require the reduction of Ag^+ or Au^+ ions and the chemisorption or physisorption of ligands on the surface of metal nanoparticles to avoid their coagulation and precipitation.

The Turkevitch method is the most popular for obtaining aqueous solutions of gold nanoparticles that are easily functionalizable with subsequent steps.[4] This method consists in the reduction of $HAuCl_4$ in a boiling aqueous solution of sodium citrate. The average particle diameter can be tuned in the range of 10 – 100 nm with limited polydispersity. The same procedure can be used to reduce whatever Ag salt, but particle size control is very limited in this case.[11] Citrate molecules act both as reducing and stabilizing agents. Nanoparticles functionalization can occur by the displacement of citrate and the ligation of the desired molecules, provided that are water soluble.

Brust and Schiffrin developed the two phases method, that is the most widely used for thiols stabilized metal nanoparticles in organic solvents.[4] Basically $HAuCl_4$ (or $AgNO_3$) is dissolved in water and subsequently transported in toluene by tetraoctylammonium bromide (TOAB), that act as a phase transfer agent. The toluene solution is then mixed and thoroughly stirred together with an aqueous solution of $NaBH_4$ in presence of thioalkanes or aminoalkanes. In this case particles size can be tuned in the 1 – 30 nm range. Further functionalization of nanoparticles can occur by place-exchange reactions between ligands or by chemical reactions with specific functionalities present on the ligands, since these particles can be handled almost as organic compounds.

Other wet chemical approach exploit reduction of metal salts by organic solvents as ethanol (EtOH) for gold and dimethylformamide (DMF) for silver or polyols like

ethylene glycol in presence of protecting polymers as polyvinylpirrolidone (PVP) or other stabilizing molecules.[11] These techniques are also the basis to control nanoparticles shape and one can obtain spheres, prisms, cubes, rods or wires by optimising reactions parameters such as the concentration of metal ions or stabilizers, the temperature, the pH or using others simple tricks. For instance silver rods can be obtained using Pt seeds before adding the Ag salt, while Ag and Au rods can be obtained starting from seeds of the relative metals and carrying out the reaction with a mild reducing agent like ascorbic acid and cetyltrimethylammonium bromide (CTAB).[11, 12] Shape anisotropy is pursued because it introduces new physical and chemical properties in metal nanoparticles. To grow an asymmetric structure like a nanorod from a material with high packing symmetry like metallic Au and Ag (face centered cubic lattice), one must minimize growth in two dimensions.[13] One example is the soft template provided by surfactants that assemble in rodlike micelles. Alternatively chemicals like surfactants, PVP, polyols, citrate or ascorbic acid are used because they bind preferentially to specific crystal faces of the particle, thus inhibiting growth on those faces.

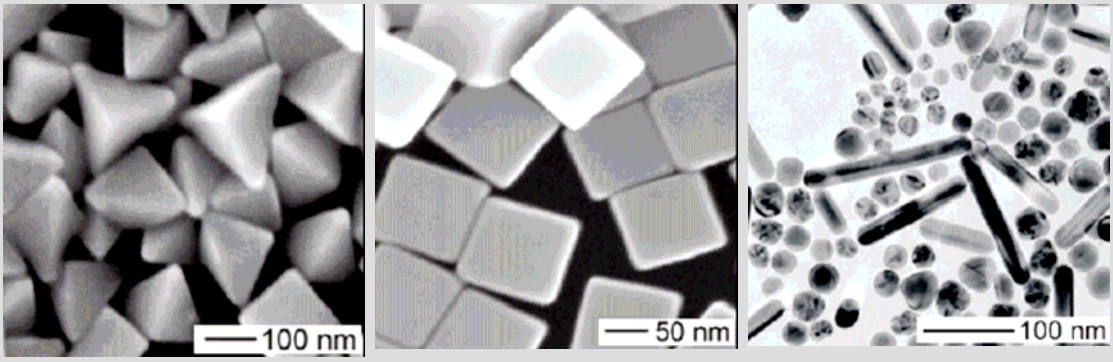

Figure 1.3 *From left to right silver bypiramids, cubes and spheres / rods obtained adding NaBr, NaCl and iron(II) acetylacetonate respectively to the silver precursor solutions. From reference 14 .*

Further control on particles morphology is achieved by galvanic replacement reactions between silver structures and $HAuCl_4$ in water.[12, 14] This is possible because the standard reduction potential of $AuCl_4^-/Au$ is higher than that of Ag^+/Ag.

The preparation of metal particles in inverse micelles is an alternative two phases approach that exploit the interior part of micelle as nanoreactors to control size and shape of nanoparticles, but with a lower precision than ordinary two phase methods.[15] The only advantage lies in the versatility of having a nanoreactors to obtain a nanobjects.

Synthesis of metal nanoparticles in organic solvents is possible with one phase approach using organic soluble precursors, usually gold complexes with triphenilphosphine or silver trifluoacetate. This synthesis approach, relatively recent, allow an high control on the size and crystallinity of final products.[16, 17] Recently the correlation between nanocrystallinity and chemical – physical properties like chemical transformation, electron–phonon interactions and nanomechanical properties was investigated exploiting this synthetic approach.[17]

The strong stabilising effect of organic thiols on gold and silver particles allowed the chemical reduction synthesis in solution of cluster composed of a really small number of atoms.[18, 19] Also other techniques based on DNA, crown ether or dendrimers templates and on triphenylphosphine ligands yield well monodisperse oligoatomic Au or Ag clusters. In every case the controlled reduction of metal precursors to synthesize clusters made of few atoms or tens of atoms with a low size dispersion are usually complicated and highly different depending on the used ligand. In a recent work a crystallization procedure have been used successfully for relatively large gold clusters (i.e. 107 atoms).[20]

1.3 Characterization

The reference technique for metal nanoparticles investigation is transmission electron microscopy (TEM).[2, 4] TEM analysis allows accurate measurement of particles average size and size distribution, high resolution TEM (HRTEM) is useful to investigate their crystalline or defective structure, and energy dispersion spectroscopy (EDS), scanning TEM (STEM), electron energy loss spectroscopy (EELS) and electron diffraction (ED) help in determining particles composition. TEM analysis becomes almost ineffective for particles smaller than about 1 nm in size, depending on the TEM performances, in this case being required mass spectrometry (MS) or X ray diffraction (XRD) analysis.

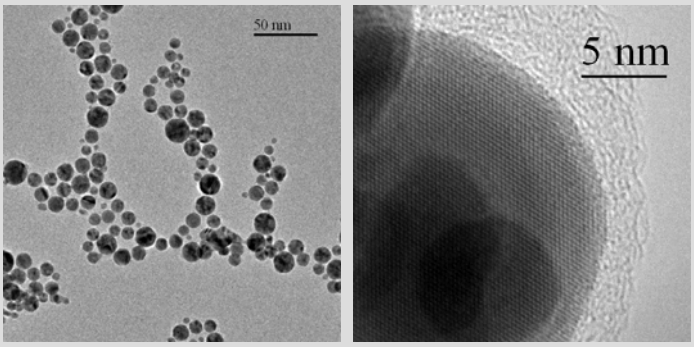

Figure 1.4 *TEM image for size distribution analysis (left) and HRTEM image for crystal lattice analysis (right) of gold nanoparticles.*

Thanks to the surface plasmon absorption of metal particles and to interband transitions in oligoatomic metal clusters, UV – visible – near infrared (UV-Vis-NIR) absorption spectroscopy is particularly helpful to obtain raw informations about size,[10] structure and composition in a fast and inexpensive way, as discussed in following chapters. Also UV – visible – near infrared (UV-Vis-NIR) fluorescence spectroscopy and Raman spectroscopy are helpful for the study of structure and electronic properties of oligoatomic metal clusters[18, 19] whereas small angle X ray scattering (SAXS) is useful to provide informations about the size and the aggregation of nanoparticles.[2, 4]

The study of ligands on metal surface requires ordinary characterization techniques of organic and biological molecules, namely ^{1}H and ^{13}C nuclear magnetic resonance (NMR) spectroscopy, Fourier transformed infrared (FTIR) spectroscopy, Raman spectroscopy and elemental analysis.[2, 4] Significant results in the study of ligands arrangement on nanoparticles surface have been obtained by scanning tunnelling spectroscopy (STM).[4, 21] Also mass spectrometry, thermogravimetry analysis (TGA) and differential scanning calorimetry (DSC) give information on the ligand number around particles.[4]

X ray photoelectron spectroscopy (XPS) is used to quantify the gold or silver to sulphur ratio and to check oxidation state of metal atoms.[4]

More sophisticated techniques as extended X ray absorption fine structure (EXAFS) and X ray absorption near edge structure (XANES) spectroscopy are able to define the chemical state and chemical surrounding of atoms in complicated situations, where other techniques fail or need corroboration, as for metal clusters.[4]

Dynamic light scattering can only provide qualitative informations about average size of nanoparticles or particles aggregates, but it is a fast and easy way to monitor the surface charge of colloidal systems when a Z spectroscopy is performed.[4]

1.4 Physical and chemical properties

Chemical properties. Gold and silver are known for being generally inert and, especially gold, for not being attacked by O_2 to a significant extent. This makes AuNP and AgNP stable in ordinary conditions.[22] Gold nanoparticles are resistant also to strong oxidizing or highly acid environments, though "*aqua regia*" or solutions containing I^- or CN^- can immediately dissolve them.[4]

Both Au and Ag are reactive with sulphur, in particular bulk silver often undergoes to tanning due to the formation of an Ag_2S surface layer. In case of organic thiols, ligation to nanoparticles surface is particularly effective for the contemporary presence of a σ type bound, in which sulphur is the electron density donor and the metal atom is the acceptor, plus a π type bound, in which metal electrons are partially delocalised in molecular orbitals formed between the filled d orbitals of the metal and the empty d orbitals of sulphur.[22] Other than thiols and disulphides, also alchilamine and phenilphosphine have been successfully used for AuNP and AgNP ligation.[4, 11]

Solutions of AgNP have applications as bactericidal agents because the Ag^+ ions interfere with bacteria metabolism. Since AgNP are exposed to a certain extent of surface oxidation by atmospheric O_2, silver sols can release Ag^+ ions with concentration sufficient to act as bactericides.[22]

Electrochemical properties of metal nanoparticles are strongly size dependent, in fact cluster made by few hundred or tens of atoms have been used to investigate the transition from the metal – like capacitive charging to the redox like charging. Up to 15 charging peaks were observed by differential pulse voltammetry in case of Au_{147}.[4]

High surface to bulk atoms ratio and overall chemical inertness confer catalytic activity to AuNP and AgNP. Silver particles are suitable for oxidation of organic compounds, CO, NO and degradation of aromatic and chlorine derivatives. Gold nanoparticles were active in the oxidation of CO and H_2 as well as in the reduction of NO and in a wide range of other typical catalytic reactions.[4, 23]

Physical properties. Since solid to liquid transition begins at interfaces, a well known feature of nanometric particles is the lower melting temperature with respect to the bulk. For instance gold undergoes a decrease in melting temperature of about 400°C going from 20 nm to 5 nm particles and of about 50°C going from the bulk to 20 nm particles.[24] Melting temperature T_m depends on particle size d as:

$$T_m = A + \frac{B}{d} \qquad (1.1)$$

following a general rule for physical properties dependent on the surface to volume ratio, that can be described by using the "*size equations*" structure as in *1.1*.

Thermal conductivity is enhanced for small particles due to higher surface to volume ratio, while phonons energy became higher for very small particles and Raman spectroscopy can be used to measure clusters size.[4]

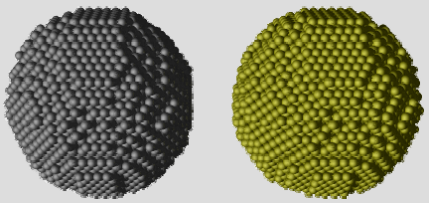

Figure 1.5 *Silver and gold nanoparticles have the same face centered cubic (f.c.c.) crystalline lattice and similar lattice parameters (cfr. Table 1.1).*

Another surface phenomenon is the plasmon – polariton absorption band due to the coherent oscillation of $6S^1$ (Au) or $5S^1$ (Ag) conduction band electrons in presence of resonant electromagnetic waves.[10] For spherical AgNP and AuNP having diameter between 2 and 100 nm, the position of this surface plasmon absorption (SPA) is about 400 nm (Ag) and 520 nm (Au). This plasmon oscillation, namely the displacement of conduction electrons from their equilibrium positions around positive ionic core, produces strong electric fields on particles surface, with intensity depending on their shape and assembly. In this case a size equation is used to describe the damping of the SPA band. In general plasmon oscillations have a fast damping times also for bigger sizes, as apparent for the intrinsic width of SPA.[24] Furthermore the SPA relaxation is essentially nonradiative.[24] This make AuNP and AgNP efficient localized converter of visible wavelengths into heat. The main parameters, applications and models for describing the SPA are discussed in chapter 2.

When nanoparticles size became comparable to de Broglie's wavelength of an electron at the Fermi energy, that is around 0.5 nm for gold and silver, quantum size effects appear. In this case optical properties of metal nanoparticles change, since the SPA is no more present while fluorescence emission due to transitions between discrete electronic states can be observed.[18]

Quantum size effects also enhance the deviation of conductivity from the usual ohmic behaviour in metal nanoparticles.[24] In this case the current voltage curve of a metal cluster has a staircase trend, instead of linear, with each step corresponding to a single electron tunnelling.[25] This behaviour can be observed only provided that thermal energy k_BT is lower than the characteristic Coulomb energy E_C of a single step:

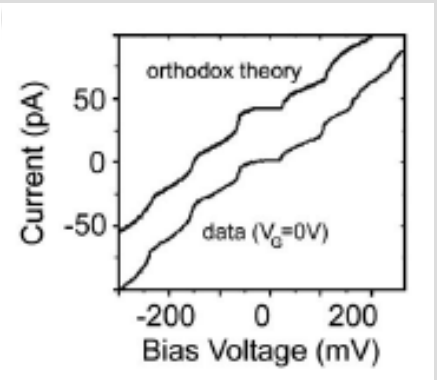

Figure 1.6 *Coulomb staircase I –V curve for a gold nanoparticle single electron transistor (SET) device at 4.2 K, along with a model fit (orthodox theory) offset for clarity, from ref. 25.*

$$E_C = \frac{e^2}{2C} + \Delta\varepsilon_C >> k_B T \qquad (1.2)$$

where e is the electron charge, $\Delta\varepsilon_C$ is a positive contribute due to energy level quantization and C is the nanoparticle capacitance. C is directly proportional to its size d as:

$$C = 2\pi\varepsilon\varepsilon_0 d \qquad (1.3).$$

Usually these experiments require low temperatures because level spacing of metal cluster as small as 50 atoms is still very close to thermal energy at room temperature and the classic electrostatic contribute to E_C is predominant.[19, 24]

Another electric effect is called Coulomb blockade and appear in capacitance measurements on small metal nanoparticles, independently of their energy level quantization. [19, 24] Very small metal particles have small capacitance C, then relatively high energy is required to add a single electron to the particle according to equation *1.2*. When this charging energy exceeds thermal energy, the quantized nature of charge transport through the nanoparticle become perceptible in the current voltage curve, that assume a staircase trend. For each step the charge transport is blocked (from here the name "*Coulomb blockade*") unless the applied potential overcomes the coulomb barrier for charging the particle with one electron at time.

Since electronic structure is the same of bulk metals, nanometric AuNP and AgNP are diamagnetic. On the contrary small oligoatomic cluster showed different magnetic properties, for instance degeneracy of *d* and *s* electronic levels in oligoatomic clusters of gold and silver originate ferromagnetic behaviour.[26]

Table 1.1

BULK PROPERTIES	SILVER	GOLD
ELECTRONIC CONFIGURATION	[Kr] $4d^{10}$ $5s^{1}$	[Xe] $5d^{10}$ $6s^{1}$
ATOMIC NUMBER - WEIGHT	47 – 107.87 u.a.	79 – 196.97 u.a.
LATTICE	f.c.c.	f.c.c.
LATTICE PARAMETER	0.409 nm	0.408 nm
DENSITY	10.50 g cm^{-3}	19.28 g cm^{-3}
ATOMIC DENSITY	5.86 10^{28} m^{-3} – 58.6 nm^{-3}	5.90 10^{28} m^{-3} – 59 nm^{-3}
VOLUME FOR ATOM	0.017 nm^{3}	0.017 nm^{3}
WIGNER – SEITZ RADIUS	0.160 nm	0.159 nm
ELECTRONIC DENSITY	5.86 10^{28} m^{-3}	5.90 10^{28} m^{-3}
FERMI SPEED	1.39 10^{8} cm s^{-1}	1.40 10^{8} cm s^{-1}
FERMI ENERGY	5.48 eV	5.51 eV
PLASMA FREQUENCY	1.30 10^{16} rad s^{-1}	1.31 10^{16} rad s^{-1}
RELAXATION TIME	4.01 10^{-14} s	2.94 10^{-14} s
IONIZATION ENERGY	7.57 eV	9.22 eV
ELECTRIC RESISTIVITY	1.61 10^{-6} Ω cm	2.20 10^{-6} Ω cm
MELTING TEMPERATURE	1235 K	1338 K
BOILING TEMPERATURE	2435 K	3243 K
THERMAL CONDUCTIVITY	4.29 W cm^{-1} K^{-1}	3.17 W cm^{-1} K^{-1}
HEAT CAPACITY	(25 °C) 25.350 $J{\cdot}mol^{-1}{\cdot}K^{-1}$	(25 °C) 25.418 $J{\cdot}mol^{-1}{\cdot}K^{-1}$
STANDARD POTENTIAL	+0.80 V	+1.69 V
ELECTRONEGATIVITY	1.9	2.4

References

1. Feynman, R. P., *Engineering and Science* **1960,** 23, 22 - 36.
2. Murray, C. B.; Kagan, C. R.; Bawendi, M. G., *Annual Review of Material Science* **2000,** 30, 545 - 610.
3. West, J. L.; Halas, N., *Current Opinion in Biotechnology* **2000,** 11, 215 - 217.
4. Daniel, M. C.; Astruc, D., *Chemical Review* **2004,** 104, 293 - 346.
5. British-Museum, *http://www.britishmuseum.org/explore/highlights/highlight_objects/pe_mla/t/the_lycurgus_cup.aspx*.
6. Padeletti, G.; Fermo, P., *Applied Physics A* **2003,** 76, 515 - 525.
7. Faraday, M., *Philos. Trans. Roy. Soc.* **1857,** 147, 145 - 181.
8. Whipple-Museum-of-the-History-of-Science, *http://www.hps.cam.ac.uk/whipple/explore/microscopes/faradaysslide/*.
9. Turkevich, J.; Stevenson, P. C.; Hillier, J., *Discuss. Faraday Soc.* **1951,** 11, 56.
10. Kreibig, U.; Vollmer, M., *Optical Properties of Metal Clusters*. Springer Verlag: Berlin, 1995.
11. Liz-Marzan, L. M., *Materials Today* **2004,** 2, 26 - 31.
12. Xia, Y.; Halas, N. J., *MRS Bulletin* **2005,** 30, 338 - 389.
13. Murphy, C. J.; Sau, T. K.; Gole, A. M.; Orendorff, C. J.; Gao, J.; Gou, L.; Hunyadi, S. E.; Li, T., *J. Phys. Chem. B* **2005,** 109, 13857 - 13870.
14. Wiley, B. J.; Im, S. H.; Li, Z.-Y.; McLellan, J.; Siekkinen, A.; Xia, Y., *J. Phys. Chem. B* **2006,** 110, 15666 - 15675.
15. Pileni, M. P., *Nature Materials* **2005,** 4, 395 - 398.
16. Zheng, N.; Fan, J.; Stucky, G. D., *Journal of American Chemical Society* **2006,** 128, 6550 - 6551.
17. Tang, Y.; Ouyang, M., *Nature Materials* **2007,** 6, 757 - 759.
18. Zheng, J.; Nicovich, P. R.; Dickson, R. M., *Annual Review of Physical Chemistry* **2007,** 58, 409 - 431.
19. Schmid, G., *Nanoparticles*. Wiley - VCH: Weinheim, 2004.
20. Jadzinsky, P. D.; Calero, G.; Ackerson, C. J.; Bushnell, D. A.; Kornberg, R. D., *Science* **2007,** 318, 431 - 433.
21. Jackson, A. M.; Myerson, J. W.; Stellacci, F., *Nature Materials* **2004,** 3, 330 - 336.
22. Greenwood, N. N.; Earnshaw, A., *Chemistry of the Elements*. Elsevier Science: Oxford, 1997.
23. Kvitek, L.; Prucek, R., *Journal of Material Science* **2005**.
24. Burda, C.; Chen, X.; Narayanan, R.; El-Sayed, M. A., *Chemical Review* **2005,** 105, 1025 - 1102.
25. Bolotin, K. I.; Kuemmeth, F.; Pasupathy, A. N.; Ralph, D. C., *Applied Physics Letters* **2004,** 84, 3154 - 3156.
26. Luo, W.; Pennycook, S. J.; Pantelides, S. T., *Nano Letters* **2007**.

Chapter 2

Photonics of gold and silver nanoparticles

The term *photonics*, in analogy to *electronics*, appeared soon after the invention of laser to describe communication technologies based on photons manipulation and, more in general, all linear and non-linear interactions of light with matter.[1] Hence, photonics is bound to laser light on one side and to materials with peculiar linear and non-linear optical properties on the other side. Though photonics is a relatively recent field, applications range in all the key technologies. In particular the combination of photonics with nanotechnology, sometimes cited as *nanophotonics*,[2] currently represents one of the hottest research topics. Photonics faces two main challenges in comparison to electronics, namely controlling photons manipulation or interactions and controlling photons confinement. Due to their charge, electrons strongly interact each other and their confinement in very small nanostructures can be simply obtained

controlling Coulomb forces. On the contrary photons have no charge and their manipulation and confinement are usually possible only through the polarization of materials. Moreover, common applications mainly exploit photon energy in the UV – Vis – NIR range. As a consequence, variation of the optical properties of the materials used for their manipulation is at least of the order of the photon wavelengths, namely hundreds of nanometers and, even using evanescent fields, it is still comparable to these wavelength.

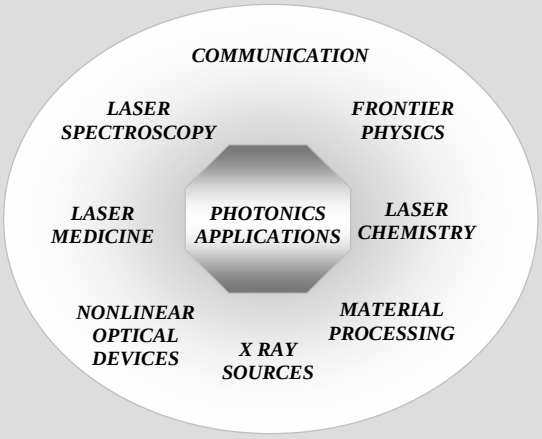

Figure 2.1 *Some applications of Photonics.*

Nanoscale materials are offering new opportunities to photonics because of their enhanced linear and non – linear optical properties and because of the ability to convert light into other forms of energy, as surface plasmons excitations. For these reasons gold and silver nanoparticles are key materials in nanophotonics. Due to their metallic nature, AuNP and AgNP possess a huge number of easily polarizable electrons, that means strong interactions of the matter with light and high non – linear optical properties. Indeed the dominant feature of AuNP and AgNP for actual photonic applications is originated by a linear optical process and consists of the surface plasmon absorption (SPA). This explains why photonics with gold and silver nanoparticles is often described as *plasmonics*.[3] The SPA lays in the visible spectral window for gold and silver particles with size of 2 – 100 nm and it is what confers the characteristic bright yellow and red colour to AgNP and AuNP colloidal solutions. The large number of electrons involved in the SPA accounts for the incredibly high extinction cross section of these nanoparticles, which is $10^5 – 10^6$ larger than that of organic chromophores.[3] Another general photonic peculiarity of AuNP and AgNP is their solid

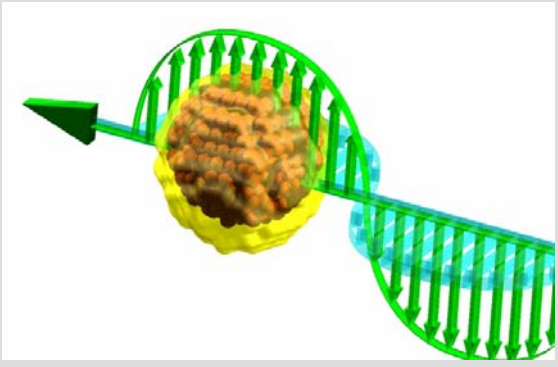

Figure 2.2 *Conduction electrons of silver and gold nanoparticles can be collectively excited (plasmon) by electromagnetic wave in the visible, originating the surface plasmon absorption (SPA) band in the UV-Vis spectra.*

state behaviour, in contrast to common molecular chromophores. Two simple consequences are the extremely high photostability and the fast conversion of light into heat, as discussed in following paragraphs.

Several models are used to describe the SPA, some exploit their symmetry to achieve an analytical formula for the extinction cross section, while others use numerical methods to obtain the optical properties of particles with complex shape and to sketch the electric field originated by the collective conduction electrons oscillations on particles surface. In both cases the electromagnetic problem, concerning the geometry and the relative size of particles to photons wavelength, is decoupled from the material problem of size effects which originates a different dielectric responses for bulk and nanometric objects.

2.1 Origin of the surface plasmon absorption.

Collective oscillation of conduction electrons in metals are known as "*plasmons*".[4-6] According to the Fermi liquid model, plasmons can be satisfactorily described as a negatively charged electron cloud displaced from its equilibrium position around a lattice made of positively charged ions, in analogy to a real plasma. The characteristic oscillation frequency is given by:[4]

$$\omega_P = \sqrt{\frac{Ne^2}{\varepsilon_0 m_e}} \qquad (2.1)$$

where ω_P is the plasma frequency, N is the conduction electron density, e is the electron charge, m_e is the electron effective mass and ε_0 is the vacuum dielectric permittivity.

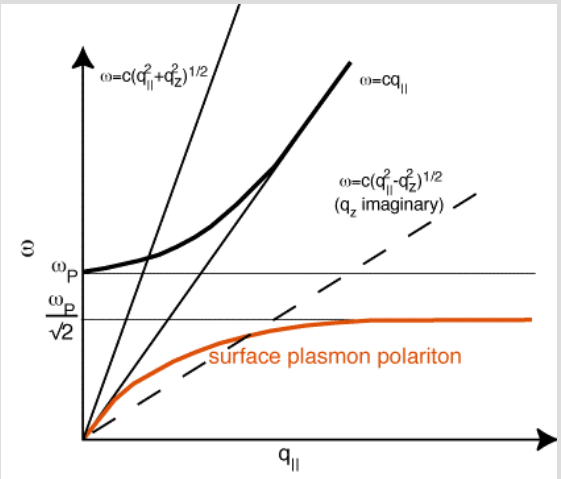

Figure 2.3 *Energy dispersion curves for plasmons on a plane metal surface cross the dispersion curve of photons with imaginary wavevectors, meaning that evanescent electromagnetic waves can excite surface plasmons - polaritons. From ref. 6.*

Excitation of bulk plasmons by photons is not allowed, since plasmons and photons energy dispersion curves never cross each other.[6] In fact, for a given wavelength, a photon in free space has a wavevector that is always smaller than the corresponding plasmon, and the momentum conservation required for their coupling cannot be fulfilled.[3] On the other hand, the presence of a surface in real materials, introducing new boundary conditions and modifying the symmetry of the electromagnetic problem, allows the existence of new

collective oscillation modes with strong difference in the energy dispersion curve. These surface confined plasmons have wave vectors compatible with those in the dispersion curve of photons and plasmon excitation by electromagnetic waves become allowed. In this case the coherent electron oscillation is called surface plasmon – polariton, in analogy to optically active surface phonons – polaritons.[6]

The typical experiment to measure plasmon oscillations in bulk metals is based on electron energy loss spectroscopy (EELS). Usually, electrons of a TEM electron beam transfer quantized amounts of energy as single or multiple plasmon excitations in the metal. Since electron transparency is required for TEM measurements, samples of bulk metal are actually metal films thick hundred of nanometers, so both surface and bulk plasmons are observed.[5]

Reflectance measurements are used to investigate surface plasmon absorptions of metal films with an attenuated total reflection (ATR) set up,[6] which have important applications in hypersensitive biological analysis.[7]

Metal nanoparticles surface plasmons can be measured by EELS or detected by UV – vis spectroscopy.[5]

When particle size is small compared to the resonant electromagnetic wavelength, the electric field distribution along the particle is uniform, electron cloud polarization is coherent in each point of the particle and dipolar plasmon oscillations are excited.

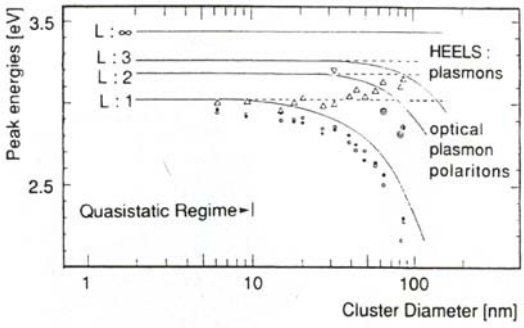

Figure 2.4 *Free plasmon energies measured by EELS have a trend different from optically measured plasmon energies for silver nanoparticles larger than 20 nm. From ref. 5.*

In this case the momentum conservation is not important, as for a bulk metal, since wavevectors loose their meaning over very short distances. When particle size is comparable to the resonant electromagnetic wavelength, the electric field distribution along the particle is non uniform, electron cloud polarization is no more coherent in each point of the particles and multipolar plasmon oscillations are excited.[5]

Typical EELS measurements on nanoparticles detect both dipolar and multipolar excitations but only in the quasistatic regime the plasmon – polaritons energies coincide with those of free bulk plasmons.[5]

Recently two new techniques for plasmon imaging on nanometer scale have been proposed, the first with a resolution of 10 nm, based on the EELS of a collimated electron beam in a scanning TEM (STEM),[8] and the second based on cathodoluminescence imaging spectroscopy with a scanning electron microscope (SEM) and a resolution of about 15 nm.[9]

The surface plasmon absorption is around 400 nm, 520 nm and 600 nm for spherical nanoparticles of silver, gold and copper respectively. One finds that dipolar oscillations dominates for particle sizes of about 20 nm, while multipolar contributes are dominant above 60 nm.[5] Gold, silver and copper are the only metals with a sharp and bright SPA in the visible range.

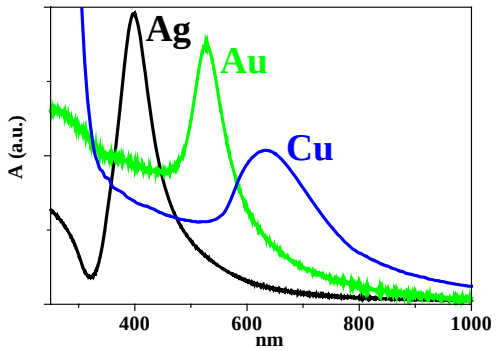

Figure 2.5 *Surface Plasmon Absorption of colloidal solutions of silver, gold and copper spherical nanoparticles obtained by laser ablation in common solvents.*

Particularly Ag and Au plasmon absorptions are unique because two kinds of characteristics affect other elements, the first being that plasmon absorption lays too high in energy for visible light, as for platinum, and the second reason being that superposition of plasmon absorption with interband transitions produce a strong damping of the former, as for lead and copper, although in the second case the damping allows in any case to observe a well definite absorption.[3] Such an effect is important for the imaginary part of the metal dielectric constant, which contributes to the SPA width.[3, 10] Interband absorption for gold and silver refer to 5d –> 6s/6p and 4d –> 5s/5p transitions respectively.

Other than size, Au and Ag SPA is primarily affected also by particles shape and physical – chemical environment, included the reciprocal distance between particles. Details of these dependences are discussed in following paragraphs with the help of specific models.

2.2 Mie model.

In the last 99 years Mie theory has been successfully applied to the calculation of noble metal nanoparticles extinction cross section. Gustav Mie solved the problem of light diffraction by a single sphere using classic electrodynamics.[11] Subsequent refinement of

the theory by Stratton[12] and Born[13] preserved the main framework, consisting in the solution of Maxwell equations in spherical coordinates with proper boundary conditions and multipoles expansion of electromagnetic field diffused and inside the sphere. The Mie model expressions of extinction cross section σ_{ext}, absorption cross section σ_{abs} and scattering cross section σ_{sca} for a single sphere of radius R are:[5]

$$\sigma_{ext} = \frac{2\pi}{\left|\bar{k}^2\right|}\sum_{L=1}^{\infty}(2L+1)\mathrm{Re}\left[a_L + b_L\right] \qquad (2.1)$$

$$\sigma_{sca} = \frac{2\pi}{\left|\bar{k}^2\right|}\sum_{L=1}^{\infty}(2L+1)\left(\left|a_L\right|^2 + \left|b_L\right|^2\right) \qquad (2.2)$$

$$\sigma_{abs} = \sigma_{ext} - \sigma_{sca} \qquad (2.3)$$

$$a_L = \frac{m\cdot\psi_L(mx)\cdot\psi_L'(x) - \psi_L'(mx)\cdot\psi_L(x)}{m\cdot\psi_L(mx)\cdot\eta_L'(x) - \psi_L'(mx)\cdot\eta_L(x)} \qquad (2.4)$$

$$b_L = \frac{\psi_L(mx)\cdot\psi_L'(x) - m\psi_L'(mx)\cdot\psi_L(x)}{\psi_L(mx)\cdot\eta_L'(x) - m\psi_L'(mx)\cdot\eta_L(x)} \qquad (2.5)$$

$$m = \frac{n}{n_m} \qquad (2.6)$$

$$x = \left|\bar{k}\right|R \qquad (2.7)$$

where k is the incident photon wavevector, n is the complex refraction index of the sphere, n_m is the real refraction index of the non absorbing surrounding medium and ψ_L and η_L are the spherical Riccati – Bessel functions. The electric and magnetic fields resultant inside the sphere are expressed as a multipolar series of spherical harmonics with different symmetry, identified by the multipolar order L. L equal to 1 corresponds

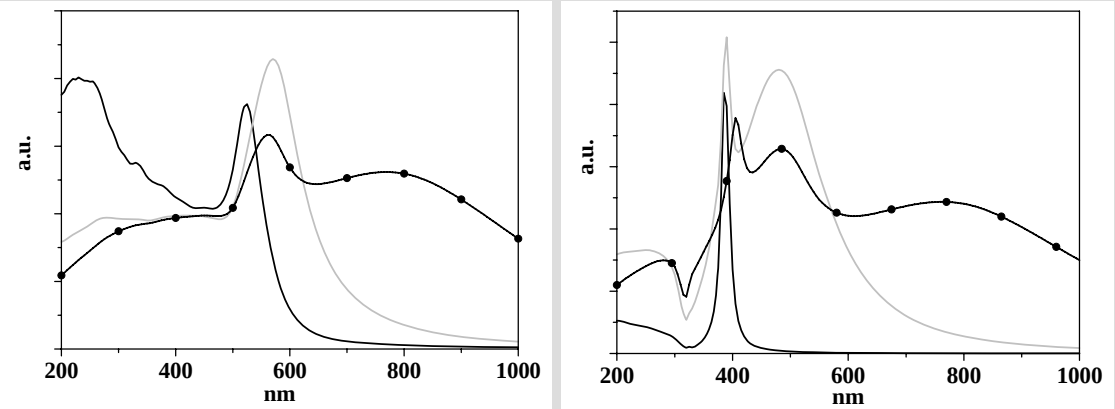

Figure 2.6 *Mie model simulations for gold (left) and silver (right) spheres with radii of 10 nm (black lines), 50 nm (grey lines) and 100 nm (black circles) in water matrix. By increasing the size, dipolar resonances red shift, while quadrupolar and octupolar resonances rise at higher wavelengths.*

to dipolar sphere excitation, L equal to 2 correspond to quadrupolar oscillation and so on. In metal spheres the excitations due to photons electric field are plasmons – polaritons, while those due to photons magnetic field are electric currents.[5]

The x parameter determines if the sphere is in quasistatic (dipolar : $R << \lambda$ then $|x| << 1$) or in dynamic regime (multipolar : $R \sim \lambda$).[5] This type of size dependence is called *extrinsic size effect* in contrast to the *intrinsic size effect* due to the metal dielectric constant dependence on the size, which is discussed in the following paragraph. In the quasistatic case, scattering contributes, that are proportional to $|x|^6$, and absorption contributes for $L > 1$, that are proportional to $|x|^i$ with $i > 4$, can be neglected to obtain a simplified expression for σ_{ext}:[5]

$$\sigma_{ext} = 9\frac{\omega}{c}\varepsilon_m^{3/2} V \frac{\varepsilon_2(\omega, R)}{[\varepsilon_1(\omega, R) + 2\varepsilon_m]^2 + \varepsilon_2(\omega, R)^2} \qquad (2.8-a)$$

$$\varepsilon(\omega, R) = \varepsilon_1(\omega, R) + i\varepsilon_2(\omega, R) \qquad (2.8\text{-}b)$$

where V is the sphere volume, $\varepsilon(\omega, R)$ is the sphere dielectric constant and ε_m is the medium real dielectric constant. Equation 2.8 points out that σ_{ext} is proportional to the sphere volume. Besides, the dielectric constant is dependent also on R, and not only on the photon frequency ω, due to intrinsic size effects.[5]

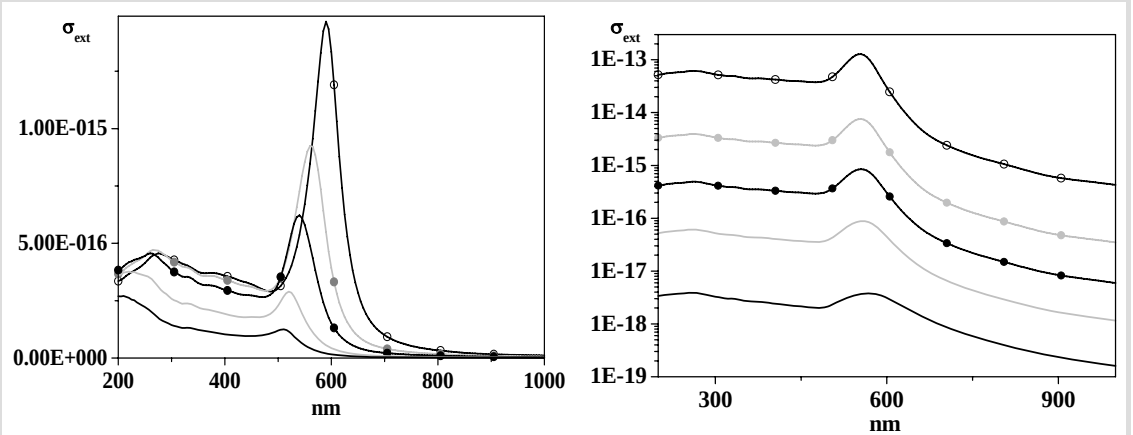

Figure 2.7 *Left: Mie model simulations for 10 nm radius gold spheres with a matrix refraction index increasing from 1 (black line) to 2 (hollow circles). Intermediate values of 1.25 (grey line), 1.55 (black circles) and 1.75 (grey circles). Right: Mie model simulations gold spheres in water matrix with increasing radius: 2 nm (black line), 5 nm (grey line), 10 nm (black circles), 20 nm (grey circles) and 50 nm (hollow circles).* σ_{ext} *expressed in* m^{-2}.

The extinction cross section determines the UV – Vis absorption spectrum of N identical metal nanoparticles for unit volume as:

$$T(\omega) = \frac{I(\omega)}{I_0(\omega)} = exp[-dN\sigma_{ext}(\omega)] \qquad (2.9)$$

$$A(\omega) = -Log_{10}[exp[-dN\sigma_{ext}(\omega)]] \qquad (2.10)$$

where T is the transmittance, A is the absorbance, d is the optical path and I is the incident light intensity.

In presence of a nanoparticles size distribution $f(R)$, the extinction coefficient $N\sigma_{ext}(\omega)$ is replaced by the integral $\gamma_{ext}(\omega)$:

$$\gamma_{ext}(\omega) = N\int_0^\infty f(R)\sigma_{ext}(\omega, R)dR \qquad (2.11).$$

2.3 Dielectric constant of metal nanoparticles.

Contrary to extrinsic size effects on the extinction cross section, that are bare electromagnetic phenomena, intrinsic size effects are only due to the dependence of metal dielectric constant on the size. In case of spherical AuNP and AgNP the extrinsic size effects are perceptible for sizes above 30 nm in diameter and become important for sizes above 60 nm, while intrinsic ones appear in the SPA below that limit.

In general the optical properties of noble metals are determined by conduction electrons and d – band electrons. Therefore the dielectric constant in the UV – Vis – NIR regime is composed of two terms:[5]

$$\varepsilon_\infty(\omega) = 1 + \chi_s(\omega) + \chi_d(\omega) \qquad (2.12)$$

where $\chi_d(\omega)$ is the contribute of d – bands electrons and $\chi_s(\omega)$ is that of s – band conduction electrons and can be expressed by a simple Drude – Sommerfield model:

$$\chi_s(\omega) = -\frac{{\omega_P}^2}{\omega^2 + {\Gamma_\infty}^2} + i\frac{{\omega_P}^2\Gamma_\infty}{\omega\left(\omega^2 + {\Gamma_\infty}^2\right)} \qquad (2.13)$$

where Γ_∞ is the bulk metal damping frequency. According to the Matthiessen rule, conduction electron damping frequency of bulk metals is the sum of three main independent processes, namely electron - electron scattering (τ_{e-e}), electron - phonon scattering (τ_{e-p}) and electron - defects scattering (τ_{e-d}):[4]

$$\Gamma_\infty = \frac{1}{\tau_{e-e}} + \frac{1}{\tau_{e-p}} + \frac{1}{\tau_{e-d}} \qquad (2.14).$$

For metal particles with nanometric size the usual scattering processes change and new contributes appear, mainly due to surface effects. The dominant process consist of

electron scattering at particle surface, that is no more negligible when conduction electrons mean free path (~ 45 nm for Au and Ag) becomes comparable to particle size. This scattering contributes overshadow other phenomena originated by changes in the phonons spectra, quantum size effects, changes in the phonon – electrons coupling for the high surface charge during plasmon oscillation and so on. Actually surface scattering produces the complete quenching of SPA in AuNP and AgNP smaller than about 2 nm and 1.5 nm respectively.[3, 14]

The most common way to account for the surface effect on the dumping frequency Γ consist in expressing the Matthiessen formula as a size equation:[5, 15]

$$\Gamma(R) = \Gamma_\infty + A\frac{v_F}{R} \qquad (2.15)$$

where v_F is the Fermi speed and A is an empirical adimensional parameter usually close to 1, used to account for some factors affecting the width for the SPA in specific cases.

When replacing Γ_∞ with $\Gamma(R)$ in equation 2.13, two terms can be isolated in the expression of the dielectric constant:[5]

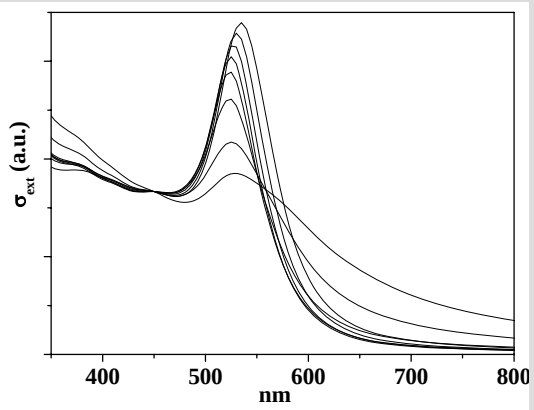

Figure 2.8 *Mie model simulations for gold spheres in water matrix with radius increasing from 1 (most damped curve) to 30 nm (sharpest curve). Intermediate values of 2, 5, 10, 15, 20 and 25 nm. All spectra normalized at 450 nm.*

$$\varepsilon(\omega, R) = \varepsilon_\infty(\omega) + \left[\omega_P{}^2\left(\frac{1}{\omega^2 + \Gamma_\infty{}^2} - \frac{1}{\omega^2 + \Gamma(R)^2}\right)\right] + i\left[\frac{\omega_P{}^2}{\omega}\left(\frac{\Gamma(R)}{\omega^2 + \Gamma(R)^2} - \frac{\Gamma_\infty}{\omega^2 + \Gamma_\infty{}^2}\right)\right] \qquad (2.16)$$

The first is equal to the bulk constant and only the second accounts for the size effect on the dielectric response of nanometric objects. For Au and Ag the $\varepsilon_\infty(\omega)$ is experimentally known with high precision,[16, 17] hence correction of $\varepsilon(\omega, R)$ for the size is straightforward.

2.4 Specific phenomena influencing the surface plasmon absorption.

A certain number of specific factors with not negligible influence on the SPA exist, other than surface electronic scattering.

When a single nanoparticle is polycrystalline, electron scattering at the grain boundaries increase the dumping frequency and produce slightly larger SPA.[18]

High temperatures produce a small broadening of the SPA because the electron – electron scattering frequency is dependent on the Fermi – Dirac electron distribution as:[15]

$$\frac{1}{\tau_{e-e}} \propto \left(E - E_F\right)^2 \qquad (2.17)$$

where E_F is the Fermi energy and E is the electron energy.

Electronic density at metal surface decays on a length scale of the Thomas – Fermi wavelength, that is less than 1 Å in noble metals. Nevertheless for particles of less than 5 nm the electron density spill out produces a slight decrease of the effective plasma frequency and an higher polarizability of the electron cloud, that originate a red shift of the SPA not contemplated by Mie model.[5]

In some cases, as for nanoparticles synthesized by laser ablation, the electron density can be different for the presence or the absence of some electrons in the nanoparticle. For particles of 2.5 nm in diameter, containing about 480 conduction electrons, one electron account for the 0.2 % of the overall charge. This is enough to influence the position and the width of the SPA of a significant quantity.[14]

Another specific effect influencing the SPA arises because metal nanoparticles change the overall dielectric properties of a material when they are present in high concentration. As a consequence, also the SPA of each single metal nanoparticle is affected by other particles present in the surrounding matrix. The Maxwell Garnett model is an effective medium model which accounts for the dielectric constant of a nanocomposite material made by spherical nanoparticles randomly dispersed in a host medium. The effective dielectric constant ε_{eff} of the nanocomposite matrix can be derived by the following expression:[5]

$$\frac{\varepsilon_{eff} - \varepsilon_m}{\varepsilon_{eff} + 2\varepsilon_m} = q\frac{\varepsilon_{NP} - \varepsilon_m}{\varepsilon_{NP} + 2\varepsilon_m} \qquad (2.36)$$

where ε_{NP} and ε_m are the nanoparticles and the matrix dielectric constant respectively, and q is the fill fraction of particles. AuNP and AgNP effects on ε_{eff} appear for q larger than 10%.

The most intense and common specific mechanism influencing the surface plasmon absorption is called chemical interface damping (CID).[5, 19] CID produces a sensible widening and red shift of the SPA when adsorbates are present on particles surface. This holds both for chemisorption, as in case of thiols stabilized nanoparticles, and for

physisorption, as in case of citrate or alchilamine stabilized nanoparticles. The SPA broadening due to CID is explained considering that adsorbates offer new relaxation pathways for both excited electrons and phonons in the metal. Persson developed a model in which the empty LUMOs of adsorbates are coupled with conduction band electrons.[5]

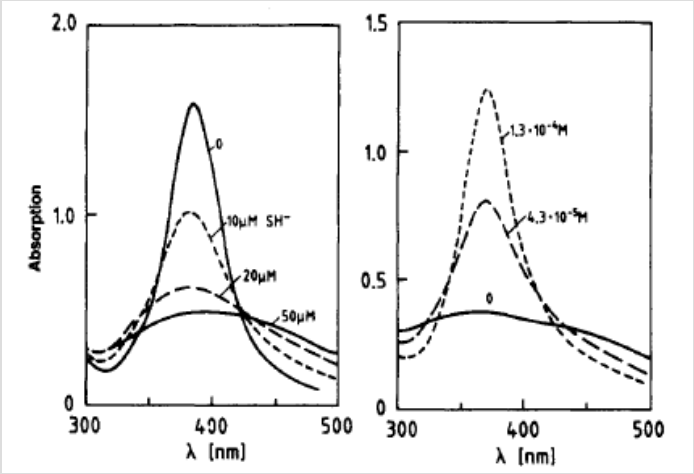

Figure 2.9 *(Left) Absorption spectrum of AgNP in water before and after addition of various concentrations of NaSH. (Right) Adsorption spectrum of AgNP in water carrying SH- on the surface before and after deposition of excess electrons (two excess electron concentrations shown). From ref. 19.*

During plasmon oscillation the reversible electron transfer into LUMOs is possible, originating fast loss of coherence with other excited electrons and a larger bandwidth. Different adsorbates have different LUMO position, then couple in a different way with the metal conduction band and originate different SPA width.

In case of adsorbed layers with monoatomic thickness the CID can be accounted by changing the *A* parameter in equation 2.15. In the main part of real cases the thickness of adsorbed layer is on the order of 1 nm or more, as for alcanthiols stabilization, then the SPA assume the typical features of a core@shell nanoparticle with metal@dielectric structure.

2.5 Sensing by surface plasmon absorption.

Metal nanoparticles SPA found large applications for chemical and biological sensing, due to sensitive spectral response to local surface environment and ease of monitoring the light signal due to the strong light scattering and absorption.[3]

The spectral sensitivity, defined as the relative shift in resonance wavelength with respect to the refractive index change of surrounding materials, is dependent on the SPA position and width, which in turn depend on metal type and on particles shape. Silver is more sensible than gold to surface environment and nanorods are better than spheres in reason of a plasmon absorption band more sharp and intense. This determines a longer

spatial range of the decaying electromagnetic field, allowing appreciable sensitivity up to a distance of 40 nm.[3, 20]

In general a linear relationship between the absorption or scattering band position and the surrounding refraction index exists, with a slope of about 100 nm for refraction index unit. This sensitivity is enough to discriminate between adsorbed alcanethiols differing of a single CH_2 unit in their chains.[21]

Nanosphere lithography is the most commonly used technique for obtaining ordered arrays of triangular silver or gold prisms on a substrate with sizes of tens - hundreds of nanometers, spacing of hundreds of nanometers and defect free domains on the scale of 10 – 100 μm over the array.[22] Silver structures on the 50 –100 nm size range have scattering efficiencies comparable to the emission of 10^6 ordinary fluorophors. Usually these metal nanoparticles are functionalized with a specific molecular receptor for a target molecule.

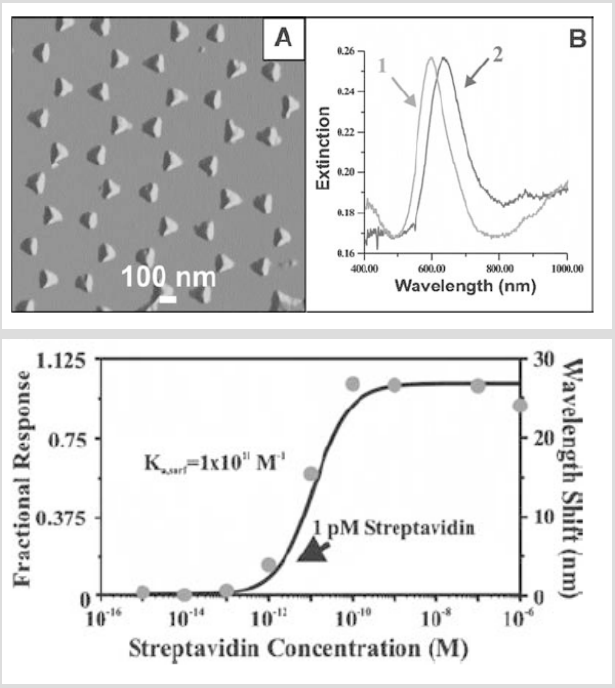

Figure 2.10 *Top: A) AFM image of Ag pyramids (width=100 nm, height=50.0 nm) obtained by nanosphere lithography on a mica substrate. B) Spectra of nanopyramids in a nitrogen environment before chemical modification (1: λ_{max}=594.8 nm) and after surface modification with hexadecanethiol (2: λ_{max}=634.8 nm). Down: Response curve of the specific binding of streptavidin to functionalized Ag nanopyramids showing picomolar sensitivity. From ref. 22.*

This approach is similar to enzyme linked immunosorbent assay (ELISA), the difference lying in that ELISA requires a second specific fluorescent label able to bind the target in a sandwich structure, while localized surface plasmon assays exploit the change in the surrounding refraction index of metal nanoparticles upon binding of the target molecule. Photostability and intensity allow detection limits of less than 1 pM.[3, 22]

2.6 Analytical models for SPA of core@shell spheres and non spherical particles.

The Mie model for simple spheres can be generalized to core@shell spheres of indefinite number of layers, exploiting the spherical symmetry of the problem. The σ_{ext} of a sphere made of *r* concentric layers can be expressed as:[5]

$$\sigma_{ext} = \frac{2\pi}{\left|\bar{k}_h{}^2\right|}\sum_{L=1}^{\infty}(2L+1)\mathrm{Re}[a_L + b_L] \qquad (2.1)$$

$$a_L = \frac{m_r \cdot \psi_L(m_r x_r)\cdot\left[\psi_L'(x_r) + T_L^r \chi_L'(x_r)\right] - \psi_L'(m_r x_r)\cdot\left[\psi_L(x_r) + T_L^r \chi_L(x_r)\right]}{m_r \cdot \eta_L(m_r x_r)\cdot\left[\psi_L'(x_r) + T_L^r \chi_L'(x_r)\right] - \eta_L'(m_r x_r)\cdot\left[\psi_L(x_r) + T_L^r \chi_L(x_r)\right]} \qquad (2.18)$$

$$b_L = \frac{\psi_L(m_r x_r)\cdot\left[\psi_L'(x_r) + S_L^r \chi_L'(x_r)\right] - m_r \cdot \psi_L'(m_r x_r)\cdot\left[\psi_L(x_r) + S_L^r \chi_L(x_r)\right]}{\eta_L(m_r x_r)\cdot\left[\psi_L'(x_r) + S_L^r \chi_L'(x_r)\right] - m_r \cdot \eta_L'(m_r x_r)\cdot\left[\psi_L(x_r) + S_L^r \chi_L(x_r)\right]} \qquad (2.19)$$

$$T_L^s = -\frac{m_s \cdot \psi_L(m_s x_s)\cdot\left[\psi_L'(x_s) + T_L^{s-1} \chi_L'(x_s)\right] - \psi_L'(m_s x_s)\cdot\left[\psi_L(x_s) + T_L^{s-1} \chi_L(x_s)\right]}{m_s \cdot \chi_L(m_s x_s)\cdot\left[\psi_L'(x_s) + T_L^{s-1} \chi_L'(x_s)\right] - \chi_L'(m_s x_s)\cdot\left[\psi_L(x_s) + T_L^{s-1} \chi_L(x_s)\right]} \qquad (2.20)$$

$$T_L^1 = -\frac{m_1 \cdot \psi_L(m_1 x_1)\cdot \psi_L'(x_1) - \psi_L'(m_1 x_1)\cdot \psi_L(x_1)}{m_1 \cdot \chi_L(m_1 x_1)\cdot \psi_L'(x_1) - \chi_L'(m_1 x_1)\cdot \psi_L(x_1)} \qquad (2.21)$$

$$S_L^s = -\frac{\psi_L(m_s x_s)\cdot\left[\psi_L'(x_s) + S_L^{s-1} \chi_L'(x_s)\right] - m_s \cdot \psi_L'(m_s x_s)\cdot\left[\psi_L(x_s) + S_L^{s-1} \chi_L(x_s)\right]}{\chi_L(m_s x_s)\cdot\left[\psi_L'(x_s) + S_L^{s-1} \chi_L'(x_s)\right] - m_s \cdot \chi_L'(m_s x_s)\cdot\left[\psi_L(x_s) + S_L^{s-1} \chi_L(x_s)\right]} \qquad (2.22)$$

$$S_L^1 = -\frac{\psi_L(m_1 x_1)\cdot \psi_L'(x_1) - m_1 \cdot \psi_L'(m_1 x_1)\cdot \psi_L(x_1)}{\chi_L(m_1 x_1)\cdot \psi_L'(x_1) - m_1 \cdot \chi_L'(m_1 x_1)\cdot \psi_L(x_1)} \qquad (2.23)$$

$$m_s = \frac{n_{s+1}}{n_s} \qquad (2.24)$$

$$x_s = \left|\bar{k}_s\right| R_s \qquad (2.25)$$

where symbols correspond to those of equations *2.1 – 2.7*, $\chi(x)$ is another spherical Riccati – Bessel function and *s* is the layer number, ranging from between 1 (the core) to *r* + 1 (the surrounding matrix).

The case of a sphere with only one shell in dipolar approximation can be expressed as:[5]

$$\alpha = \frac{4\pi}{3}(R+d)^3 \varepsilon_0 \frac{(\varepsilon_s - \varepsilon_m)(\varepsilon + 2\varepsilon_m) + \left(\frac{R}{R+d}\right)^3 (\varepsilon - \varepsilon_s)(\varepsilon_m + 2\varepsilon_s)}{(\varepsilon_s + 2\varepsilon_m)(\varepsilon + 2\varepsilon_s) + \left(\frac{R}{R+d}\right)^3 (\varepsilon - \varepsilon_s)(2\varepsilon_s - \varepsilon_m)} \qquad (2.26)$$

$$\sigma_{ext} = 4\pi\, k\, \mathrm{Im}[\alpha] \qquad (2.27)$$

where R represents the core radius, d the shell thickness, ε, ε_s and ε_m the dielectric constants of core, shell and matrix respectively.

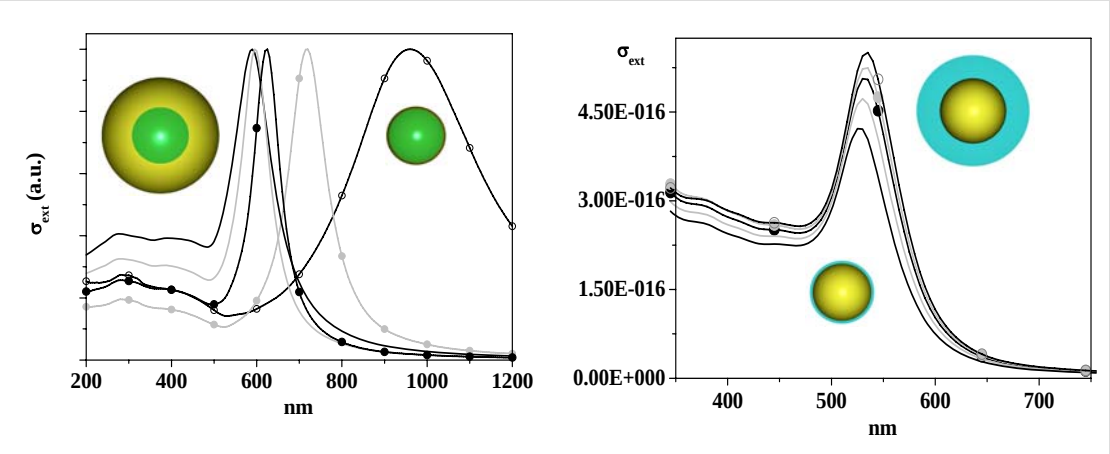

Figure 2.11 *Left: Mie model simulations for core@shell nanoparticles in water with a silica core of radius 25 nm and a gold shell of thickness 25 nm (black line), 15 nm (grey line) 10 nm (black circles), 5 nm (grey circles) and 2 nm (hollow circles). Right: core@shell nanoparticles in water with a gold core of radius 10 nm and a silica shell of thickness 2 nm (black line), 5 nm (grey line) 10 nm (black circles), 15 nm (grey circles) and 25 nm (hollow circles).*

Another analytical model which describes core@shell metallic nanoparticles is the hybridization model (HM).[3, 23, 24] According to the HM one can treat the optical response of a core@shell structure as the interaction, or hybridization in analogy to the molecular orbital theory, of the plasmon of a metal sphere and that of a cavity in a metal matrix. Coupling derives from the interaction of the local charge inhomogeneities characteristic of plasmon oscillations. This interaction produces two new plasmonic states with energy higher and lower than pristine plasmons. Only the lower in energy can be excited by electromagnetic radiation and is defined as bright or bonding state, while the other one is a dark or anti bonding state non optically active.

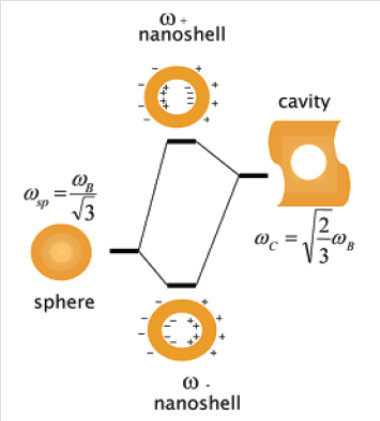

Figure 2.12 *Energy level diagrams depicting plasmon hybridization in metal nanoshells resulting from interacting sphere and cavity plasmons with the two hybridized plasmon modes being an antisymmetric or "antibonding" plasmon (ω^+) and a symmetric or "bonding" plasmon resonance (ω^-). From ref. 24.*

The hybridization model can be generalized to metal nanostructures of greater geometrical complexity but in case of a core@shell sphere its accuracy is that of the Mie theory.[23]

Analytical solutions within classical

electromagnetic theory are possible also for non spherical nanoparticles with high symmetry like spheroids and cubes, provided that the dipolar approximation is appropriate.

The Gans model is used to calculate the σ_{ext} of spheroids having the longer axis smaller than about 50 nm, otherwise multipolar effects are no more negligible. Spheroids have lower symmetry compared to a sphere and this produces the quenching of multipolar plasmon oscillations.[19]

For ~~a~~ spheroids with random orientation σ_{ext} is:[5]

$$\sigma_{ext} = \frac{2\pi V \varepsilon_m^{3/2}}{3\lambda} \sum_j \frac{\frac{1}{P_j^2}\varepsilon_2(\omega,R)}{\left(\varepsilon_1(\omega,R)+\frac{1-P_j}{P_j}\varepsilon_m\right)^2+\varepsilon_2(\omega,R)^2} \qquad (2.28)$$

$$P_a = \frac{1-e^2}{e^2}\left[\frac{1}{2e}\ln\left(\frac{1+e}{1-e}\right)-1\right] \qquad (2.29)$$

$$P_b = P_c = \frac{1-P_a}{2} \qquad (2.30)$$

$$e = \sqrt{1-\left(\frac{b}{a}\right)^2} = \sqrt{1-\left(\frac{1}{D}\right)^2} \qquad (2.31)$$

where λ is the incident photon wavelength, a is the larger semiaxis and $b=c$ are the shorter. The eccentricity is e and the aspect ratio characteristic of the spheroid is D. As expected for a metal particle with lower symmetry, a spheroid with two different axis has two surface plasmon absorption bands. The first, corresponding to oscillation along the minor axis, is slightly blue shifted with respect to the equivalent sphere SPA, while the other, corresponding to oscillation along the major axis, is red shifted. The wavelength of the longitudinal plasmon absorption is almost linearly dependent on the aspect ratio and the matrix dielectric constant:[25]

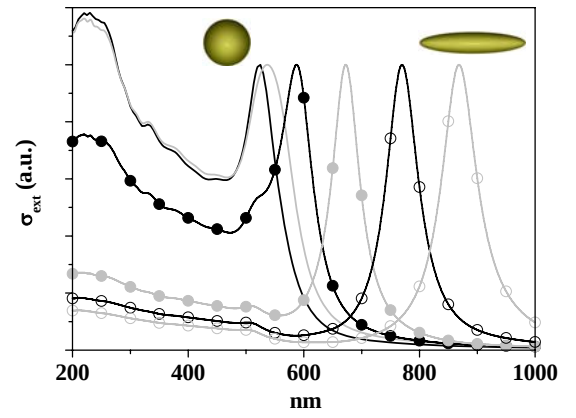

Figure 2.13 *Gans model simulations for gold spheroids in water with aspect ratio equal to 1 (black line), 1.5 (grey line), 2 (black circles), 3 (grey circles), 4 (black hollow circles) and 5 (grey hollow circles) .*

$$\lambda_{SPA} = (Kost'D - Kost'')\varepsilon_m + Kost''' \quad (2.32)\,.$$

The red shifted plasmon absorption band is narrower compared to a sphere due to the decreased importance of interband transitions, especially for gold.

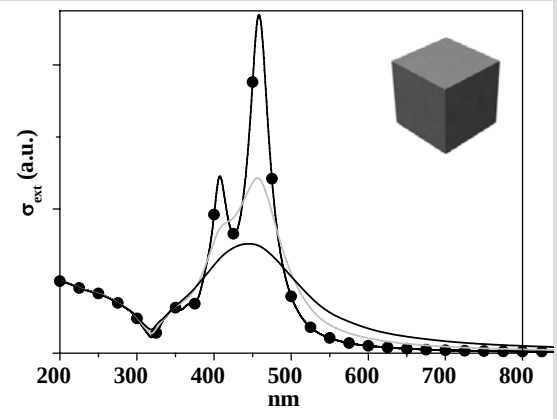

Figure 2.14 *Fuchs model simulations for silver cubes of side 2 nm (black line), 4 nm (grey line) and 10 nm (circles) in dimethylformamide matrix.*

A rough estimation of cubic metal nanoparticles σ_{ext} is provided by the Fuchs model.[5, 26] The presence of edge and corners prevents uniform polarization in a metal cube and originates several plasmon resonances. The resulting Fuchs polarization α of a cube is:[5]

$$\alpha = \varepsilon_0 V \sum_{j=1}^{N} \frac{C_j\left(\varepsilon(\omega,R) - \varepsilon_m\right)}{L_j\left(\varepsilon(\omega,R) - \varepsilon_m\right) + \varepsilon_m} \qquad (2.32.a)$$

$$\sigma_{ext} = \frac{4\pi\omega}{3c\varepsilon_0\sqrt{\varepsilon_m}} Im[\alpha] \qquad (2.32.b)$$

where C_j are the oscillator strengths and L_j are geometry factors due to depolarization. Plasmon resonances for a cube are 9, but only 6 have significant intensity, therefore N=6.[26] The accord between Fuchs model and experimental data is only qualitative, while other models based on numerical methods are required for the correct prediction of cubic metal particles SPA.

2.7 Discrete dipole approximation.

Maxwell equations cannot be solved analytically for particles with low symmetry, then numerical methods are necessary. For isolated metal nanoparticles of arbitrary shape the most widely used method is the discrete dipole approximation (DDA).[10] In DDA the nanostructure of interest, also called target, is represented by a cubic array of N polarizable points, i.e. N cubic dipoles. There are no restrictions about the complexity or the shape of the target, the only limitation being the discrete structure of the target due to the finite number of dipoles utilised.

Basically, the polarization P_j induced on each point j of position r_j and polarizability α_j is given by:[10]

$$\overline{P_j} = \alpha_j \overline{E}_{Loc}\left(\overline{r}_j\right) \qquad (2.33)$$

where E_{Loc} is the electric field originated by the incident radiation plus the contributes of all other dipoles:[10]

$$\overline{E}_{Loc}\left(\bar{\mathrm{r}}_{\mathrm{j}}\right)=\overline{E}_{0}\exp\left(i\bar{k}\cdot\bar{\mathrm{r}}_{\mathrm{j}}+i\omega t\right)-\sum_{\mathrm{l}\neq\mathrm{j}}\overline{\overline{A}}_{jl}\,\overline{P}_{l} \qquad (2.34)$$

where $\overline{\overline{A}}_{jl}$ is the interaction matrix. The full expression of $\overline{\overline{A}}_{jl}\,\overline{P}_{l}$ is:[10]

$$\overline{\overline{A}}_{jl}\,\overline{P}_{l}=\frac{\exp\left(ik\bar{r}_{jl}\right)}{\bar{r}_{jl}^{\,3}}\times\left\{k^{2}\bar{r}_{jl}\times\left(\bar{r}_{jl}\times\overline{P}_{l}\right)+\frac{\left(1-ik\bar{r}_{ij}\right)}{\bar{r}_{jl}^{\,2}}\left[\bar{r}_{jl}^{\,2}\overline{P}_{l}-3\bar{r}_{jl}\left(\bar{r}_{jl}\cdot\overline{P}_{l}\right)\right]\right\} \quad (2.35)\,.$$

The core of DDA is characterized by the way in which α_i is expressed. The most reliable formula has been developed by Draine and Goodman as a correction of the Clausius - Mossotti polarizability by a series expansion of kd and ε_m, where d is the interdipole spacing. It allows the calculation of targets extinction spectra within 10% of exact result, independently of size, shape and particle composition, provided that the number of dipoles N is large enough. For metal particles with nanometric size an error smaller than 10% is achieved using N on the order of 40000.[10]

Draine and Flatau developed a free code named DDSCAT which adopts fast Fourier transform methods and complex conjugate gradient techniques to reduce the calculation time.[27] The extinction cross sections of a series of silver and gold nanoparticles with different shapes have been calculated by using the DDSCAT code and are reported in appendix A.

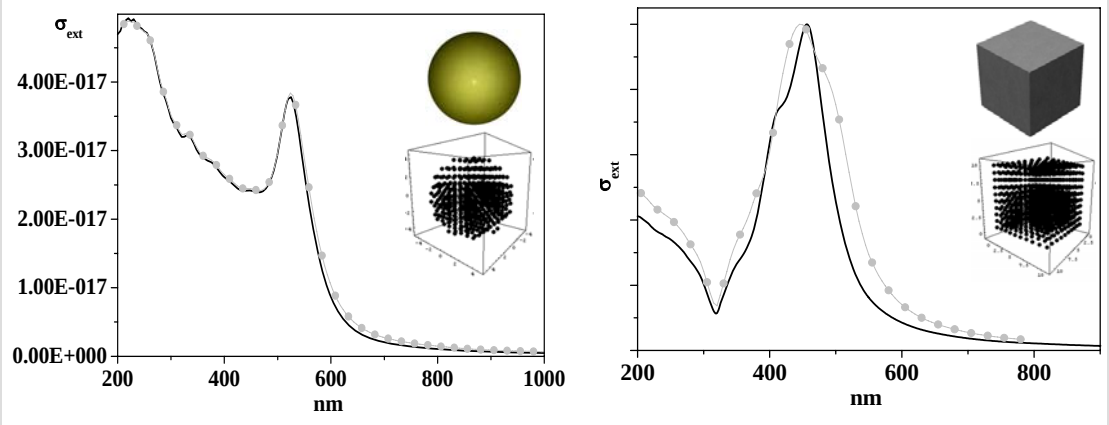

Figure 2.15 *Comparison of the extinction cross sections as obtained by analytical models (black lines) and DDA model (grey circles - N larger than 40000) for a gold sphere in water (left) and a silver cube in dimethylformamide (right).*

Main application of DDA can be found in the calculation of local electromagnetic field enhancement on the surface of single metal nanoparticles with complex shape or in the interstices of nanoparticles assembly as spheres dimers or trimers. Also in this case

more than 40000 dipole points are necessary to avoid artefacts in calculated electric field due to the discrete structure of the target in DDA.[28] Particles with sharp edge and corners are particularly interesting for surface field enhancement phenomena because fields near curved surface are intrinsically higher for higher curvatures.[10] A lot of non linear optical phenomena derive from the strong field enhancement caused by plasmon oscillation on metal particles surface and they will be discussed in following chapters.
In case of large numbers of particles or in case of particles interacting with large interfaces (i.e. infinite dielectric surfaces) accurate DDA calculations requires too many dipoles and other methods based on different ways to solve Maxwell's equations can be used.

2.8 Finite difference time domain method.

The finite difference time domain (FDTD) technique is an implementation of Maxwells's time dependent equations for solving the temporal variation of electromagnetic waves within a finite space that contains a target of arbitrary shape and has recently become the state of the art method for solving Maxwell's equations for complex geometries.[29] In this method the differentials in Maxwell's equations are replaced by finite differences to connect the electromagnetic fields in one time interval to the one in the next interval. Because FDTD is a direct time and space solution, it offers the user a unique insight into all types of problems in electromagnetism and photonics. It can also be used to obtain the frequency solution by exploiting Fourier transforms, thus a full range of useful quantities in addition to fields around particles can be calculated, such as the complex Poynting vector and the transmission/reflection of light.[29] In the FDTD technique, Maxwell's equations are discretized by using finite difference approximations in both time and space that are easy to program. The unit cell of the lattice that constitutes the FDTD computational domain is called the Yee cell.[29, 30]
The advantage of this method is that results for a large frequency range can be obtained in a single run. A strong limitation to the accuracy of FDTD method comes out from the utilization of Drude – Sommerfield expression for fitting experimental tabled values of the metal dielectric constant, instead of the actual values.[31]

2.9 Local electric field enhancement and plasmons mutual interactions.

As anticipated previously about the hybridization model, plasmons on distinct nanoparticles can reciprocally influence each other, depending on particles distance, geometry and relative photons polarization. The extremely high surface electric field originated by the oscillation of coherent conduction electrons has an important influence on the polarization of metal nanoparticles close enough to experience this field. Several studies pointed out as the local electric field at the interstices of metal nanoparticles dimers, trimers and quadrimers is hundred to thousand times higher than for isolated particles.[2, 32, 33] For this reason interparticles gaps are called hot spots and the effect of local field amplification on nanoscale volumes is called nanolensing.[2] Other than dimers or multimers, linear chains of several metal nanospheres with progressively decreasing sizes and separations are very efficient nanolenses.[34] The maximum field amplification is achieved, within a dimer, when incident light is polarized parallel to the dimer axis, and for wavelength resonant with the SPA of the dimer. The effect is larger for wavelength in resonance with SPA: for a dimer of Ag particles 36 nm in size with 2 nm spacing the electric field enhancement is 3500 times at 430 nm (quadrupolar resonance) and 11000 times at 520 nm (dipolar resonance) with respect to the incident wave.[2]

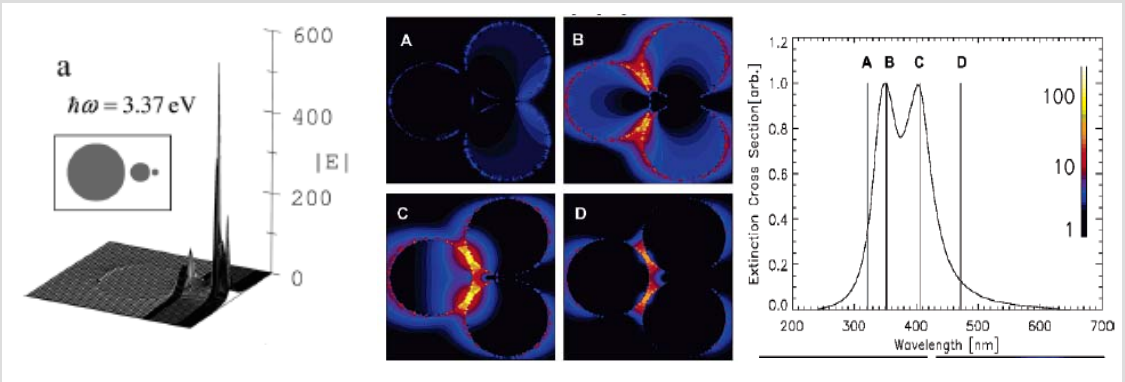

Figure 2.16 *Left: Local fields (absolute value relative to that of the excitation field) in the equatorial plane of symmetry for the linear chain of three silver nanospheres. From ref. 34. Center: Electric field enhancements of a 10 nm silver trimer with a separation of 1 nm as calculated by FDTD. The incoming light is polarized along the x-axis. The four cases A, B, C, D correspond to 4 different excitation wavelengths reported on the left picture, relative to extinction cross-section of the trimer system. From ref. 33.*

In general multimers have new SPA because when the nanoparticle separation decreases, the plasmons of individual nanoparticles begin to interact and hybridize with the plasmons of the other particles. In case of dimers, plasmon hybridization produces a SPA red shift that decays near-exponentially with the interparticle gap over a distance

that is roughly 0.2 times the particle size, independent of the nanoparticle size, shape, material, and the medium dielectric constant.[35-38] This universal decaying behaviour of the SPA in nanoparticle pairs originates from the distance decay of the interparticle near-field that couples the particles together. El Sayed et al. developed a plasmon ruler equation that estimate with good accuracy the distance between dimers from the measured fractional SPA shift:[35]

$$\frac{\Delta\lambda_{SPA}}{\lambda_{SPA}} = K\exp\left(\frac{s/D}{L}\right) \qquad (2.37)$$

where K is a constant depending on particles geometry and dielectric environment, s is the edge to edge distance, D is particles diameter and L is a decay length close to 0.2 and almost independent on particles type, shape and dielectric environment. The same expression can be used to estimate the position of core@shell SPA for different core to shell ratios just replacing s with the shell thickness and D with the core radius.[36]

When nanoparticles are in conductive contact the hybridization effects disappear and the SPA abruptly blue shifts to that of normal particles aggregates.[39]

Recently it has been found that near-field coupling between particles shifts not only the SPA frequency but also the coherent lattice oscillation frequency.[37] The shift in the phonon oscillation frequency follows an exponential decay with respect to the interparticle gap, that is the same decay observed for the shift in the surface plasmon resonance frequency. This similar trend due to the effect of interparticle coupling on the plasmon frequency and the phonon frequency is a consequence of the general scaling behaviour of the distance decay of the interparticle plasmonic near-field. In particular the decrease in the phonons frequency with decrease in the interparticle distance is the result of a reduction in the effective free electron density within each nanoparticle pair partner as a result of the polarizing perturbation of the plasmonic field of the other nanoparticle in the pair.[37]

Theoretical calculations and direct measurements on these hot spots showed that local electric field enhancement at particles interstice are useful to amplify spectroscopic signals of adsorbed organic molecules.

One popular application of plasmon coupling are molecular ruler based on the SPA dependence on the distance between two metal nanoparticles as an alternative to fluorescence quenching systems based on two interacting acceptor – donor molecules. Plasmon molecular ruler have been applied to the real time sensing of DNA

hybridization processes as well as to DNA folding in presence of different saline buffers.[40, 41] In particular the SPA sensitivity on the coupling distance of two metal nanoparticles is so high that each step of dimer formation is measurable, included elastic recoil after the first contact. AuNP and AgNP of 40 nm in diameter allows to monitor distances up to 70 nm.[41]

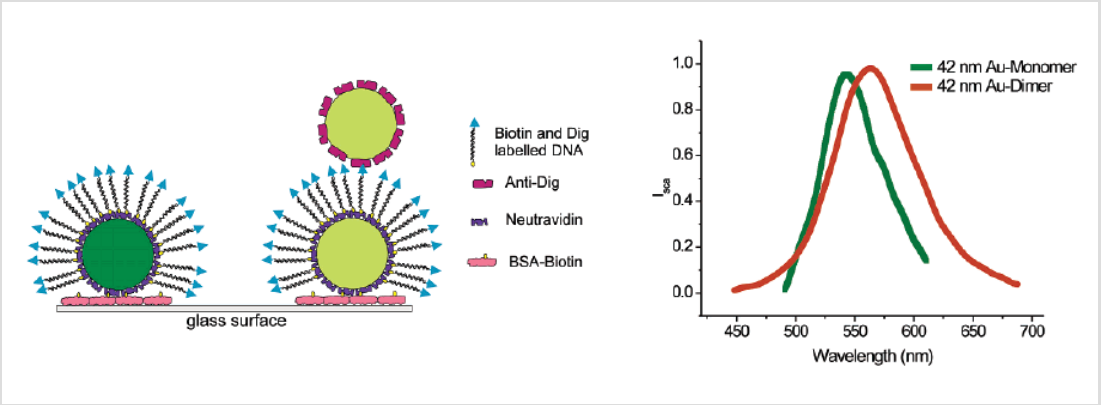

Figure 2.17 *Left: Assembly example of gold nanoparticles based plasmon rulers. First, a eutravidin-coated nanoparticle is immobilized on a BSA-biotin functionalized surface. Then, a second antidigoxigenin coated nanoparticle is tethered to the immobilized nanoparticle using double strands DNA that is labeled with both biotin and digoxigenin. Right: Spectra before and after dimer formation for 42-nm gold particles (DNA tether length: 67 base pairs). From ref. 40.*

2.10 Aggregated metal nanoparticles.

When two or more nanoparticles are in touch through a conductive junction, the resultant SPA corresponds to that of the whole object.[39] In case of a dimer, DDA calculations show how the SPA strongly recalls that of a spheroid with equivalent volume and aspect ratio.

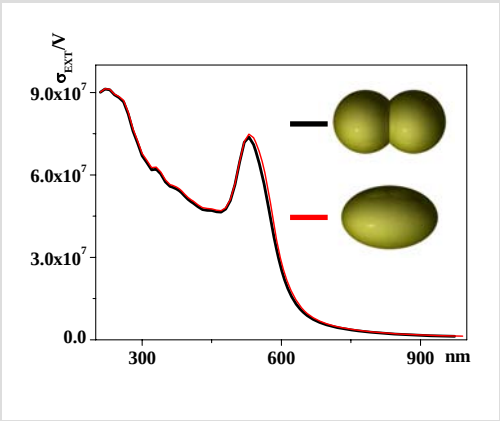

Figure 2.18 *DDA calculations for a gold spheroid and a spheroidal like gold nanosphere aggregate in water, with same overall volume and same aspect ratio.*

Agglomerates with fractal structure made by tens of particles have two main bands, one close to the original spheres position and another red shifted. Both are sensibly broader than single particles SPA.[42, 43] When particles in the aggregates are several hundreds, only one very broad red shifted band is present.[42] Two limiting regimes of irreversible kinetic colloid aggregation can be identified, both of which lead to the

formation of fractal aggregates: rapid, diffusion limited cluster-cluster aggregation (DLCA) and slow, reaction limited cluster-cluster aggregation (RLCA). In DLCA, it is assumed that the nanoparticles stick whenever they collide, whereas in RLCA, it is assumed that there is a barrier to sticking such that numerous collisions are needed to produce sticking. DLCA produces less dense aggregates than RLCA and in both cases as the fractal dimension increases, the SPA red-shift becomes bigger. Compact aggregates show larger red shift than fractal ones.[43] Changes in metal nanoparticles SPA upon aggregation have important applications. In a typical strategy metal nanoparticles in solution are coated with specific receptors as single stranded DNA polynucleotides or appositely designed peptides that in presence of the target biomolecules promote particles aggregation and sensible change in the colour of the solution with detection limits from femtomoles to nanomoles.[3, 44, 45] In case of DNA detection, the target polynucleotide bridge two particles during the hybridization process with receptor oligonucleotides on the metal surface. Since more than one receptor is present on each nanoparticles, hundred to thousands of nanoparticles are connected together during the hybridization process.[46] Nanoparticle labelled DNA also have sharper melting hybridization – dehybridization transition than unlabeled DNA, as a consequence of the dense loading of oligonucleotides on nanoparticles surface and of the cooperative hybridization process.[46] Also DNA melting temperature is exploited for the discrimination of different polynucleotides.[47]

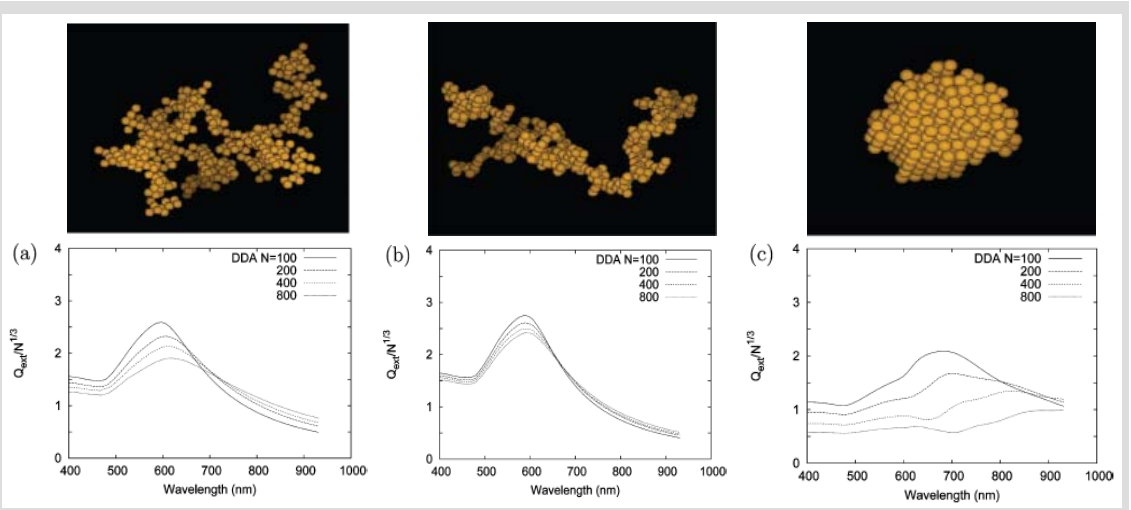

Figure 2.19 *Up: Typical morphology of a cluster with 400 nanoparticles disposed as a reaction-limited cluster-cluster aggregate (left), a diffusion-limited cluster-cluster aggregate (center) and a compact cluster (right). Bottom: Calculated extinction coefficients Q_{ext} using DDA, for (a) a RLCA cluster; (b) a DLCA cluster; (c) a compact cluster in an aqueous solution, varying the number of nanoparticles N in a cluster from 100 to 800. The resulting plots were averaged over 10-100 cluster realizations. The diameter of the nanoparticles is 60 nm. From ref. 43.*

For DNA targets, gold nanoparticles based labels have better target specificity and sensitivity that polymerase chain reactions (PCR). For protein targets, these nanoparticles assays are up to 10^6 times more sensitive than conventional protein detection methods like ELISA.[3, 44]

2.11 Surface enhanced Raman scattering.

When molecules are adsorbed on metal nanoparticles or roughened metallic surfaces a huge amplification of Raman signal is observed, called surface enhanced Raman scattering (SERS). Enhancements up to 14 orders of magnitude for the Raman scattering cross section have been reported.[48] SERS is due to the coupling of surface plasmons with vibrational modes of molecules adsorbed on the metal surface. Indeed the coupling involves both infrared and Raman active vibrational modes, therefore also surface enhanced infrared absorption (SEIRA) spectroscopy is possible on the same samples showing SERS.[3, 49]

The discovery of SERS by Van Duyne is dated up to 1977, but only in the last years theoretical modelling, local field calculations and optimally designed experiments explained the main parameters involved in this phenomenon. Two distinct mechanisms can originate SERS: electromagnetic field enhancement and chemical first layer effects. In the latter case an electronic coupling between the molecule and the metal can produce resonance Raman effect due to a new metal – molecule charge transfer transition. The role of nanometric curvature radii in metal nanoparticles or roughened surfaces is to provide efficient pathways for the electron transfer. The magnitude of chemical enhancement has been estimated to reach no more than factors of 10 –100.[48, 50]

The electromagnetic field enhancement is due to surface plasmon oscillations and the best conditions are obtained for molecules absorbed in hot spots as at the junctions of metal nanoparticles dimers. Furthermore the plasmon oscillation corresponding to a certain hot spots has to be resonant at the probe wavelength energy and polarization.[32, 50, 51] Therefore, the SERS signal is non homogeneously originated by all the molecules in the probed volume, but only by those in the hot spots, corresponding to about 0.01% of the total in normal conditions.[48] This also makes difficult the exact estimation of the enhancement factors for single molecule and obtaining reproducible SERS active substrate for analytical purposes.

A finite optimum gap size exists for SERS, given a specific excitation wavelength, not only to fulfil the requirements of resonance with the SPA, but also to allow the best compromise between local field amplification and excitation light confinement in the gap.[50]

Sensitivity of SERS is as high that single molecule Raman spectroscopy is possible,[52, 53] as well as in vivo molecular probing of cellular components.[54] A typical application of SERS is the scanometric method for DNA analysis, which is based on the ability of Raman spectroscopy to perform multiplexed analysis. Raman spectrum is like a molecular fingerprint and in principle the detection of each single genome base is possible by SERS also for a single cell. In the scanometric method gold nanoparticles are immobilized on chip surface by complementary base pairing when the target DNA is present. Then the reduction of silver ions on the gold particles is promoted, originating larger nanoparticles which originate stronger SERS signals. Combining each base with a distinct Raman active molecule or a collection of Raman active molecules with a specific ratio allows the identification of the target DNA sequence. Advantages of Raman with respect to ordinary fluorescence assays are various: only one excitation wavelength is necessary, there is no photobleaching, Raman spectra have higher specificity than fluorescence spectra and a large number of Raman active molecules are available.[3, 44, 55]

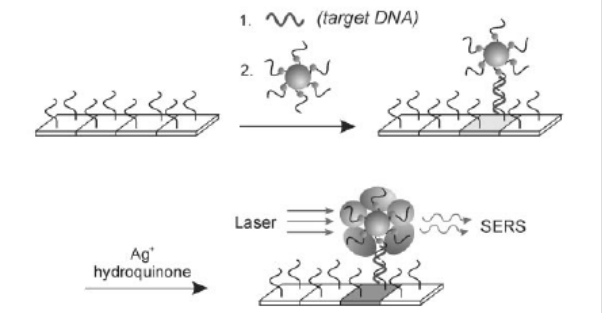

Figure 2.20 *Scheme of a typical Ag enhancement experiment for DNA detection: Au nanoparticles modified with alkylthiol-capped oligonucleotide strands and a group with large Raman cross section (like rhodamine 6G) bound to the substrate in the presence of specific target DNA strands; addition of Ag^+ promotes the nucleation and growth of silver nanostructures on the free oligonucleotide strands on AuNP surface; the SERS signal of the Raman active group is detected. From ref. 55.*

2.12 Surface plasmon excitation dynamics.

Time evolution of plasmon excitation has been matter of study with ultrashort pulse laser spectroscopies for a long time. The plasmon bandwidth, assumed to be homogeneous, can be associated with the dephasing of coherent electron oscillation,

therefore a large bandwidth corresponds to a fast loss of coherence. Using a two level model, the width Γ of the SPA can be expressed as:[15]

$$\pi c\Gamma = \frac{1}{T_2} = \frac{1}{2T_1} + \frac{1}{T_2^*} \qquad (2.38)$$

where two contributes to the overall dephasing time T_2 are present: T_1 describes the population relaxation times and T_2^* is the pure dephasing time. Pure dephasing mechanisms change electrons wavevectors but not their energy, contrary to relaxation mechanisms that can change both energy and wavevector. Electron dephasing times of about 2 -10 fs corresponds to the SPA bandwidth of metal nanoparticles and T_2^* is predominant in *2.38*.[15] Single electron – electron scattering events in the metal nanoparticles is the main dephasing mechanism on this time scale, followed by radiative decay, intraband and interband excitation. For spheres of about 20 nm the radiative decay accounts for few percents in the total damping rate.[56] Due to the energy overlap of plasmon absorption and the edge of interband transitions in gold, interband excitation corresponding to the creation of holes in lower lying *d* bands have a non negligible contribute to the SPA width, contrariwise to silver spheres or nanorods.[57]

The relaxation processes following plasmon loss of coherence can be modelled according to the two temperature model (TTM), in which the electrons and the lattice are treated as two coupled subsystems with different initial temperature after SPA and with different heat capacities.[15]

While pure dephasing mechanism dominates the first ~10 fs after plasmon excitation, cascade elastic electron – electron scattering takes place on a time scale of ~500 fs after the SPA and drive to the electrons thermalization. In this way electrons energies rearrange from a non equilibrium distribution to the quasi equilibrium Fermi – Dirac distribution corresponding to the system thermal energy plus the absorbed photon energy. Therefore ~500 fs after plasmon excitation the electronic temperature is still higher than the lattice temperature.[15, 58]

In 1 – 5 ps electron – phonons scattering processes drive to the thermalization of the electronic bath with the lattice. The last process involves phonon – phonon interactions between the lattice and the surrounding medium, with a time scale of hundred of picoseconds.[15, 58]

Transient SPA spectra show the bleaching and the broadening of the plasmon absorption in the first picoseconds, as a consequence of the higher electronic

temperature and higher electron scattering rate. After complete thermalization of conduction electrons, two phenomena are visible in the transient absorption traces, the first is the red shift and the slight bleaching of the SPA due to heat expansion of metal nanoparticles and the second is the oscillation of transient absorption with a period of about 5 ps due to low frequency acoustic breathing mode of the lattice. Both phenomena are the effect of the electronic density modulation due to thermal dilatation of the lattice, with electron density drop corresponding to a red shift of the SPA.[15, 58]

In general all the precedent relaxation mechanisms are not actually consecutive but overlapping processes. Also their precise time scale depends on the pump intensity of pump – probe experiments, mainly because sequential plasmon absorption raise the average nanoparticles temperature and all thermalization rates are temperature dependent.[15, 58]

Nanoparticles size has no remarkable effect on relaxation processes, while it is important only in pure dephasing mechanisms (cfr. equation *2.15*).[15, 58]

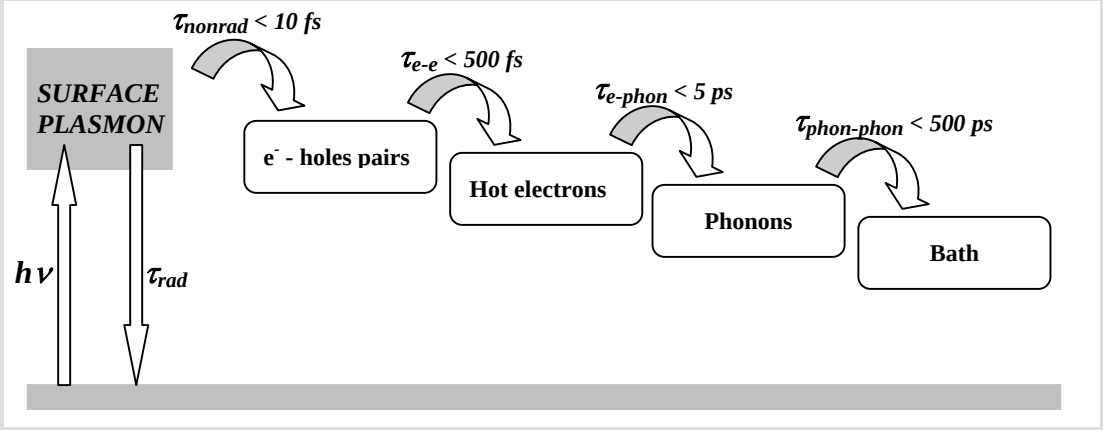

Figure 2.21 *Typical dynamics of a surface plasmon excitation.*

2.13 Surface plasmon radiative dynamics.

In bulk gold and silver luminescence efficiency of about 10^{-10} are known.[59] The main luminescence mechanism involves three processes: the formation of holes in the lower lying *d* bands due to light absorption, the relaxation of excited electrons and holes in the *sp* and *d* bands respectively and finally the radiative recombination of the electron – hole couple. The emission spectra show some structures due to the relaxation of the excited electrons and holes toward energy levels of specific symmetry in the metal bands. Non radiative energy relaxation processes such as electron-electron scattering are

much faster than radiative decay in metals, thus low yields of photoluminescence are observed.[59]

In general surface roughness can enhance the efficiency of this process, as well as nanostructured metals. Several authors reported significant luminescence enhancement factors of 10^4 in metal nanospheres[57, 60] and of 10^6 in gold nanorods.[61] Since the band structure of particles with size larger than about 2 nm is almost exactly that of bulk metals and no quantum size effects are perceivable, the origin of such emission enhancement is attributed to the surface plasmon oscillation. In particular some authors suggested that the local field enhancement due to the surface plasmon absorption can favour the radiative recombination efficiency of *sp* bands electrons with *d* bands holes, according to a phenomenon called *lighting rod effect*.[10, 15, 61] Other authors observed the same luminescence enhancement in metal nanospheres without any distinction about their size.[57] Since the curvature radius depends on the size and the local field originated by plasmon oscillation depends on the curvature radius, another mechanism for the enhanced emission has been proposed, based on the excitation of surface plasmons by the electron – hole couple. In this model a fraction around 20% of the electron – hole pairs can polarize the nanoparticle and can excite a surface plasmon via the screening motion of the conduction electrons. At this point the plasmon can decay radiatively or not radiatively as usual. This last mechanism is supported by the good overlap between luminescence spectra and the SPA spectra of corresponding metal nanoparticles.

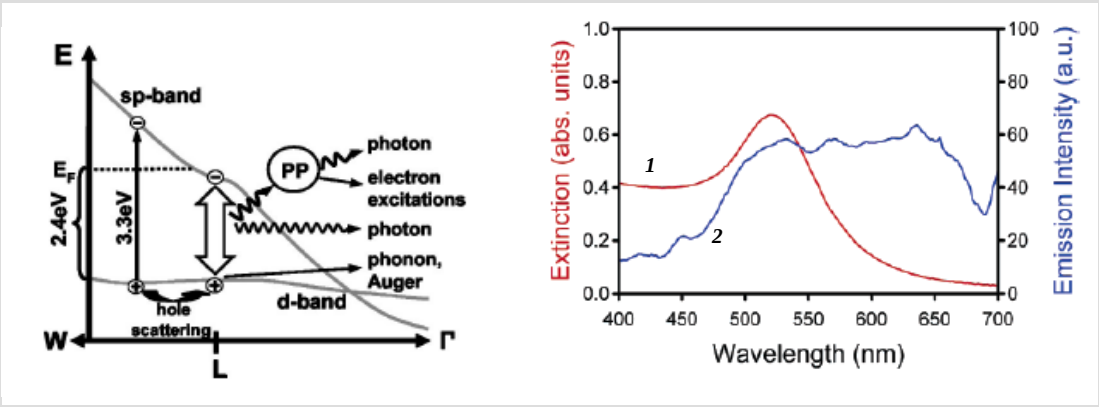

Figure 2.22 *Left: Schematic representation of excitation of surface plasmons by the electron – hole couple: a photon with 3.3 eV energy promotes electrons from the d band into the sp band well above the Fermi level; the holes in the d band undergo Auger scattering and hole-phonon scattering; direct radiative recombination of a d-band hole with an electron in the sp band below the Fermi surface or emission of a surface plasmon may occur; the plasmon subsequently decays either radiatively or nonradiatively. From ref. 57. Right: extinction (1) and time-averaged single particle luminescence (2) spectra under 790 nm – 100 fs laser irradiation of 15-nm Au particles. From ref. 62.*

The larger luminescence yield for nanorods than for nanospheres is in accord with the higher polarizability of longitudinal plasmon oscillations in the formers.[57]

Multiphoton absorption induced luminescence can be sensibly more intense with respect to the single photon process. The emission yield grows with particles size and with particles asymmetry. In case of 790 nm - 100 fs laser pulses excitation, the mechanism following multiphoton absorption requires that more than one photon is emitted per laser pulse and that a three photon absorption process is dominant. Observed photoluminescence spectra are broad and do not show any correlation with the plasmon absorption or scattering.[62]

Completely different is the luminescence mechanism for oligoatomic metal clusters, which show quantum size effects in their electronic level spectrum. Metal clusters behave like multielectrons artificial atoms possessing discrete size dependent fluorescence emission throughout the visible and the near infrared.[63] These emissions correspond to intraband transitions between discrete energy levels. For gold clusters quantum yield as high as 70% and 10% have been measured for 5 and 35 atoms clusters respectively.[64] In case of gold cluster in the 3 – 15 atoms range, lower energy transition can be estimated with good accuracy applying the jellium model and considering a three - dimensional harmonic potential to obtain:[63]

$$\Delta E = \frac{E_F}{N^{\frac{1}{3}}} \qquad (2.39)$$

where E_F is the Fermi energy of the bulk metal, independent on the cluster size, and N is the atoms number. For clusters in the 15 – 40 atoms range a slight correction for potential anharmonicity is required and the emission energy is corrected as following:[63]

$$\Delta E = \frac{E_F}{N^{\frac{1}{3}}}\left[1 - U\left(l_e^{\,2} - l_g^{\,2} - \frac{n+2}{3}\right)\right] \qquad (2.40)$$

where U is the anharmonicity parameter, l_e and l_g are the angular quantum numbers of excited and ground state respectively and n is the principal quantum number or the shell number.

Usually, cluster sizes are determined by closed shell configurations, in analogy to the multielectrons artificial atoms behaviour. Therefore, only specific numbers of atoms are attainable, corresponding to magic cluster sizes. Despite the high number of surface atoms, fluorescence emission of gold cluster showed no dependence on the surrounding

or stabilizing medium. Furthermore the fluorescence emission has the characteristic of an antibunched photon source, useful for photonic applications.[65]

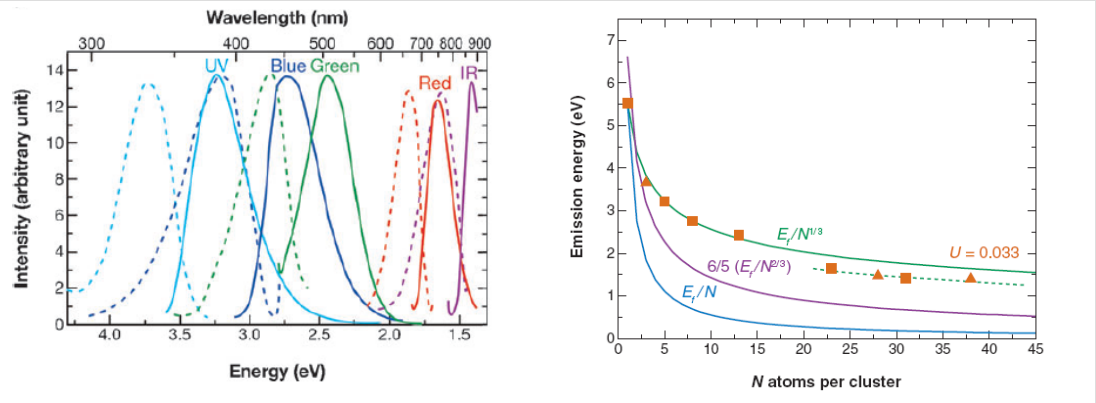

Figure 2.23 *Left: Excitation (dashed) and emission (solid) spectra of different Au nanoclusters in water. Right: The correlation of the number of atoms (N) per cluster with emission energy quantitatively fit with equation 2.39, as predicted by the jellium model. Emission energies of clusters after Au_{23} exhibit slight deviations from the $E_{Fermi}/N^{1/3}$ scaling, consistent with potential anharmonicity expressed by equation 2.40. Other models cannot accurately fit the scaling of emission-energy for Au clusters. From Ref. 63.*

2.14 Plasmonic modulation of molecular fluorescence.

Metallic nanoparticles, due to their high polarizability, show strong interactions with nearby fluorescent chromophores. In general the fluorescence emission rate R_{em} can be expressed as:[66]

$$R_{em} = R_{ex}\eta \qquad (2.41)$$

$$\eta = \frac{R_{rad}}{R_{rad} + R_{nonrad}} \qquad (2.42)$$

where R_{ex}, R_{rad} and R_{nonrad} are the excitation, radiative decay and non radiative decay rates respectively, and η is the fluorescence quantum efficiency. The molecular fluorescence can either decrease or increase depending on how nanoparticles affect the chromophore excitation rate and the radiative and nonradiative decay rates of its excited states. The mechanisms of metal nanoparticles interactions with molecular chromophores can be very complicated and several parameters govern which of the processes is predominant, like nanoparticles size and shape, molecule – nanoparticles separation and orientation or the overlap of fluorophores excitation and emission energy with the plasmon resonance.[67-71]

At separations distances as small as few nanometers fluorescence quenching close to 100% were explained with two phenomena: the increase in R_{nonrad} by energy transfer from the chromophore to the metal particle and the decrease in R_{rad} for the out of phase

oscillation of molecular dipole and the dipole induced on the metal nanoparticle, when the molecule is tangentially oriented on the metal surface.[67] The Gertsen - Nitzan model used for ordinary dipole – dipole Forster resonance energy transfer (FRET) on distances of few nm is no more valid for metal - chromophores interactions, since the theoretical d^{-6} decay is faster than experimentally observed quenching effects (d is the dipole – dipole distance).[67-70] Other theories afforded the specific problem of nanomaterial surface energy transfer (NSET) like the Persson – Lang model and were successful in reproducing the d^{-4} dependence experimentally observed.[69, 70] Though both cases concern dipole – dipole interactions, NSET has a longer range than FRET because the nanoparticle has an isotropic distribution of possible dipole vectors on its surface to accept energy from the chromophore. Relaxation of the dependence on the molecular orientation implies that NSET has higher probability of energy transfer than FRET, is less specific on the chromophore type and can be applied to distance over 10 nm. [69, 70]

The high polarizability of metal nanoparticles induce a further degree of control on the NSET process by application of an external electric field.[72]

NSET can find applications in monitoring biochemical processes, such as accurately tracking DNA length scales and conformational changes in DNA following protein binding in the distance range of 30-200 Å or structure conformational change and cleavage kinetics of hammerhead ribozyme.[70, 73]

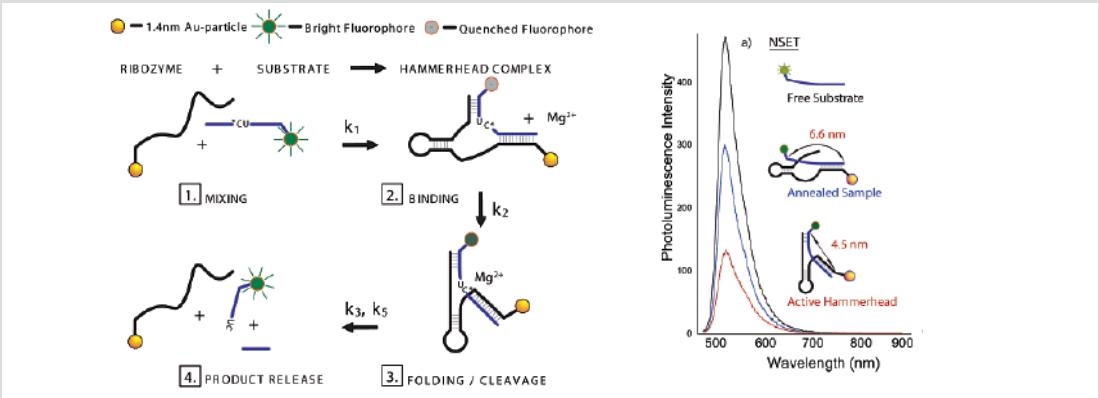

Figure 2.24 *Left: Scheme of hammerhead ribozyme cleavage: the ribozyme binds to the substrate strand (1) to form the "hammerhead complex" (2), which in the presence of Mg^{2+} will cleave the substrate at the scissile bond (3) (dashed line). The products are released as two separate strands (4), and the ribozyme is regenerated. Right: Photoluminescence quenching correlated to structural changes in the hammerhead ribozyme. From Ref. 70.*

In presence of low quantum yield fluorophores spaced more than about 10 nm from the metal surface of nanostructures having high scattering cross sections like SiO_2@Au core@shell particles, a 10 – 50 fold emission enhancement has been measured due to a

nanolensing effect.[67,74] The luminescence process is particularly amplified when plasmon scattering efficiency matches the molecular emission wavelength. This could be an effect of near field enhancement of the optical intensity incident on the molecule or a consequence of the increase in the effective photon mode density at the emission wavelength. Both effects are active for a chromophore – nanoparticle distance of 5 – 20 nm, therefore fluorescence enhancement has a distance range complementary to SERS, which involves molecules closer than 5 nm to the metal surface.

The Fermi golden rule defines the quantum mechanical emission probability per unit time W_{ij} as:[2]

$$W_{ij} = \frac{2\pi}{h}\left|\mu_{ij}\right|^2 \rho\left(v_{ij}\right) \qquad (2.43)$$

Where h is the Plank constant, μ_{ij} is the transition dipole moment between the initial i and final j states and $\rho(v_{ij})$ is the photon mode density at the transition frequency v_{ij}. One of plasmon resonance effects is amplifying the $\rho(v_{ij})$ term because localization of photon interactions in nanoscopic domains enhances the density of photon states. Conversely to fluorescence quenching, the effect of radiative rate enhancement is more pronounced, and easily measurable, for low quantum yield molecules.[2]

2.15 Plasmonic transmission and waveguiding.

Diffraction of light confines size and performances of conventional optical devices in structures with size comparable or smaller than $\lambda/2n$, where λ is the electromagnetic wavelength and n is the device refraction index.[75, 76] For this reason optoelectronic devices are larger than electronic equivalents.[3]

Metal nanostructures attracted great interest in optoelectronics research because by converting the optical modes into nonradiating surface plasmons, electromagnetic energy can be transferred in structures with lateral dimensions of less than 10% of the free – space wavelength, finally allowing photonics at the nanoscale.[3] The transition of photonic devices to a sub 100 nm scale is also bound to the advance in metal nanoparticles synthesis and lithography techniques. To date a variety of passive and active plasmonic devices have been fabricated, like filters, waveguides, polarizers, Bragg reflectors and nanoscale light sources, switches, modulators and light output enhancers.[3]

Two main phenomena are driving the research in this field: subwavelength hole light transmission and plasmonic waveguiding.

In light transmission through subwalenght holes, the aperture is obtained in thick metallic screens by lithography. Periodic patterns around the hole are necessary to achieve a transmittance even larger than 100% (calculated only on the holes area). The phenomenon is strongly wavelength dependent, because it comes out from the matching between the light wavevector, the surface plasmon wavevector and the wavevector of light diffracted by the patterned surface. Periodic nanohole arrays are studied for lithography applications and for couplers and decouplers of photonic circuits as plasmonic waveguides.[3]

The basic plasmonic waveguide consists of a linear chain of metal nanoparticle with size much smaller than the exciting wavelength.[3, 76] Particles act as interacting electric dipoles, with two regimes depending on their spacing *s*. For spacing comparable to the light wavelength far field dipolar interaction dominates, with an s^{-1} dependence. For spacing much smaller than light wavelength, near field dipolar interactions dominate (near field coupling), with an s^{-3} dependence, originating collective plasmon modes in the whole chain. The loss is usually high in the near field coupling regime, but a propagation distance of 0.5 μm have been reported for silver nanorods arrays. FDTD calculations showed that centimeter scale propagation is possible in plasmonic waveguides with group velocity around 1 – 10 % of the light speed in vacuum. Though a tradeoff between loss and spatial localization exists, metal nanostructure can localize, extract and enhance the light electromagnetic field, contrary to dielectric waveguides. Light in the Vis – NIR range can be converted in propagating plasmons with wavelength as short as 1 nm. Peculiar dispersion

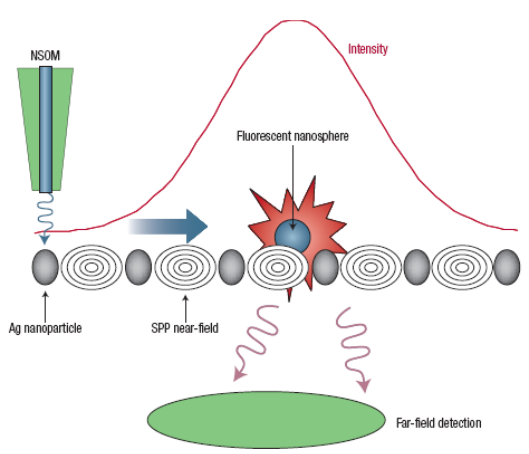

Figure 2.25 *Excitation and detection of energy transport in metal nanoparticle chains by near-field optical microscopy. The nanoparticle waveguide is locally excited by light emanating from the tip of an NSOM. The electromagnetic energy is transported along the waveguide towards a fluorescent nanosphere sitting on top of the nanoparticles. The NSOM tip is scanned along the nanoparticle chain, and the fluorescence intensity for varying tip positions along the particle chain is collected in the far-field. The energy transport to the nanosphere manifests itself in an increase in width of the nanosphere fluorescence. From 76.*

properties of gold and silver plasmons in concomitance of the Vis – NIR light window enables the excitation of plasmons with a large range of wavevectors over a narrow frequency range.[3]

2.16 Non linear optics of metal nanoparticles.

Silver and gold nanoparticles have many highly polarizable electrons, which ensure a strong nonlinear optical (NLO) response. Indeed the strong non linear properties of metal nanoparticles is usually attributed to local field enhancement effects for the plasmon oscillation, because nonlinear optical susceptibility (χ) measured on nanostructures are extremely larger than in bulk metals.[77-79]

Three main categories of nonlinear optical phenomena are common as research subject: optical limiting (discussed in chapter 5), optical Kerr effect and second or third harmonic generation. Except for optical limiting, all others NLO effects require fast spectroscopies, of the order of femtoseconds or at least picoseconds, to be observed with negligible contribution from bare thermal effects or particles degradation. This is because excitation wavelengths are always resonant or close to resonance with the broad AuNP and AgNP SPA. Due to SPA high absorption efficiency and ultrafast nonradiative decay rate, AuNP and AgNP have to be considered first of all as converter of light into heat, especially at laser intensities typical of nonlinear optics. In order to limit the number of photons that are absorbed and converted into heat by each nanoparticle, the laser pulse has to be as short as possible compared to SPA dynamics, so that intensity of the laser pulse is sufficiently high to observe non-linear processes, but the number of photons is sufficiently low.[15]

Due to their enhanced third-order nonlinear susceptibility, especially near the surface plasmon resonance frequency, noble-metal nanoparticles embedded in dielectric matrices have practical applications in ultrafast all optical switching devices.[77-83] The switching phenomenon is based on the optical Kerr effect and consists in the intensity dependent variation of the refraction index of the nanocomposites. Z – scan and degenerate four wave mixing (DFWM) experiments are used to estimate the optical Kerr susceptibility $\chi^{(3)}$ of such nanocomposites. The magnitude of the nonlinear response varies with size and shape as well as volume fraction of metal nanoclusters embedded in the dielectric matrix, therefore the resultant nanocomposite susceptibility $\chi_{nc}^{(3)}$ can be expressed as:[82]

$$\chi_{nc}^{(3)} = pf(\omega)^2 |f(\omega)|^2 \chi_m^{(3)} \qquad (2.44)$$

where p ad $\chi_m^{(3)}$ are the particles volume fraction and optical Kerr susceptibility respectively, ad $f(\omega)$ is the local field amplification factor, which is a complex number.

Three main mechanisms contribute to $\chi_m^{(3)}$: (*i*) a fast mechanism on a time scale of hundreds of femtoseconds due to electron-electron scattering, after the plasmon absorption, driving to the electrons thermalization, (*ii*) an interband transition which contribute is on the same time scale of the former and (*iii*) an hot electrons mechanism on a time scale of nanoseconds. Only the first two mechanisms are fast enough for optical switching applications.[82]

Second harmonic generation (SHG) is only possible in non-centrosymmetric systems when nanoparticles size is smaller than excitation wavelength.[84, 85] In metals the SHG signal has two origins: a surface contribution arising from the breaking of the centrosymmetry at the metal surface and a bulk contribution arising from the electromagnetic field gradients due to the presence of the interface. For small particles with diameters of few nanometers, the bulk origin is the dominant contribution to the SHG response. Typically SHG is observed in random metal nanostructures such as aggregated particles or in arrays of non spherical particles as rods or L – shaped structures. Best SHG efficiency is achieved for excitation wavelength resonant with particles SPA.[84-88]

In isotropic dispersions of non-centrosymmetric particles SHG is not allowed, but a weak frequency doubling phenomenon is still possible, called hyper Rayleigh scattering (HRS).[89] HRS is a non-linear second-order light scattering that has been used in the study of non-centrosymmetric molecules or nanoparticles in solutions. The HRS relies upon the fluctuations of the density or orientation of molecules or nanoparticles, which instantaneously break the centrosymmetry of isotropic media as liquid solutions and create conditions of net frequency doubling. Spherical metal nanoparticles functionalized with antibodies that conjugate a target antigen with a sandwich structure, forming a dimer of nanoparticles, found application in biosensing. The symmetry break upon the target antigen coordination enabled the generation of HRS signal.[89]

Also third harmonic generation (THG) has been reported for metal nanoparticles on a substrate, due to third order HRS mechanism.[90]

Local field effects due to strong localization of collective plasmon modes in fractal metal clusters have been also exploited for enhancing the non linear properties of

molecules adsorbed on metal nanoparticles. Beyond SERS effect, previously discussed, strong enhancement of HRS signal using gold nanoparticles aggregates with adsorbed pyridine molecules[87] and of two photon absorption of organic molecules near silver nanoparticle fractal clusters,[91] have been observed. Similarly gold nanoparticles have been used to enhance two photon absorption induced fluorescence for in vivo cells imaging.[92]

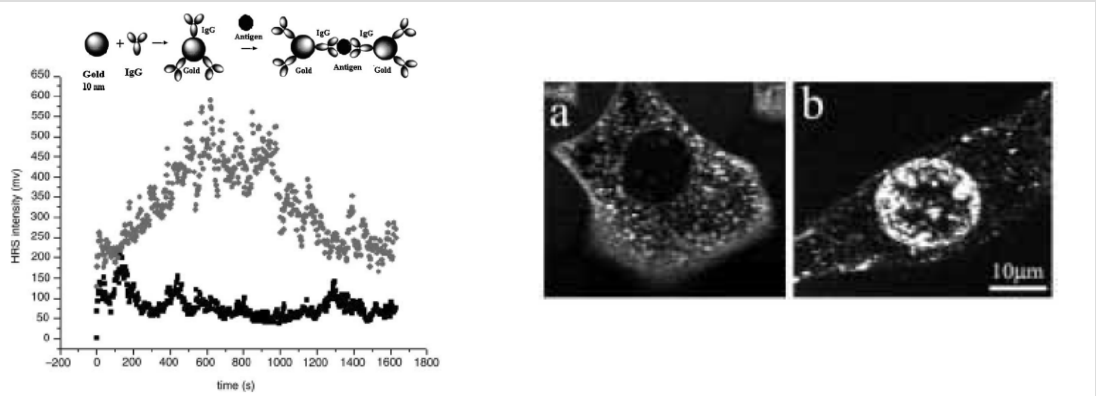

Figure 2.26 *Left: HRS signals at 532 nm of gold nanoparticles and gold–antibody conjugates pumped by 1064 nm laser pulse. The HRS intensity of the gold–antibody conjugates varied greatly with the measurement time. When the target protein was added to the gold nanoparticle suspension, the HRS signals were increased with measurement time at the beginning, reached a peak value in about 10 min, and then decreased to a stable value that was still higher than that of the bare gold nanoparticles due to the gold–antibody aggregation induced by antigen, as shown in the upper part. From Ref. 89. Right: THG image of a normal fixed cell and of a fixed cell in which the nucleus membrane was labelled by 10nm gold nanoparticles followed by silver enhancement. From Ref. 92.*

References

1. Menzel, R., *Photonics*. Springer Berlin, 2001.
2. Prasad, P. N., *Nanophotonics*. Wiley: 2004.
3. Xia, Y.; Halas, N. J., *MRS Bulletin* **2005,** 30, 338 - 389.
4. Kittel, C., *Introduction to Solid State Physics*. Wiley: 1996.
5. Kreibig, U.; Vollmer, M., *Optical Properties of Metal Clusters*. Springer Verlag: Berlin, 1995.
6. Raether, H., *Surface Plasmons*. Springer - Verlag: Berlin.
7. Fang, S.; Lee, H. J.; Wark, A. W.; Corn, R. M., *J. Am. Chem. Soc.* **2006,** 128, 14044 -14046.
8. Nelayah, J.; Kociak, M.; Stephan, O.; F. J. G. de Abajo; Tence, M.; Henrard, L.; Taverna, D.; I. Pastoriza-Santos; Liz-Marzan, L. M.; Colliex, C., *Nat. Phys.* **2007,** 3, 348 - 353.
9. Vesseur, E. J. R.; Waele, R. d.; Kuttge, M.; Polman, A., *Nano Lett.* **2007,** 7, 2843-2846.
10. Kelly, K. L.; Coronado, E.; Zhao, L. L.; Schatz, G. C., *J. Phys. Chem. B* **2003,** 107, 668-677.
11. Mie, G., *Ann. Phys.* **1908,** 25, 377.
12. Stratton, J. A., *Electromagnetic Theory*. McGraw Hill: 1941.
13. Born, M., *Optik*. Springer: 1972.
14. Daniel, M. C.; Astruc, D., *Chemical Review* **2004,** 104, 293 - 346.
15. Link, S.; El-Sayed, M. A., *Int. Rev. Phys. Chem.* **2000,** 19, 409-453.
16. Johnson, P. B.; Christy, R. W., *Phys. Rev. B* **1972,** 6, 4370-4379.
17. Palik, E., *Handbook of Optical Constants of Solids*. Academic Press: New York, 1985.
18. Tang, Y.; Ouyang, M., *Nature Materials* **2007,** 6, 757 - 759.
19. Llnaert, T.; Mulvaney, P.; Henglein, A., *J. Phys. Chem.* **1993,** 97, 679 - 682.
20. Lee, K.-S.; El-Sayed, M. A., *J. Phys. Chem. B* **2006,** 110, 19220 -19225.
21. McFarland, A. D.; Duyne, R. P. V., *Nano Lett.* **2003,** 3, 1057.
22. Haes, A. J.; Duyne, R. P. V., *Anal. Bioanal. Chem.* **2004,** 379, 920–930.
23. Prodan, E.; Radloff, C.; Halas, N. J.; Nordlander, P., *Science* **2003,** 302, 419-422.
24. Wang, H.; Brandl, D. W.; Nordlander, P.; Halas, N. J., *Acc. Chem. Res.* **2007,** 40, 53-62.
25. Link, S.; El-Sayed, M. A., *J. Phys. Chem. B* **1999,** 103, 8410-8426.
26. Fuchs, R., *Phys. Rev. B* **1975,** 11, 1732.
27. Draine, B. T.; Flatau, P. T., *Source code DDSCAT 6.0 http://www.astro.princeton.edu/_draine/DDSCAT.html*.
28. Kelly, K. L.; Lazarides, A. A.; Schatz, G. C., *Computing in Science & Engineering* **2001,** 4, 67-73.
29. Chang, S.-H.; Gray, S. K.; Schatz, G. C., *Opt. Express* **2005,** 13, 3150-3165.
30. Zhang, J.; Fu, Y.; Chowdhury, M. H.; Lakowicz, J. R., *Nano Letters* **2007,** 7, 2101 -2107.
31. Vial, A.; Grimault, A.-S.; Macías, D.; Barchiesi, D.; Chapelle, M. L. d. l., *Phys. Rev. B* **2005,** 71, 085416.
32. Imura, K.; Okamoto, H.; Hossain, M. K.; Kitajima, M., *Nano Lett.* **2006,** 6, 2173 -2176.
33. Brandl, D. W.; Mirin, N. A.; Nordlander, P., *J Phys. Chem. B* **2006,** 110, 12302 -12310.
34. Li, K.; Stockman, M. I.; Bergman, D. J., *Phys. Rev. Lett.* **2003,** 22, 227402.
35. Jain, P. K.; Huang, W.; El-Sayed, M. A., *Nano Lett.* **2007,** 7, 2080 -2088.
36. Jain, P. K.; El-Sayed, M. A., *Nano Lett.* **2007,** 7, 2854 -2858.
37. Huang, W.; Qian, W.; Jain, P. K.; El-Sayed, M. A., *Nano Lett.* **2007,** 7, 3227 -3234.
38. Dahmen, C.; Schmidt, B.; Plessen, G. v., *Nano Lett.* **2007,** 7, 318 -322.
39. Atay, T.; Song, J.-H.; Nurmikko, A. V., *Nano Lett.* **2004,** 4, 1627-1631.
40. Reinhard, B. M.; Siu, M.; Agarwal, H.; Alivisatos, A. P.; Liphardt, J., *Nano Lett.* **2004,** 5, 2246-2252.
41. Sonnichsen, C.; Reinhard, B. M.; Liphardt, J.; Alivisatos, A. P., *Nat. Biotech.* **2005,** 23, 741-745.
42. Norman, T. J.; Grant, C. D.; Magana, D.; Zhang, J. Z.; Liu, J.; Cao, D.; Bridges, F.; Buuren, A. V., *J. Phys. Chem. B* **2002,** 106, 7005-7012.
43. Park, S. Y.; Lee, J.-S.; Georganopoulou\, D.; Mirkin, C. A.; Schatz, G. C., *J Phys. Chem. B* **2006,** 110, 12673 -12681.
44. Rosi, N. L.; Mirkin, C. A., *Chem. Rev.* **2005,** 105, 1547-1562.
45. Guarise, C.; Pasquato, L.; Filippis, V. D.; Scrimin, P., *Proceedings of the National Academy of Science* **2006,** 103, 3978 - 3982.
46. Elghanian, R.; Storhoff, J. J.; Mucic, R. C.; Letsinger, R. L.; Mirkin, C. A., *Science* **1997,** 277, 1078-1081.
47. Taton, T. A.; Mirkin, C. A.; Letsinger, R. L., *Science* **2000,** 289, 1757-1760.
48. Kneipp, K.; Kneipp, H.; Itzkan, I.; Dasari, R. R.; Feld, M. S., *Chem. Rev.* **1999,** 99, 2957-2975.

49. Jensen, T. R.; Duyne, R. P. V.; Johnson, S. A.; Maroni, V. A., *Appl. Spectr.* **2000,** 54, 371-377.
50. Qin, L.; Zou, S.; Xue, C.; Atkinson, A.; Schatz, G. C.; Mirkin, C. A., *Proceedings of the National Academy of Science* **2006,** 103, 13300–13303.
51. McLellan, J. M.; Li, Z.-Y.; Siekkinen, A.; Xia, Y., *Nano Lett.* **2007,** 7, 1013-1017.
52. Kneipp, K.; Wang, Y.; Kneipp, H.; Perelman, L. T.; Itzkan, I.; Dasari, R. R.; Feld, M. S., *Phys. Rev. Lett.* **1997,** 78, 1667-1670.
53. Nie, S.; Emory, S. R., *Science* **1997,** 275, 1102-1106.
54. Kneipp, J.; Kneipp, H.; McLaughlin, M.; Brown, D.; Kneipp, K., *Nano Lett.* **2006,** 6, 2225 - 2231.
55. Cao, Y. C.; Jin, R.; Mirkin, C. A., *Science* **2002,** 197, 1536-1540.
56. Sönnichsen, C.; Franzl, T.; Wilk, T.; Plessen, G. v.; Feldmann, J.; Wilson, O.; Mulvaney, P., *Phys. Rev. Lett.* **2002,** 88, 077402.
57. Dulkeith, E.; Niedereichholz, T.; Klar, T. A.; Feldmann, J.; Plessen, G. v.; Gittins, D. I.; Mayya, K. S.; Caruso, F., *Phys. Rev. B* **2004,** 70, 205424.
58. Burda, C.; Chen, X.; Narayanan, R.; El-Sayed, M. A., *Chemical Review* **2005,** 105, 1025 - 1102.
59. Boyd, G. T.; Yu, Z. H.; Shen, Y. R., *Phys. Rev. B* **1986,** 33, 7923-7936.
60. Wilcoxon, J. P.; Martin, J. E.; Parsapour, F.; Wiedenman, B.; Kelley, D. F., *J. Chem. Phys.* **1998,** 108, 9137-9143.
61. Mohamed, M. B.; Volckov, V.; Link, S.; El-Sayed, M. A., *Chem. Phys. Lett.* **2000,** 317, 517-523.
62. Farrer, R. A.; Butterfield, F. L.; Chen, V. W.; Fourkas, J. T., *Nano Lett.* **2005,** 5, 1139-1142.
63. Zheng, J.; Nicovich, P. R.; Dickson, R. M., *Annual Review of Physical Chemistry* **2007,** 58, 409 - 431.
64. Zheng, J.; Zhang, C.; Dickson, R. M., *Phys. Rev. Lett.* **2004,** 93, 077402.
65. Peyser, L. A.; Vinson, A. E.; Bartko, A. P.; Dickson, R. M., *Science* **2001,** 291, 103–106.
66. Soller, T.; Ringler, M.; Wunderlich, M.; Klar, T. A.; Feldmann, J.; Josel, H.-P.; Markert, Y.; Nichtl, A.; Kurzinger, K., *Nano Lett.* **2007,** 7, 1941 -1946.
67. Dulkeith, E.; Ringler, M.; Klar, T. A.; Feldmann, J.; Javier, A. M.; Parak, W. J., *Nano Lett.* **2005,** 5, 585-589.
68. Dulkeith, E.; Morteani, A. C.; Niedereichholz, T.; Klar, T. A.; Feldmann, J.; Levi, S. A.; Veggel, F. C. J. M. v.; Reinhoudt, D. N.; Moller, M.; Gittins, D. I., *Phys. Rev. Lett.* **2002,** 89, 203002.
69. Jennings, T. L.; Singh, M. P.; Strouse, G. F., *J. Am. Chem. Soc.* **2006,** 128, 5462 -5467.
70. Jennings, T. L.; Schlatterer, J. C.; Singh, M. P.; Greenbaum, N. L.; Strouse, G. F., *Nano Lett.* **2006,** 6, 1318-1324.
71. Schneider, G.; Decher, G.; Nerambourg, N.; Praho, R.; Werts, M. H. V.; Blanchard-Desce, M., *Nano Lett.* **2006,** 6, 530 -536.
72. Cannone, F.; Collini, M.; D'Alfonso, L.; Baldini, G.; Chirico, G.; Tallarida, G.; Pallavicini, P., *Nano Lett.* **2007,** 7, 1070 -1075.
73. Ray, P. C.; Fortner, A.; Darbha, G. K., *J Phys. Chem. B* **2006,** 110, 20745 -20748.
74. Tam, F.; Gooldrich, G. P.; Johnson, B. R.; Halas, N. J., *Nano Lett.* **2007**.
75. Barnes, W. L.; Dereux, A.; Ebbesen, T. W., *Nature Materials* **2003,** 424, 824-830.
76. Krenn, J. R., *Nat. Mater.* **2003,** 2, 210 - 211.
77. Pincon, N.; Palpant, B.; Prot, D.; Charron, E.; Debrus, S., *Eur. Phys. J. D* **2002,** 19, 395–402.
78. Jun, H.-S.; Lee, K.-S.; Yoon, S.-H.; Lee, T. S.; Kim, I. H.; Jeong, J.-H.; Cheong, B.; Kim, D. S.; Cho, K. M.; Kim, W. M., *Phys. Stat. Sol. (A)* **2006,** 203, 1211–1216.
79. Faccio, D.; Trapani, P. D.; Borsella, E.; Gonella, F.; Mazzoldi, P.; Malvezzi, A. M., *Europhys. Lett* **1998,** 43, 213-218.
80. Hu, M.-S.; Chen, H.-L.; Shen, C.-H.; Hong, L.-S.; Huang, B.-R.; Chen, K.-H.; Chen, L.-C., *Nat. Mater.* **2006,** 5, 102-106.
81. Schrof, W.; Rozouvan, S.; Keuren, E. V.; Horn, D.; Schmitt, J.; Decher, G., *Adv. Mater.* **2002,** 3, 338-341.
82. Wang, Y.; Xie, X.; Goodson, T., *Nano Lett.* **2005,** 5, 2379-2384.
83. Gu, J. L.; Shi, J. L.; You, G. J.; Xiong, L. M.; Qian, S. X.; Chen, H. R., *Adv. Mater.* **2005,** 17, 557-560.
84. McMahon, M. D.; Lopez, R.; Haglund, R. F.; Ray, E. A.; Bunton, P. H., *Phys. Rev. B* **2006,** 73, 041401.
85. Bozhevolnyi, S. I.; Beermann, J.; Coello, V., *Phys. Rev. Lett.* **2003,** 90, 197403.
86. Canfield, B. K.; Kujala, S.; Jefimovs, K.; Turunen, J.; Kauranen, M., *Opt. Express* **2004,** 12, 5418-5423.

87. Galletto, P.; Brevet, P. F.; Girault, H. H.; Antoine, R.; Broyer, M., *J Phys. Chem. B* **1999,** 103, 8706-8710.
88. Jin, R.; Jureller, J. E.; Kim, H. Y.; Scherer, N. F., *J. Am. Chem. Soc.* **2005,** 127, 12482-12483.
89. C. X. Zhang; Zhang, Y.; Wang, X.; Tang, Z. M.; Lu, Z. H., *Anal. Biochem.* **2003,** 320, 136–140.
90. Lippitz, M.; Dijk, M. A. v.; Orrit, M., *Nano Lett.* **2005,** 5, 799-802.
91. Wenseleers, W.; Stellacci, F.; Meyer-Friedrichsen, T.; Mangel, T.; Bauer, C. A.; Pond, S. J. K.; Marder, S. R.; Perry, J. W., *J Phys. Chem. B* **2002,** 106, 6853-6863.
92. Yelin, D.; Oron, D.; Thiberge, S.; Moses, E.; Silberberg, Y., *Opt. Express* **2003,** 11, 1385-1391.

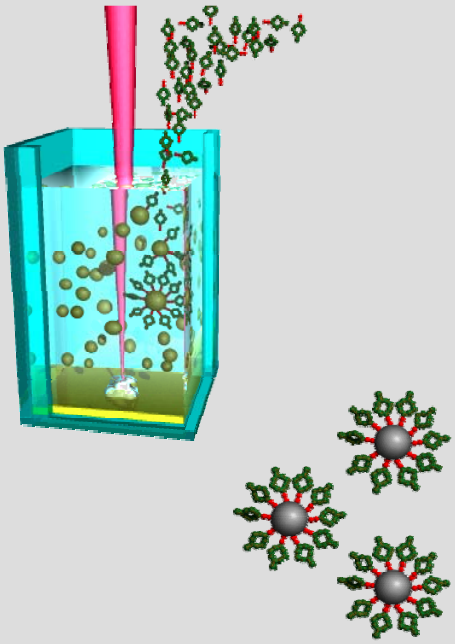

Section II:

Synthesis

Chapter 3

LASiS and characterization of metal nanoparticles

Gold and silver nanoparticles have applications in many distinct fields due to their peculiar physical and chemical properties. A gamut of applications is triggered by surface conjugation, which confer further specific functions to nanoparticles, such as solubility in a desired solvent, sensing with spectroscopic labels or targeted delivery with biovectors. Moreover the high tolerability and nontoxicity of AuNP figured out an increasing number of applications in biology.

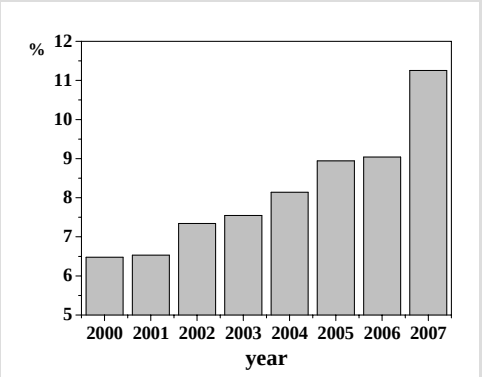

Figure 3.1 *Percentage of ACS paper containing in their abstract or title the words "Nanoparticles" and "Cell" or "Biological" on all the ACS papers published each year.*

Chemical reduction synhtesis, described in chapter 1, is a powerful method and offers several advantages. For instance high versatility over the choice of solvents and ligands

is allowed by the wet chemistry approach. Contrary to all other synthesis techniques, an high control of size and shape is possible, which boosted nanoscience in the last decades. Besides, wet chemistry approaches are easily scalable to the synthesis of large quantities of nanoparticles.

On the other hand some limitations are imposed by chemical reduction approaches to the synthesis of metal nanoparticles in solution. At a first glance, wet chemistry synthesis seems expensive mainly due to chemicals, like metal precursors, reducing and stabilizing agents needed for the synthesis. Indeed the amount of pollutant waste produced during the purification of the final product is the main source of costs. Purification is a forced step towards every kind of application, particularly biological and sensing ones, and can be very laborious in terms of time, materials and lab equipment. Secondly, chemical reduction synthesis always requires the presence of a stabilizing agent around nanoparticles surface, which hinder further functionalization with other molecules, since place exchange reactions are not at all trivial. One should also consider that procedures required for an accurate control of size and shape work only with a specific set of solvent, precursor, reductant, stabilizing agent and, eventually, functional ligand. If one changes only one of the previous parameters, all the procedures have to be reoptimized, as the temperature, the reagents concentration and the time of each synthesis step, which represents a strong limitation to the versatility of chemical reduction methods. As a consequence, in last years several papers facing these problems came out.[1-5]

In several occurrences laser ablation synthesis in solution (LASiS) proved to be an useful technique to overcome the limitations of wet chemistry approaches. LASiS consists in the laser ablation of a metal target immersed in a buffer solution. The obtained metal nanoparticles are recovered by the liquid and can be stable without the need of any ligand or stabilizing agent because particles are charged and consist of a colloidal suspension. Hence stabilizing molecules are not required, purification is unnecessary and no further costs are originated by pollutant waste disposal. LASiS allows the utilization of a wide choice of solvents and, therefore, of functional molecules. Functionalization is straightforward and the sensing of surface coverage is possible, contrary to wet chemistry approaches. LASiS procedures, when compared to the chemical reduction ones, are extremely easier and do not need constant care. On the other side only particles with spherical shape can be obtained, a limited control on the

monodispersity of nanoparticles size is allowed and LASiS is usually designed for the synthesis of limited amounts of particles.

3.1 Laser ablation synthesis in solution.

The most common technological applications of laser ablation consist in thin film synthesis by pulsed laser deposition in presence of a gas buffer in ultra high vacuum systems, in matrix – assisted laser desorption ionization mass spectrometry (MALDI – MS) and in cutting or drilling of materials as well as of biological tissues for surgery.

Laser ablation of matter is a process which starts on the material surface, where the laser beam is absorbed. It requires that the energy of absorbed light is high enough to raise the temperature of the material above the ablation threshold. This temperature is sensibly higher than the boiling temperature and, usually, a plasma, formed on the metal surface, is ejected by thermal expansion into the buffer medium (gas or liquid) forming a plasma plume. Studies of laser ablation processes principally exploit time resolved spectroscopy to characterize the plasma plume, to analyse ablated materials by time of flight mass spectroscopy and to use Monte Carlo simulations for understanding the dynamics of the ejection process.

In case of metal nanoparticles obtained by laser ablation in liquid buffer, two synthesis mechanisms have been suggested by studying particle size distribution and the morphology of target surface after LASiS. The first one consists of an explosive boiling process in which particles are originated by nanometric melted fragments of the ablated material.[6-9] The second one requires the nucleation and growth of particles due to cooling and supersaturation of the ablation plume.[6-8, 10, 11] Laser fluence and wavelength determine which one is the dominant regime, with higher fluences and lower wavelengths being more favourable to the former, namely to the explosive boiling process. Also the presence of absorbing defects can favour the coexistence of the explosive mechanism in localized points while the vaporization mechanism is dominant on the whole laser spot. The explosive ablation process usually originates particles with a large size distribution or, when happen at the same time with

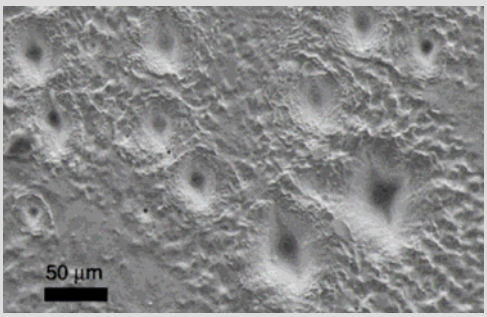

Figure 3.2 *SEM image of a platinum target after laser ablation at 1064 nm, 9 ns and 11 J cm^{-2} showing the compresence of explosive boiling ablation (deep holes) and vaporization ablation. From Ref. 6.*

the vaporization mechanism, bimodal distributions of nanoparticles size, because the two mechanisms originate particles with different average size. Moreover the droplet ejection mechanism implies that only particles surface can react in presence of a reactive environment.[6, 7]

Obtaining pure metal nanoparticles is not possible if the buffer solvent is reactive with the ablated metal, like CH_2Cl_2 or CS_2.[12] Also water, which is the most stable liquid for LASiS, has a limited oxidative effect on surface atoms of gold and silver nanoparticles. It has been estimated that about the 4 – 7 % of surface atoms in gold nanoparticles obtained by LASiS in water are oxidised to Au-O^-, which confer a negative Z – potential to the colloidal suspension. This explains the long time stability of AuNP and AgNP colloidal suspensions obtained by LASiS in water without any stabilizer.[13, 14]

In general, for thermally and chemically stable liquids, thermal and viscosity properties are of extreme importance for the final nanoparticles average size and size distribution, because they affect the expansion of the ablation plume and the nucleation and growth process. Experimental studies revealed that mixture of different solvents produced different average sizes and particles with different stability.[15, 16] Solvents polarity is important for particles stabilization, since one deals with a colloidal suspension. Organic solvents like alkanes usually promotes significant aggregation of particles obtained by LASiS.[12, 17] In the vaporization regime of laser ablation, solvent plays a role also because the metal – liquid interface energy γ_{S-L} determines the free energy barrier ΔG_N, the minimum radius R_N of nuclei and the speed for the nucleation process J_N as:[18]

$$\Delta G_N \propto \frac{\gamma_{S-L}^{\ 3}}{\left\{k_B T \ln\left[\frac{p}{p_0}\right]\right\}^2} \qquad (3.1)$$

$$R_N \propto \frac{\gamma_{S-L}}{k_B T \ln\left[\frac{p}{p_0}\right]} \qquad (3.2)$$

$$J_N \propto exp\left[-\frac{\Delta G_N}{k_B T}\right] \qquad (3.3)$$

where the ratio p/p_0 is the ratio of partial vapour pressure p to the equilibrium vapour pressure p_0 and represents the supersaturation of the metal vapour, T is the temperature and k_B is the Boltzmann constant. Next to nucleation, the growth process takes place,

where the nuclei radius *R(t)* increases in time *t* with respect to the starting radius R_N as:[10, 11]

$$R(t) = R_N + kV_a d(t)vt \qquad (3.4)$$

where V_a is the volume of a single metal atom, *d(t)* is the free atom density in solution at the time *t*, which decreases for increasing time, and *k* is the sticking probability of each atom to the particle surface. The growth process involves all free atoms present in a range of about 50 – 100 nm around the metal nucleus.[11]

Another important growth process, which is contemporary to the previous process, is represented by the coalescence of particles embryos.[10, 11] This mechanism accounts for the highly polycrystallinity and defective lattice structure of metal nanoparticles obtained by LASiS, in comparison to chemical reduction synthesis.

LASiS results are strongly affected by laser pulse wavelength and duration. On one side, shorter wavelengths with same fluence are more efficiently absorbed by the metal target. On the other side, AuNP and AgNP have a strong surface plasmon absorption which suggests the utilisation of laser frequencies out of the UV – Vis range. This is to avoid particles fragmentation due to reabsorption, which in general could result in the broadening of the size distribution if performed contemporary to the ablation process. Laser pulse duration primarily affect the efficiency of ablation process and the amount of ablated material. Indeed shorter pulses originates broader size distributions, therefore nanoseconds pulses are usually preferred to picoseconds or femtoseconds as a compromise between the ablation efficiency and a reasonable particles size distribution.[8, 10, 11]

The presence of a solute in the liquid solution provides a further degree of control over particles obtained by LASiS. The most common strategy consists in the use of stabilizing agents like sodium dodecyl sulfate (SDS),[10, 11, 19-21] cetyl-trimethyl-ammonium bromide (CTAB)[22], cyclodextrines[23, 24] or even thiols[25]. The primary effect of these chemicals is that of increasing the long term stability of metal nanoparticles. The secondary effect consists in reducing the average particles size and the width of particles size distribution if a strong interaction between the particles surface and the molecules takes place, like using thiols or cyclodextrines.[23-25]

3.2 Colloidal systems.

Metal nanoparticles obtained by LASiS bear a surface charge due to partial surface oxidation and to the ablation mechanism which favours the ionization of metal atoms and solvent molecules.[10, 11, 13, 14] Hence metal nanoparticles obtained by LASiS are colloidal solutions and can be stable for hours up to years even in absence of any stabilizing agents, only due to their surface charge.

In general the development of a net charge at the particle surface affects the distribution of ions in the surrounding interfacial region, resulting in an increased concentration of counter ions (ions of opposite charge to that of the particle) close to the surface. Thus an electrical double layer exists around each particle. The liquid layer surrounding the particle is formed by two parts; an inner region, called the Stern layer where the ions are strongly bound, and an outer diffuse region where they are less firmly attached. Within the diffuse layer there is a notional boundary inside which ions and particles form a stable entity. When a particle moves, ions within the boundary move with it, while ions beyond the boundary do not travel with the particle. This boundary is called the surface of hydrodynamic shear or slipping plane. The potential that exists at this boundary is known as the Zeta potential (or Z potential). The magnitude of the Zeta potential gives an indication on the stability of the colloidal system.

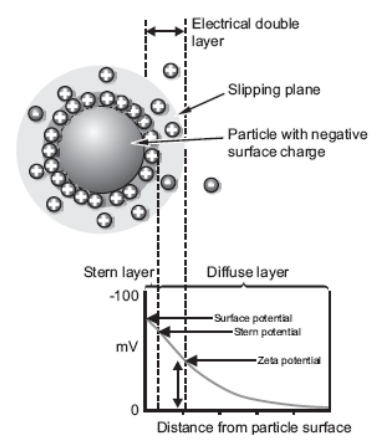

Figure 3.3 *Sketch of the characteristic parameters for a charged particle in a colloidal system.*

Zeta Potential can be derived by measuring the mobility distribution of a dispersion of charged particles as they are subjected to an electric field. Electrophoretic mobility is defined as the velocity of a particle per electric field unit and is measured by applying an electric field to the dispersion of particles and measuring their average velocity. The Henry equation connects the electrophoretic mobility μ_E to the Zeta potential ζ:[26]

$$\mu_E = \frac{2\varepsilon F_{IS}}{3\eta}\zeta \qquad (3.5)$$

where ε and η are the liquid dielectric constant and viscosity respectively, and F_{IS} is the Henry function. Depending on the concentration of ions, either the Smoluchowski (for

high ionic strengths - $F_{IS} = 1.5$) or Huckel (for low ionic strengths - $F_{IS} = 1.0$) approximations of the Henry function are used to obtain the Zeta potential from the measured mobilities.

In solutions with low ionic strengths, the Zeta potential is determined by the sphere potential, partially screened by the electrical double layer. Several Z – spectroscopy measurements showed that a negative charge is usually present on the surface of AuNP and AgNP obtained by LASiS in water,[13, 14] which was confirmed by our own Z – spectroscopy measurements (see Figure 3.4).

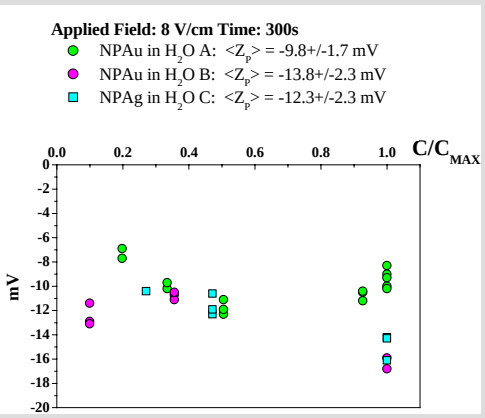

Figure 3.4 *Z – potential measurements on AuNP and AgNP obtained by LASiS in water performed by a SpectraPhysics Nicomp 380 instrument (Particle Sizing Systems, Santa Barbara, CA, USA) equipped with a 633 nm He – Ne laser.*

3.3 UV-Vis characterization of AuNP and AgNP using Mie theory.[27, 28]

Despite AuNP and AgNP have a distinctive SPA in the easily accessible UV-Vis spectrum, the most common technique for obtaining accurate data about nanoparticles average size and size distribution is TEM analysis. Unfortunately TEM measurements are relatively expensive in terms of costs and time and, sometimes, sample preparation can alter AuNP structure, due to surface coalescence in case of free particles or due to ion beam induced modifications in case of solid matrix inclusions.[29] Other techniques like small angle X ray scattering (SAXS),[30-35] differential mobility analysis (DMA),[36] confocal correlation spectroscopy (CCS)[37] or dynamic light scattering (DLS) [38-43] have been used to characterize AuNP and AgNP solutions, however, SAXS, DMA and CCS analysis are even more expensive or less accessible than TEM, while DLS accuracy is not satisfactory due to biased diffusion, i.e. the variation of the estimated size varying the measurements laser power when particles are very small.[36, 37] Contrariwise to the other techniques, UV – Vis spectroscopy represent a valid alternative to TEM for systematic analysis of AuNP solutions because spectrometers are easily accessible in every laboratories, measurements do not need sample preparation and do not alter the sample itself. However one has to be careful in the interpretation of the fitting of UV – visible spectra using the Mie theory, which is appropriate when particles have diameters larger than 1.5 nm. We showed in chapter 2 that SPA shape is correlated with AuNP

size because of extrinsic size effects, relevant for nanospheres with radii greater than 20 nm, and intrinsic size effects, very important below 20 nm of radius. Direct measurements on single AuNP demonstrated that both effects are well predicted by the Mie model with the appropriate correction of the metal dielectric constant. Indeed we have found in almost all cases that the fitting of UV-Vis spectra with the Mie model is not adequate in the wavelength range above 600 nm for AuNP and 500 nm for AgNP, where the experimental absorption is larger than the calculated one. This finding can be explained if we consider that the Mie model accounts only for particles with spherical shape, which is usually the shape obtained by a laser ablation synthesis (see below). However, AuNP in solution also form aggregates with nonspherical shapes, particularly when surfactants are not present, and this is the most important reason for observing deviations of the experimental spectra above 600 nm for AuNP and 500 nm for AgNP with respect to the calculated spectra with the Mie model. TEM images, although only in part representative of particle aggregation in solution, often show cigarlike shapes, which can be modeled, in a first approximation, by prolate spheroids. UV-Vis spectra of spheroidal nanoparticles have two characteristic absorption bands, one at the same frequency of spherical particles due to the polarization along the shorter axes and the other due to the polarization along the longer axis, red shifted and usually more intense with respect to the first. This last feature can account for the absorption above 600 nm for AuNP and 500 nm for AgNP that we observed. DDA simulations show that two or more metal nanoparticles in conductive bound have an absorption spectrum close to that of an equivalent spheroidal nanoparticle (cfr. paragraph *2.10*). Instead of DDA calculations, which requires long computation times and powerful calculators, it is possible to account for the contribution of small particles aggregates or nonspherical particles to the overall extinction spectra using the Gans model, that is the Mie theory extension to particles with spheroidal shape.

Moreover one can think that spheroidal particles show a distribution of aspect ratios because aggregation can involve two or more particles and we have assumed a Gaussian probability $G(a/b)$ centered at a/b

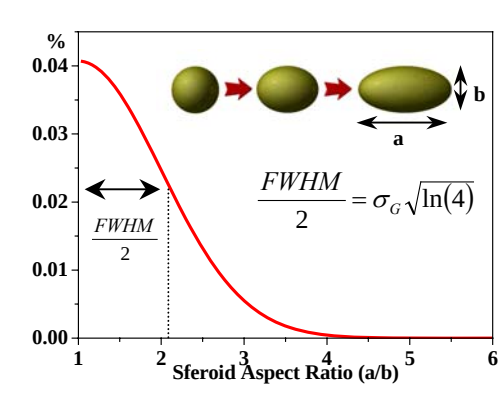

Figure 3.5 *Gaussian distribution of spheroids aspect ratio.*

= 1 for such a distribution:

$$G(a/b) = \frac{1}{\sigma_G \sqrt{2\pi}} exp\left[-\frac{(a/b - 1)^2}{2\sigma_G{}^2} \right] \qquad (3.6)$$

where $a/b > 1$ and σ_G is the standard deviation, which indicates that 68% of spheroidal particles have a/b smaller than $1 + \sigma_G$. Samples contain nanoparticles with different radii and different levels of aggregation. However, one can try to have an average description of the nanoparticles in particular when their distribution is not very wide. Following this approach we found that the UV-Vis experimental data can be reproduced by using Mie and Gans models and only three fitting parameters (MG fitting): (i) one average radius of the nanoparticles (R); (ii) the standard deviation (σ_G) of the a/b Gaussian distribution; (iii) the fraction of spherical to spheroidal gold nanoparticles. Furthermore, the geometrical average of the spheroid's semiaxes was considered to be equal to the average sphere radius, that is $R = \sqrt[3]{ab^2}$, hence considering that all the particles have the same volume and avoiding the introduction of other parameters. A χ^2 fitting was used for the calculation of the spectra. Initialization of the calculation was obtained estimating the initial average radius, R, by fitting the spectral region around 520 – 530 nm for AuNP and around 380 – 420 nm for AgNP with the Mie model, whereas the initial fraction of spheroids and their distribution was obtained by fitting the region above 600 nm for AuNP and 500 nm for AgNP using the Gans model.

Scaling the values of the calculated spectra to the experimental ones allows the determination of the concentration of the nanoparticles.

For gold and silver we used the expression of the dielectric function corrected for the size as described in paragraph 2.3 and the bulk dielectric function tabulated by Johnson and Christy[44] for gold and by Palik[45] for silver.

We have used the MG fitting for characterizing the synthesis in different solvents and to understand the evolution of the spectra with time and under laser irradiation (see below). Comparison with TEM images has given further support to the MG model fitting, as discussed later, and allowed to point out its limitations.

3.4 LASiS set up and nanoparticles characterization.

For the LASiS of metal nanoparticles we used the system described in figure 3.6. Laser pulses at 1064 nm (9 ns) Nd:YAG Q-switched laser (Quantel YG981E) were focused with a 10-cm focus lens on a metal plate placed at the bottom of a cell containing the solvent or the solution. We used pulses of about 10 - 50 J cm^{-2} at a 10 Hz repetition rate. Ablation times were in the range of minutes to hours depending on the desired metal nanoparticles concentration. The ablation rate is about 1 – 5 mg per hour with fluences in the 10 - 50 J cm^{-2} range.

All solvents were of spectroscopic grade and the targets were of 99.9% or higher purity metal.

The standard characterization techniques of metal nanoparticles obtained by LASiS was based on the interpretation of UV-Vis-NIR spectra aided by fitting of the data with the MG model described in the previous paragraph and with TEM analysis. All UV-Vis-NIR spectra were recorded with a Varian Cary 5 spectrometer in 2 mm optical path quartz cells. TEM images were collected at 300 kV with a JEOL JEM 3010 microscope equipped with a Gatan Multiscan CCD Camera model 794. The samples were prepared by evaporating some gold nanoparticles solution on a copper grid covered with an amorphous carbon holey film.

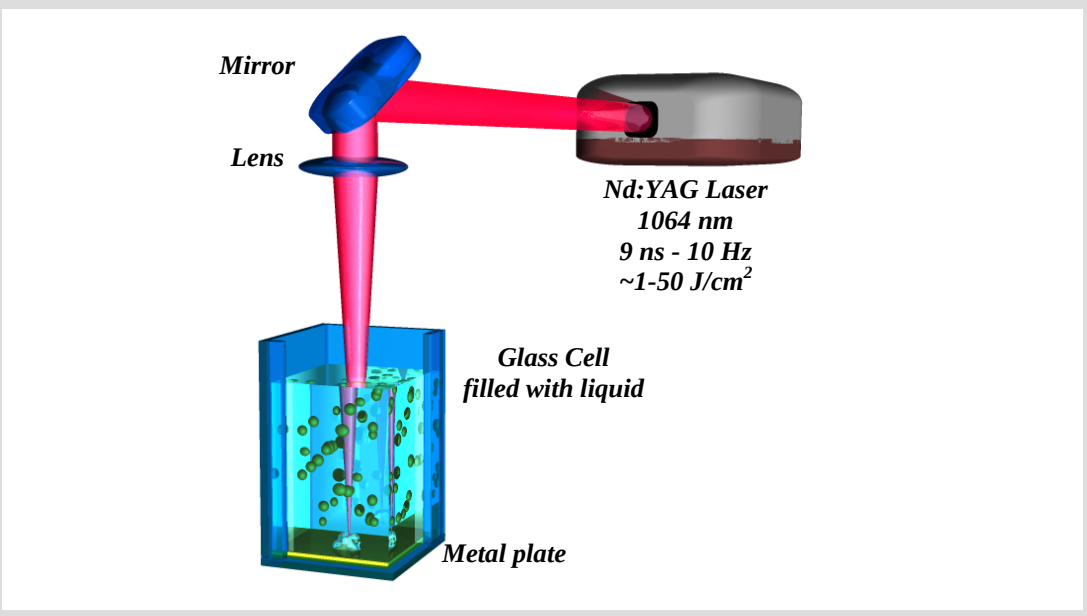

Figure 3.6 *Experimental set up of LASiS.*

3.5 LASiS of gold nanoparticles.[27]

The control of size, shape, and surface functionalization are very important issues in AuNP synthesis. Laser ablation in water solutions of surfactants like SDS or in solvents such as alkanes and aliphatic alcohols, have been reported in the last years. Unfortunately, many molecules useful for functionalizing AuNP are not soluble in these solvents. Therefore, we studied the synthesis of gold nanoparticles by laser ablation in solutions of dimethylsulfoxide (DMSO), tetrahydrofuran (THF), and acetonitrile (CH_3CN), which are solvents largely used in organic synthesis. We obtained free or functionalized AuNP in a one step process by LASiS with pure solvents or in solutions of ligand molecules. This makes it possible to obtain a direct and easy functionalization of the nanoparticles without other interfering reagents and therefore to obtain a new nanostructure with new properties. For example, an enhancement of the multiphoton absorption properties was found when gold nanoparticles excited with nanosecond pulses at 532 nm were coupled to a functionalized fullerene or to non functionalized zinc – phtalocyanine in DMSO and in THF respectively, where these molecules are sufficiently soluble, as will be discussed in chapter 5.

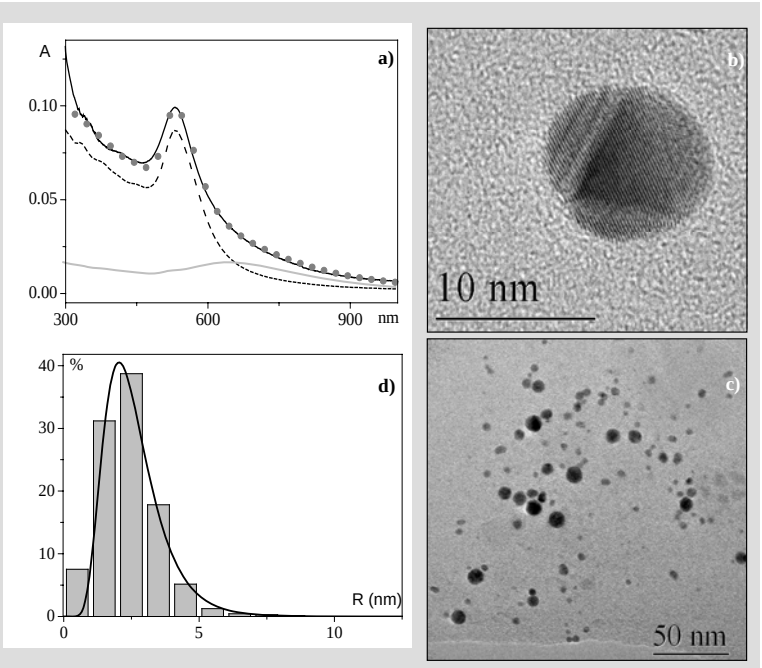

Figure 3.7 *a: UV – vis spectrum of AuNP synthesized in DMSO (black line), the Mie – Gans fitting (circles) [see text], the spherical particles contribution to the fitting (dashed line) and the spheroids contribution (grey line). b – c: HRTEM images of AuNP from the same solution. d: The nanoparticles size distribution fitted with a Log – Normal curve.*

Figure 3.7a shows the UV-Vis experimental spectrum of gold nanoparticles synthesized by laser ablation in pure DMSO, where the SPA maximum is observed at 530 nm. Figure 3.7b and 3.7c shows representative TEM images of the same sample where particles with largely spherical shapes can be observed, as expected for a laser ablation synthesis. Aggregation can also be observed

but cannot be, evidently, considered representative of the situation in solution. AuNP show clear crystalline structures, and we measured an average radius R = 2.4 nm with a standard deviation of 0.9 nm on 360 nanoparticles. As it is possible to see in Figure 3.7d, the size distribution obtained from TEM images can be fitted by a log-normal curve with a peak at 2.4 nm and a width of 0.4. The MG fitting of the UV-Vis spectrum (Figure 3.7a) finds an average radius of R = 2.5 nm, that is in very good agreement with TEM measurements. Figure 3.7a also shows the separate contributions of spheres and spheroids to the final fitting. Only 10% of gold nanoparticles are found to be spheroids with a Gaussian distribution of aspect ratio with a standard deviation σ_G = 1.4.

Figure 3.8a shows the UV-Vis spectrum of AuNP synthesized in pure THF, where the SPA is centered at 528 nm. Figures 3.8b and 3.8c show TEM images of the same sample. The nanoparticle average radius measured with TEM analysis is R = 4.1 nm with a standard deviation of 2.5 nm, analyzing more than 440 particles. The particle size distribution (Figure 3.8d) is similar to that reported for AuNP in DMSO although with a larger width. The log-normal curve shows a peak at 3.6 nm and a width of 0.55. The MG fitting of the UV-Vis spectra (Figure 3.8a) indicates an average radius of R = 4.5 nm, which is close to the average radius measured with TEM analysis. In this case the peak of the log-normal is at lower values because of the larger width of the distribution. The spheroid's contribution is found to be 34% with σ_G = 1.0 and it is reported in Figure 2a together with the sphere's contribution.

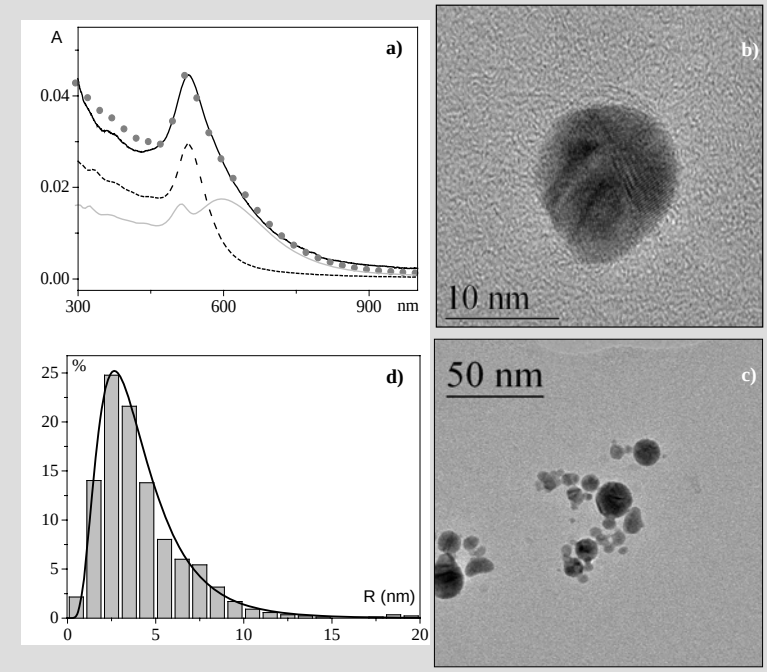

Figure 3.8 *a: UV – vis spectrum of AuNP synthesized in THF (black line), the Mie – Gans fitting (circles) [see text], the spherical particles contribution to the fitting (dashed line) and the spheroids contribution (grey line). b – c: HRTEM images of AuNP from the same solution. d: The AuNP size distribution fitted with a Log – Normal curve.*

Figure 3.9a shows the UV-Vis experimental spectrum of a AuNP synthesized by laser ablation in pure CH_3CN, in which the SPA is located at 522 nm. TEM images relative to the same sample are reported in Figure 3.9b and 3.9c. In this case the AuNP average radius is found to be R = 1.8 nm with a standard deviation of 1.2 nm observing 430 particles. The log-normal curve of the distribution of particles has a peak at 1.8 nm and a width of 0.5. The Mie-Gans fitting (Figure 3.9a) finds an average radius R = 2.7 nm with a fraction of 14% of spheroids with σ_G = 1.2. The solutions of free nanoparticles, without any stabilizing agent, are stable at least for several hours at room temperature without any appreciable change of their UV-Vis spectrum. This allows an easy manipulation of the particles for further functionalization or for their inclusion in solid matrices such as polymers or sol-gel materials. This situation also offers the possibility of an easy functionalization of the nanoparticles without the problem of controlling exchange equilibrium with capping agents. Figure 3.10 shows that analogous results have been obtained with others commonly used solvents as water, dimethylformamide (DMF) and ethanol.

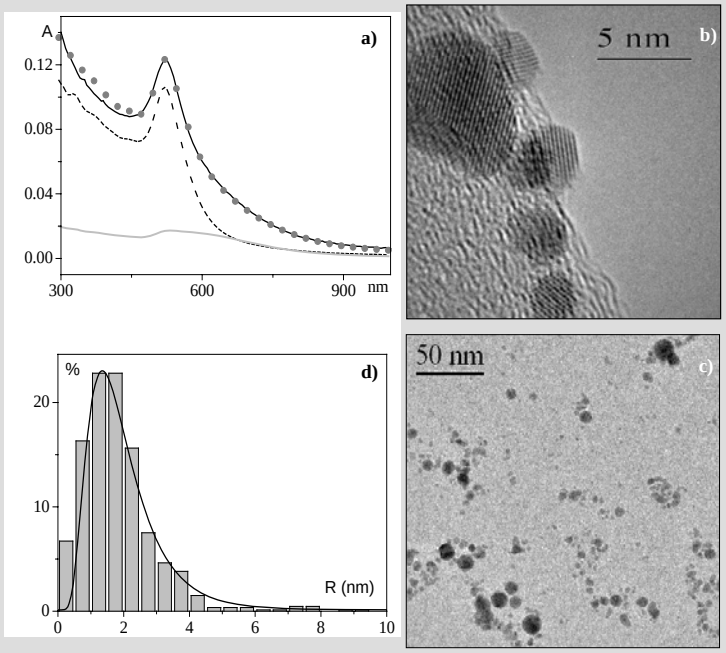

Figure 3.9 *a: UV – vis spectrum of AuNP synthesized in CH3CN (black line), the Mie – Gans fitting (circles) [see text], the spherical particles contribution to the fitting (dashed line) and the spheroids contribution (grey line). b – c: HRTEM images of AuNP from the same solution. d: The nanoparticles size distribution fitted with a Log – Normal curve.*

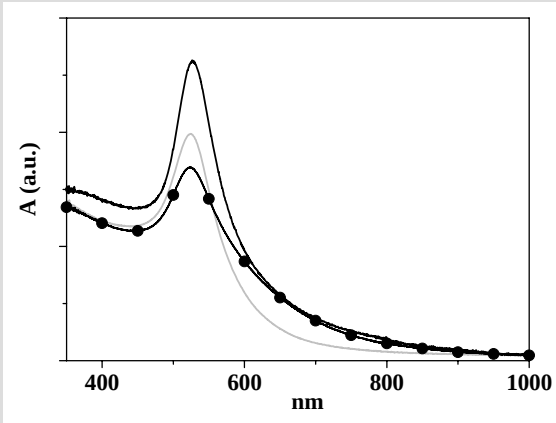

Figure 3.10 *LASiS of AuNP in H_2O (black line), DMF (grey line) and ethanol (black circles).*

3.6 Processing gold nanoparticles: size reduction, reshaping and ageing.[27]

It is expected that laser treatment of AuNP allows a size reduction or reshaping of the AuNP as a function of the energy and duration of pulses.[8, 46-48] For larger energies, which also depend on the duration of pulses, one can obtain a reduction of the average diameter of the particles. The interpretation of such a reduction is believed, in particular using nanosecond pulses, to be due to photothermal effects.[8, 46-48] One finds that larger particles are reduced as a consequence of their increased temperature to the boiling point, or, if such a temperature is not reached, to a temperature that allows the formation of a layer of vapour on the surface of the nanoparticles.[47] Clearly, such a behavior can be observed when the dissipation of energy is not sufficient and therefore the temperature can increase, and this also depends on the surrounding of the molecules and if they are capped or not. However, also not considering the details, one expects that smaller particles show time constants of heat dissipation that are proportional to the square of their radius.[47] Smaller nanoparticles show, therefore, fast heat dissipation and they are less expected to reach a temperature sufficient for size reduction. This explains, therefore, the observation that larger particles are reduced to smaller particles. We obtained results that agree with such a prediction. As an example, Figure 3.11 shows the UV-Vis spectra of AuNP solution in DMSO as synthesized, after 5 min of size reduction at 532 nm (4 J/cm^2 at 1 Hz) and after 10 min. The MG fitting (inset of Figure 3.11) indicates that the average size goes from 2.5 to 1.8 nm after 5 min and to 1.5 nm after 10 min. The presence of spheroids goes from 21% (σ_G = 1.0) after the synthesis to 9% (σ_G = 1.4) after 5 min of treatment to 11% (σ_G = 1.4) after 10 min. Therefore, the aggregation also decreases after the size reduction. The resulting solutions are stable for several days without any capping agent.

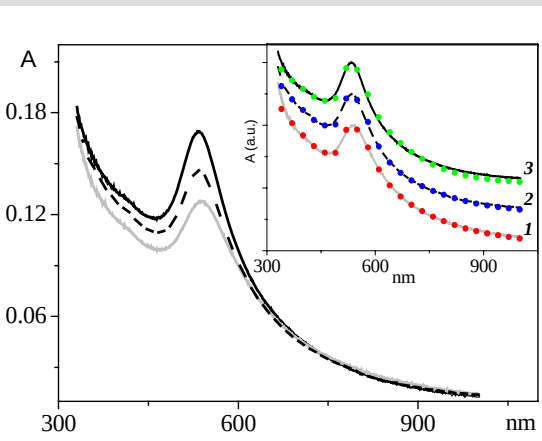

Figure 3.11 *UV – vis spectra of AuNP in DMSO as synthesized (black line), after 5 minutes of size reduction at 532 nm (dashed line) and after 10 minutes (grey line). Inset: Mie – Gans fitting of the UV – Vis spectra before the treatment (green circles - 1), after 5 minutes of treatment (blue circles - 2) and after 10 minutes (red circles - 3). Curves are displaced for clarity.*

When the laser fluence is not high enough, AuNP do not absorb the energy required by size reduction. However, this process usually leads to the reshaping of AuNP with edges or spheroidal forms into spheres.[47, 49-51] Also in our case we observe some changes of the UV-Vis spectra, but because most of the particles are already spheres we interpret the variation as due to a different aggregation of the particles, which is the main source of nonspherical forms of our particles. To show this effect, Figure 3.12a reports the UV-Vis spectra of a solution of AuNPs in THF before and after treatment at 532 nm with a fluence of 1 J/cm^2 for 5 min at 1 Hz. The MG fitting of the UV-Vis spectra (Figure 3.12b) indicates that the as synthesized solution has a 76.5% fraction of spheroidal particles (average radius R = 9.0 nm and σ_G = 0.9), whereas after treatment there are only 22% of spheroids (R = 10.0 nm and σ_G = 1.0). Therefore, one finds that the aggregation is reduced strongly after the laser treatment at low energy. However, the process is fully reversible. In fact, after 1 day the aggregation again increases the spheroid fraction to 59% (R = 9.0 nm and σ_G = 1.0), but irradiating the solution at 532 nm (5 min, 1 Hz and 1 J/cm^2) the fraction of spheroidal particles is again reduced to 22% (R = 10.0 nm and σ_G = 1.0).

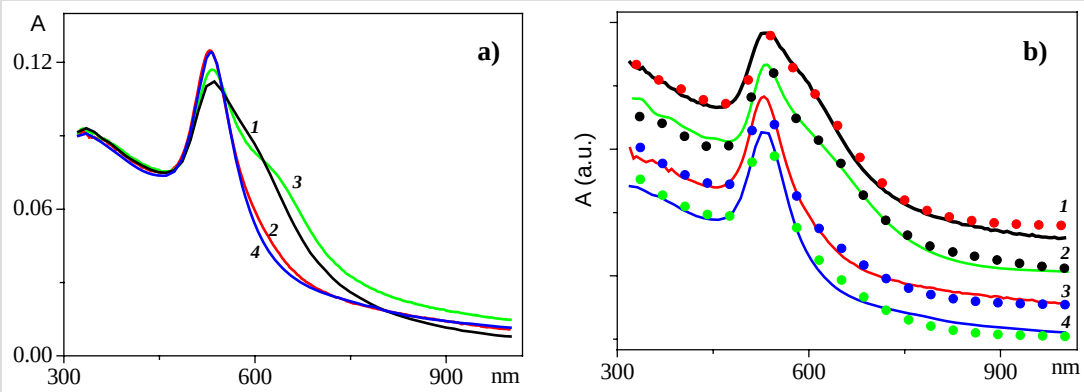

Figure 3.12 *a: UV – Vis spectra of AuNP in THF as synthesized (black line - 1), after reshaping at 532 nm (red line - 2), after 24 hours (green line - 3) and after the second reshaping treatment (blue line - 4). b: Mie – Gans fitting of the as synthesized solution (1 - experimental: black line, fitting: red circles), of the treated solution (2 - experimental: red line, fitting: blue circles), of the solution after 24 hours (3 - experimental: green line, fitting: black circles) and after the last reshaping (4 - experimental: blue line, fitting: green circles). Curves are vertically displaced for clarity.*

These results represent a simple way to control AuNP size or aggregation without other interfering molecules absorbed on their surface.

Aging of the solution of free nanoparticles leads to large aggregation in particular because they are not capped with other molecules that could induce electrostatic repulsion between the particles, if they are charged, or to steric effects like in the case of

polymers.[46] Figure 3.13a shows the aging effect on the UV-Vis spectra of AuNP in DMSO. The MG fitting (inset of Figure 3.13a) indicates that the as synthesized solution has 25% of spheroidal nanoparticles with σ_G = 0.9 and average radius R = 2.5 nm, while the same solution after 6 days has 100% of spheroidal particles with σ_G = 1.0 and average radius R = 4.0 nm. Similar situations were found with other solvents. The aggregation of the AuNP solutions can also be controlled without any capping molecule by simply reducing the concentration of AuNP. For example, Figure 3.13b shows that the dynamics of aggregation of an AuNP solution in CH_3CN, which at last determines the precipitation of the particles, changes as a consequence of a variation of the particle concentration. We evaluated, by an MG fitting, that the concentration of the solution that showed a large precipitation after 20 h was 5.2 10^{13} AuNP/cm^3 (R = 2.5 nm, 29% of spheroids with σ_G = 0.8) and that of a solution with a larger stability (more than 2 weeks before significant precipitation) 3.8 10^{13} AuNP/cm^3 (R = 2.5 nm, 12% of spheroids with σ_G = 1.2).

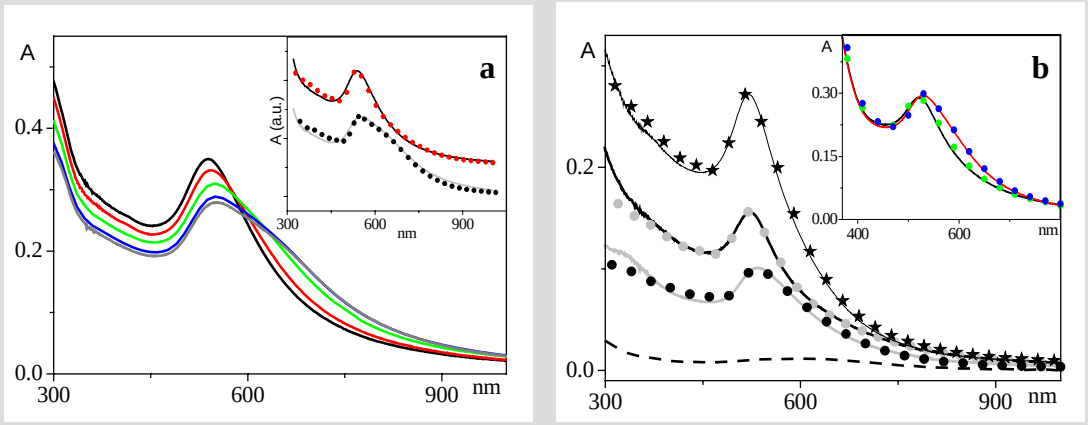

Figure 3.13 *a: UV – vis spectra of AuNP in DMSO as synthesized (black line), after 2 hours (grey line), after 1 day (green line), after 5 days (blue line) and after 6 days (red line). Inset: Mie – Gans fitting of the as synthesized solution (experimental black line, fit red circles) and of the 6 days aged solution (experimental: grey line, fitting: black circles). Curves are vertically displaced for clarity. b: UV – vis spectrum of AuNP as synthesized in CH_3CN with 5.2 10^{13} AuNP/cm^3 concentration (thin black line), the Mie – Gans fitting (black stars), the UV –vis spectrum of the same solution after 20 hours (dashed line) with almost all particles precipitated. The spectrum of a 3.8 10^{13} AuNP/cm^3 solution as synthesized (thick black line), the Mie – Gans fitting (grey circles) and the spectrum of the same solution after 2 weeks (grey line) with the Mie – Gans fitting (black circles). Inset: UV – vis spectra of 1.3 10^{14} AuNP/cm^3 as synthesized in a 10^{-2} M solution of AT in CH_3CN (black line), of the same solution after 20 hours (red line), the Mie – Gans fitting for the AuNP as synthesized in AT + CH_3CN (green circles) and after 20 hours (blue circles).*

Further experiments are needed to understand the concentration dependence of the dynamics of aggregation. However, as expected, one can control the process of aggregation and the following precipitation by adding a ligand molecule, for example, thioctic acid (AT: $C_8H_{14}O_2S_2$) at a concentration of 10^{-2} M. AT has a disulfide group

able to form two chemical S-Au bonds on the AuNP surface. The inset of Figure 3.13b shows that the synthesis of AuNP in a solution of thioctic acid slows down aggregation and precipitation. In this case the MG fitting of the as synthesized AuNP indicates a concentration of 1.3 10^{14} AuNP/cm^3, larger with respect to the above cases, an average radius R = 2.0 nm and a 19% fraction of spheroids with σ_G = 0.8. After 20 h one finds that the UV-Vis spectrum changes are only due to some initial aggregation. In fact, the fitting indicates that there are 51% of spheroids with σ_G = 0.8 and an average radius of R = 2.5 nm.

3.7 LASiS of gold nanoparticles in toluene.[52]

The synthesis by laser ablation of gold nanoparticles in toluene produces a very different and interesting result with respect to what is obtained with other solvents. As widely discussed, colloidal AuNP have a characteristic absorption band, while the synthesis in toluene produced particles which do not show any SPA. To the naked eye, the solution of AuNP obtained by LASiS in toluene has a yellow amber colour, though LASiS has been performed in a toluene solution with the same experimental conditions of all other solvents previously discussed.

In Figure 3.14a is reported the UV-Vis spectrum of the toluene AuNP solution, where one can note the absence of any SPA. We also used another aromatic solvent like benzonitrile, which is similar to toluene, and we found the same result, namely the absence of the SPA. This suggests the importance of a solvent like a benzene derivative for obtaining the observed SPA quenching. The inset of Figure 3.14a shows that the UV-Vis spectrum of the evaporated solution on a microscopy slide has the same structure of the colloidal solution.

Figure 3.14b reports the micro-Raman spectrum of the nanoparticles deposited on the slide recorded with a Renishaw InVia Raman microscope and using the 488 nm line of an Ar laser. One observes two broad peaks which are characteristic of graphitic carbon: one at 1355 cm^{-1} (D band) and another more intense one at 1592 cm^{-1} (G band).[53, 54] For comparison in Figure 3.14b, the spectra of graphite and carbon black are also reported. One can see that the ratio of the D band to the G band integrated intensities for our sample (I_{DG} = 1.6) is smaller than that of carbon black (I_{DG} = 2.0), indicating a larger amount of crystalline graphite. For an evaluation of the dimension of the crystals, we can use the linear relationship reported by Tuinstra et al.[55] between the reciprocal of the

in-plane graphite crystal length ($1/L_a$) and the ratio of the D band to the G band integrated intensities (I_{DG}). We find that the graphite crystals present in our samples have an average size of 2.7 nm. Micro-Raman spectra of nanoparticles obtained with solvents others than toluene or benzonitrile did not show the graphitic bands.

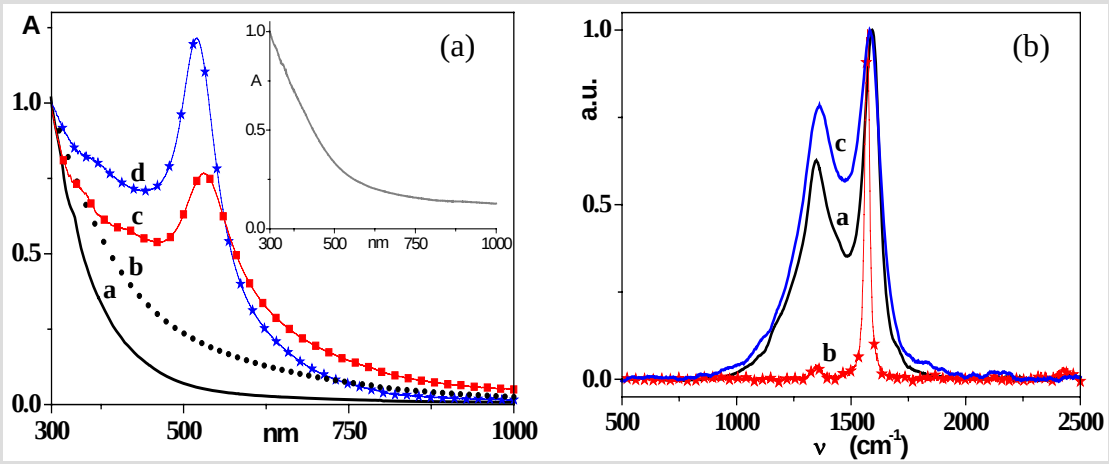

Figure 3.14 *a: UV-Vis spectra of AuNP solutions obtained by laser ablation in toluene (curve a - black line), in benzonitrile (curve b - dotted line) and, for comparison, in DMSO (curve c - red squares) and water (curve d - blue stars). Inset: AuNP obtained in toluene evaporated on a microscopy slide. All spectra are normalized at 300 nm. b: Raman spectra (exciting line at 488 nm) of AuNP deposited on the microscopy slide (curve a - black line). Graphite (curve b - red stars) and carbon black (curve c - blue line) spectra are reported for comparison. All spectra are normalized with respect to the G – band peak.*

X-ray photoelectron spectroscopy (XPS) analysis confirmed the result obtained with the Raman spectra. A custom-made ultrahigh vacuum chamber equipped with an EA125 Omicron analyzer and an Al K_α source and an operating pressure of 10^{-9} mbar have been used for the XPS measurements. The XPS spectrum shows a strong carbon 1s peak centered at 284.0 eV which confirms the presence of graphitic carbon, whereas a tail toward higher binding energies shows that amorphous carbon is also present. Furthermore, we observed a doublet at 83.7 and 87.4 eV, as expected, corresponding to the gold $4f^{7/2}$ and $4f^{5/2}$ doublet. Since the ratio of C 1s to Au 4f peak integrated intensities is 12:1, one can deduce that carbon is present in a large amount.

We also recorded transmission electron microscopy images at 300 kV. The TEM image reported in Figure 3.15a shows AuNP surrounded by graphitic nanocrystals with sizes variable among nanometer fractions to tens of nanometers, in agreement with the estimation made with the Tuinstra relationship. These nanocrystals show well-defined planes and are present in remarkable concentration around AuNP. The interplanar distance of such crystals corresponds to the 3.4 Å value of bulk graphite along the *c* axis direction (inset of Figure 3.15a). Around small nanoparticles, graphite crystals are not

clearly observed, but the contours of these particles are not well-defined. This suggests their inclusion in an amorphous carbon matrix which also prevents their growing, although the interparticle distance is very small.

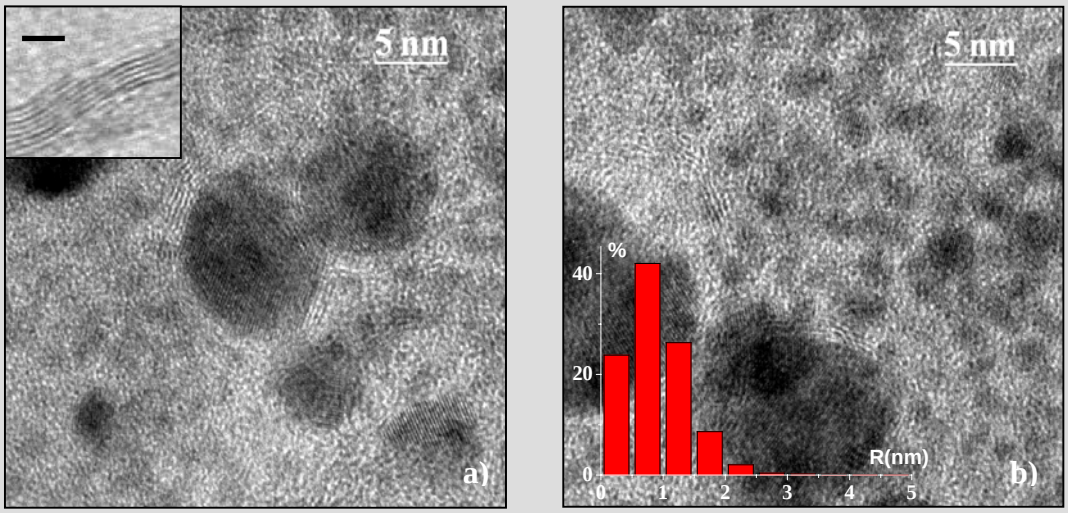

Figure 3.15 *TEM images of AuNP included in a graphitic carbon matrix. a) Planes of graphitic nanostructures surrounding AuNP; inset shows a magnification of such nanostructure, where the interplanar distance of 0.34 nm can be appreciated (bar = 2 nm). b) Distribution of AuNP in the carbon matrix; inset shows the radius distribution of more than 1000 AuNP.*

A statistical analysis on more than 1000 AuNP shows that they have an average radius of only 0.9 nm, with a standard deviation of (0.5 nm. The graphitic carbon matrix formation can be explained by recalling that the synthesis of graphitic materials based on the pyrolysis of benzene is reported in the literature.[56, 57] We can deduce that the process which produces graphitic structures around AuNP in our samples is of the same nature, since we measured a Raman spectrum very similar to that reported for the graphitic materials obtained by benzene pyrolysis.[58]

It was experimentally shown that, for very small AuNP, with a radius below 1.0 nm, the SPA is almost vanishing.[20, 59-61] Since the distribution of the particles we obtained (see Figure 3.15b) shows that almost 70% of the particles have a radius below 1.0 nm, quenching of the SPA can be explained considering that the carbon matrix precludes the formation of larger particles and therefore, indirectly, the presence of the SPA. However, 30% of the particles have radii which are larger than 1.0 nm and therefore they should show a clear SPA,[59] which is not observed. Mie theory can help create an understanding of this phenomenon. To take into account the influence of the carbon matrix on the extinction cross section (σ_{ext}), we use the Mie theory extension for core@shell spheres, considering that carbon is a shell around Au nanoparticles with a radius of 1.5 nm (see inset of Figure 3.16). In the quasi-static regime, we can use

dipolar approximation for the polarizability of the core@shell sphere. For the shell dielectric function we used the ordinary component of the graphite.[62] Simulations in Figure 3.16 shows that the SPA is sensibly reduced already with $d = R = 1.5$ nm and that for $d = 3.75$ nm it is completely suppressed. Therefore, the SPA quenching is obtained for a value of d which is in agreement with TEM images and with the value for the dimension of crystallites (2.7 nm) obtained with the Tuinstra relationship. Therefore this shows that the carbon matrix has not only the role of controlling the growth of the nanoparticles but also that of suppressing the SPA of larger nanoparticles.

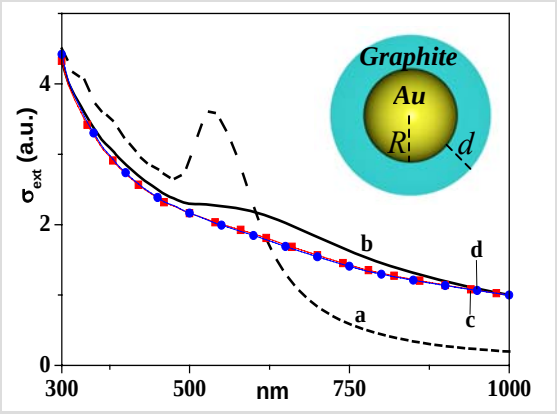

Figure 3.16 *SPA calculated with Mie model for a compact gold sphere of radius R = 1.0 nm (curve a - dashed line) and for a core@shell sphere with Au core radius R = 1.5 nm and a graphite shell of thickness d = 1.5 nm (curve b - black line), d = 3.75 nm (curve c - red squares) and d = 5.0 nm (curve d - blue circles). In all calculations toluene is the external medium.*

According to Mie theory results, a recovery of AuNP SPA can be obtained by removing the carbon matrix. We have obtained this result both for the colloidal solution and for the solid nanocomposite by oxidizing the carbon matrix. For the gold colloidal solution, we adopted the following procedure: The AuNP solution was evaporated to remove toluene; then, the residue was resolubilized in a 4:1 mixture of a 96% solution of H_2SO_4 and a 30% solution of H_2O_2. The solution was kept at 70 °C overnight. Figure 3.17 reports the UV-Vis spectrum of the solution after the oxidation, where a weak but clear SPA near 560 nm can be observed. The spectrum shows an SPA frequency characteristic of aggregated nanoparticles, although a fitting with the Mie model is difficult to obtain due to its weakness and to the presence of the absorptions of other compounds

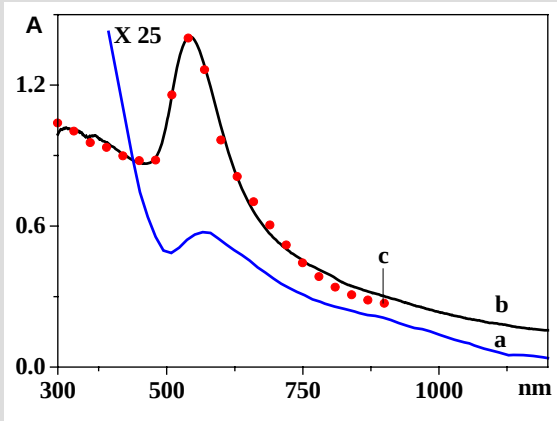

Figure 3.17 *UV-Vis spectra of the nanocomposite after oxidation in solution (curve a - blue line, magnification x25) and after thermal treatment (curve b - black line). Mie fitting of the annealed sample in air is reported as filled red circle (curve c).*

such as residual carbon particles. We obtained better results for the solid nanocomposite. In this case we oxidized in air at 525 °C the composite deposited on a microscopy slide using a tubular furnace model Carbolite MTF 10/25/130. Figure 3.17 reports UV-Vis spectra after 90 min of oxidation. One can clearly see the recovery of a sharp SPA at 545 nm. Fitting of these data can be obtained by using MG theory. The fitting (see Figure 3.17) indicates the presence of 65.5% nanospheres with a radius of 32.5 nm and of 34.5% ellipsoidal particles with σ_G = 1.1. The remarkable increase of the average radius with respect to the TEM measured value and the presence of a spheroid fraction indicates that, by removing the graphitic carbon matrix, gold nanoparticles underwent aggregation and growth. The micro-Raman spectrum after the thermal treatment shows the complete disappearance of both D and G bands. Also, the XPS spectrum shows that the 1s graphitic carbon peak at 284.0 eV disappears and only a very weak peak at 284.7 eV remains, with a relative intensity of 0.125:1 with respect to the Au 4f doublet, against the value of 12:1 observed before the treatment. We observed a different result using a thermal treatment of the nanocomposite in a N_2 atmosphere for 3 h at 525 °C. In this case, the carbon matrix is not removed but, on the contrary, the matrix graphitization was promoted. The micro-Raman spectrum recorded after this treatment shows a decrease of the intensity of the D band with respect to the G one. The ratio of the integrated intensity of these bands (I_{DG}) changed from 1.6 to 1.0, and applying the Tuinstra relationship, this indicates that the graphite particles have an average in-plane length of 4.7 nm. The UV-Vis spectrum of the nanoparticles, obtained after the treatment, does not show any SPA, as expected. Composites of graphite and AuNP have been considered interesting for sensors,[63, 64] and the present synthesis approach can be a simple way for obtaining such materials.

3.8 LASiS of silver nanoparticles.[65]

Similarly to gold nanoparticles, LASiS of stable AgNP in pure organic solvents such as acetonitrile (AN), *N*,*N*-dimethylformamide (DMF), tetrahydrofuran (THF), and dimethyl sulfoxide (DMSO) and toluene is possible without using reducing agents or stabilizing molecules. AgNP are obtained as free nanoparticles when synthesized in AN and DMF, while they are embedded in a carbon matrix when DMSO is used. An intermediate structure with a metal core surrounded by a thin shell of carbon was obtained using THF. LASiS of silver particles in toluene originated analogous results to

those shown for gold in paragraph 3.7. Fitting the AgNP SPA at about 400 nm with the Mie-Gans theory allowed an easy characterization of the structure of the nanoparticles, also when a core@shell structure was present.

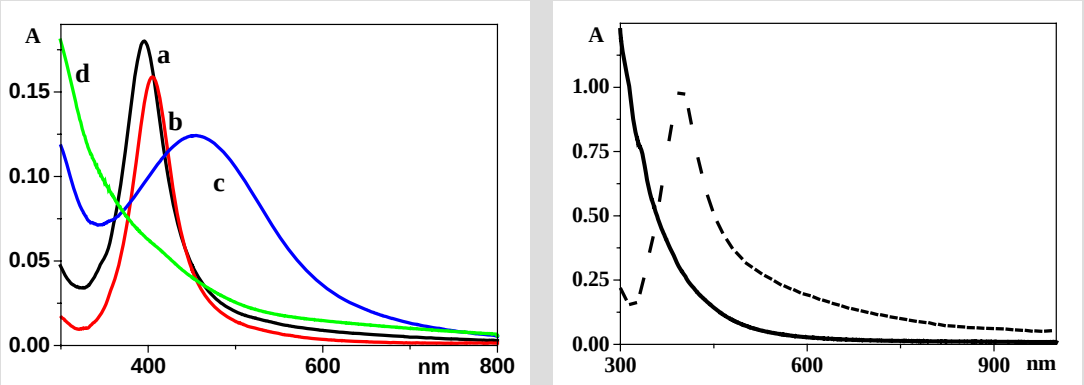

Figure 3.18 *Left: UV – vis spectra of AgNP synthesized in DMF (a, black), CH_3CN (b, red), THF (c, blue) and DMSO (d, green). Right: UV – vis spectra of AgNP synthesized in toluene (black line) and, for comparison, in water (dashed line). In toluene the characteristic silver nanoparticles SPA is completely absent.*

UV-Vis spectra of the solutions obtained by laser ablation of a silver plate immersed in AN, DMF, THF, DMSO and toluene are reported in Figure 3.18. One can see that AgNPs obtained in AN and DMF have a sharp SPA near 400 nm, as usual for spherical silver particles of nanometric size. On the contrary the AgNP solution obtained in THF is red to the naked eye, instead of yellow as usual, its SPA being red-shifted to 455 nm and very broad. The AgNP solutions obtained in DMSO and in toluene do not show, on the other hand, any SPA. HRTEM images of the same samples used for Figure 3.18 are reported in Figure 3.19. AgNPs synthesized in AN (Figure 3.19a) and DMF (Figure 3.19b) show a clear crystalline structure, and they have a prevalently spherical shape and small sizes. The insets of Figure 3.19a-b give the size histograms obtained with more than 350 particles in both cases, which can be well fitted with lognormal curves.

Average AgNP radii are found to be R = 1.9 nm in AN, with a standard deviation of 1.5 nm, and R = 2.2 nm in DMF, with a standard deviation of 2.5 nm. HRTEM images of the THF solution show that also in this case we produced nanoparticles of crystalline silver, but that they are always surrounded by an amorphous shell a few nanometers thick like that in Figure 3.19c. The usual log-normal distribution fits the size histogram for the AgNP core (inset of Figure 3.19c, obtained with more than 490 particles). The average size for the crystalline core is R = 2.4 nm with a standard deviation of 1.1 nm, while the shell thickness ranges from subnanometric size to several nanometers for the

biggest nanoparticles. HRTEM images indicate that also the DMSO solution contains crystalline AgNP (Figure 3.19d), although the SPA is not observable in the UV-Vis spectrum.

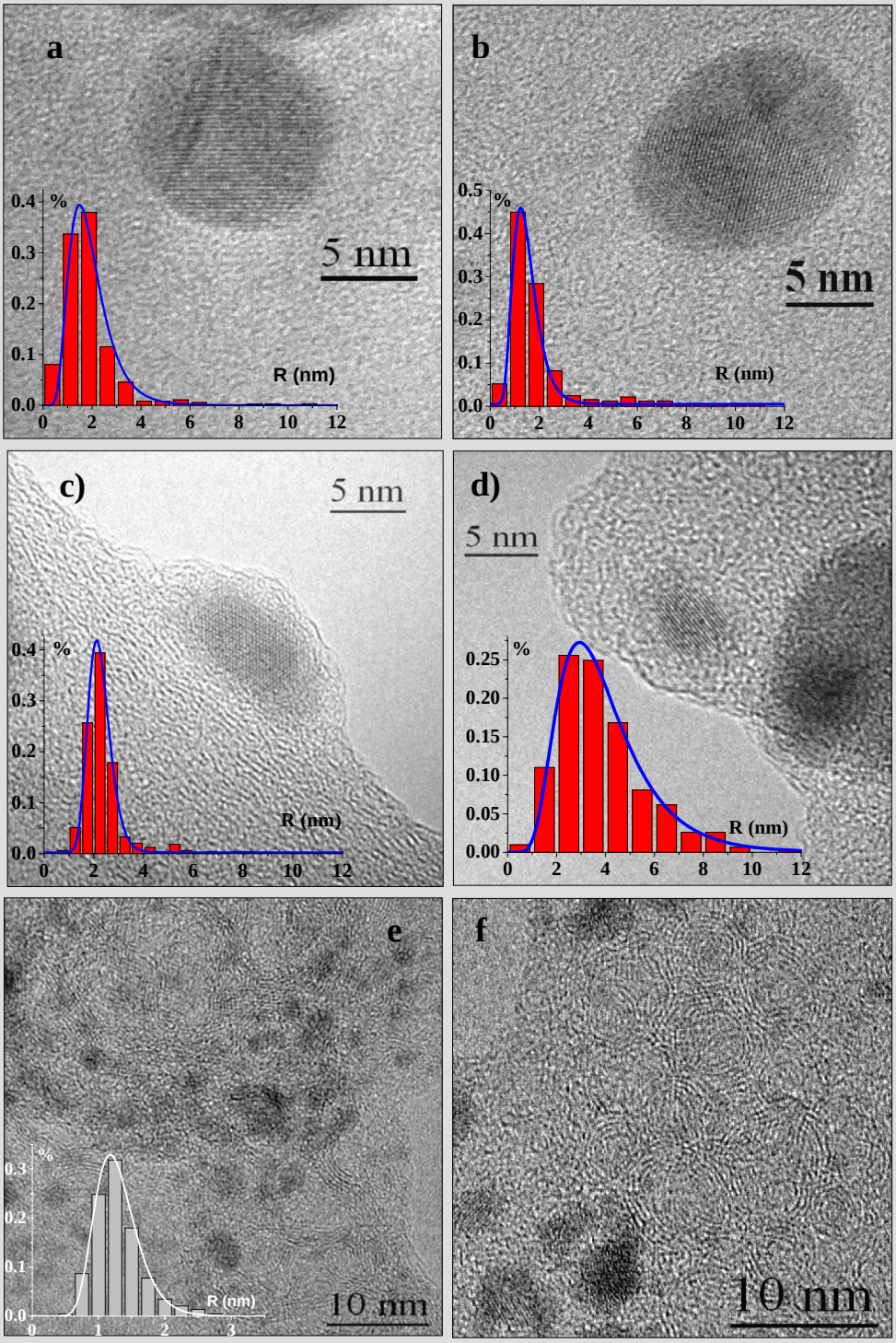

Figure 3.19 *HRTEM images of AgNP obtained in CH_3CN (a), DMF (b), THF (c) and DMSO (d). Insets show size histograms. e: HRTEM image of AgNP synthesized in toluene. The graphitic matrix completely surround silver particles. Inset: The nanoparticles size distribution fitted with a Log – Normal curve. f: HRTEM image showing onion shaped graphite crystals.*

In this case the AgNP are found to be completely embedded in a thick amorphous matrix. We calculated, on more than 300 particles, an average radius of R = 3.9 nm with a standard deviation of 1.9 nm (the inset of Figure 3.19d shows the size histogram with the usual log-normal structure). The presence of a graphitic matrix around AgNP obtained by LASIS in toluene is evident from figure 3.19e-f. Figure 3.19f also shows several onion like graphitic structures with nanometric size. This suggests that hot AgNP could catalyse the graphitization of toluene, like in the case of AuNP. The average AgNP radius is R = 1.3 nm with a standard deviation of 0.5 nm calculated on more than 440 particles.

We confirmed the presence of the carbon matrix for AgNPs synthesized in DMSO observing in the Raman spectrum the presence of two bands with comparable intensities at about 1360 (D-band) and 1580 (G-band) cm^{-1}. In case of AgNP obtained in toluene the G-band is sensibly higher than the D-band and corresponds to graphite crystals of about 60 nm in size, according to the Tuinstra relationship.[55]

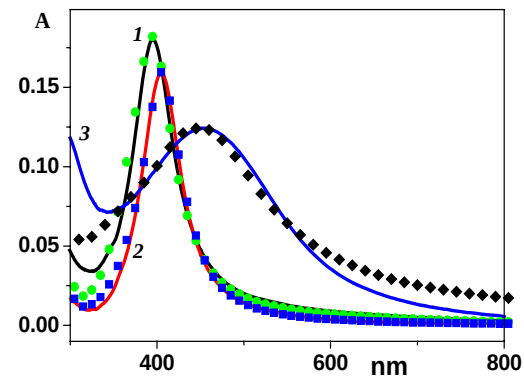

Figure 3.20 *Fittings of UV – Vis spectra using the Mie Theory. Fitting of AgNP in DMF, CH_3CN and THF are the green circles, blue squares and black diamonds respectively. Experimental UV – vis spectra of AgNP in DMF, CH_3CN and THF are the black line (1), red line (2) and blue line (3), respectively.*

The strong differences observed in the UV-Vis spectra of AgNP synthesized in AN, DMF, THF, DMSO and toluene can be understood by using the Mie theory for the calculation of the optical extinction cross section of metal nanoparticles. For the AN solution the MG fitting reported in Figure 3.20 indicates that the nanoparticles have an average radius of R = 3.5 nm and that a spheroid contribution of only 2% with σ_G = 1.5 is present, while for DMF R = 5.0 nm with 100% spherical nanoparticles. The negligible amount of spheroidal particles points out the low aggregation of AgNP obtained in these solvents. This is also confirmed by aging experiments since AN and DMF solutions are stable for weeks to months, depending on the concentration. This can be explained considering that the synthesized nanoparticles are charged and their aggregation is contrasted by Coulomb interactions. The calculated radii are slightly larger than the average radii measured by HRTEM (R = 1.9 and 2.2 nm for AgNP

obtained in AN and DMF, respectively). This is understood on the basis of Mie theory, which shows that the UV-Vis spectra depend on R^3, namely, on the volume of the nanoparticles. In fact, averaging the volumes of the particles, observed in HRTEM images, we found a corresponding average value R = 3.5 nm for particles synthesized in AN and R = 5.2 nm for those synthesized in DMF, which are remarkably close to the values calculated with the fitting of the UV-Vis spectra. This result confirms that the UV-Vis spectra depend more on large particles than on small ones and that a correct comparison with TEM based size histograms has to be considered.

In the case of AgNP synthesized in THF, fitting of the UV-Vis spectrum with the Mie-Gans model failed. However, we have shown above that, in this case, AgNP are surrounded by a shell of amorphous carbon. Then, we used the Mie theory extension for a core@shell sphere to describe a AgNP@graphite structure. Fitting reaches the best agreement for a silver core of R = 2.9 nm and a graphite shell of d = 0.85 nm (see Figure 3.20). Both R and d values are compatible with HRTEM analysis, which gives an indication of subnanometric thin carbon layers around the core particles of average radius R = 2.4 nm. Also in this case a better agreement is obtained considering the average core volume experimentally observed, equivalent to R = 3.0 nm. The same AgNP@graphite model can account for the quenching of the SPA for silver particles synthesized in DMSO and in toluene. In fact, the model shows that the SPA of a AgNP of radius R = 3.9 nm is completely quenched when the graphite layer reaches d = 6.0 nm. These values are again compatible with those measured by HRTEM images.

We were able to remove the amorphous carbon around the AgNP synthesized in THF, DMSO or toluene by a heat treatment at 550 °C for 1 h in air. Figure 3.21 shows the UV-Vis spectra of the samples, deposited on soda lime slides, before and after the heat treatment. For AgNP synthesized in THF the blue shift and the shrinking of the SPA are clearly visible, which indicates the effective removal of the carbon shell. Analogous results are shown in Figure 3.21b-c for AgNP synthesized in DMSO and toluene. The same heat treatment carried out in a nitrogen atmosphere on the same samples does not produce any difference in the UV-Vis spectra, confirming the importance of removing the matrix surrounding the particles with an oxidative treatment. This result also shows that other possible reactions, for example, with the sulphur of DMSO, did not occurred.

Free nanoparticles can be easily functionalized within the same solvent in which they are synthesized and without any preliminary treatment of the nanoparticles.

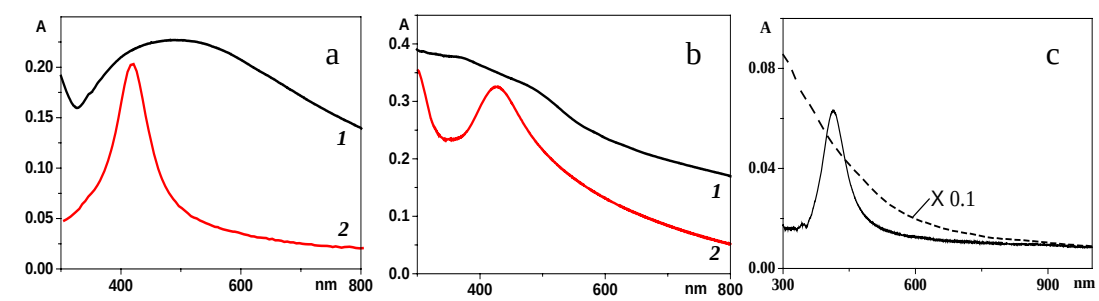

Figure 3.21 *UV – vis spectra of AgNP in THF (a) and DMSO (b) deposited on soda lime slides before (black lines - 1) and after (red lines - 2) the heat treatment in air at 550°C. c) UV – vis spectra of AgNP synthesized in toluene and deposed on a soda lime slide before (dashed line) and after (black line) an heat treatment in air at 550°C for 1 hour. After the treatment the characteristic AgNP SPA is completely restored.*

We report in Figure 3.22a the spectra of free AgNP in AN and of AgNP functionalized with α-lypoic acid and dodecanethiol, which are soluble in AN but not, for example, in water.

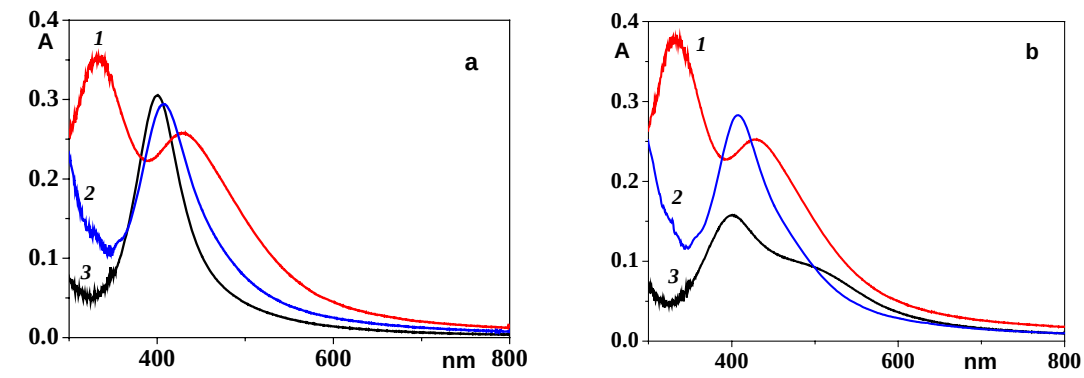

Figure 3.22 *Solutions spectra of free (black line - 1) and funtionalized AgNP with α–lypoic acid (red line - 2) and dodecanthiol (blue line - 3). Spectra without (a) and with (b) NaCl show the evolution of the spectra in presence of an aggregating agent.*

The functionalization was simply obtained by adding the molecules to the nanoparticle solution. One can see a red shift of the nanoparticle SPA with both molecules. This clearly indicates that the nanoparticles were functionalized since the shift can be understood as a consequence of a change of the dielectric constant induced in the surroundings of the nanoparticles by the new molecules linked to the surface. Further confirmation of the functionalization is found in Figure 3.22b where the spectra of the free and functionalized AgNP after addition of NaCl to the solutions are given. The salt induces aggregation of the nanoparticles as can be clearly seen by the presence of the pronounced shoulder at about 520 nm in the spectrum of free AgNP. On the other hand, spectra of the functionalized nanoparticles are very similar to those obtained without

addition of the salt (see Figure 3.22a), showing that the functionalization was present and is able to prevent the aggregation of the nanoparticles. One should note that the solutions of the functionalized nanoparticles do not contain other molecules (reducing agents, other surfactant molecules, byproducts) which could interfere in applications such as biological or SERS experiments.

3.9 Insight of the Mie – Gans fitting.[28]

In paragraph 3.8 we showed that average radii calculated by the Mie – Gans model fitting are in better agreement with radii corresponding to the experimental average volumes of silver nanoparticles. The same correspondence is usually found also for gold nanoparticles, as shown in Table 3.1.

Table 3.1 *Comparison between estimated and measured average radii*

METAL	SOLVENT	Mie – Gans Fitting (A = 1)	TEM Average Radius	Δ Mie -TEM (%)	Radius equivalent to Average Volume	Δ Mie -TEM (%)
Au	H_2O	17.8 nm	8.9 nm	50%	12.0 nm	33%
	CH_3CN	2.7 nm	1.8 nm	33%	2.7 nm	0%
	DMSO	2.5 nm	2.4 nm	4%	2.8 nm	-12%
	THF	4.5 nm	4.1 nm	9%	5.7 nm	-27%
Ag	CH_3CN	3.5 nm	1.9 nm	46%	3.5 nm	0%
	DMF	5.0 nm	2.2 nm	56%	5.2 nm	-4%
	THF	2.9 nm	2.4 nm	17%	3.0 nm	-3%

This finding is justified when considering that UV-Vis spectra depend on R^3, namely, on the volume of the nanoparticles, as also showed by equation *2.8*. As a proof of concept in figure 3.23 we reported the results of a Mie model calculation to evidence the different contribution to the overall extinction cross section for an AuNP sample obtained by LASiS in water (R were 8.9 nm ± 64 %).

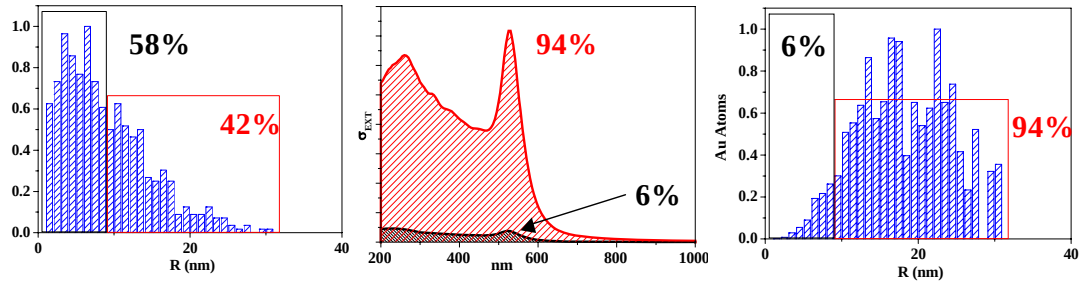

Figure 3.23 *Left: size distribution of the AuNP sample, arbitrarily divided in two fractions with smaller and larger radii, containing respectively the 58% and the 42% of the particles. Center: Mie model simulations of the contributes to the overall extinction cross section coming from the two fractions (considering a water matrix). The 42% of AuNP with larger radii accounts for the 94% of the total extinction of the colloidal solution. Right: the ratio of the two contributes to the σ_{ext} exactly matches the ratio of the volumes percentage.*

The overall extinction of the sample is accounted for more than 94% only by the distribution tail of particles with larger radii, corresponding to the 42% of the total. The volume of this 42% of particles actually corresponds to the 94% of the total, exactly as their contribution to σ_{ext}. Therefore the comparison between the radii relative to the average AuNP volumes and values calculated by the three fitting models is statistically correct.

The Mie - Gans fitting (MG fitting) can provide a good estimation of the average volume of metal nanoparticles, but it is less reliable for the estimation of the average radius and it cannot provide any information about the size distribution of these particles. Indeed this drawback can be overcome considering a simple statistic concept, based on the direct experimental observation of AuNP size distribution obtained by TEM analysis. Usually, AuNP synthesis, which involve nucleation and growth, originates particles with a Log Normal size distribution,[66-69] as found in case of some reduction methods,[70-73] LASiS,[27, 52, 74] ion implantation[75] and other preparation techniques.[76, 77] Therefore, we improved the previous MG fitting model replacing the old parameter R with two new parameters necessary to describe a Log Normal radii distribution, i.e. the centre of the distribution R_C and its width w. We adopted the following expression of the particles radii distribution to weight the σ_{ext} calculated for a certain R with the corresponding probability:

$$F(R) = \frac{1}{\sqrt{2\pi}(wR)} exp\left[-\frac{1}{2w^2}\left(Log\left[\frac{R}{R_C} \right] \right)^2 \right] \qquad (3.7)$$

$$LN(R) = \frac{F(R)}{\int_0^\infty F(R)dR} \qquad (3.8)\,.$$

Despite the complex ensemble of particles contained in every sample, the Log Normal Mie Gans model fitting (LNMG fitting) used for describing the whole system depends only on four parameters: *i*) the centre of the Log Normal radii distribution R_C ; *ii*) the width of the Log Normal radii distribution w; *iii*) the fraction of spherical to spheroidal gold nanoparticles and *iv*) the standard deviation (σ_G) of the *a/b* gaussian distribution. As for the MG fitting, the geometrical average of spheroids semi axes was considered to be equal to the average spheres radius, i.e $R = \sqrt[3]{ab^2}$, hence considering that all the particles have the same volume and avoiding the introduction of other parameters. A χ^2

fitting was used for the calculation of the spectra, which were normalized on the SPA peaks, with a point discretization every 5 nm. Calculated curves were allowed to shift of 1 point (5 nm), if necessary, to improve the matching with the experimental SPA. Computation was initialized estimating the initial average radius *R* by fitting the spectral region around 400 - 550 nm with the Mie model for a simple sphere.

Using only four parameters, the Log Normal Mie Gans fitting model (LNMG fitting) here described was able to: *i*) improve the accuracy of the experimental UV – Vis spectra fits; *ii*) improve the calculated average radius accuracy; *iii*) obtain a convenient evaluation of the AuNP size dispersion; *iv*) obtain an estimation of nonspherical and aggregated particles percentage.

We applied the LNMG fitting to the analysis of four solutions in pure water of AuNP with different average size. All the starting AuNP solutions were obtained by LASiS in ordinary conditions. Sample *Au1* was used as obtained by LASiS. Sample *Au2* and *Au3* were further processed with a size reduction treatment, as reported in paragraph 3.13. Sample *Au4* was processed with a size increase treatment as reported in paragraph 3.13. TEM analysis indicated Log Normal size distributions for all the four samples. The average radii *R* were 8.9 nm ± 64 % for sample *Au1*, 2.2 nm ± 22 % for sample *Au2*, 5.0 nm ± 42 % for sample *Au3* and 12.6 nm ± 76 % for sample *Au4*, while average volumes corresponding to radii R_V of 12.1 nm ± 124 % for sample *Au1*, 2.3 nm ± 87 % for sample *Au2*, 5.8 nm ± 107 % for sample *Au3* and 19.0 nm ± 139 % for sample *Au4*. The radius R_V relative to the average volume $\langle V \rangle$ is obtained from TEM measured size distributions through the following equation:

$$R_V = \left[3\langle V \rangle / 4\pi\right]^{\frac{1}{3}} = \left[\left\langle R^3 \right\rangle\right]^{\frac{1}{3}} \qquad (3.9)\,.$$

In figure 3.24 we compared the M (red line), MG (green line) and LNMG (blue line) fits of the *Au1* sample UV – Vis spectrum (grey line). The disagreement of the M fit with the experimental data around 650 nm is remarkable, as well as one can see that this drawback is absent in the case of MG and LNMG fits. Indeed both M and MG fits have a scarce agreement with experimental data around 250 nm. On the contrary the LNMG fit is reliable also around 250 nm. These remarks are well visible also in the inset of figure 3.24, where the difference between the calculated and experimental spectra (ΔA) is reported for the three models. The increase in fits reliability can be correlated with the

progressive increase from the one parameter Mie fitting to the four parameters Log Normal Mie Gans fitting by values reported in table 3.2.

In figures 3.25a we compared the average radii calculated by the M (red circles), MG (green squares) and LNMG (blue triangles) fittings with the experimental values of the four AuNP samples (black crosses) measured by TEM analysis. We found that the three models provided good estimations of R for AuNP samples *Au2* (R = 2.2 nm ± 22 %) and *Au3* (R = 5.0 nm ± 42 %), which have small average radii and standard deviations. Contrariwise the M fitting is imprecise with sample *Au4* (R = 12.6 nm ± 76 %) and the MG fitting is imprecise with samples *Au1* (R = 8.9 nm ± 64 %) and *Au4*, which are AuNP samples with large size and standard deviation. Only the Log Normal Mie Gans fitting model allowed a reliable estimation of the average radius for all the four samples, in the whole average radii interval and standard deviation spread.

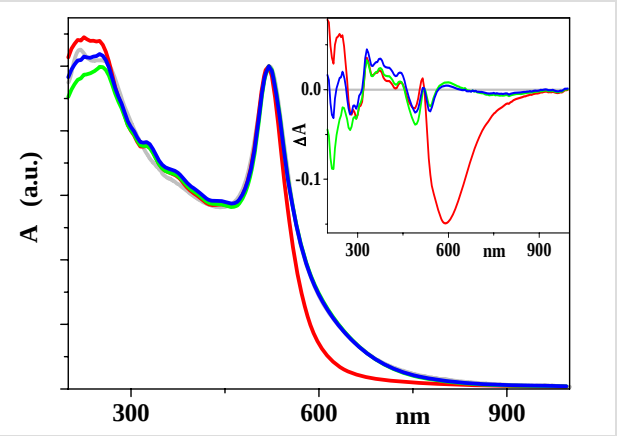

Figure 3.24 *UV – Vis spectrum of sample Au1 (grey line) and the M (red line), MG (green line) and LNMG (blue line) fits. Inset shows the difference between the experimental spectrum and the three fittings.*

Table 3.2

Fitting Model	*R (nm)*	R_C *(nm)*	*w*	*% Spheres*	σ_G	*Correlation coefficient*
M	*10.75*	-	-	-	-	***0.9886***
MG	*17.75*	-	-	*86.0*	*0.95*	***0.9986***
LNMG	-	*12.00*	*0.25*	*78.5*	*0.95*	***0.9993***

In figure 3.25b we compared the radii referred to the average volume estimated by the M (red circles), MG (green squares) and LNMG (blue triangles) fittings with the experimental values of the four AuNP samples (black crosses). It is remarkable that values estimated by the M and MG fittings coincide with those of figure 3.25a, while those obtained by the LNMG fittings and the experimental measurement do not, because in these two cases one must consider the calculated Log Normal size distribution and the Log Normal type experimental size distribution, respectively.

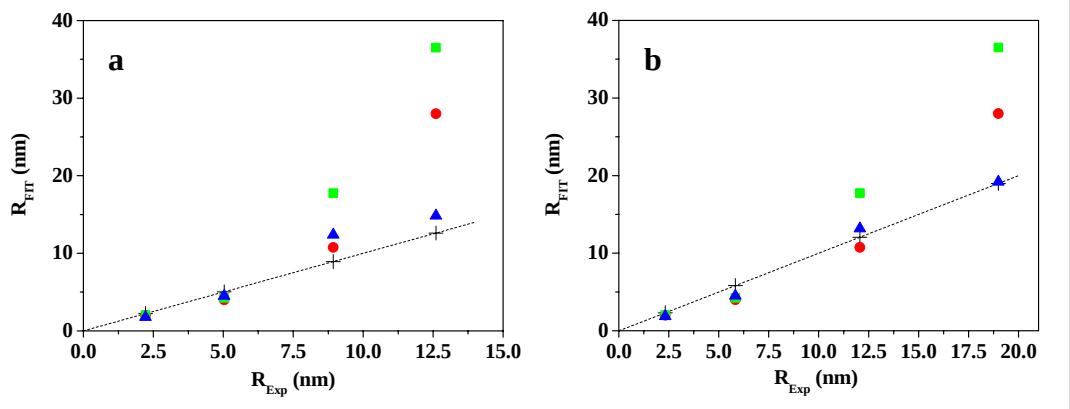

Figure 3.25 *a: Experimental (black crosses) and calculated (M: red circles, MG: green squares, LNMG: blue triangles) average radii of the four AuNP samples. b: Same of a) but referred to the radii correspondent to the average particles volume.*

The results in Fig. 3.25b show that the LNMG fitting values and the experimental values reach a very good agreement, while the estimations of both M and MG fittings are not satisfactory for bigger AuNP. The average errors on the estimation of the experimental *R* value of the four AuNP samples are 26 %, 45 % and 13 % for the M, MG and LNMG fittings respectively. The comparison of these values with errors relative to the average particles radii proof that all the three fitting models are more reliable for the estimation of the average volume than for the average radii.

The LNMG fitting provided better estimations of the average radii and the average volumes of the four AuNP samples, but it provided a scarce agreement between experimental and calculated Log – Normal distributions. The average error is 41% on the width *w* of experimental Log – Normal distribution and 26 % on the Log – Normal R_C. A useful parameter for testing the accuracy of the LNMG fitting on the experimental size distribution is provided by the comparison between experimental and calculated standard deviation of the four AuNP samples. In figure 3.26 we reported the difference (Δ) between the experimental and calculated standard deviation on the average radii (black

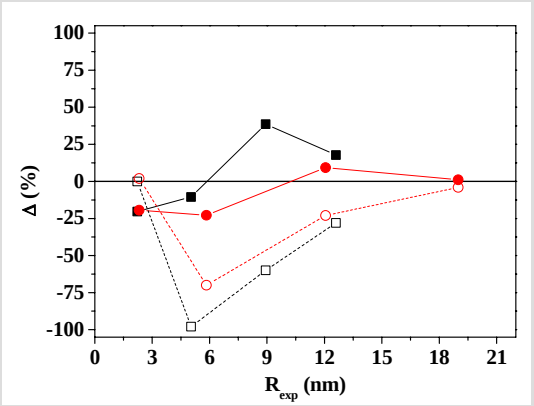

Figure 3.26 *Difference between the average radii and the relative standard deviations calculated with the LNMG fittings and the values measured by TEM for the four AuNP samples. Average radii and the relative standard deviations: black squares and black hollow squares respectively. Radii corresponding to the average volumes and the relative standard deviations: red circles and red hollow circles respectively.*

hollow squares) and on the radii relative to the average volumes (red hollow circles) for the AuNP samples. On average the LNMG fitting model underestimate the experimental standard deviation of 46% for average radii and of 25% for average volumes, while the M and MG fittings can not produce any estimation. In figure 3.26 we also reported the difference between the experimental and calculated average radii (black filled squares) and the radii relative to the average volumes (red filled circles) as obtained by the LNMG fitting model. One can see that the LNMG fitting estimations of particle size as well as the relative standard deviation are more reliable in the case of average particle volumes than for average radii.

The LNMG fitting model can be extended to other metal particles with strong SPA in the UV – Vis range, like silver or copper nanoparticles. It can also be optimized for non Log Normal size distributions or non Gaussian aspect ratio distributions. In case of particles with strong surface interactions, one can foresee that better estimations can be obtained by setting the appropriate value of the *A* parameter in the damping frequency (cfr. equation *2.15*).

3.10 LASiS of copper nanoparticles.

LASiS of stable copper nanoparticles (CuNP) has been performed successfully in several solvents like water, ethanol and tetrahydrofuran. The obtained colloidal solutions show the characteristic SPA band of copper around 600 nm (Figure 3.27). Remarkable differences are present in SPA of CuNP for the different solvents, suggesting that different average sizes and different nanostructures have been obtained by varying the liquid buffer. A good stability in time has been observed in all the above solvents. Further structural characterization analysis are in progress.

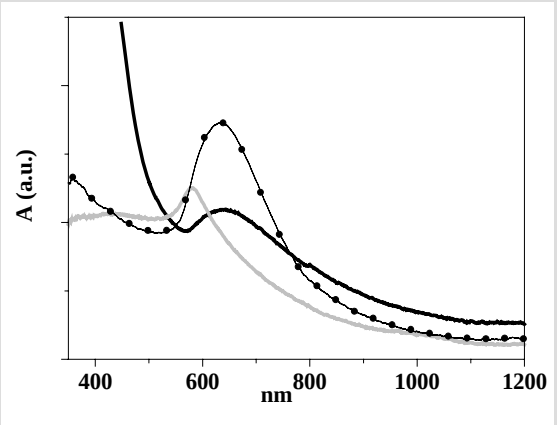

Figure 3.27 *UV-Vis spectra of CuNP obtained by LASiS in H_2O (black line), EtOH (grey line) and THF (black circles).*

3.11 Sequential laser ablation synthesis of gold and silver nanoparticles.[#1]

Synthesis of AuNP by LASiS in a solution of silver nanoparticles or synthesis of AgNP by LASiS in a solution of gold nanoparticles originates particles with a less definite structure and intermediate plasmonic properties, which recall those of an Au-Ag alloys. Given a certain AuNP concentration, the time devoted to the LASiS of AuNP is the parameter for a continuous shift of the initial silver SPA towards that of AuNP, passing through that of a silver-gold alloy with a progressively increasing gold amount. Figure 3.28 shows the SPA evolution for the laser ablation of gold in a solution of AgNP at different ablation times (5, 10 and 15 minutes of AuNP LASIS respectively). TEM and EDS analysis showed that gold particles form small aggregates embedding the pristine AgNP. Figure 3.28 shows an example of such aggregated structure, where a "core" with higher electronic contrast (possibly gold) is surrounded by a shell with oblong and irregular shape and lower electronic contrast (possibly silver).

This result suggest that gold nanoparticles obtained by LASiS promoted the aggregation of pre-existing silver nanoparticles, similarly to the embryos coalescence process described in paragraph 3.1. The conductive bonding between the particles originates an averaged plasmonic response like an alloy, instead of a weighted contribute of the distinct Au and Ag SPA.

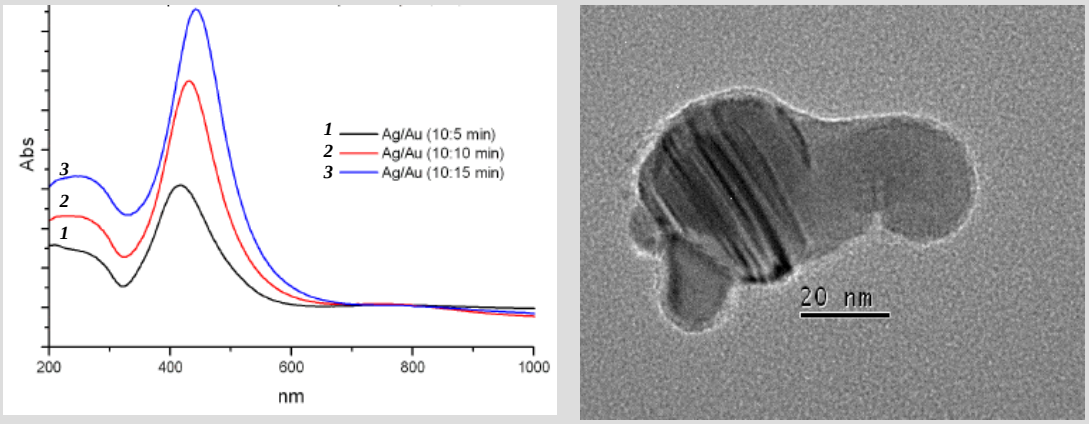

Figure 3.28 *Left: UV-Vis spectra of laser ablation of a gold target in solution of silver nanoparticles, for three different ablation times. A progressive shift of the SPA from 400 nm to 520 nm is observed. Right: TEM image of a nanoparticle from the sample Ag/Au (10:10min).*

[#1] *A. Moresco, Master Thesis A.A. 2004-05, Padova University, Title: "Sintesi per ablazione laser di nanoparticelle di argento, oro e di leghe argento-oro in acqua e loro caratterizzazione", Advisor: Prof. M. Meneghetti.*

3.12 Controlled aggregation of gold nanoparticles for SPA engineering.[#2]

Controlling the aggregation of gold nanoparticles have useful applications in nanotechnology. In chapter 2 we discussed how aggregation can be used for sensing when promoted by a specific target molecule, and how it can enhance the SERS signal of adsorbed molecules due to local field effects. We tried to control the aggregation of spherical gold nanoparticles obtained by LASiS for building new, more complex, nanostructures by a bottom up approach.

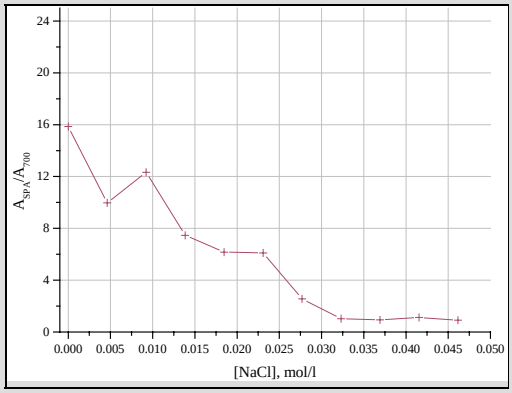

Figure 3.29 *Ratio of the SPA absorbance to the absorbance at 700 nm for a 10^{-9} M AuNP solution in water 18 hours after the addition of NaCl with various concentration in the 5 10^{-3} - 5 10^{-2} M range.*

Aggregation of AuNP obtained by laser ablation in pure water, i.e. in absence of any stabilizing ligand, can be controlled by acting on the main parameter which is responsible of the stability of colloidal systems, namely the Zeta potential of particles. Therefore we explored the effects of the addition of controlled amounts of NaCl on the stability of AuNP solutions. Figure 3.29 reports the ratio of the absorbance at SPA maximum to that at 700 nm, indicative of AuNP aggregation, measured after 18 hours from the addition of NaCl (to obtain concentration between 5 10^{-3} M and 5 10^{-2} M) to 1 10^{-9} M AuNP solutions. A massive aggregation takes place for the higher NaCl amounts, which also produce progressive particles precipitation. The results show that the control of AuNP aggregation by only adding NaCl is not easy. Since LASiS of AuNP in alkanes originated less stable and irregularly shaped nanoparticles, probably also because of the low polarity of the solvent,[12, 17] we explored the effect of the addition of common organic solvents to analogous solutions of AuNP obtained by LASiS in H_2O. In this case we only found a relationship between the purity of the solvent and particles stability, for instance solvents non spectroscopic grade negatively affected the long term stability of the colloidal system. On the contrary, interesting results figured out from the combined addition of both organic solvents and salt to AuNP in water. In these case a high degree of control was achieved on the

[#2] *S. Scaramuzza, Bachelor Thesis A.A. 2005-06, Padova University, Advisor: Prof. M. Meneghetti; E. Antonello, Bachelor Thesis A.A. 2005-06, Padova University, Advisor: Prof. M. Meneghetti; Title: "Sintesi di nanoparticelle di oro per mezzo di ablazione laser in acqua e studio della loro aggregazione indotta da solventi ed NaCl".*

aggregation of nanoparticles. In particular, calibrating the amounts of solvents like ethanol or THF and of salts like NaCl o KCl, it was possible to control the ratio of the SPA maximum absorption to the absorption at 700 nm, as described more in details in the following paragraph.

The control of particles aggregation by addition of both THF and KCl has been exploited to obtain anisotropic aggregates and core@shell structures with new plasmonic absorptions at longer wavelengths. In the first case we tried to obtain AuNP aggregation into one preferential direction by using ethylene glycol and polyvinylpyrrolidone (PVP). Ethylene glycol and PVP are known for being physisorbed preferentially on some crystallographic facets of gold particles (cfr. chapter 1), hence they leave only a fraction of particles surface available for the formation of conductive junctions with other particles. Figure 3.30 shows that PVP with concentration between 0.5 10^{-3} M and 1.5 10^{-3} M or 5 – 25 % in volume of ethylene glycol were effective in originating AuNP aggregates with a strong absorption band around 700 nm, which is typical of elongated gold structures. The broad band appearance indicates that several tens of particles form aggregates and that there is a large dispersion of aggregate size and shape.

A different approach for the control of the frequency of the SPA maximum is to obtain core@shell structures with a dielectric core and a gold shell. We started from SiO_2 nanoparticles of 30 nm in diameter, synthesized with the Stober method[78] in ethanol and surface functionalized with mercaptopropyl trimethoxysilane.[#3]

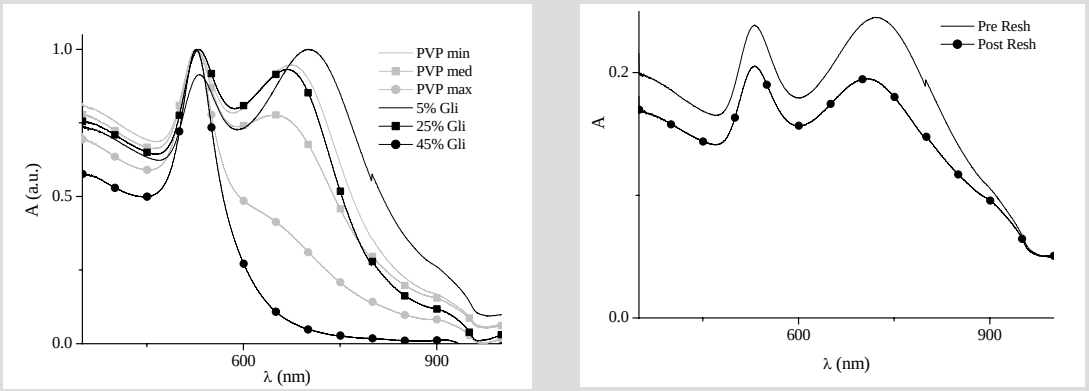

Figure 3.30 *Left: AuNP aggregated in presence of variable amounts of PVP or ethylene glycol. Right: AuNP aggregated in presence of silica nanoparticles bearing thiols on their surface, before and after 532 nm – 9 ns irradiation (7 hours. 10 Hz) at 50 mJ/cm^2.*

[#3] This work has been developed in collaboration with Prof. F. Mancin of the Department of Chemical Sciences of Padova University.

Promoting the aggregation of AuNP in presence of silica nanoparticles originated a broad intense band around 750 nm, compatible with the formation of a core@shell structure as well as with large nanoparticles aggregates. Since laser irradiation induce the melting of aggregates into spherical particles,[46] we performed the irradiation at 532 nm with 50 mJ/cm^2 fluence for 7 hours at 10 Hz of the so obtained nanostructures. Figure 3.30 show that the SPA revealed stable upon 532 nm irradiation, which suggested that aggregation actually took place around the silica core. These preliminary results show that control of the SPA maximum can be obtained, but further investigations are required for a better control of the new plasmonic structures.

3.13 Chemical free size manipulation of AuNP by laser irradiation.[74]

The main advantage offered by chemical reduction methods, with respect to the laser ablation technique, is good control of the AuNP average size and size distribution by appropriate choice of the reagent mixture and reaction parameters (cfr. chapter 1) LASiS does not allow good control of these parameters, although various methods to reduce the nanoparticle size distribution are known, like centrifugation,[11, 79, 80] size exclusion chromatography[80, 81] and membrane filtration.[82] On the other hand, several authors reported the reduction of the size of AuNP only by laser irradiation, but they were not able to obtain predetermined sizes.[47, 83-85] It is remarkable that most of these studies were made in particular on AuNP covered by stabilizing agents, which influence the size reduction experiments in the same way they influence the synthesis process. Furthermore, to our knowledge, no one has tried to increase the radius of nanoparticles above their initial value by laser treatment. Control of particle size in a range of tens of nanometers is, however, an important parameter for AuNP applications for example in biology, since it can determine, for instance, cellular inclusion.[86-88] Therefore we found a way to predetermine the average radii of AuNP by laser treatment using few simple parameters, although no attempts were made to reduce their distribution in particular for size increased nanoparticles. We used AuNP free from ligands, synthesized by LASiS in pure water or dimethyl sulfoxide, and obtained their size reduction or increase by two complementary techniques based on laser irradiation with 9 ns pulses at 532 nm and without using any stabilizing agent. The first technique adopts a top–down approach to obtain a predetermined decrease of the AuNP radius (size reduction) by laser vaporization of particles with increasing irradiation fluence. The second technique is a

bottom–up approach since we obtained larger nanoparticles (size increase) by inducing controlled AuNP aggregation in solution and then melting the aggregates by laser irradiation at low fluence. Since the starting AuNP solutions were obtained by LASiS, the whole synthesis process and size manipulation is very simple and the nanoparticles can be immediately functionalized.

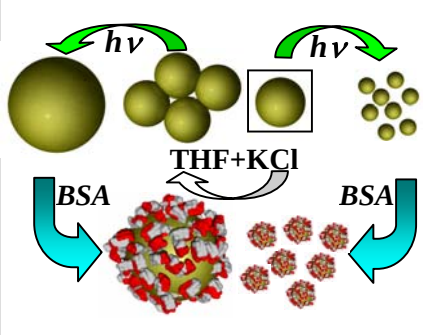

Figure 3.31 *Scheme of AuNP size manipulation by laser irradiation and of their easy functionalization (see text).*

Interaction of nanosecond laser pulses with gold spherical nanoparticles and nanorods has been investigated in various experiments of size reduction,[83, 84, 89] reshaping[46, 51] and optical limiting.[90, 91] All these processes involve transfer of laser energy to AuNP by a multiphoton absorption process and, therefore, the variation of particles structure is a consequence of their photothermal heating.[46, 47] As previously discussed, for the size reduction mechanism it is required that the AuNP temperature exceeds the vaporization threshold, as in laser ablation synthesis, whereas less energy is required when the absorbed laser energy has to cause the melting of AuNP, as in case of reshaping. Nanosecond pulses are usually considered because in this time regime the multiphoton absorption process competes with the heat transfer from the AuNP to the solvent, and this process is strongly size dependent.[47, 92, 93] As a consequence it becomes possible to heat large particles more than small ones, because of the better heat dissipation of the latter. In contrast, picosecond or femtosecond pulses have less effect on the size of the nanoparticles.[43, 46] A consequence of this behaviour is represented, for example, by selective melting of gold nanorods (hole burning experiments) studied by El Sayed et al.,[46] which were possible only with nanosecond pulses, but not with femtosecond pulses.

All the initial AuNP in water and in dimethyl sulfoxide (DMSO) solutions were obtained by LASiS as described in paragraph 3.4 and 3.5.

Size reduction of AuNP. The top–down technique to reduce the size of AuNP exploited the second harmonic of the same Nd : YAG laser (532 nm, 9 ns, 10 Hz), with fluences between 10 and 500 mJ cm^{-2}. The nanoparticles solution was irradiated for 15 min using a focused beam (f: 30 cm) on a 2 mm optical path quartz cell in constant rotation. For size reduction experiments we used AuNP solution with initial surface plasmon

absorption (SPA) of 0.11 in a 2 mm optical path cell. Fig. 3.32a compares experimental UV-Vis spectra of the AuNP solution before (grey circles) and after the size reduction process with irradiation fluence increasing from 12 to 442 mJ cm^{-2} (black lines). The experiments were carried out using the same initial AuNP solution. All spectra are normalized at 450 nm to make clearly visible the continuous decrease of the SPA band with increasing fluence.

The Mie model shows that the spectral variation is due to the reduction of the average AuNP size,[27, 94] in agreement with experiments on single nanoparticles, which showed that intrinsic size effects cause a continuous broadening of the SPA for decreasing sizes.[94, 95] The experimental results of Fig. 3.32a compare very well to the spectra reported in Fig. 3.32b, obtained by Mie model simulations of AuNP spheres in water with a radius variable between 20 nm (larger SPA) and 2 nm (smaller SPA). TEM analysis carried out on the initial AuNP solution (sample 1), on the solution irradiated at 88 mJ cm^{-2} (sample 2) and at 442 mJ cm^{-2} (sample 3) gives full confirmation of gradual nanoparticles size reduction. Fig 3.32 reports TEM images of the three samples, where the average size decrease is clearly visible. From TEM images we found that the average AuNP radius for sample 1 is R = 9 nm, for sample 2 R = 5 nm and for sample 3 R = 2.2 nm with standard deviations of 64%, 41% and 22% respectively.

The wide distributions, characteristic of LASiS (see Fig. 3.33 for a plot of the distributions), decrease with the average size. The nanoparticles show in any case a log-normal distribution and we found a decreasing width (w) and corresponding center radius (R_{LN}) of the distributions for the three samples (sample 1: w = 0.7 , R_{LN} = 8 nm; sample 2: w = 0.4 , R_{LN} = 5 nm; sample 3: w = 0.25 , R_{LN} = 2.2 nm; see Figure 3.33).

HRTEM images of some particles of the three solutions are also reported in Figures 3.33 e, f and g, where one can see that fewer defects seems to be present after resizing.

In Fig. 3.32f we report the distribution of the percentage of gold atoms present in different nanoparticles. This graph cannot be used for evaluating the average size of nanoparticles but it allows one to understand in which particles the ablated mass of gold is actually localized. The log scale allows a simple comparison of all the three samples showing that monomodal dispersions have been obtained (a linear scale is reported in Figure 3.33).

Comparison with the optical spectra, which are reliable and more simple to obtain than TEM images, can be done considering that the Mie model for the calculation of the optical response shows a dependence on the average volume of the particles.

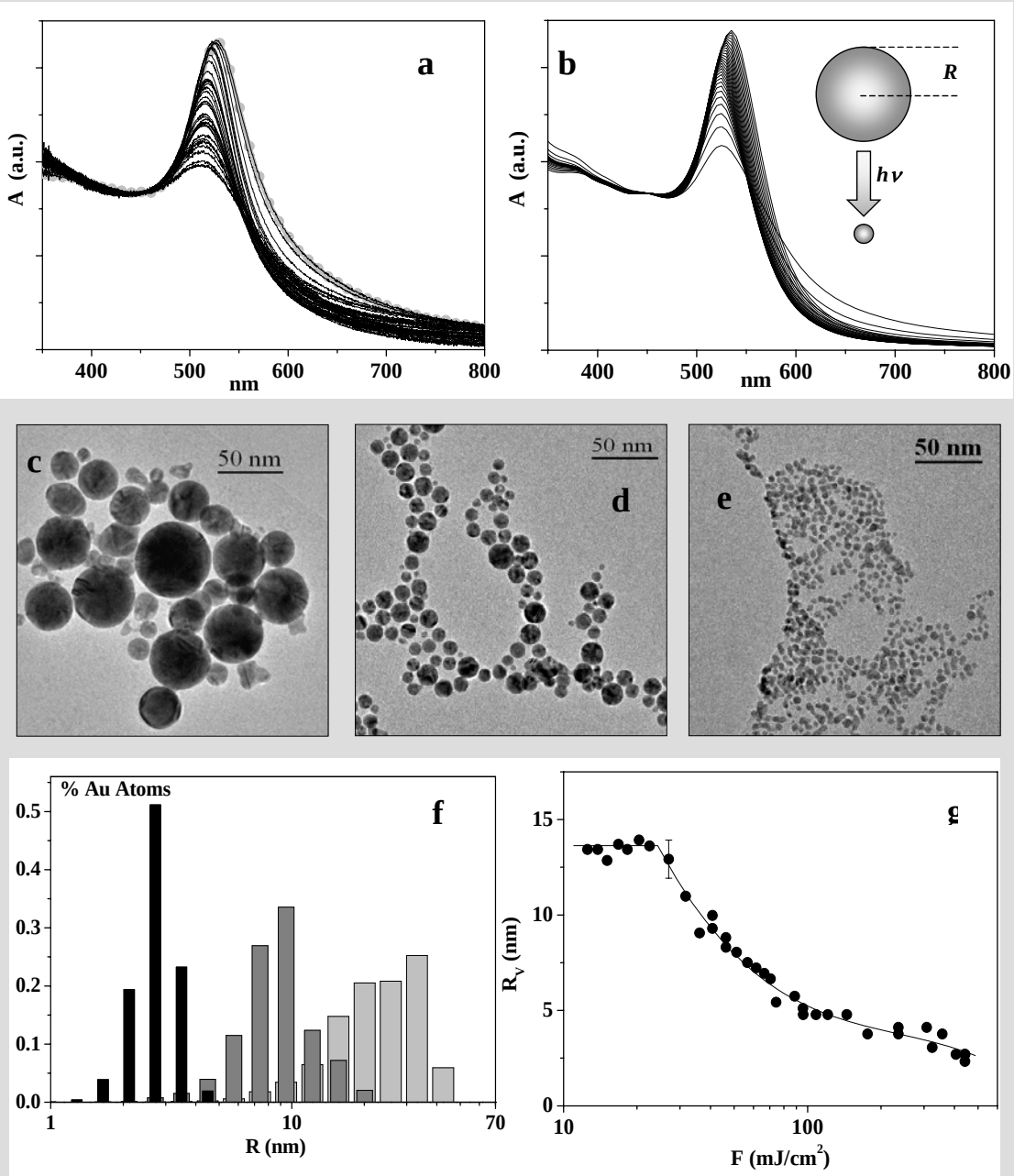

Figure 3.32 *a) UV-Vis spectra of AuNP in H2O solution after size reduction process. Initial AuNP UV-Vis spectrum is the line with grey circles. Spectra of particles irradiated at increasing fluence show a decreasing plasmon absorbance peak. All spectra are normalized at 450 nm for easier comparison. b) Mie model simulation of the extinction cross-sections of AuNP with R variable between 20 and 2 nm. All spectra are normalized at 450 nm. TEM images of samples 1 (c), 2 (d) and 3 (e) show the progressive size reduction of particles. f) Gold atom distributions with respect to particle radii (sample 1: light grey; sample 2: dark grey; sample 3: black) confirm the size reduction process. g) Correlation between average size of AuNP and irradiation fluence (error bar indicates an estimated error of 1 nm). Line is a guide to eyes.*

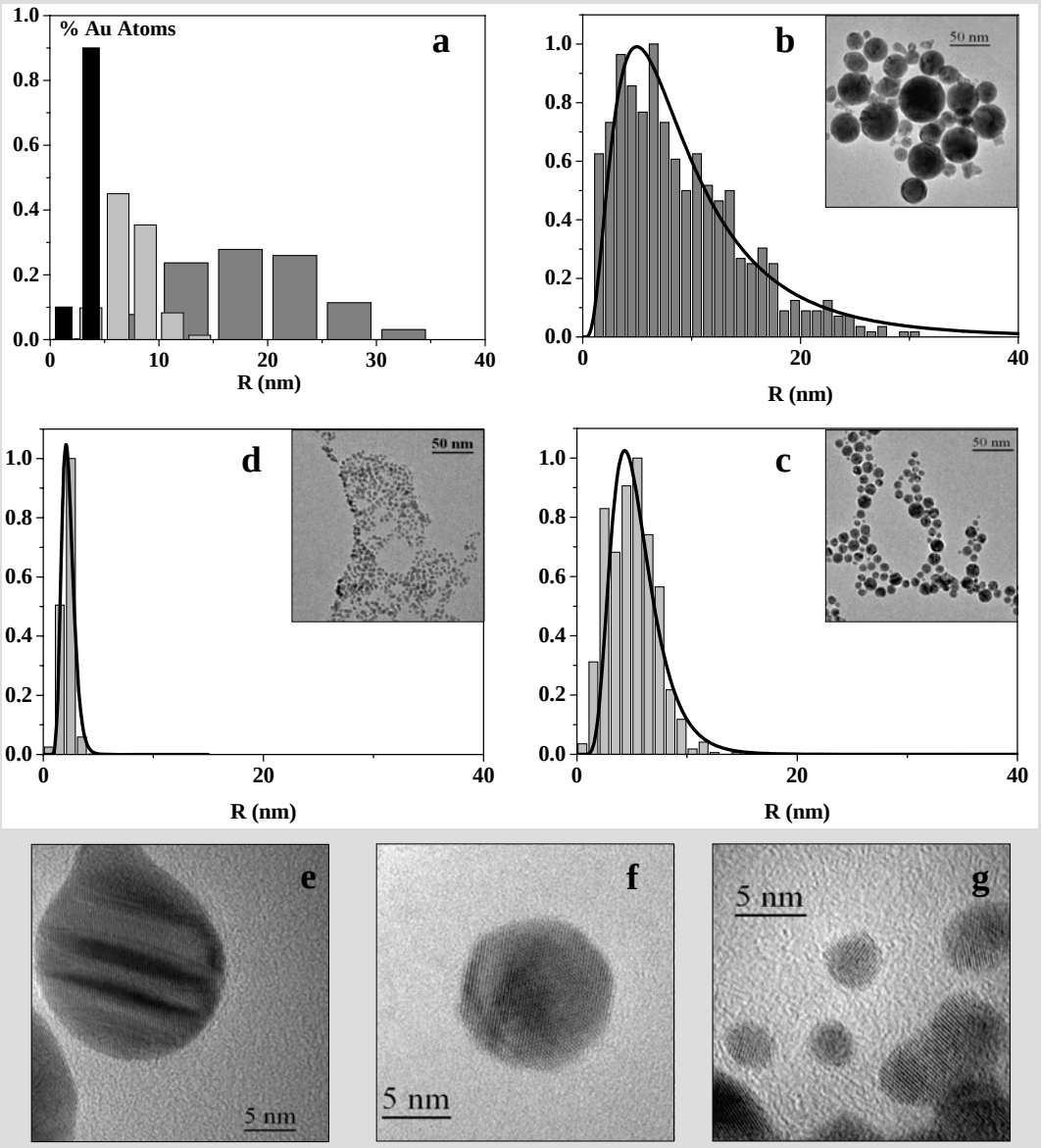

Figure 3.33 *a) Gold atoms distributions with respect to particles radii (sample 1: dark grey; sample 2: light grey; sample 3: black) as in fig. 1f but on a linear scale. Gold nanoparticles distributions and the relative Log – Normal fittings are reported for sample 1 (b), sample 2 (c) and sample 3 (d). High resolution TEM images are reported for sample 1 (e), sample 2 (f) and sample 3 (g).*

Table 3.3 *Average radii (R) with relative root mean square distribution, radii corresponding to average volumes (R_V), the center R_{LN} and the width w of the Log – Normal curves used for fitting the size distribution of the AuNP samples (see fig. b, c, d).*

AuNP Sample	*R (R_V)/nm*	*Standard deviation*	*R_{LN}/nm*	*w*
Sample 1 (Size Reduction)	9 (12)	64 %	8	0.7
Sample 2 (Size Reduction)	5 (6)	41 %	5	0.4
Sample 3 (Size Reduction)	2.2 (2.3)	22 %	2.2	0.25
AuNP in H_2O before Size Increase	9 (12)	64 %	8	0.7
AuNP in H_2O after Size Increase	13 (19)	76 %	10	0.8
AuNP in DMSO before Size Increase	3 (4)	55%	3	0.4
AuNP in DMSO after Size Increase	15 (25)	88%	10	0.5

This suggests that the average volume rather than the average radius of the particles can be obtained fitting the SPA. The average radius (R_V) obtained from the average volume differs a little from R, in particular at larger radii, and for the three samples analyzed with TEM we find R_V = 12 nm for sample 1, R_V = 6 nm for sample 2 and R_V = 2.3 nm for sample 3 (see data in Table 3.3 for a summary of all the above data).

We performed size reduction experiments with increasing fluence to obtain predetermined average AuNP radii. The average radii were obtained by fitting the UV-Vis spectra with the Mie theory and using the usual expression for the damping constant Γ (cfr. equation *2.15)*, where the parameter *A* was corrected according to Lounis et al.[94] using the TEM analysis. The average radius for all the preparations is reported in Fig. 3.32g. One can see that size reduction starts only for fluences higher than 22 mJ cm^{-2} and that the process slows for radii below 2 nm, when SPA becomes weak. It is remarkable that, in the experiments reported in Fig. 3.32g, we showed that it is possible to obtain a nearly nanometric precision of AuNP average radius simply by setting the appropriate fluence of the size reduction treatment. This shows a new result, namely that the average radius of AuNP can be governed on the scale of few nm by laser treatment, without any chemical reaction.

Size increase of AuNP. The bottom – up technique to increase the size of AuNP consists of two steps. In the first step we promoted the aggregation of gold particles by adding controlled amounts of KCl solution and of tetrahydrofuran (THF) to the AuNP solution.[96, 97] In the second step the solution containing AuNP aggregates was irradiated in a 2 mm quartz cell in constant rotation for 90 min with 1 mJ cm^{-2} laser pulses at 532 nm (9 ns, 10 Hz). The concentration range of KCl used (between 10^{-2} M and 10^{-3} M) is unable to promote aggregation of AuNP in water solution, but after the addition of a limited amount of THF (from 15% to 33% in volume) we obtained a controlled coalescence of nanoparticles in a time scale of 15 min and stable from days to weeks. The amount of THF and the KCl concentration determine the aggregation level and the addition of THF without KCl did not produce any effect. We removed the THF at the end of the process simply by evaporation at room temperature under a nitrogen flux. Spectroscopic grade THF was used for the experiments. For size increase experiments of Fig. 3.34a and d we used AuNP solution with initial SPA absorbances of 0.23 and 0.53, respectively, in a 2 mm optical path cell.

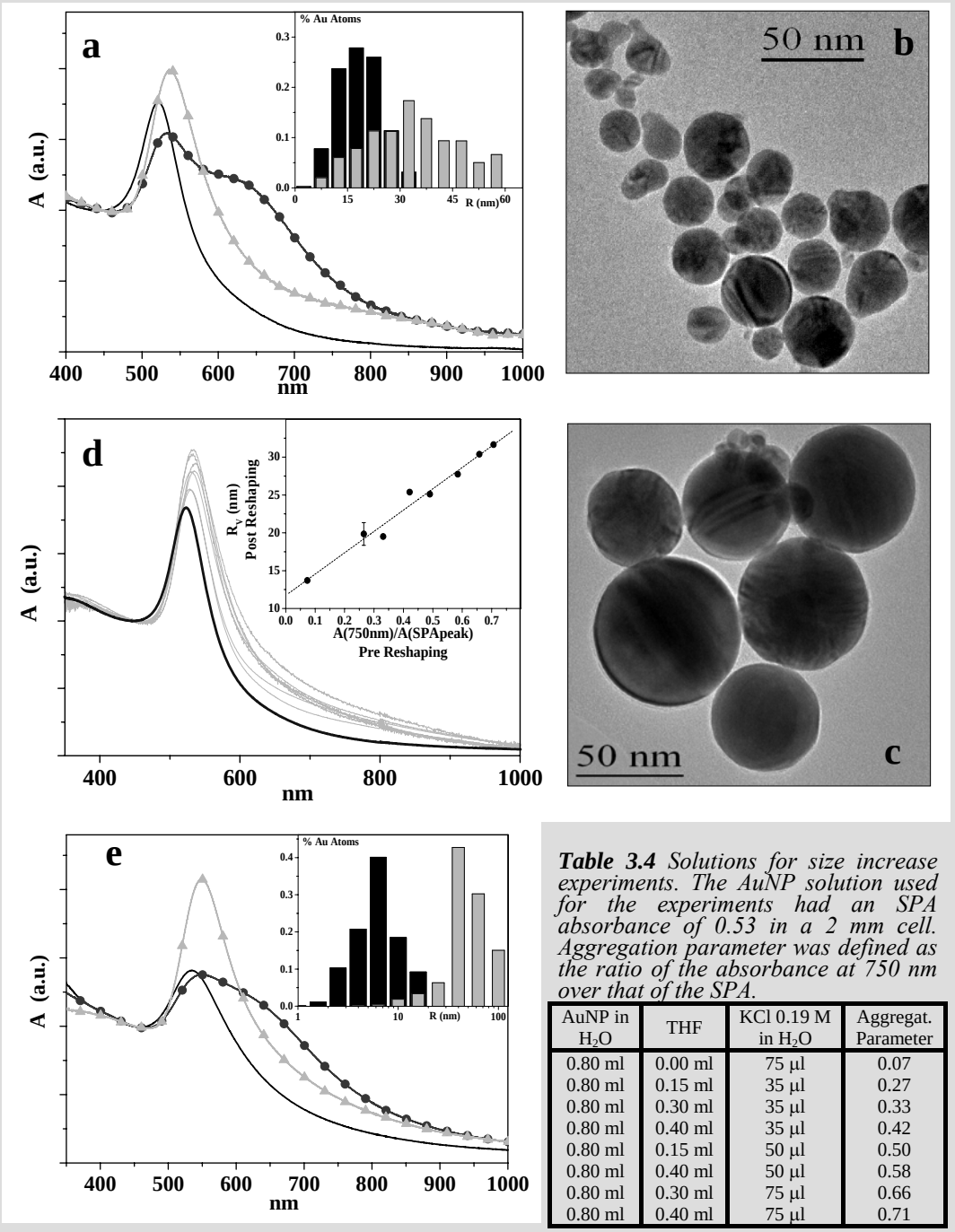

Table 3.4 *Solutions for size increase experiments. The AuNP solution used for the experiments had an SPA absorbance of 0.53 in a 2 mm cell. Aggregation parameter was defined as the ratio of the absorbance at 750 nm over that of the SPA.*

AuNP in H_2O	THF	KCl 0.19 M in H_2O	Aggregat. Parameter
0.80 ml	0.00 ml	75 µl	0.07
0.80 ml	0.15 ml	35 µl	0.27
0.80 ml	0.30 ml	35 µl	0.33
0.80 ml	0.40 ml	35 µl	0.42
0.80 ml	0.15 ml	50 µl	0.50
0.80 ml	0.40 ml	50 µl	0.58
0.80 ml	0.30 ml	75 µl	0.66
0.80 ml	0.40 ml	75 µl	0.71

Figure 3.34 *a) UV-Vis spectra of the AuNP solution in water as synthesized (black line), after the addition of KCl in THF (black circles) and after 90 minutes of laser irradiation at 532 nm (grey triangles). Inset: Au atoms distributions with respect to particle radius for the as synthesized solution (black) and the irradiated solution (grey). TEM images of the AuNP before (b) and after (c) the laser treatment. d) UV-Vis spectra of a series of AuNP solutions obtained with different amounts of THF and KCl concentration after laser irradiation. The initial AuNP UV-Vis spectrum corresponds to the black line. Inset: the linear correlation between the aggregation parameter and the final radius (error bar in the inset corresponds to an estimated error of 1.5 nm). e) UV – Vis spectra of the AuNP solution in DMSO as synthesized (black line), after 48 hours ageing (black circles) and after 90 minutes of laser irradiation at 532 nm (grey triangles). Inset: Au atoms distributions with respect to particles radii for the as synthesized solution (black) and the irradiated solution (grey). All UV-Vis spectra are normalized at 450 nm for easier comparison.*

The conditions for the various experiments of Fig. 3.34d are reported in Table 3.3. Fig. 3.34a shows an example of the results obtained by the size increase technique. In this case we promoted the aggregation of the initial AuNP solution (black line) adding 33% in volume of THF and a KCl concentration of 10^{-2} M. Half an hour after the addition, a strong band near 650 nm was present in the UV-Vis spectrum (black circles), clearly indicating that aggregation of AuNP took place.[43, 97, 98]

After 90 min irradiation at 532 nm (1 mJ cm^{-2}) the red shifted band completely disappeared, while a new, more intense band at 560 nm was present (grey triangles). TEM images (Fig. 3.34b - c) show that AuNP have increased their initial average radius from R = 9 nm (R_V = 12 nm) to R = 13 nm (R_V = 19 nm) whereas the standard deviation increased a little from 64% to 76% (log-normal fitting from R_{NL} = 8 nm, w = 0.7 to R_{NL} = 10 nm, w = 0.8) (see Table 3.2). The change of the gold atoms distribution is reported in the inset of Fig. 3.34a and shows that gold atoms, after size increase, are present in particles with larger radii. Fig. 3.34d reports the SPA of AuNP after laser treatment in a series of experiments carried out with amounts of THF variable between 15% and 33% in volume and for KCl concentrations variable between 10^{-2} M and 10^{-3} M (see Table 3.4 for details). The UV-Vis spectrum of the initial AuNP solution corresponds to the lower SPA peak (black line). Evaluating the aggregation of AuNP with the ratio between absorbance at 750 nm and that of the SPA peak,[99] we found a linear correlation between the aggregation before laser irradiation and the final radius at the end of the size increase treatment (inset of Fig. 3.34d). Fitting of the spectra with the Mie model shows that we obtained particles with R_V up to 32 nm. Hence by using only the KCl and THF concentration as parameters it was possible to obtain a gradual increase of the average size of free from ligands AuNP with nanometric precision.

The size increase technique can be successfully applied to AuNP solutions synthesized in other solvents, for instance with AuNP obtained in DMSO by LASiS.[27, 100] The UV-Vis spectra of AuNP solutions as synthesized, after 48 h ageing (without adding THF or KCl) and after 90 min laser treatment at 532 nm (2 mJ cm^{-2}) are analogous to those of Fig. 3.34a (see Fig. 3.34e). The large increase of the SPA after the laser treatment corresponds to a remarkable increase of AuNP average size. TEM analysis confirms that AuNP have an initial average radius R = 3 nm (R_V = 4 nm) (55% standard deviation), while after the size increase process the radius becomes R = 15 nm (R_V = 25 nm) (88% standard deviation). The log-normal fittings show a similar trend, from R_{NL} =

3 nm, w = 0.4 to R_{NL} = 10 nm, w = 0.5. Also in this case we find a linear correlation between the aggregation parameter before laser irradiation and the final radius at the end of the size increase treatment.

3.14 AuNP bioconjugation.[74]

We applied the size reduction and increase techniques to bind a commonly used protein, bovine serum albumin (BSA), to gold nanoparticles of two different sizes (R_V = 4 nm for solution 1 and R_V = 15 nm for solution 2). Functionalization of AuNP with peptides or proteins is an important topic in nanobiotechnology,[99, 101-103] and in particular BSA is frequently used because it is very common in biochemistry and can be easily attached to other peptides or fluorescent markers.[41, 42, 104, 105] Furthermore AuNP smaller than R = 5 nm are usually exploited for transport into cell nuclei and other organelles,[41, 42] while AuNP larger than R = 10 nm are useful for spectroscopic[106, 107] and toxicological[88, 106] studies because of their stronger extinction coefficients and higher endocytosis efficiency. Usually AuNP stabilizers used in reduction synthesis, like citrate molecules, as well as unreacted $NaBH_4$ and other chemical reduction byproducts, create some difficulties for particle functionalization with BSA and interfere with the protein during the replacement process.[104, 105] Moreover pH buffer and heating are necessary to carry out the reaction with a satisfactory yield.[41, 104-106] Using gold nanoparticles which are free from ligands, the reaction does not need any precaution, because the functionalization is simply obtained by adding BSA to the AuNP solution.

Bovine serum albumin (BSA) (in powder, fatty acid free) was purchased from Sigma-Aldrich. The BSA solutions (in double distilled water with increasing protein concentration) were added to previously synthesized AuNP solutions 1 and 2 ($1.1\ 10^{-8}$ M and $2.3\ 10^{-10}$ M in AuNP respectively); the UV-Vis spectra were recorded 15 min after the addition. Estimation of BSA binding percentage was carried out by UV-Vis spectroscopy determining the albumin quantity still present in solution after centrifugation ($13.4\ 10^3$ rpm) of solutions 1 and 2 (exploiting the BSA absorbance band at 278 nm) and subtracting it from the initial BSA quantity. The precipitated BSA-AuNP are easily redissolved by stirring for a few minutes. The functionalization of AuNP with BSA can be monitored with SPA maximum red shift (ΔSPA) and its absorbance increase (ΔA) for a progressively increasing concentration of albumin (see Fig. 3.35a). These results can be understood with the formation of a BSA layer around

particles according to Mie theory for core@shell particles[95, 99] and to Nath and Chilkoti[108] (see experimental and simulated spectra in Fig. 3.36). In Fig. 3.35a one can also see that, for smaller AuNP (grey triangles), surface functionalization is clearly observed even for a 1 : 10 concentration ratio of BSA : AuNP, corresponding to a BSA concentration of 1.2 nM and to 3 picomoles of total BSA. In fact smaller particles are more sensitive to chemical and physical changes of their surroundings than larger AuNP and allow immediate detection of surface functionalization. This result was not possible before for AuNP obtained by chemical reduction because of the stabilizing molecules surrounding the particles. At higher BSA concentration and depending on the size of nanoparticles, the sigmoid reaches a plateau that can be interpreted as AuNP surface saturation. For these solutions we calculated an average number of attached BSA per particle of the order of 10^2 for smaller AuNP and of 10^5 for the larger ones. These figures are between 10^2 – 10^3 times larger than values previously reported in the literature[104] and are compatible with the formation of a protein multilayer around the particles, showing that free AuNP are highly available for interaction with the proteins. The specific interaction of the protein with the AuNP was not investigated although it is probable that the disulfide groups present on the protein have an important role.[105]

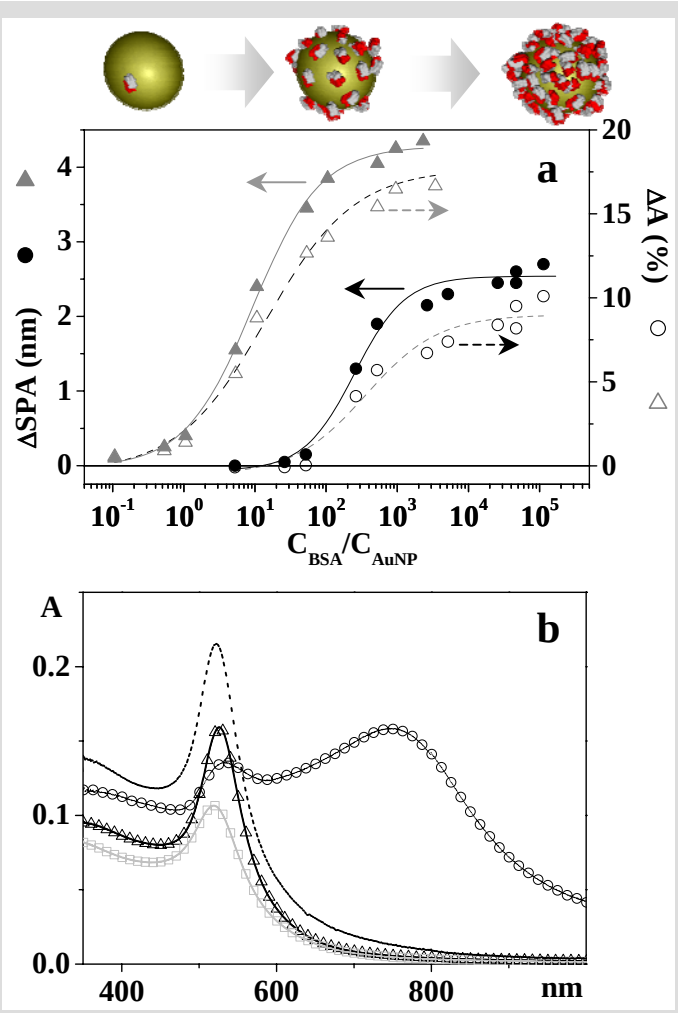

Figure 3.35 *a) Red shift (ΔSPA in nm, filled symbols) and absorbance difference (ΔA in percentage, open symbols) of solution 1 (grey triangles) and solution 2 (black circles) for increasing AuNP : BSA ratio. b) Solution 1 (grey line), solution 2 (black line) and free AuNP solution (dashed line) before the addition of KCl. Solution 1 (grey squares), solution 2 (black triangles) and free AuNP solution (black circles) in the presence of KCl 0.07 M.*

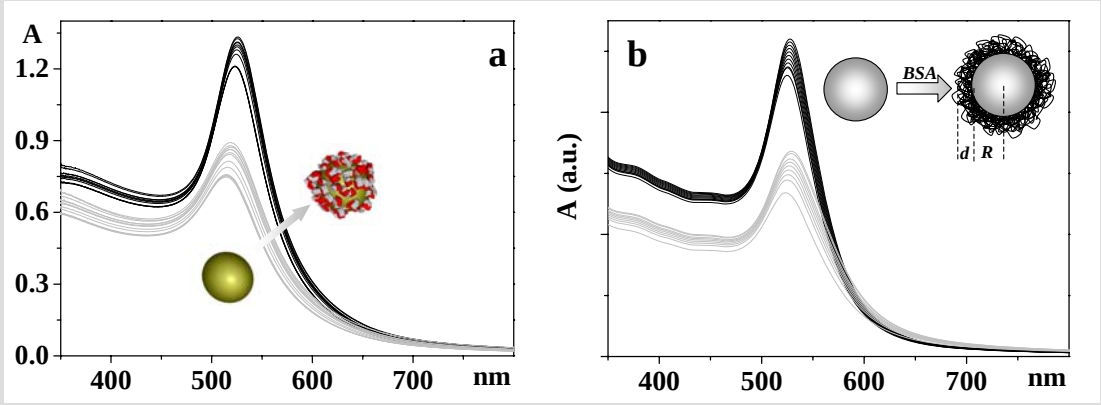

Figure 3.36 *a) UV – Vis spectra of solution 1 (grey lines) and solution 2 (black lines) for different BSA:AuNP ratio. The red shift of SPA and the increase of SPA absorbance with increasing BSA:AuNP ratio are clearly visible for the two solutions. b) Simulation within the Mie theory for core@shell Au@BSA particles in water. Grey lines: gold core radius 4.5 nm; black lines: gold core radius 14.6 nm. Shell thickness d variable between 0 and 2 nm (0.2 nm steps) and with a refraction index n = 1.5.*

Further experiments, which go beyond the scope of the present paper, are planned also to investigate the possible structural variation of the protein. Further proof of BSA functionalization of AuNP has been obtained adding KCl (0.07 M final KCl concentration) to solution 1, solution 2 and to a control solution of as synthesized AuNP in H2O. As shown by the UV-Vis spectra reported in Fig. 3.35b, the KCl promotes the immediate aggregation of AuNP, observed as a broad band around 750 nm, while AuNP : BSA conjugates are completely stable and their spectra are indistinguishable before and after KCl addition.

The unprecedent high accessibility of AuNP obtained by LASiS in water also allows sequential multibioconjugation or multifunctionalization. The SPA red shift and the absorbance increase upon the progressive surface saturation were exploited to monitor the sequential functionalization of AuNP with a fluoresceine derivative (fluoresceine isothiocyanate – FITC, see figure 3.37) and with a test bacterial spore.

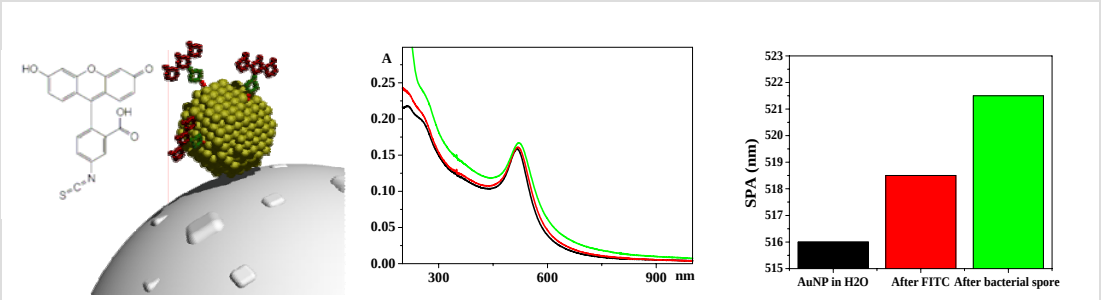

Figure 3.37 *Left: Formula of FITC and scheme of the multi – bioconjugation of a gold nanoparticle with FITC and with a bacterial spore. Centre: UV – Vis spectra of AuNP solution in water as synthesized (black), after the addition of FITC (red) and after the addition of bacterial spores (green). Right: the evolution of gold SPA position upon the sequential addition of FITC and spores.*

The fluorescent marker allows to monitor the immunological response to the spore during in vivo tests. It is remarkable that no specific chemical reactions or complex procedures were necessary for obtaining the multibioconjugate, except for the simple mixing of desired molecules and the following purification by centrifugation at 5000 rpm. This work is currently in progress.[#4]

[#4] *Work in collaboration with Dr. F. Tonello and Prof. C. Montecucco of the Neurosciences Institute and of the Department of Biomedical Sciences of Padova University.*

References

1. Abad, J. M.; Mertens, S. F. L.; Pita, M.; Fernndez, V. M.; Schiffrin, D. J., *J. Am. Chem. Soc.* **2005,** 127, 5689 -5694.
2. Ackerson, C. J.; Jadzinsky, P. D.; Jensen, G. J.; Kornberg, R. D., *J. Am. Chem. Soc.* **2006,** 128, 2635 -2640.
3. Pernodet, N.; Fang, X.; Sun, Y.; Bakhtina, A.; Ramakrishnan, A.; Sokolov, J.; Ulman, A.; Rafailovich, M., *Small* **2006,** 2, 766-773.
4. Raveendran, P.; Fu, J.; Wallen, S. L., *J. Am. Chem. Soc.* **2003,** 125, 13940 -13941.
5. Sweeney, S. F.; Woehrle, G. H.; Hutchison, J. E., *J. Am. Chem. Soc.* **2006,** 128, 3190 -3197.
6. Nichols, W. T.; Sasaki, T.; Koshizaki, N., *J. Appl. Phys.* **2006,** 100, 114911.
7. Nichols, W. T.; Sasaki, T.; Koshizaki, N., *J. Appl. Phys.* **2006,** 100, 114912.
8. Kabashin, A. V.; Meunier, M., *J. Appl. Phys.* **2003,** 94, 7941-7943.
9. Sylvestre, J.-P.; Kabashin, A. V.; Sacher, E.; Meunier, M., *Appl. Phys. A* **2005,** 80, 753–758.
10. Mafuné, F.; Kohno, J.; Takeda, Y.; Kondow, T., *J. Phys. Chem. B* **2000,** 104, 9111 -9117.
11. Mafuné, F.; Kohno, J.; Takeda, Y.; Kondow, T., *J. Phys. Chem. B* **2001,** 105, 5114 -5120.
12. Compagnini, G.; Scalisi, A. A.; Puglisi, O., *Phys. Chem. Chem. Phys.* **2002,** 4, 2787 - 2791.
13. Muto, H.; Yamada, K.; Miyajima, K.; Mafuné, F., *J. Phys. Chem. C* **2007,** 1, in press.
14. Sylvestre, J.-P.; Poulin, S.; Kabashin, A. V.; Sacher, E.; Meunier, M.; Luong, J. H. T., *J. Phys. Chem. B* **2004,** 108, 16864-16869.
15. Tilaki, R. M.; Irajizad, A.; Mahdavi, S. M., *J. Nanop. Res.* **2007,** 9, 853–860.
16. Nichols, W. T.; Sasaki, T.; Koshizaki, N., *J. Appl. Phys.* **2006,** 100, 114913.
17. Compagnini, G.; Scalisi, A. A.; Puglisi, O., *J. Appl. Phys.* **2003,** 94, 7874-7877.
18. Greenwood, N. N.; Earnshaw, A., *Chemistry of the Elements*. Elsevier Science: Oxford, 1997.
19. Mafuné, F.; Kohno, J.; Takeda, Y.; Kondow, T.; Sawabe, H., *J. Phys. Chem. B* **2000,** 104, 8333-8337.
20. Mafuné, F.; Kohno, J.; Takeda, Y.; Kondow, T., *J. Phys. Chem. B* **2002,** 106, 7575-7577.
21. Mafuné, F.; Kohno, J.; Takeda, Y.; Kondow, T., *J. Phys. Chem. B* **2003,** 107, 4218-4223.
22. Chen, Y.-H.; Yeh, C.-S., *Coll. Surf. A* **2002,** 197, 133–139.
23. Sylvestre, J.-P.; Kabashin, A. V.; Sacherù, E.; Meunier, M.; Luong, J. H. T., *J. Am. Chem. Soc.* **2004,** 126, 7176-7177.
24. Kabashin, A. V.; Meunier, M.; Kingston, C.; Luong, J. H. T., *J. Phys. Chem. B* **2003,** 107, 4527-4531.
25. Compagnini, G.; Scalisi, A.; Puglisi, O.; Spinella, C., *J. Mater. Res.* **2004,** 19, 2795-2798.
26. Rajagopalan, R.; Hiemenz, P. C., *Principles of Colloid and Surface Chemistry*. Marcel Dekker: New York, 1997.
27. Amendola, V.; Polizzi, S.; Meneghetti, M., *J. Phys. Chem. B* **2006,** 110, (14), 7232-7237.
28. Amendola, V.; Meneghetti, M., *In preparation*.
29. Corbierre, M. K.; Cameron, N. S.; Sutton, M.; Mochrie, S. G. J.; Lurio, L. B.; Ruhm, A.; Lennox, R. B., *J. Am. Chem. Soc.* **2001,** 123, 10411 - 10412.
30. K.Corbierre, M.; Cameron, N. S.; Sutton, M.; Laaziri, K.; Lennox, R. B., *Langmuir* **2002,** 18, 4584-4591.
31. Boal, A. K.; Ilhan, F.; DeRouchey, J. E.; Thurn-Albrecht, T.; Russell, T. P.; Rotello, V. M., *Nature 2000* **2000,** 404, 746-748.
32. Tatumi, R.; Fujihara, H., *Chem. Comm.* **2005**, 83-85.
33. Frankamp, B. L.; Rotello, V. M., *Chem. Comm.* **2002**, 1892-1893.
34. Terrill, R. H.; Postlethwaite, T. A.; Chen, C.; Poon, C.-D.; Terzis, A.; Chen, A.; Hutchison, J. E.; Clark, M. R.; Wignall, G.; Londono, J. D.; Superfine, R.; Falvo, M.; Jr., C. S. J.; Samulski, E. T.; Murray, R. W., *J. Am. Chem. Soc.* **1995,** 117, 12537-12548.
35. Dahmen, C.; Plessen, G. v.; Grésillon, S.; Plech, A.; Kotaidis, V., *Phys. Rev. B* **2004,** 70, 195423.
36. Lenggoro, I. W.; Xia, B.; Okuyama, K.; Mora, J. F. d. l., *Langmuir* **2002,** 18, 4584-4591.
37. Kuyper, C. L.; Fujimoto, B. S.; Zhao, Y.; Schiro, P. G.; Chiu, D. T., *J. Phys. Chem. B* **2006,** 110, 24433-24441.
38. Delden, R. A. v.; Wiel, M. K. J. t.; Pollard, M. M.; Vicario, J.; Koumura, N.; Feringa, B. L., *Nature* **2005,** 437, 1337-1340.
39. Raula, J.; Shan, J.; Nuopponen, M.; Niskanen, A.; Jiang, H.; Kauppinen, E. I.; Tenhu, H., *Langmuir* **2003,** 19, 3499-3504.
40. McIntosh, C. M.; Esposito, E. A.; Boal, A. K.; Simard, J. M.; Martin, C. T.; Rotello, V. M., *J. Am. Chem. Soc.* **2001,** 123, 7626-7629.

41. Tkachenko, A. G.; Xie, H.; Lin, Y.; Coleman, D.; Ryan, J.; Glomm, W. R.; Shipton, M. K.; Franzen, S.; Feldheim, D. L., *Bioconjugate Chem.* **2004,** 15, 482-490.
42. Tkachenko, A. G.; Xie, H.; Coleman, D.; Glomm, W.; Ryan, J.; Anderson, M. F.; Franzen, S.; Feldheim, D. L., *J. Am. Chem. Soc.* **2003,** 125, 4700-4701.
43. Grant, C. D.; Schwartzberg, A. M.; Norman, T. J.; Zhang, J. Z., *J. Am. Chem. Soc.* **2003,** 125, 549-553.
44. Johnson, P. B.; Christy, R. W., *Phys. Rev. B* **1972,** 6, 4370-4379.
45. Palik, E., *Handbook of Optical Constants of Solids*. Academic Press: New York, 1985.
46. Link, S.; El-Sayed, M. A., *Int. Rev. Phys. Chem.* **2000,** 19, 409-453.
47. Inasawa, S.; Sugiyama, M.; Yamaguchi, Y., *J. Phys. Chem. B* **2005,** 109, 9404-9410.
48. Inasawa, S.; Sugiyama, M.; Yamaguchi, Y., *J. Phys. Chem. B* **2005,** 109, 3104-3111.
49. Link, S.; El-Sayed, M. A., *J. Phys. Chem. B* **1999,** 103, 8410-8426.
50. Link, S.; Burda, C.; Mohamed, M. B.; Nikoobakht, B.; El-Sayed, M. A., *J. Phys. Chem. B* **1999,** 103, 1165-1170.
51. Link, S.; Burda, C.; Nikoobakht, B.; El-Sayed, M. A., *J. Phys. Chem. B* **2000,** 104, 6152-6163.
52. Amendola, V.; Rizzi, G. A.; Polizzi, S.; Meneghetti, M., *J. Phys. Chem. B* **2005,** 109, (49), 23125-23128.
53. Matthews, M. J.; Pimenta, M. A.; Dresselhaus, G.; Dresselhaus, M. S.; Endo, M., *Phys. ReV. B* **1999,** 59, 6585-6588.
54. Wang, Y.; Alsmeyer, D. C.; Mccreery, R. L., *Chem. Mater.* **1990,** 2, 557-563.
55. Tuinstra, F.; Koenig, J. L., *J. Chem. Phys.* **1970,** 53, 1126-1130.
56. Koyama, T., *Carbon* **1972,** 10, 757-765.
57. Koyama, T.; Endo, M.; Onuma, Y., *Jpn. J. Appl. Phys.* **1972,** 11, 445-449.
58. Chieu, T. C.; Dresselhaus, M. S.; Endo, M., *Phys. ReV. B* **1982,** 26, 5867-5877.
59. Alvarez, M. M.; Khoury, J. T.; Schaaff, T. G.; Shafigullin, M. N.; Vezmar, I.; Whetten, R., *J. Phys. Chem. B* **1997,** 101, 3706-3712.
60. Peng, Z.; Walther, T.; Kleinermanns, K., *J. Phys. Chem. B* **2005,** 109, 15735-15740.
61. Subramanian, V.; Wolf, E. E.; Kamat, P. V., *J. Am. Chem. Soc.* **2004,** 126, 4943-4950.
62. Borghesi, A.; Guizzetti, G., *Handbook of Optical Constants of Solids II*. Academic: Boston, 1991.
63. Simm, A. O.; Banks, C. E.; Wilkins, S. J.; Karousos, N. G.; Davis, J.; Compton, R. G., *Anal. Bioanal. Chem.* **2005,** 381, 979-985.
64. Biswas, P. C.; Nodasaka, Y.; Enyo, M.; Haruta, M., *J. Electroanal. Chem.* **1995,** 381, 167-177.
65. Amendola, V.; Polizzi, S.; Meneghetti, M., *Langmuir* **2007,** 23, (12), 6766-6770.
66. Soderlund, J.; Kiss, L. B.; Niklasson, G. A.; Granqvist, C. G., *Phys. Rev. Lett.* **1998,** 80, 2386-2388.
67. Granqvist, C. G.; Buhrman, R. A., *Solid State Comm.* **1976,** 18, 123-126.
68. Granqvist, C. G.; Buhrman, R. A., *J. Appl. Phys.* **1976,** 47, 2200-2219.
69. Granqvist, C. G.; Hunderi, O., *Phys. Rev. B* **1977,** 16, 3513-3554.
70. Chen, W.; Cai, W.; Wang, G.; Zhang, L., *Appl. Surf. Sci.* **2001,** 174, 51-54.
71. Vogel, W.; Dufft, D. G.; Baiker, A., *Langmuir* **1995,** 11, 401-404.
72. Averitt, R. D.; Sarkar, D.; Halas, N. J., *Phys. Rev. Lett.* **1997,** 78, 4217-4220.
73. Shi, W.; Sahoo, Y.; Swihart, M. T., *Coll. Surf. A* **2004,** 246, 109–113.
74. Amendola, V.; Meneghetti, M., *J. Mater. Chem.* **2007,** 17, 4705–4710.
75. Miotello, A.; Marchi, G. D.; Mattei, G.; Mazzoldi, P.; Sada, C., *Phys. Rev. B* **2001,** 63, 075409.
76. Bardotti, L.; Prevel, B.; Treilleux, M.; Melinon, P.; Perez, A., *Appl. Surf. Sci.* **2000,** 164, 52–59.
77. Chatterjee, K.; Banerjee, S.; Chakravorty, D., *Phys. Rev. B* **2002,** 66, 085421.
78. Stober, W.; Fink, A., *J. Colloid Interface Sci.* **1968,** 26, 62.
79. Zheng, J.; Zhang, C.; Dickson, R. M., *Phys. Rev. Lett.* **2004,** 93, 077402.
80. Novac, J. P.; Nickerson, C.; Franzen, S.; Feldheim, D. L., *Anal. Chem.* **2001,** 73, 5758–5761.
81. Wey, G. T.; Liu, F. K.; Wang, C. R. C., *Anal. Chem.* **1999,** 71, 2085–2091.
82. Akthakul, A.; Hochbaum, A. I.; Stellacci, F.; Mayers, A. M., *Adv. Mater.* **2005,** 17, 532–535.
83. Mafuné, F.; Kohno, J.; Takeda, Y.; Kondow, T., *J. Phys. Chem. B* **2001,** 105, 9050–9056.
84. Takami, A.; Kurita, H.; Koda, S., *J. Phys. Chem. B* **1999,** 103, 1226–1232.
85. Besner, S.; Kabashin, A. V.; Meunier, M., *Appl. Phys. Lett.* **2006,** 89, 233122.
86. Rosi, N. L.; Mirkin, C. A., *Chem. Rev.* **2005,** 105, 1547-1562.
87. Niemeyer, C. M., *Angew. Chem., Int. Ed.* **2001,** 40, 4128–4158.
88. Chithrani, B. D.; Ghazani, A. A.; Chan, W. C. W., *Nano Lett.* **2006,** 6, 662–668.
89. Yamada, K.; Tokumoto, Y.; Nagata, T.; Mafuné, F., *J. Phys. Chem. B* **2006,** 110, 11751–11756.

90. Francois, L.; Mostafavi, M.; Belloni, J.; Delouis, J. F.; Delaire, J.; Feneyrou, P., *J. Phys. Chem. B* **2000,** 104, 6133–6137.
91. Francois, L.; Mostafavi, M.; Belloni, J.; Delaire, J., *Phys. Chem. Chem. Phys.* **2001,** 3, 4965–4971.
92. Plech, A.; Kotaidis, V.; Gresillon, S.; Dahmen, C.; Plessen, G. V., *Phys. Rev. B* **2004,** 70, 195423.
93. Hu, M.; Hartland, G. V., *J. Phys. Chem. B* **2002,** 106, 7029–7033.
94. Berciaud, S.; Cognet, L.; Tamarat, P.; Lounis, B., *Nano Lett.* **2005,** 5, 515-518.
95. Kreibig, U.; Vollmer, M., *Optical Properties of Metal Clusters*. Springer Verlag: Berlin, 1995.
96. Wilcoxon, J. P.; Martin, J. E.; Schaefer, D. W., *Phys. Rev. A* **1989,** 39, 2675–2689.
97. Israelachvili, J. N., *Intermolecular And Surface Forces*. Academic Press: New York, 1985.
98. Zhang, Y.; Gu, C.; Schwartzberg, A. M.; Chen, S.; Zhang, J. Z., *Phys. Rev. B* **2006,** 73, 16540.
99. Levy, R.; Thanh, N. T. K.; Doty, R. C.; Hussain, I.; Nichols, R. J.; Schiffrin, D. J.; Brust, M.; Fernig, D. G., *J. Am. Chem. Soc.* **2004,** 126, 10076–10084.
100. Amendola, V.; Mattei, G.; Cusan, C.; Prato, M.; Meneghetti, M., *Synth. Met.* **2005,** 155, 283–286.
101. Jung, J.; Kwon, K. Y.; Ha, T. H.; Chyng, B. H.; Jung, H. T., *Small* **2006,** 2, 1010–1015.
102. Slocik, J. M.; Stone, M. O.; Naik, R. R., *Small* **2005,** 1, 1048–1052.
103. Zin, M. T.; H.Ma; Sarikaya, M.; Jen, A., *Small* **2005,** 1, 698–702.
104. Brewer, S. H.; Glomm, W. R.; Johnson, M. C.; Knag, M. K.; Franzen, S., *Langmuir* **2005,** 21, 9303–9307.
105. Burt, J. L.; Gutierrez-Wing, C.; Miki-Yoshida, M.; Jose-Yacaman, M., *Langmuir* **2004,** 20, 11778–11783.
106. Kneipp, J.; Kneipp, H.; McLaughlin, M.; Brown, D.; Kneipp, K., *Nano Lett.* **2006,** 6, 2225 - 2231.
107. Sonnichsen, C.; Reinhard, B. M.; Liphardt, J.; Alivisatos, A. P., *Nat. Biotech.* **2005,** 23, 741-745.
108. Nath, N.; Chilkoti, A., *Anal. Chem.* **2004,** 76, 5370–5378.

Chapter 4

Chemical reduction of silver thiolated complexes[#]

In last years the variety and heterogeneity of photonic applications drove to an intense quest for materials with new optical and plasmonic properties. As a consequence, strong efforts were made in obtaining gold and silver nanoparticles with controlled and complex shapes, since the surface plasmon absorption is known for being strongly dependent on particles size and geometry. The synthesis of metal nanostructures with nonspherical shape requires a high control on the reaction parameters and the presence of external factors which can favour the anisotropic growth

[#] *This project has been developed at the Department of Material Science and Engineering of Massachusetts Institute of Technology (Cambridge, MA, US), in laboratories of Prof. Francesco Stellacci and in partnership with Mr. Osman Bakr, PhD student of the School of Engineering and Applied Sciences at Harvard University.*

despite the high symmetry and packing of Au and Ag fcc lattices. Therefore the chemical reduction approach is the most versatile technique for the synthesis of metal nanoparticles with shape controlled optical properties. The mild conditions achievable by chemical reduction synthesis and the utilization of strong stabilizing molecules, like small organothiols, also pushed Chemists synthetic skill towards smaller nanostructures made of few tens or hundreds of atoms. The study of oligoatomic metal clusters stabilized by molecules with peculiar optical or electronic properties currently represents the frontier for material scientists and theoreticians. This is because metal clusters have several unknown and, up to date, almost unpredictable properties which place them half a way between molecular and solid state physics. The application of gold clusters as antibunched photon sources is an example.[1] Moreover the easy surface chemistry of metals like Ag and Au open the route to an infinite series of conjugations with functional molecules which interact in surprisingly ways with the metal core. Even the crystalline structure of these oligoatomic metal clusters in presence of strongly interacting organic molecules can show uncommon characteristics, as pointed out by the recent work of Kornberg et al.[2] In other words, oligoatomic clusters with functional stabilizers undergo to dramatic changes in their physical-chemical properties by *minor* changes in their structure, as it was not found before in material science.

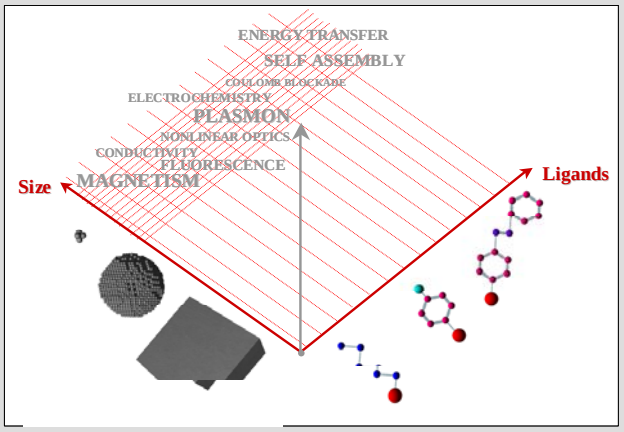

Figure 4.1 *Chemical reduction synthesis of AgSR compounds is an effective way for expanding the field of material science towards oligoatomic metal clusters. Combining these metal clusters with a series of ligands with specific functionalities could originate a gamut of materials with dramatically different physical-chemical properties.*

In the present work we approached the syntesis of silver thiolated structures with new optical properties by the chemical reduction of silver complexes in organic solvents. We will show how this approach allowed to obtain silver particles with very different properties and nanostructures just by changing few parameters in the same synthetic scheme. However, the way toward the complete understanding of the properties of these materials is still long.

4.1 Silver thiolated complexes.[3, 4]

In presence of organothiols (HSR, with R alkanes or phenyl derivatives), silver ions form layered compounds with stoichiometry AgSR. In these compounds the substituents R extend perpendicularly to both sides of the AgS units, which assemble in two directions. Stacking of the layers involves only Van der Waals contact between the distal atoms of the thiolated substituents. The stoichiometry AgSR requires that the coordination numbers of Ag and SR be the same, but not geometries. Two-coordinated Ag and SR can form only chains, so one concludes that, to obtain a layer, Ag and SR must to be, at least, three-coordinated. In fact, based on XRD measurements, a network with trigonal planar coordination of Ag by three SR moieties is attributed to these layered compounds, with Ag atoms occurring in a central plane, the S atoms occuring in planes on either sides and the R groups extending perpendicular to the slab on both sides. More sterically hindered R groups yield small cyclic molecules with a lower tendency to form large insoluble crystals. [3, 4]

Sometimes these layered compounds have been compared to thiols monolayers on Au or Ag surfaces, but a big difference holds between these two systems, being that the packing density of substituents is determined by the AgS lattice structure and not by the cross section of the substituents as it is in the monolayers on bulk metals.

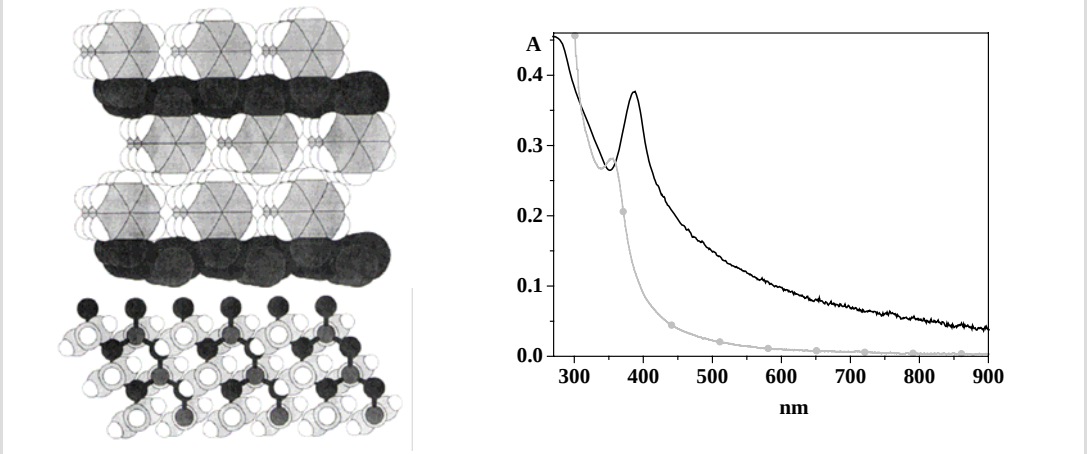

Figure 4.4 *Left: side view ({0k0} planes showing the layered structure) and top view of the resolved structure adopted for complexes of the type Ag:4-FTP. From Ref.1. Right: UV-Vis absorption spectra of Ag:4-FTP complex with crystals of different sizes.*

In the present case we worked on layered compounds of silver with phenyl mercaptanes like 4 – fluorothiophenol (4-FTP). Typical UV-Vis absorption spectra of these complexes are shown in figure 4.2, with a peak close to 370 nm over a scattering

background due to the micrometric size of AgSR crystals. The position of the absorption peak usually is red shifted for larger crystals.

4.2 Chemical reduction procedure.

We performed the reduction of the AgSR complex using the same sequence of operations, but varying many parameters to obtain the different final results. Basically, the synthesis consists of mixing the silver precursor with thiols in an organic solvent. We commonly used silver trifluoroacetate ($AgCF_3COO$) as Ag precursor and 4-fluorothiophenol (4-FTP) as thiol in dimethylformamide (DMF) solution. Other than 4-FTP, also its meta and ortho analogues (3-FTP and 2-FTP), 4 – methylbenzenethiol (4-MBT) and other mercaptophenyls have been used. After the formation of the AgSR complex with layered structures, we added a $NaBH_4$ solution in DMF as reducing agent. After stirring a few hours, we added H_2O to the solution and then we stored it in freezer.

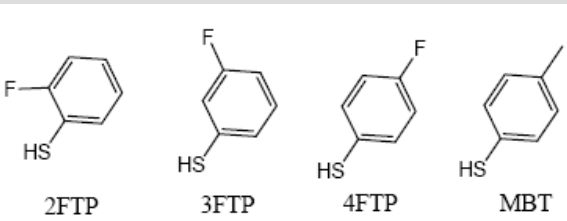

Figure 4.3 *Molecular structure of some of the thiols used in this study: 2-fluorthiophenol (2-FTP), 3-fluorthiophenol (3-FTP), 4-fluorthiophenol (4-FTP), 4-methylbenzenethiol (4-MBT).*

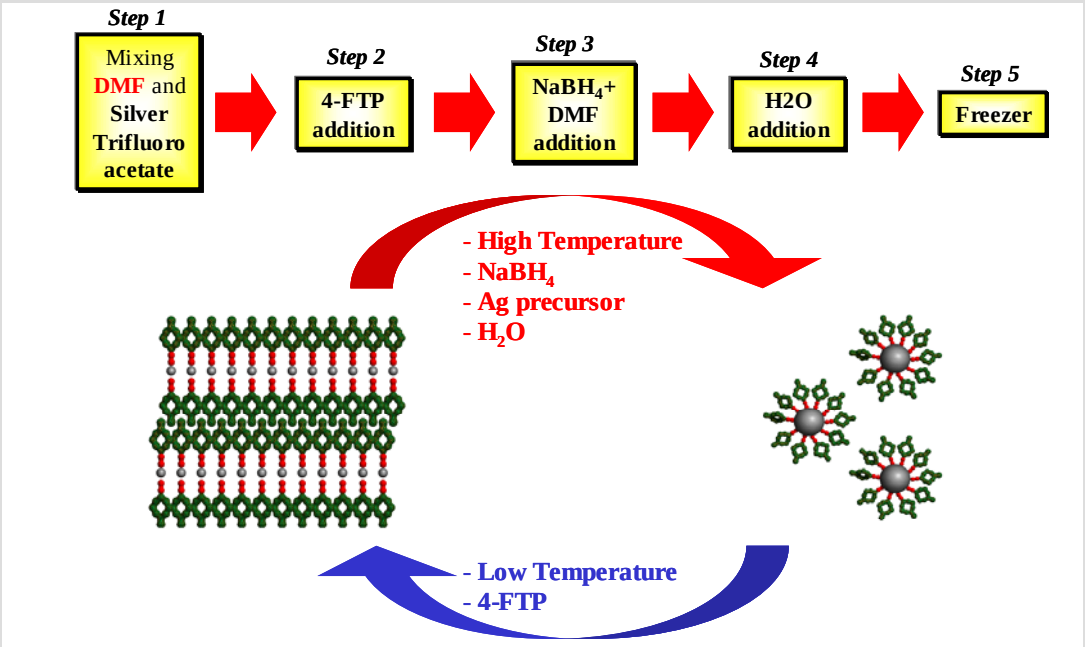

Figure 4.5 *Outline of the approach to the chemical reduction of AgSR and main parameters which allow the synthesis government.*

The final particles structure and properties are influenced by several parameters, like temperature and stirring time at each step, solvent, precursor concentration, ligand type and concentration, reductant concentration and water amount, but not changing $AgCF_3COO$ with $AgNO_3$. In general, high temperatures or reductant and silver concentrations or the addition of water favour metal nanoparticles formation, while low temperature or high thiols concentration shift the reaction equilibrium toward the formation of the complex with layered structures.

Typical purification procedures exploited gel permeation chromatography (Sephadex LH20 gel in a 3x25 cm column eluted with the same solvent of the synthesis) or, in case of metal nanoparticles obtained in DMF, also precipitation induced by toluene addition was effective.

All chemicals were ACS grade purchased from Sigma Aldrich and used as received. The reference investigation technique consisted of UV-Vis spectroscopy, but also other specific types of analysis, like TEM, FT-IR, NMR and photoluminescence were carried out.

UV-Vis absorption spectroscopy was done using an Agilent 8453 diode array absorption spectrometer. TEM images were taken using a JEOL 2100 FX transmission electron microscope (TEM) at 200 kV accelerating voltage. FT-IR was carried out on samples embedded in a KBr matrix. IR-Photoluminescence measurements were conducted using a custom made system with an Argon Ion laser source and an InGaAs detector. A Varian 300 was used to register NMR spectra.

4.3 Synthesis of spherical Ag:4-FTP nanoparticles.

Spherical silver nanoparticles stabilized by a shell of 4-FTP molecules can be easily obtained by using high concentrations of Ag precursor and of reducing agent as well as reaction and storing temperatures of 20-25°C. Fig. 4.6 reports the UV-Vis spectra of the AgNP synthesized in these conditions, which show the characteristic SPA absorption. TEM analysis indicates that AgNP have an average diameter of about 4 nm with a standard deviation of about 15%. By changing temperature and reagents concentration, particles with size in the range of 3 – 10 nm can be obtained, but at the moment the synthesis parameters are under investigation and a systematic study to improve the control on the AgNP synthesis is currently ongoing.

The Mie model for simple spheres is unable to match the experimental UV-Vis spectra (figure 4.6), due to the red shift of the observed spectra with respect to the calculated one. This red shift is attributed to the effect of the 4-FTP shell, in fact the core@shell model succeeded in matching the data and giving reliable estimations of the silver core size and of the dielectric shell thickness and refraction index.

Due to the strong interactions of 4-FTP molecules on AgNP surface, anomalous packing symmetries have been observed for two-dimensional monolayers of nanoparticles on TEM grids (figure 4.6). Usually spherical nanoparticles arrange in hexagonal two-dimensional close packing with 60° angles between adjacent particles,[5, 6] but 4-FTP coated AgNP have the tendency to form stripes or to arrange in a squared or quasi squared lattice with angle between 75° and 90° depending also on the average particles size. Similar behaviours have been reported peviously for silver and gold thiolated nanoparticles both for two- and tri-dimensional arrays[5-7] and it is common in metal nanoparticles bearing thiophenyl groups, because they have a strong stacking tendency by bridging different particles.[7]

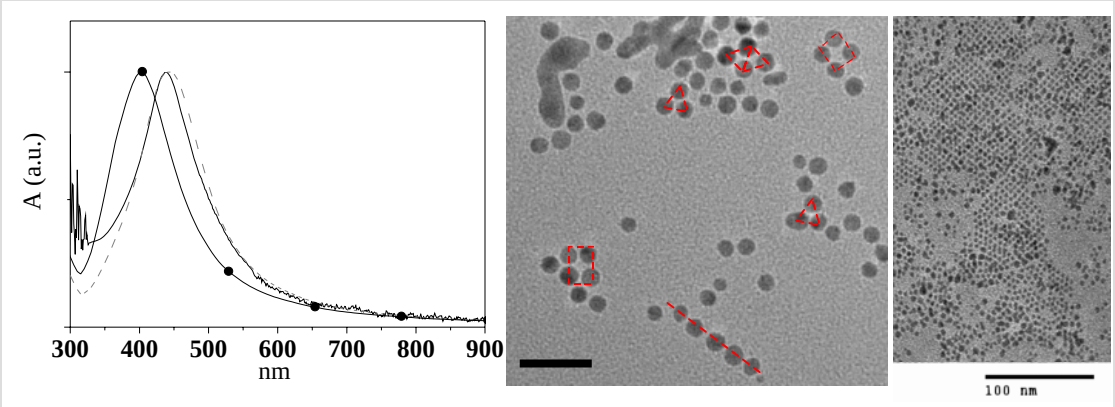

Figure 4.6 *Left: experimental UV-Vis spectrum of AgNP coated by a 4-FTP shell in DMF (black line), fitting with the Mie model for spheres (black circles – calculated R = 0.7 nm) and fitting with the Mie model for core@shell spheres (dashed line – core radius R = 1.5; shell thickness d = 1.1; shell refraction index n = 1.8). Center: TEM image showing exagonal, squared and linear packing for a sample of AgNP coated by 4-FTP in DMF with average size of 6 nm (scale bar is 20 nm). Right: AgNP:4-FTPwith average size of 3 nm showing distorted squared packing with angles close to 75°.*

4.4 Synthesis of Ag:4-FTP nanoparticles with exotic absorption properties.

Silver nanoparticles with exotic absorption (EA) properties, as shown in figure 4.7, are obtained by using high 4-FTP:Ag ratios and low storage temperatures. The UV-Vis spectra shows five primary absorption bands (410 nm, 480 nm, 540 nm, 640 nm and 845 nm), and several shoulders covering the entire visible range.

The same EA with the same peaks positions has been obtained in several solvents, like DMF, DMSO, EtOH and THF. Slightly different EA but with the same structure came out using different thiophenyl molecules, like 4-FTP, 3-FTP, 2-FTP, 4-MBT, thiophenol, mercaptobenzene, 4-clorothiophenol and others. The ligand effect on the EA peaks position is not due to the different dielectric properties of different ligands. In fact some of the EA peaks underwent to a red shift, others to a blue shift and others remained unchanged, taking Ag:4-FTP as a reference, when changing the thiophenol, while no rigid shift has been observed.

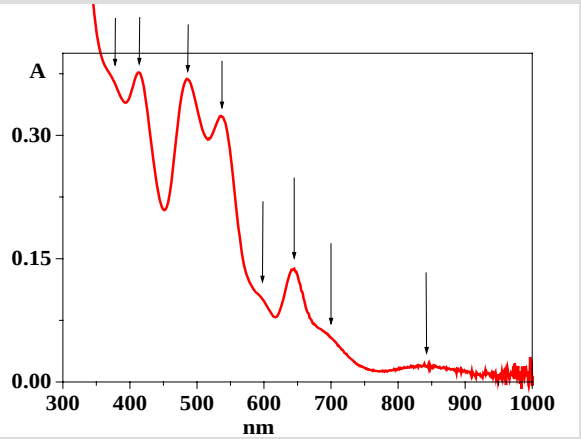

Figure 4.7 *UV-Vis spectrum of Ag:4-FTP nanoparticles synthesized in DMF.*

On the contrary alkanethiols were ineffective in producing the EA, but the common surface plasmon absorption of spherical AgNP was obtained.

A series of experiments have been carried out on Ag:4-FTP nanoparticles synthesized in DMF, which is our reference sample, as described below.

TEM images (figure 4.8) showed normal silver nanoparticles with small diameters (3 nm on average) and a relatively large size distribution (40% on average). Electron diffraction confirmed the presence of fcc Ag lattice reflections.

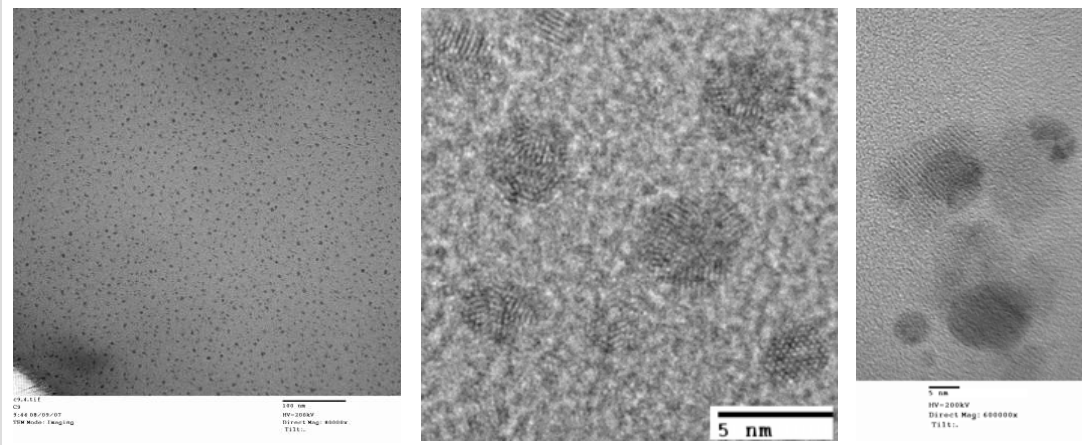

Figure 4.8 *TEM images of some Ag:4-FTP samples synthesized in DMF. Left: zoomed out image of AgNP deposition on the carbon grid, showing no coalescence between particles and no dominant sizes. Centre: HRTEM image showing the highly faceted structure of AgNP, uncommon for chemical reduction of AgNP on this size scale. Right: HRTEM image showing the coalescence of AgNP with low contrast crystals having an interference pattern of about 0.75 nm.*

It was also found that the nanoparticles had a weak tendency to agglomerate, and in general each particle was well separated from its neighbouring particles even in areas of the grid with a high density of particles. The crystal structure and shape of the particles was further investigated using high-resolution TEM (Fig. 4.8). In addition to being highly faceted, most of the nanoparticles were polycrystalline with complex grain orientations. These results strongly contrasted with 4-FTP functionalized nanoparticles showing the "normal" SPA spectrum, which were more round shaped and aggregated with more organization.

In some samples with EA spectra we found that AgNP coalesced with crystals having low electronic contrast and relatively large spacing of about 0.75 nm (figure 4.8). The lattice spacing measured by TEM for these crystals corresponds to half the value reported by Dance at al. for Ag:4-FTP crystals, as measured by powder XRD (1.47 nm).[3]

By performing a continuous wave laser irradiation of the Ag:4-FTP solution with a Spectra Physics Ar/Kr laser we concluded that all the absorption bands are originated by the same silver structure. The irradiation experiment has been performed with different laser lines (458 nm - 488 nm - 514 nm - 521 nm - 568 nm - 647 nm), resonant each time with the different absorption bands of the EA. We always found the disappearance of the whole exotic absorption pattern at the same time (figure 4.9), which supported our conclusion that all the bands of the EA derive from only one type of particles. Moreover the AgNP with EA properties evolved into the Ag:4-FTP complex, as shown by the strong peak raised at 380 nm after few minutes of laser irradiation.

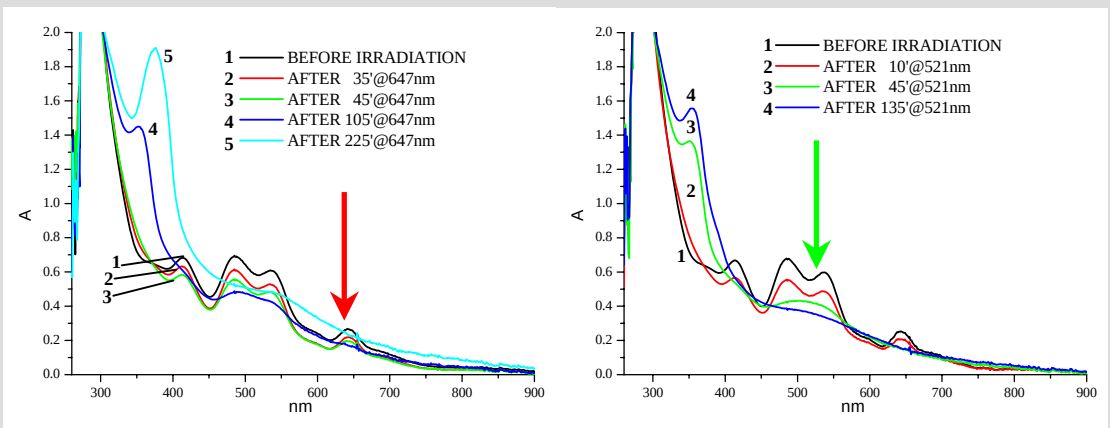

Figure 4.9 *UV-Vis of exotic 4-FTP nanoparticles as a function of time shown that irradiation at different wavelength (left: $\lambda_{irradiation}$=521 nm; right: $\lambda_{irradiation}$=647 nm) results in the disappearance of all peaks and in the growth of one peak attributed to the Ag:4-FTP layered compound around 370nm.*

STM measurements (figure 4.10a) confirmed the strong tendency for the AgNP with EA properties of turning into the complex when dried on a silicon substrate in air. Similarly, UV-Vis spectroscopy of these particles dried on a soda lime slides only showed the Ag:4-FTP complex absorption peak and/or AgNP plasmon absorptions (figure 4.10b), without any traces of EA.

Other analysis like atomic force microscopy and dynamic light scattering gave no indications about size or structure of particles with EA. Mass spectrometry performed on the dried sample (MALDI-MS) as well as on the liquid solution (Electrospray ionization MS) gave no indications about the presence of specific Ag clusters sizes too small to be observed by TEM analysis.

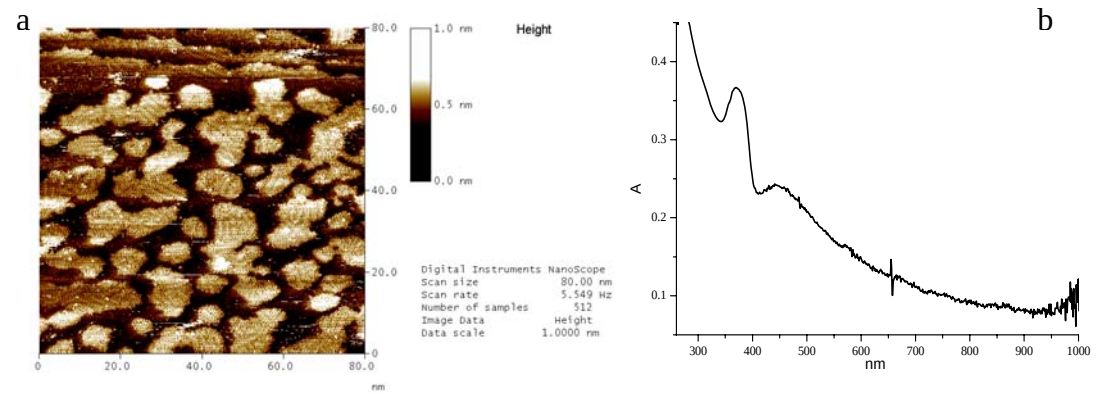

Figure 4.10 *a: STM image of an Ag:4-FTP sample cast on a silicon substrate. b: UV-Vis spectrum of Ag:4-FTP nanoparticles in THF showing EA, cast on a soda lime slide.*

NMR and FTIR spectroscopies have been used to check the sample purity, but no indications about specific properties of the ligands were evidenced, nor other structural indications emerged.

No visible fluorescence has been measured for AgNP with EA properties, but near infrared fluorescence has been measured in the 1200 – 1600 nm range, by exciting at 488 nm (figure 4.11). The fluorescence of metal nanoparticles in this interval has never been reported before now.

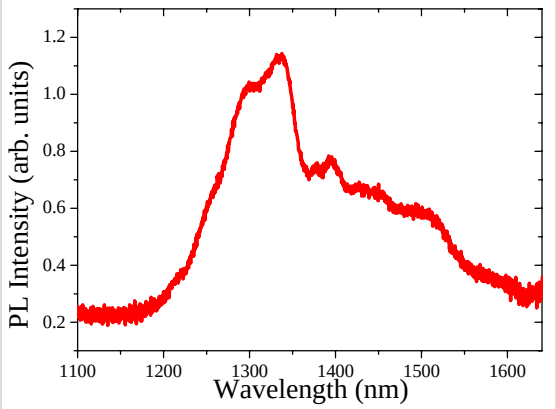

Figure 4.11 *Luminescence spectrum of Ag:4-FTP nanoparticles in DMF excited at 488 nm.*

Some variation have been observed for the EA of Ag:4-FTP nanoparticles. For example adding other thiophenols to the 4-FTP functionalized particles produced

slight changes in the exotic absorption spectrum according to the different EA spectrum of the nanoparticles obtained with the different pure molecules.

Analogous results can be obtained by adding alkanethiols instead of thiophenols to the reference solution of Ag:4-FTP nanoparticles. In this case the spectrum underwent to more significant changes, with the reshaping of all peaks in a broad band close to 500 nm (figure 4.11).

An alternative way for obtaining these "intermediate" absorption properties consists of synthesizing AgNP in a mixture of different thiophenols or mixtures of 4-FTP with alkanethiols (figure 4.11).

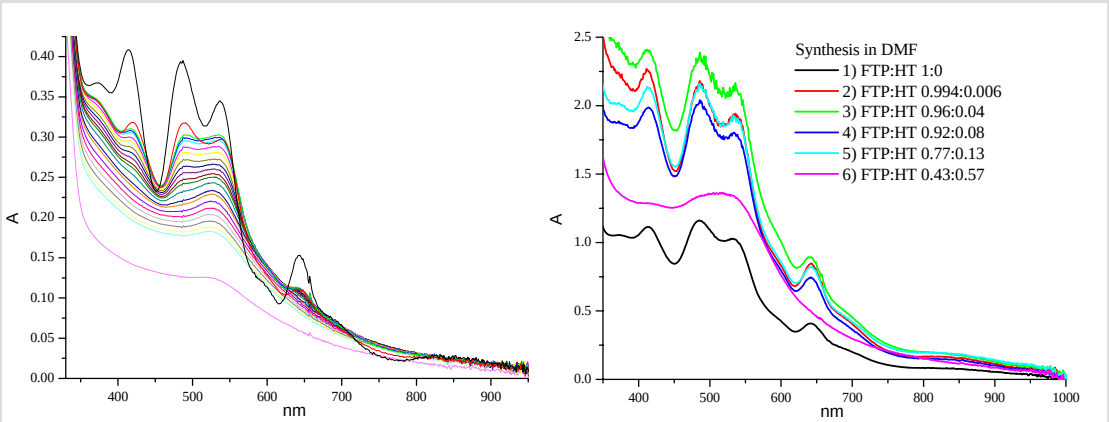

Figure 4.11 *Left: UV-Vis spectra of a 3 ml Ag:4-FTP solution before and after the addition of 0.05µl of hexanethiol (HT). The EA evolved in a time frame of 1 hour. Right: UV-Vis spectra of AgNP solutions synthesized using a mixture of 4-FTP and HT with different ratios.*

At the same time, the addition of Ag^+ or Au^+ to the reference solution allowed the control of the EA shape, as well as the synthesis in a mixture of Au and Ag precursors.

The addition of H_2O_2 to the reference Ag:4-FTP solutions turned the EA in the absorption spectrum of the Ag:4-FTP complex (figure 4.12).

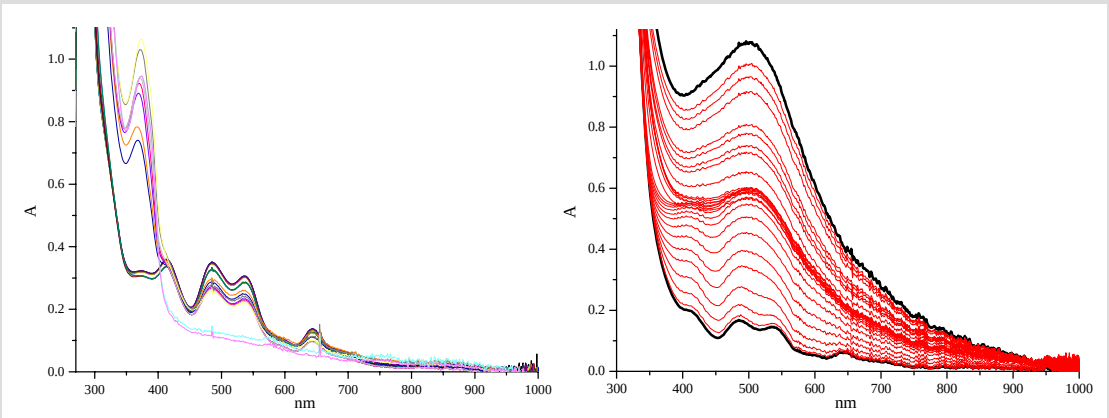

Figure 4.12 *Left: UV-Vis spectra evolution upon addition of increasing amounts of H_2O_2 (5 – 500 µl of 35% H_2O_2) to 3 ml of AgNP with EA. Right: UV-Vis spectra evolution of Ag:4-FTP particles upon heating from 25°C to 85°C.*

Further characterization analysis on the AgNP bearing these exotic absorption properties are currently ongoing, with the aim of identifying the origin of their behaviour.

4.5 Synthesis of Ag:4-FTP nanowires embedding AgNP.

The EA disappears when heating purified Ag:4-FTP nanoparticles synthesized in DMF. When heating experiments are carried out for more than 10 hours at a temperature higher than 100°C, two new absorption features appear in the UV-Vis spectrum, corresponding to the Ag:4-FTP complex at 370 nm and to AgNP at 420 nm respectively (figure 4.13). TEM analysis shows that long wires with low electronic contrast constitute the sample, with diameters on the order of 30 nm and length of several microns (figure 4.13). These wires host a large number of homogeneously dispersed silver nanoparticles with a broad size distribution in the 3 – 20 nm range. The peak at 370 nm in the UV-Vis spectra suggests that nanowires embedding AgNP are made of Ag:4-FTP complex. A systematic study to improve the control on the nanowires synthesis is currently ongoing.

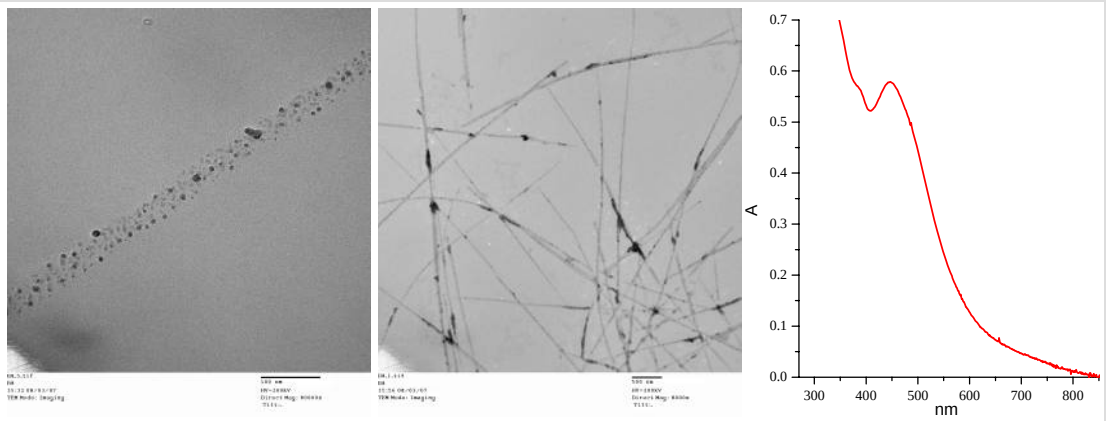

Figure 4.13 *TEM images of a sample of Ag:4-FTP nanoparticles heated for several hours at 100°C. Scale bar is 100 nm (left) and 500 nm (centre). Left: UV-Vis spectra of the same solution cast on the TEM grid.*

References

1. Zheng, J.; Nicovich, P. R.; Dickson, R. M., *Annual Review of Physical Chemistry* **2007,** 58, 409 - 431.
2. Jadzinsky, P. D.; Calero, G.; Ackerson, C. J.; Bushnell, D. A.; Kornberg, R. D., *Science* **2007,** 318, 431 - 433.
3. Dance, I. G.; Fisher, K. J.; Banda, R. M. H.; Scudder, M. L., *Inorg. Chem.* **1991,** 30, 183-187.
4. Parikh, A. N.; Gillmor, S. D.; Beers, J. D.; Beardmore, K. M.; Cutts, R. W.; Swanson, B. I., *J. Phys. Chem. B* **1999,** 103, 2850-2861.
5. Taleb, A.; Petit, C.; Pileni, M. P., *Chem. Mater.* **1997,** 9, 950-959.
6. Taleb, A.; Petit, C.; Pileni, M. P., *J. Phys. Chem. B* **1998,** 102, 2214-2220.
7. Shen, Z.; Yamada, M.; Miyake, M., *J. Am. Chem. Soc.* **2007**, In press.

Section III:

Photonic applications

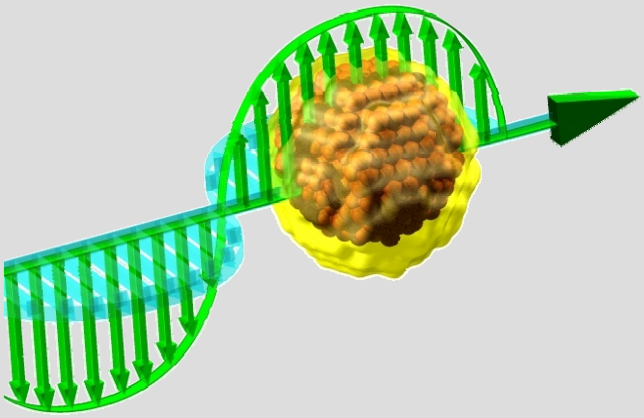

Chapter 5

Multiphoton absorption properties of organic molecules and AuNP

Multiphoton absorptions represent a wide family of optical processes investigated by nonlinear optical spectroscopies. Frequently, different pulse lengths allow the investigation of different multiphoton processes. For instance nanoseconds spectroscopies are suitable for the study of sequential multiphoton absorption processes, while femtoseconds spectroscopies are suitable for the investigation of ground state two photon absorption processes. Usually multiphoton absorptions are characteristic of organic molecules bearing delocalized electrons, like in extended π structures, and of nanostructures with large numbers of polarizable electrons, like metal nanoparticles or semiconductor quantum dots.

Nonlinear optical phenomena investigated by nanosecond spectroscopy have a key role in three main fields of photonics, which are optical limiting, photodynamic or photothermal therapy and charge or energy transfer.

Optical limiting consists of an increased opacity for a material when the incident light intensity is increased. This is a nonlinear optical phenomenon because ordinary materials have constant absorption for increasing light intensity, i.e. the transmitted light intensity increases linearly with incident intensity. Optical limiting is exploited for the protection of sensors or human eyes from high power laser radiation.[1]

Photodynamic or photothermal therapies are unconventional strategies for the selective cell death of cancerous tissues. Photodynamic therapy consists of photoinduced production of singlet oxygen by energy transfer from the triplet state of an absorbing chromophore or of production of highly reactive radicals. In particular singlet O_2 is a strongly oxidizing agent and, when present with appreciable concentration, it can produce the destruction of tissues.[2, 3] Alternatively, photothermal therapy exploits the heat released in the surrounding environment by strongly absorbing materials, like metal nanoparticles, and will be discussed in Chapter 7.

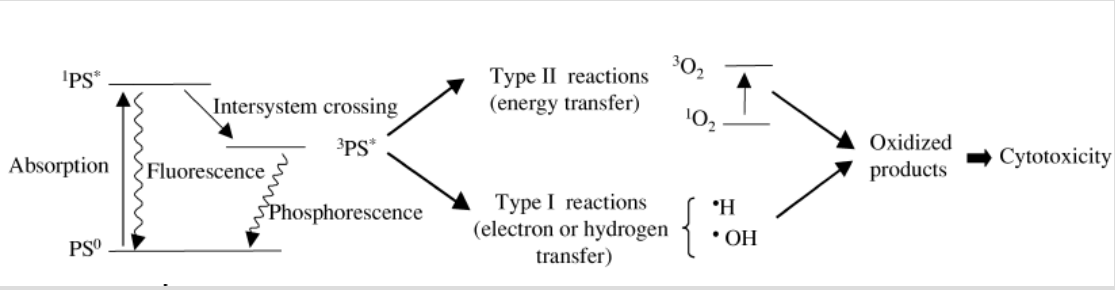

Figure 5.1 *Mechanism of photodynamic therapy, based on the excitation of the photosensitizer (PS) to the first singlet excited level and the subsequent intersystem crossing to a triplet state. From Ref. 2.*

Photoinduced electron transfer and energy transfer in a number of donor-acceptor systems have been extensively studied with the aim of mimic natural photosynthesis, by converting the charge-separated state into chemical or electrical energy.[4] In particular, photoinduced charge separation is a key function in photovoltaic devices. Other than charge separation yield, also the lifetimes of the charge separated state is important for the efficiency of devices. To establish the excited state deactivation pathways and the characteristic times for a donor acceptor couple in a given matrix, transient absorption spectroscopy is often used on the nanosecond and femtosecond time scale.[5, 6]

Strongly enhanced nonlinear optical phenomena of the type described above, can derive from the peculiar properties of metal nanoparticles. On one hand, the huge extinction cross sections of AuNP and AgNP are suitable for their application in light harvesting, possibly with a subsequent energy or charge transfer to surrounding organic

chromophores. On the other hand, local field enhancement on the metal nanoparticles surface due to plasmon oscillations can potentially amplify every kind of nonlinear optical phenomenon. Finally the large number of polarizable electrons provides large intrinsic nonlinear optical response in metal nanoparticles. As a consequence, several authors studied interactions of AuNP and AgNP with organic molecules as well as the properties of bare AuNP and AgNP for nonlinear optical applications and energy or charge transfer.[5, 7-9]

In this chapter we deal with multiphoton absorption mechanisms of a series of organic molecules with extended systems of π electrons and we also show that AuNP can interact with organic molecules yielding enhanced optical limiting properties. These superior performances exploit a simple but efficient self healing mechanism, which is possible for gold nanoparticles only in presence of a specific type of organic molecule.

5.1 Concepts of nonlinear optics.[1, 10]

The optical response of a given material is determined by its polarization in the presence of electromagnetic radiation. The interaction of photons electromagnetic field and elemental charges of a material is the origin of radiation - material interaction. The electromagnetic waves equation which describes its propagation in a material (equation *5.2*) can be derived by Maxwell equations:[10]

$$\overline{\nabla} \cdot \overline{D} = \frac{\rho}{\varepsilon_0} \qquad (5.1a)$$

$$\overline{\nabla} \cdot \overline{B} = 0 \qquad (5.1b)$$

$$\overline{\nabla} \times \overline{E} = -\frac{1}{c}\frac{\partial}{\partial t}\overline{B} \qquad (5.1c)$$

$$\overline{\nabla} \times \overline{B} = \frac{1}{c}\frac{\partial}{\partial t}\overline{D} + \frac{1}{\varepsilon_0 c}\overline{J} \qquad (5.1d)$$

$$\nabla^2 \overline{E} = \frac{1}{c^2}\frac{\partial^2}{\partial t^2}\overline{E} + \frac{1}{c^2 \varepsilon_0}\frac{\partial^2}{\partial t^2}\overline{P} \qquad (5.2)$$

where t is the time, c is the light speed, ε_0 is the vacuum dielectric permittivity, E is the electric field, D is the electric displacement, B is the magnetic displacement, ρ is the total charge density, J is the current density and P is the polarization. On one hand, equation *5.2* shows that photons electromagnetic field induces a polarization oscillating

in time in the material. On the other hand, this equation indicates that the same oscillating polarization term can act as a source of electromagnetic radiation.

The general expression for the polarization dependence on time is:[10]

$$P(t) = \varepsilon_0 \int_{-\infty}^{+\infty} R(t-\tau)E(\tau)d\tau = R(t) * E(t) \qquad (5.3)$$

That is the convolution of a response function *R(t)*, dependent on the material, with the electric field *E(t)*of the impinging electromagnetic radiation. According to the *5.3*, the polarization can be expressed as linearly dependent on the electric field component in the space of frequencies:[10]

$$P(\omega) = \varepsilon_0 \chi(\omega) E(\omega) \qquad (5.4a)$$

$$E(t) = \int_{-\infty}^{+\infty} E(\omega) exp(-i\omega t) d\tau \qquad (5.4b)$$

$$P(t) = \int_{-\infty}^{+\infty} P(\omega) exp(-i\omega t) d\tau \qquad (5.4c)$$

$$R(t) = \int_{-\infty}^{+\infty} \chi(\omega) exp(-i\omega t) d\tau \qquad (5.4d)$$

where the proportionality constant $\chi(\omega)$ is the electric susceptibility, which contains all the linear optical properties of the material.

Equation *5.4a* cannot satisfactorily describe the optical properties of a material when the intensity of electromagnetic field is high, and new terms are required, which are proportional to increasing powers of the electric field. Hence, in scalar approximation, equation *5.4a* can be expanded as:[10]

$$P(\omega) = \varepsilon_0 [\, \chi^{(1)}(\omega)E(\omega) + \chi^{(2)}(\omega)E^2(\omega) + \chi^{(3)}(\omega)E^3(\omega) + ... \,] \qquad (5.5).$$

The meaning of equation *5.5* is that the analytical expression for the polarization of a material is unknown, and a series expansion of $P(\omega)$ in powers of $E(\omega)$ is necessary for the correct interpretation of the material response to the electromagnetic radiation.

The complete expression for the polarization, which considers the vectorial nature of the physical quantities, is the following:[10]

$$\overline{E}(\overline{r},t) = \sum_{n\geq 0} (\overline{E}(\omega_n)e^{-i\omega_n t} + c.c.) = \sum_{n\geq 0} (\overline{A}(\omega_n)e^{i(\overline{k}_n \cdot \overline{r} - \omega_n t)} + c.c.) \qquad (5.6a)$$

$$\overline{E}(\omega_n) = \overline{E}(-\omega_n)^* \quad e \quad \overline{A}(\omega_n) = \overline{A}(-\omega_n)^* \qquad (5.6b)$$

$$\overline{P}(\overline{r},t) = \sum_n \overline{P}(\omega_n)e^{-i\omega_n t} \qquad (5.6c)$$

$$P_i(\omega_n) = P_i^{(1)}(\omega_n) + P_i^{(2)}(\omega_n) + P_i^{(3)}(\omega_n) + ... \qquad (5.6d)$$

$$P_i^{(1)}(\omega_n) = \varepsilon_0 \sum_j \chi_{ij}^{(1)}(\omega_n = \omega_n) E_j(\omega_n) \qquad (5.6e)$$

$$P_i^{(2)}(\omega_n = \omega_p + \omega_q) = \varepsilon_0 \sum_{j,k} \sum_{p,q} \chi_{ijk}^{(2)}(\omega_n = \omega_p + \omega_q) E_j(\omega_p) E_k(\omega_q) \qquad (5.6f)$$

$$P_i^{(3)}(\omega_n = \omega_p + \omega_q + \omega_r) = \varepsilon_0 \sum_{j,k,l} \sum_{p,q,r} \chi_{ijkl}^{(3)}(\omega_n = \omega_p + \omega_q + \omega_r) E_j(\omega_p) E_k(\omega_q) E_l(\omega_r) \qquad (5.6g)$$

where *c.c.* stands for complex conjugate, P_i is the component *i* of the polarization vector *P*, $P^{(n)}$ are the *n*-order terms of polarization and $\chi^{(n)}$, which are tensors of order $n+1$, are the susceptibilities of order *n*. Therefore the *n*-order response of a material to the electric field is represented by the *n*-order susceptibility.

In general, the order of magnitude for the first three susceptibilities are related as $\chi^{(1)}:\chi^{(2)}:\chi^{(3)}=1:10^{-8}:10^{-15}$ in c.g.s. system of units (1:cm/statvolt:cm^2/statvolt^2) and as $\chi^{(1)}:\chi^{(2)}:\chi^{(3)}=1:10^{-12}:10^{-23}$ in S.I. system of units (1:m/V:m^2/V^2). Hence nonlinear contributes to the polarization become appreciable only in presence of high electric fields. At the same time, terms with order higher than $n=3$ are observed only in special cases, because they usually require electric fields intensities which are close to the damaging threshold of common materials.

Non linear optical susceptibility can be derived by the quantum mechanical time-dependent perturbation theory of the atomic wave function. The resultant expressions are accurate for what concern non resonant response of atomic and molecular systems, while relaxation processes, which are important in the case of near resonant excitation, can be adequately described only by the density matrix formalism.

The perturbation potential *V(t)* in dipolar approximation is given by:[10]

$$\bar{\mu} = \sum_i -e\bar{r}_i \qquad (5.7a)$$

$$V(t) = -\bar{\mu} \cdot \bar{E}(t) \qquad (5.7b)$$

$$E(t) = \sum_p \bar{E}(\omega_p) e^{-i\omega_p t} \qquad (5.7c)$$

where μ is the electric dipole moment operator and *-e* is the electron charge. Consequently the hamiltonian of the time dependent Schrodinger's equation of the system and the relative eigenfunctions are:[10]

$$H = H_0 + \lambda V(t) \qquad (5.8a)$$

$$i\hbar \frac{\partial}{\partial t} \Psi = H\Psi \qquad (5.8b)$$

$$\Psi_n(\bar{r}, t) = u_n(\bar{r}) e^{-i\omega_n t} \qquad (5.8c)$$

where λ is a parameter ranging from 0 to 1 that characterizes the strength of the perturbation and allow to seek for a solution to Schrodinger's equation in the form of a power series in λ:[10]

$$\Psi_n(\bar{r},t) = \Psi_n^{(0)}(\bar{r},t) + \lambda\Psi_n^{(1)}(\bar{r},t) + \lambda^2\Psi_n^{(2)}(\bar{r},t) + \ldots \qquad (5.9a)$$

$$i\hbar\frac{\partial}{\partial t}\left[\Psi_n^{(0)}(\bar{r},t) + \lambda\Psi_n^{(1)}(\bar{r},t) + \ldots\right] = \left[H_0 + \lambda V(t)\right]\left[\Psi_n^{(0)}(\bar{r},t) + \lambda\Psi_n^{(1)}(\bar{r},t) + \ldots\right] \qquad (5.9b).$$

The eigenfunction, according to the *5.9a,* can be solution of the *5.9b* for any value of λ only if any term proportional to λ^m satisfies, separately, the equalities:[10]

$$i\hbar\frac{\partial}{\partial t}\left[\Psi_n^{(0)}(\bar{r},t)\right] = \left[H_0\Psi_n^{(0)}(\bar{r},t)\right] \quad \leftrightarrow \quad \lambda^0 \qquad (5.10a)$$

$$i\hbar\frac{\partial}{\partial t}\left[\Psi_n^{(m)}(\bar{r},t)\right] = \left[H_0\Psi_n^{(m)}(\bar{r},t) + V(t)\Psi_n^{(m-1)}(\bar{r},t)\right] \quad \leftrightarrow \quad \lambda^m \qquad (5.10b).$$

Equation *5.10a* is the Schrodinger equation for the non perturbed system, with solutions of the form of *5.8b*, while the solutions for the series of equations *5.10b* can be expressed using *5.8b* as a complete set of basis functions, as:[10]

$$\Psi_n^{(m)}(\bar{r},t) = \sum_l a_l^{(m)}(t)\Psi_l^{(0)}(\bar{r},t) = \sum_l a_l^{(m)}(t)u_l^{(0)}(\bar{r},t)e^{-i\omega_l t} \qquad (5.11)$$

where $a_l^{(m)}(t)$ are the probability amplitude that, to *m-th* order in the perturbation, the system is in the eigenstate *l* at time *t*. By replacing the *5.11* in the *5.10b* a recursive expression for calculation of the *m-th* order probability amplitudes from those of *(m-1)-th* order is obtained as:[10]

$$a_l^{(m)}(t) = \frac{1}{i\hbar}\sum_j \int_{-\infty}^{t} dt' V_{lj}(t') a_l^{m-1}(t') e^{i\omega_{lj}t'} \qquad (5.12).$$

Once the eigenfunctions are known, expectation values can be obtained. The optical properties of a material depends on the expectation value of the electric dipole moment *p* given by:[10]

$$\bar{P}(t) = N\langle\bar{p}\rangle = N\langle\Psi_n|\bar{\mu}|\Psi_n\rangle \qquad (5.13)$$

where *N* is the number of atoms or molecules described by the *5.8b* which compose the material with polarization *P*. Replacing expression *5.6d* for the polarization in the *5.13* and solving for each order, one obtains the quantum mechanical expression of linear (*1*-order) and nonlinear (*m*-order, with *m>1*) susceptibilities:[10]

$$\chi_{ij}^{(1)}(\omega = \omega_p) = \frac{N}{\hbar}\sum_m\left(\frac{\mu_{gm}^i\mu_{mg}^j}{\omega_{mg} - \omega_p} + \frac{\mu_{gm}^j\mu_{mg}^i}{\omega_{mg}^* + \omega_p}\right) \qquad (5.14a)$$

$$\chi^{(2)}_{ijk}(\omega=\omega_p+\omega_q)=\frac{N}{\hbar^2}\mathrm{P}_I\sum_{m,n}\left(\begin{array}{c}\dfrac{\mu^i_{gn}\mu^j_{nm}\mu^k_{mg}}{(\omega_{ng}-\omega_p-\omega_q)(\omega_{mg}-\omega_p)}+\dfrac{\mu^j_{gn}\mu^i_{nm}\mu^k_{mg}}{(\omega^*_{ng}+\omega_q)(\omega_{mg}-\omega_p)}+\\ \dfrac{\mu^j_{gn}\mu^k_{nm}\mu^i_{mg}}{(\omega^*_{ng}+\omega_q)(\omega^*_{mg}+\omega_p+\omega_q)}\end{array}\right) \qquad (5.14b)$$

$$\chi^{(3)}_{ijkl}(\omega=\omega_p+\omega_q+\omega_r)=\frac{N}{\hbar^3}\mathrm{P}_I\sum_{m,n,h}\left(\begin{array}{c}\dfrac{\mu^i_{gh}\mu^j_{hn}\mu^k_{nm}\mu^l_{mg}}{(\omega_{hg}-\omega_p-\omega_q-\omega_r)(\omega_{ng}-\omega_p-\omega_q)(\omega_{mg}-\omega_p)}+\\ \dfrac{\mu^j_{gh}\mu^i_{hn}\mu^k_{nm}\mu^l_{mg}}{(\omega^*_{hg}+\omega_r)(\omega_{ng}-\omega_p-\omega_q)(\omega_{mg}-\omega_p)}+\\ \dfrac{\mu^j_{gh}\mu^k_{hn}\mu^i_{nm}\mu^l_{mg}}{(\omega^*_{hg}+\omega_r)(\omega^*_{ng}+\omega_r+\omega_q)(\omega_{mg}-\omega_p)}+\\ \dfrac{\mu^j_{gh}\mu^k_{hn}\mu^l_{nm}\mu^i_{mg}}{(\omega^*_{hg}+\omega_r)(\omega^*_{ng}+\omega_r+\omega_q)(\omega^*_{mg}+\omega_r+\omega_q+\omega_p)}\end{array}\right) \qquad (5.14c)$$

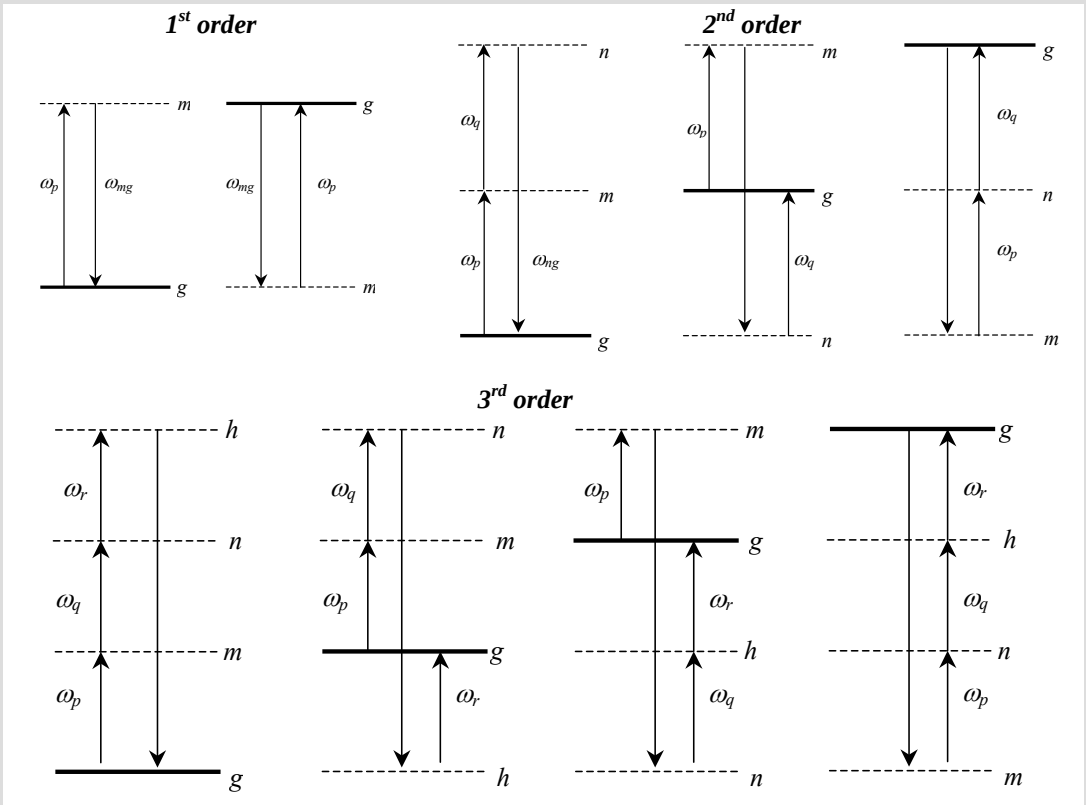

Figure 5.2 *Energy levels diagrams for the first three orders of nonlinear optical susceptibilities obtained by the quantum mechanical time-dependent perturbation theory.*

where P_I is the intrinsic permutation operator. The frequency ω_{xy} and the transition dipole moment μ_{xy} relative to the levels x and y are expressed by:[10]

$$\omega_{xy}=\omega_{xy}{}^0-i\frac{\Gamma}{2}=\frac{E^0_x\text{-}E^0_y}{\hbar}-i\frac{\Gamma}{2} \qquad (5.15a)$$

$$\mu_{xy}=\left\langle u_x(\bar{r})\middle|\bar{\mu}\middle|u_y(\bar{r})\right\rangle \qquad (5.15b)\,.$$

The *5.15a* allows the "phenomenological" inclusion of damping phenomena into the theory by the population decay rate Γ.

Each summation in the *5.14a-c*, for a given value of the summation indexes, is composed by several terms. The nature of each one of these terms can be understood by energy levels diagrams reported in Fig. 5.2, which are also helpful for the localization of resonances. Dashed lines correspond to virtual levels, i.e. levels not included in the energy spectrum of the system, except in case of resonance, when they are coincident to real levels.

In case of near resonant excitation, only the density matrix formalism can adequately describe microscopic processes involved in the optical response of a material. This formalism is still based on a perturbing potential, expressed according to *5.7a-c* and *5.8a*, and a set of eigenfunctions:[10]

$$\Psi_s(\bar{r},t) = \sum_n C_n^s(t) u_n(\bar{r}) \qquad (5.16).$$

Moreover one defines the density matrix operator ρ as:[10]

$$\underline{\rho} = \sum_s p(s) \left|\Psi_s\right\rangle\left\langle\Psi_s\right| \qquad (5.17)$$

where *p(s)* is the "classical" probability for the system of being in the eigenstate Ψ_s. The elements of density matrix are:[10]

$$\rho_{mn} = \left\langle \Psi_m \left| \underline{\rho} \right| \Psi_n \right\rangle = \sum_s p(s) C_m^{s*} C_n^s \qquad (5.18)$$

where diagonal elements ($m=n$) correspond to the population of each eigenstate and out of diagonal elements ($m\neq n$) correspond to the coherence amongst these eigenstates. By using *5.18* in Schrodinger's equation, one obtains the dynamic equation of the density matrix:[10]

$$\frac{\partial}{\partial t}\rho_{nm} = -\frac{i}{\hbar}[H,\rho]_{nm} - \gamma_{nm}\left(\rho_{nm} - \rho_{nm}^{eq}\right) \qquad (5.19)$$

where $\gamma_{mn}(\rho_{nm}-\rho_{nm}^{eq})$ has been introduced to account for the system relaxation. Equation *5.19* can be solved by using the perturbation theory and expressing the density matrix as:[10]

$$H = H_0 + \lambda V(t) \qquad (5.20)$$

$$\rho_{nm} = \rho_{nm}^{(0)} + \lambda\rho_{nm}^{(1)} + \lambda^2\rho_{nm}^{(2)} + \ldots \qquad (5.21).$$

As shown for the *5.13*, the susceptibilities at various orders can be obtained from:[10]

$$\overline{P}(t) = N\langle \overline{p} \rangle = Ntr\left(\underline{\rho}\,\overline{\mu}\right) \qquad (5.22).$$

All susceptibilities obtained by the density matrix formalism already include the relaxation terms in their expression.

Moreover the nonlinear susceptibilities derived by the density matrix formalism contain more addends than those obtained by the quantum mechanical time-dependent perturbation theory. For instance the summation of $\chi^{(2)}$ contains eight terms instead of six:[10]

$$\chi_{ijk}^{(2)}(\omega = \omega_p + \omega_q) = \frac{N}{2\hbar^2}\sum_{m,n}\left(\begin{array}{l}
\dfrac{\mu_{gn}^{i}\mu_{nm}^{j}\mu_{mg}^{k}}{\left[(\omega_{ng} - \omega_p - \omega_q) - i\gamma_{ng}\right]\left[(\omega_{mg} - \omega_p) - i\gamma_{mg}\right]} + \\
\dfrac{\mu_{gn}^{i}\mu_{nm}^{k}\mu_{mg}^{j}}{\left[(\omega_{ng} - \omega_p - \omega_q) - i\gamma_{ng}\right]\left[(\omega_{mg} - \omega_q) - i\gamma_{mg}\right]} + \\
\dfrac{\mu_{gn}^{k}\mu_{nm}^{i}\mu_{mg}^{j}}{\left[(\omega_{mn} - \omega_p - \omega_q) - i\gamma_{mn}\right]\left[(\omega_{ng} - \omega_p) - i\gamma_{ng}\right]} + \\
\dfrac{\mu_{gn}^{j}\mu_{nm}^{i}\mu_{mg}^{k}}{\left[(\omega_{mn} - \omega_p - \omega_q) - i\gamma_{mn}\right]\left[(\omega_{ng} - \omega_q) - i\gamma_{ng}\right]} + \\
\dfrac{\mu_{gn}^{j}\mu_{nm}^{i}\mu_{mg}^{k}}{\left[(\omega_{nm} + \omega_p + \omega_q) + i\gamma_{mn}\right]\left[(\omega_{mg} - \omega_p) - i\gamma_{ng}\right]} + \\
\dfrac{\mu_{gn}^{k}\mu_{nm}^{i}\mu_{mg}^{j}}{\left[(\omega_{nm} + \omega_p + \omega_q) + i\gamma_{nm}\right]\left[(\omega_{mg} - \omega_p) - i\gamma_{mg}\right]} + \\
\dfrac{\mu_{gn}^{k}\mu_{nm}^{i}\mu_{mg}^{j}}{\left[(\omega_{mg} + \omega_p + \omega_q) + i\gamma_{mg}\right]\left[(\omega_{ng} + \omega_p) + i\gamma_{ng}\right]} + \\
\dfrac{\mu_{gn}^{j}\mu_{nm}^{k}\mu_{mg}^{i}}{\left[(\omega_{mg} + \omega_p + \omega_q) + i\gamma_{mg}\right]\left[(\omega_{ng} + \omega_p) + i\gamma_{ng}\right]}
\end{array}\right) \qquad (5.23)$$

The reason for this difference lies in the different sequence of the processes involved in the nonlinear optical response. The sequence derived from the density matrix approach, allows a more rigorous treatment of the dephasing mechanisms. Diagrams in Fig. 5.3 sketches the differences amongst the eight processes described by the *5.23*. An alternative schematization of these process, useful for higher order susceptibilities with a more complicated level structure, consists of Feynman diagrams.

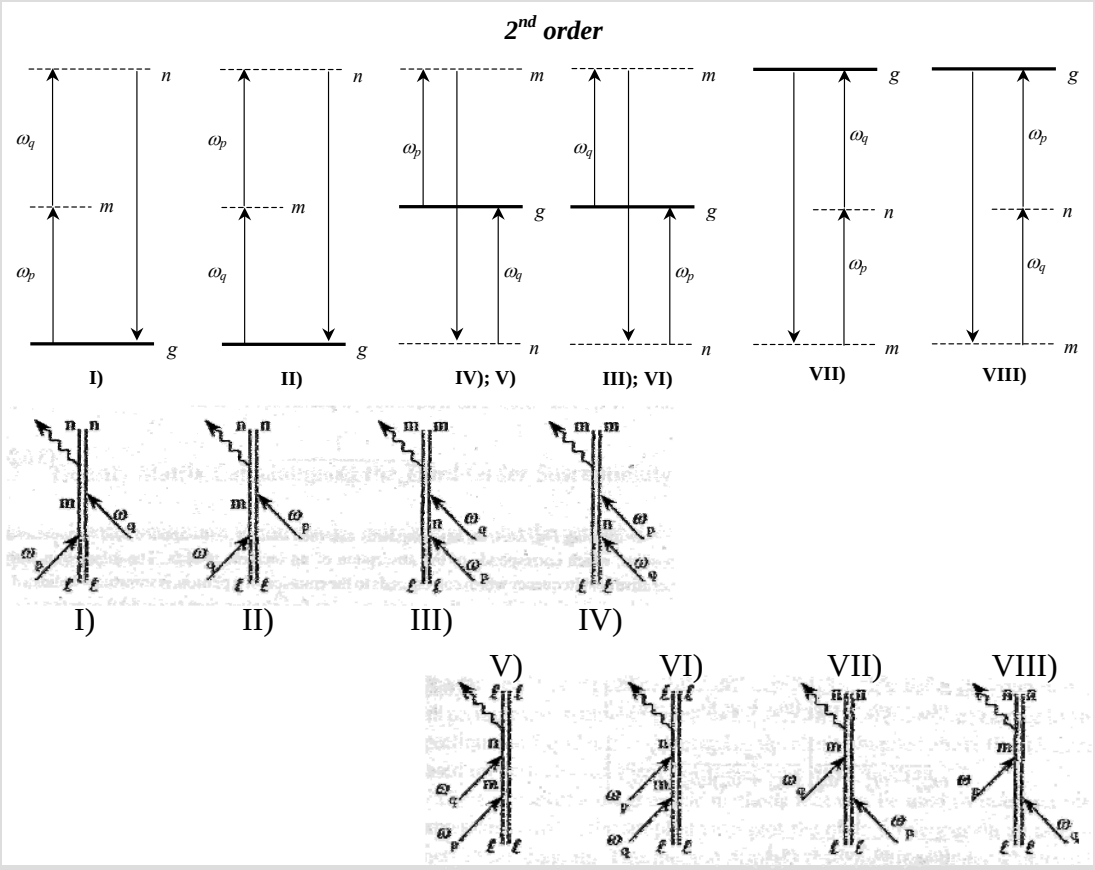

Figure 5.3 *Energy levels diagrams (up) and Feynman diagrams (down – ground state labelled as" l") for the2nd order of nonlinear optical susceptibilities obtained by the density matrix formalism. Each number corresponds to a term in equation 5.23. From ref. 10.*

5.2 Overview of the principal nonlinear optical phenomena.[1, 10]

Nonlinear optical phenomena can be divided in two groups: parametric and non parametric processes. In all parametric processes the final state coincides with the starting state, while in all non parametric processes the final state is different from the starting state. Therefore the system energy balance is zero for the former and non zero for the latter. All the parametric processes are described by the real part of susceptibility, while non parametric ones involves also its imaginary component. A consequence of this statement is that only odd orders phenomena can be non parametric, while all the nonlinear optical processes described by even order susceptibilities are parametric. This is because when considering the expression of the work made by the electromagnetic electric field on a medium:[10]

$$W = \frac{1}{\tau}\int_0^{\tau} \overline{E}(t)\cdot\frac{\partial}{\partial t}\overline{P}(t)dt \qquad (5.24)$$

where the expressions *5.6d-g* can be used for the polarization, one can demonstrate that the integral is always zero only for even orders of the electric susceptibility, i.e. even order susceptibilities are real.

Two-photons absorption (TPA). TPA represents the most popular non parametric nonlinear optical process. TPA consists of the transition from an initial state to a final state higher in energy by the simultaneous annihilation of two photons. Photons are absorbed simultaneously since the process can be sketched as a sequential absorption of the first photon from the initial level to a virtual level plus a second absorption from the virtual level to the final system level, but no intermediate real system levels are involved (see Fig. 5.4). In the common case in which the two photons have same energy, equal to one half of the overall transition energy of the TPA process, the two photons absorption contribute to the decrease transmittance *T* of the medium is:[10]

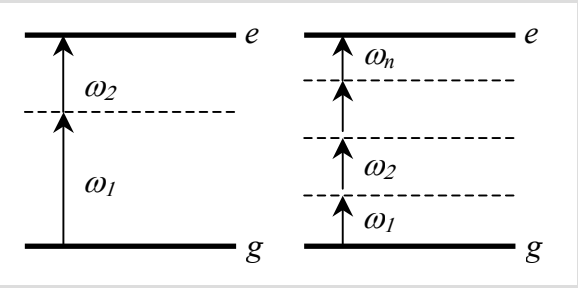

Figure 5.4 *Energy levels diagrams for simultaneous two photon absorption (left) and multiphoton absorption (right).*

$$\frac{dI}{dz} = -\beta I^2 \qquad (5.25a)$$

$$\beta = \frac{3\pi}{\varepsilon_0 n^2 c\lambda} Im\left\{\chi^{(3)}\left(\omega = \omega_1 + \omega_2 - \omega\right)\right\} \qquad (5.25b)$$

$$T(I) = \frac{I(z)}{I_0} = \frac{1}{1 + z\beta I_0} \qquad (5.25c)$$

where I is the photons intensity, z is the optical path and β is the TPA cross section. The *5.25a* shows the dependence on the square of I proper of third order non parametric processes. Typical values for β are about 10^{-10} - 10^{-14} cm W^{-1}.

In case of the simultaneous absorption of more than two degenerate photons, the generalization for the *5.25a* and the *5.25c* is straightforward:[10]

$$\frac{dI}{dz} = -\gamma^{(n)} I^n \qquad (5.26a)$$

$$T = \frac{I(z)}{I_0} = \left[\frac{1}{1 + (n-1) z\gamma^{(n)} I_0^{n-1}}\right]^{\frac{1}{n-1}} \qquad (5.26b)$$

where the *n*-photons absorption coefficient depends on the *2n-1* order susceptibility.

A common application of TPA consists in the two-photon absorption induced fluorescence (TPF) for depth resolved microscopy of biological samples. This is a consequence of the high level of space confinement of the excited volume in presence of a focused beam, since the fluorescence intensity is proportional to the number of absorbed photons, which depends on I^2.

Excited state absorption (ESA). The excited state absorption is a process composed by several steps in which, for instance, ground state linear absorption allows the population of an excited state that is able of absorbing another photon. Usually the double absorption process is not simultaneous and the multiphoton absorption processes regard real states of the system. This means that the overall transmittance through the medium depends on the incident light intensity, because the population of the first excited state, from which further absorption takes place, increases for increasing light intensity. Multiphoton absorption involving ESA processes are nonlinear phenomena dependent on the odd-order nonlinear susceptibilities.

Two main kinds of excited state absorbers are known, saturable absorbers (SA) and reverse saturable absorbers (RSA). Considering the simple case of a three level system with equal energy spacing $\omega_{eg}=\omega_{ee'}$ as that of Fig. 5.5a, the increase in the *e*-level population depends on the resonant photons intensity and on the absorption cross section σ_{ge}, while the decrease in the *e*-level population depends on the decay rate k_{eg}. For high photons intensities the *e*-level population becomes significant, allowing the absorption due to the transition *e*-*e'* with a probability dependent on the photons intensity and on the absorption cross section σ_{ee}. If the excited state absorption is negligible, the *e*-level population increases and the *g*-level population decreases until when they become equal. At this point, since $\sigma_{eg}=\sigma_{ge}$, the net flux of energy is zero and the medium becomes transparent. This phenomenon is called bleaching or saturable absorption. In the opposite case, when $\sigma_{ee'}>\sigma_{ge}$, an increase in the *e*-level population will be accompanied by an increase in the overall number of absorbed photons, i.e. by a lower transmittance. Such a system is a reverse saturable absorber.

Usually, molecular excited states have larger polarizability than ground states, therefore the condition $\sigma_{ee'}>\sigma_{ge}$ is easily fulfilled. However, good RSA requires that the *e*-level population be significant also at low laser fluences, i.e. that relaxation to the ground state be slow. The most efficient RSA systems are those based on a four level scheme as in Fig. 5.5b, which is found in molecules like fullerenes, phthalocyanines and

porphyrins. In these classes of molecules the intersystem crossing relaxation from the excited singlet state S_1 to the ground triplet state T_0 is comparable with the singlet – singlet relaxation, allowing a significant population of T_0 also for low fluences. Since the T_0-S_0 relaxation process is slow and the absorption cross section of the T_0-T_1 transition is larger than the S_0-S_1 transition cross section, these systems act as reverse saturable absorbers.

Materials with RSA properties are used for optical limiting devices.

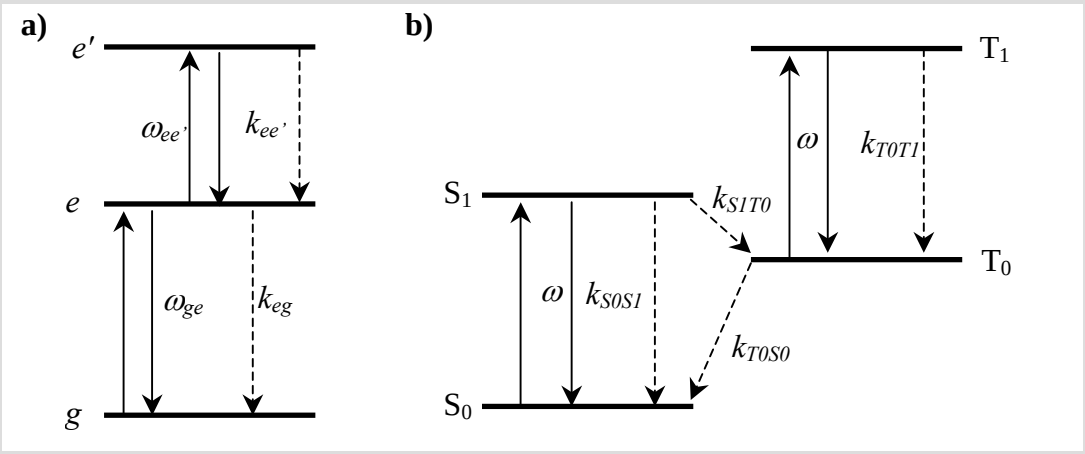

Figure 5.5 *Energy levels diagrams for a generic three level system (a) and for a four level system with intersystem crossing between the excited singlet S_1 and the ground triplet state T_0 (b).*

5.3 Model for the dynamics of excited states.[1]

As stated previously, only the density matrix formalism can adequately describe microscopic processes involved in the optical response of a material in case of near resonant excitation. Though being generally complex, the density matrix approach becomes relatively simple for incoherent phenomena, i.e. when all extradiagonal elements of the matrix are zero. In this case the problem consists in the determination of the in diagonal elements, i.e. of the levels populations.

For definition, an optical phenomenon is coherent only if the following three requirements are fulfilled:

- the laser pulse is shorter than the dephasing time of the involved energy levels;
- the reciprocal pumping system velocity is shorter than the dephasing time of the involved energy levels;
- the spontaneous radiative relaxation time to the ground state is shorter than the dephasing time of the involved energy levels.

These three requirements are not usually fulfilled in case of nonlinear optical spectroscopy in the nanoseconds time regime for the investigation of common organic molecules or metal nanoparticles.

Nonlinear incoherent resonant processes are described by determining the population densities for the various levels and the photons flux density $\tilde{I}$ ([$\tilde{I}$]=fotoni/cm^{2}s) defined as:[1]

$$\tilde{I} = \frac{I}{\hbar\omega} \qquad (5.27)$$

where I is the photons intensity and $\hbar\omega$ is the single photon energy.

Considering the easy case of a two level system, only three processes are possible: absorption, stimulated emission and spontaneous relaxation. The two populations change in time depending on the photon flux and on the three processes as:

- absorption

$$\begin{cases} \frac{\partial N_l}{\partial t} = -\sigma_{lm}\tilde{I}N_l & (5.28a) \\ \frac{\partial N_m}{\partial t} = +\sigma_{ml}\tilde{I}N_l & (5.28b) \end{cases}$$

- emission

$$\begin{cases} \frac{\partial N_l}{\partial t} = +\sigma_{ml}\tilde{I}N_m & (5.29a) \\ \frac{\partial N_m}{\partial t} = -\sigma_{lm}\tilde{I}N_m & (5.29b) \end{cases}$$

- relaxation

$$\begin{cases} \frac{\partial N_l}{\partial t} = +k_{ml}N_m & (5.30a) \\ \frac{\partial N_m}{\partial t} = -k_{ml}N_m & (5.30b) \end{cases}$$

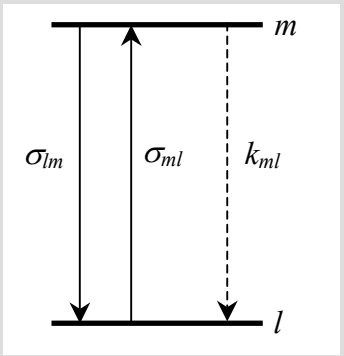

Figure 5.6 *A two level system with only three possible processes: absorption (σ_{lm}), stimulated emission (σ_{ml}) and spontaneous relaxation (k_{ml}).*

while the overall population variation in time is given by:[1]

$$\begin{cases} \frac{\partial N_l}{\partial t} = -\sigma_{lm}\tilde{I}N_l + \sigma_{ml}\tilde{I}N_m + k_{ml}N_m & (5.31a) \\ \frac{\partial N_m}{\partial t} = +\sigma_{lm}\tilde{I}N_l - \sigma_{ml}\tilde{I}N_m - k_{ml}N_m & (5.31b) \end{cases}$$

where N_l and N_m are the populations of the two states m and l, σ_{ml} and σ_{lm} are the absorption and stimulated emission cross sections respectively, k_{ml} is the spontaneous relaxation velocity which comprises all the relaxation terms like spontaneous emission $k_{ml}^{spontem}$ and nonradiative decay due to anelastic interactions with the thermal bath k_{ml}^{nonrad} as:

$$k_{ml} = k_{ml}^{spontem} + k_{ml}^{nonrad} + \ldots \qquad (5.32).$$

The overall population is constant:

$$N_{TOT} = \sum_i N_i = Konst \qquad (5.33)\,.$$

The photon intensity variation with respect to the optical path z is expressed by the *transport equation*:[1]

$$\left(\frac{\partial}{\partial z} + \frac{1}{c}\frac{\partial}{\partial t}\right)\tilde{I}(z,t) = -\sigma_{lm}\left[-N_l(z,t) + N_m(z,t)\right]\tilde{I}(z,t) \qquad (5.34)$$

where one considers that $\sigma_{ml} = \sigma_{lm}$, that the propagation is only along the z direction and that the laser spot have uniform intensity (top hat laser spot).

Equations *5.31a*, *5.31b* and *5.34* are a set of coupled differential equations called "*rate equations*", useful for describing the dynamics of the excited states. The solution of these equation system provides the variation of N_l, N_m and $\tilde{I}$ as a function of the optical path z. The ratio $\tilde{I}(t,z)/\tilde{I}(0,0)$ gives the transmittance dependence as a function of the photon intensity simply by changing the $\tilde{I}(0,0)$ value in the boundary conditions of the differential equation system.

The extension of this formalism to real systems bearing more than two levels and three processes is straightforward, as well as for more than one laser beam. For instance, one common multiphoton absorption process consists of simultaneous absorption of two photons with same energy from the generic molecular level l to the level m and it can be accounted by:

- absorption

$$\begin{cases} \dfrac{\partial N_l}{\partial t} = -\sigma_{lm}^{TPA}\tilde{I}^2 N_l & (5.35a) \\ \dfrac{\partial N_m}{\partial t} = +\sigma_{ml}^{TPA}\tilde{I}^2 N_l & (5.35b) \end{cases}$$

- emission

$$\begin{cases} \dfrac{\partial N_l}{\partial t} = +\sigma_{lm}^{TPA}\tilde{I}^2 N_m & (5.36a) \\ \dfrac{\partial N_m}{\partial t} = -\sigma_{ml}^{TPA}\tilde{I}^2 N_m & (5.36b) \end{cases}$$

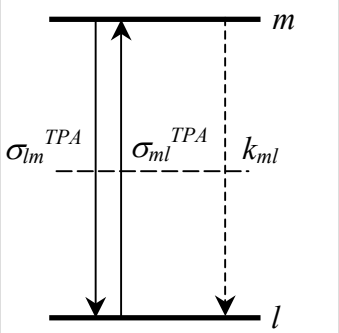

Figure 5.7 *Sketch of a two photons absorption process in a two level system.*

where the TPA absorption and emission cross sections are σ_{lm}^{TPA} and σ_{ml}^{TPA} respectively.

The solution of the differential equation system is possible by time discretization methods, which results are precise within the 1% of error. In the present case we used a free code called PRES (photon transport equation and rate equation solver) developed

by Ehlert et al.[11] The matrix formulation of the problem in the PRES code for a *n* levels system is the following:[11]

$$\frac{\partial}{\partial t}\underline{N} = \underline{A}(\widetilde{I})\underline{N} + \underline{N}\overline{V}\underline{N} \qquad (5.37a)$$

$$\left(\frac{1}{c}\frac{\partial}{\partial t} + \frac{\partial}{\partial z}\right)\widetilde{I} = -C_0 f\left[\widetilde{I}, \underline{N}\right] \qquad (5.37b)$$

where N is a nxn matrix containing all the n levels populations, A is a nxn matrix containing all the contributes of the various processes to the populations variations in time (i.e. relaxations or absorptions), V is a vector which accounts for special processes like energy transfer phenomena, C_0 is the concentration of the system bearing the n levels, $f\left[\widetilde{I}, \underline{N}\right]$ is a function accounting for the photon intensity variation through the medium due to all the processes, similarly to the *5.34*. The PRES code requires that all the system population be in the ground state at time t = 0, and the calculation is performed over a time interval which is much larger than the pulse temporal duration.

The main parameters required by the PRES code for the calculations are the time interval for the discretization of the differential equations, the photons fluence, the laser pulse time duration and time profile, the number of levels, the number and the type of processes and the linear absorption cross section σ for single system expressed in cm^2/molecule according to:

$$A = \varepsilon z C \qquad (5.38a)$$

$$\sigma = ln10\frac{\varepsilon}{N_A} \qquad (5.38b)$$

where A is the system absorbance, ε is the molar absorption coefficient, z is the optical path, C is the concentration and N_A is the Avogadro number.

5.4 Experimental set up for nonlinear optical measurements.

In the present case, nonlinear transmittance (NLT) and pump & probe (P&P) measurements with nanoseconds laser pulses have been used for almost all the nonlinear optical investigations.

We used a Q-switched Nd:YAG laser model Quantel YG-981E-10 for the production of the fundamental (1064 nm) and the duplicate (532 nm) harmonic. The Q-switch of the Fabry – Perot cavity is based on a KDP Pockels cell and another KDP crystal is used for the SHG generation. The output have a gaussian temporal profile with FWHM of 9 ns, a

spatial intensity profile that is of top hat type and the output frequency can be varied in the range of 1 – 10 Hz.

NLT set up. Nonlinear transmittance measurements consist in measuring the transmittance *T* of a sample for increasing intensities of the incident light *I* at a given wavelength. In linear optics *T* is independent on the *I* value, while in nonlinear optics *T* changes with *I*.

In the present work we performed NLT measurements with laser pulses at 532 nm. The experimental set – up is sketched in Fig. 5.8. A λ/2 plate is coupled to a cube beam splitter for the continuous and controlled variation of the laser intensity. The central part of the laser spot is selected by a diaphragm, for obtaining homogeneous intensity distribution over all the spot size. A couple of two lens, a focusing one (*f# 300*) and a defocusing one (*f# –50*) are exploited for obtaining the desired spot size on the sample. For the analysis of liquid solutions we used optical glass (SiO_2) cells with 2 mm optical path. A pyroelectric detector Scientech SPDH25 is used for the measurement of the transmitted energy. A photodiode coupled to a soda lime glass slide is used for the measurement of laser energy impinging on the sample. A series of neutral filters is used for the protection of detectors at high energies. The ratio of the transmitted energy to the incident energy gives the transmittance for a given value of incident light intensity.

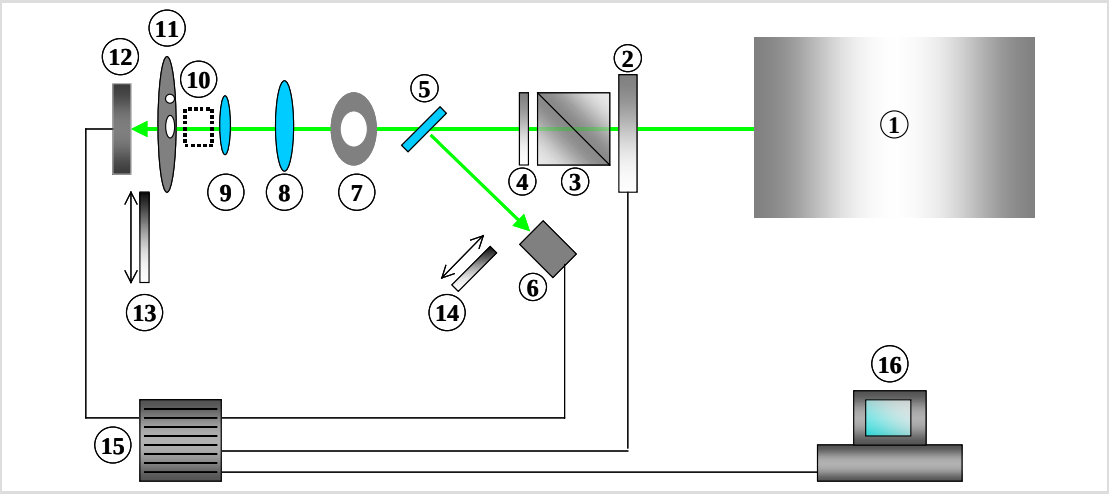

Figure 5.8 *Sketch of the nonlinear transmittance measurement set up:1) Nd:YAG laser; 2)λ/2 plate; 3) Cube beam splitter; 4) high pass filter; 5) soda lime slide; 6) photodiode detector; 7) iris diaphragm; 8) f# 300 focusing lens; 9) f# -50 defocusing lens; 10) sample holder; 11) diaphragm for closed aperture configuration; 12) pyroelectric detector; 13) and 14) neutral filters; 15) PC interface; 16) PC.*

A measurements without any sample allows the calibration of the photodiode response (in Volt) with respect to the absolute energy measurement of the pyroelectric detector

(in Joule). The measurement of the spot size by a photosensitive paper allows the conversion of the measured energy into the laser fluence, expressed in mJ cm^{-2}.

All the procedures are controlled in real time from the PC by a LabView 7.0® routine.

A typical nonlinear transmittance measurements is shown in Fig. 5.9. The plot of fig. 5.9a is called nonlinear transmittance (NLT) plot, since is referred to the transmittance *T* versus the incident fluence *F* on a Log scale. One can see that the first part of the NLT curve, corresponding to lower fluences, is constant, while only at higher fluences the curve deviates from the linear behaviour. The plot of fig. 5.9b is called optical limiting (OL) plot, since it is referred to the transmitted fluence versus the incident fluence on a linear scale. The NLT plot is useful for examining the low fluence behaviour of the sample, while the OL plot is useful for the high fluence behaviour.

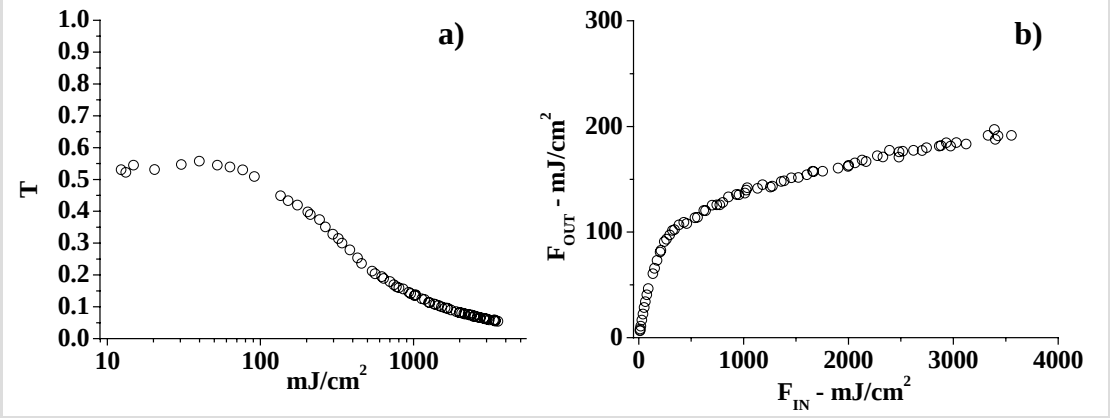

Figure 5.9 *Typical nonlinear transmittance (a) and optical limiting (b) plots for a solution with linear transmittance of 54% at 532 nm and optical limiting behaviour.*

By positioning a diaphragm in between the sample and the pyroelectric detector, the solid angle of collection for the signal can be varied in a range corresponding to the 10% - 1% of the overall solid angle (4π sterad). The largest collection angle corresponds to the open aperture (OA) configuration, while the smallest collection angle corresponds to the closed aperture (CA) configuration. From the difference in the OA and CA NLT measurements, the nonlinear scattering and nonlinear absorption contributes can be distinguished.

Pump & Probe set up. In P&P measurements the absorption spectrum of the sample is probed by a low intensity light beam (usually a lamp light) during the irradiation with a pump beam at high intensity (usually a laser beam). This is to monitor the changes in absorbance or emission at the probe wavelength after the excitation at the pump wavelength.

In the present work we performed P&P measurements with pump laser pulses at 532 nm. The experimental set – up is sketched in Fig. 5.10.

The P&P measurements is carried out with constant intensity for the pump as well as the probe beams. For the analysis of liquid solutions we used optical glass (SiO_2) cells with 2 mm optical path. The measurement is performed on the sample solution and, subsequently, to a reference solvent solution in the same conditions. The probe beam source is selected between a W lamp and a Xe lamp. The W lamp provides an output stable in time, while the Xe lamp is used when an intense probe beam is necessary also at shorter wavelengths in the visible window. The probe beam is focused on the sample by a *f#100* lens. The transmitted probe beam is focused on an optical fiber by a *f#25* lens. Band pass filters or a notch filter are used in front of the optical fiber to remove any components of the pump beam due to reflection. The optical fiber is connected to a Jobin-Yvon TRIAX 320 spectrometer equipped with two gratings (600 grooves/mm and 300 grooves/mm) and two phototubes Hamamatsu (R2257 and R5108). The phototube signal is collected by a 1GHz oscilloscope model LeCroy LC564A, triggered by the pump laser beam. The coupling of the two lamps with the optical fiber, the spectrometer and the two phototubes allow to monitor the probe signal in the 400 – 900 nm wavelength range. The pump laser beam is crossed with the probe lamp beam within the sample at an angle of about 30°, while the laser spot size is selected by a diaphragm to guarantee that the pumped volume of the sample is larger than the probed volume.

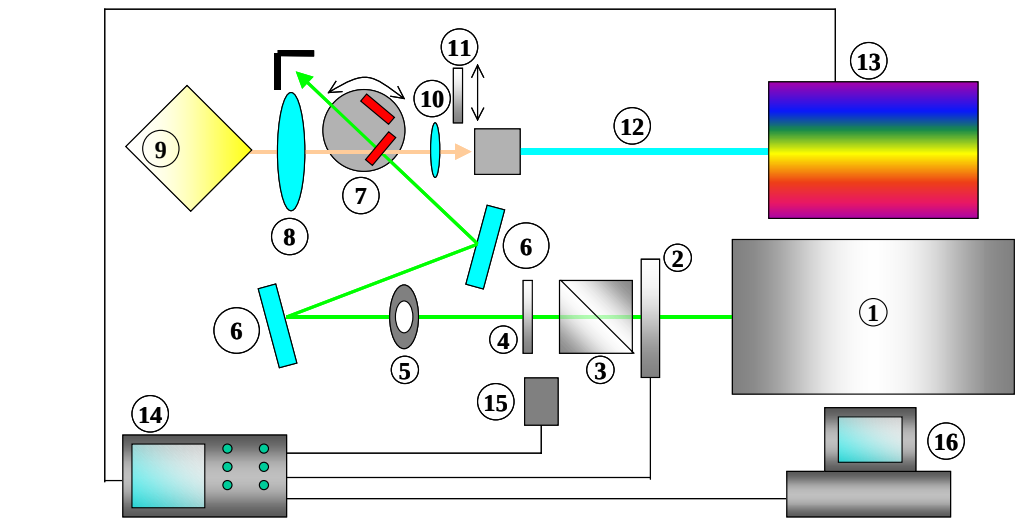

Figure 5.10 *Sketch of the pump & probe measurement set up: 1) Nd:YAG laser; 2)λ/2 plate; 3)Cube beam splitter; 4) high pass filter; 5) iris diaphragm; 6) mirrors; 7) sample holder; 8) f#100 focusing lens; 9) probe source (W or Xe lamp); 10) f#25 focusing lens; 11) band pass filter; 12) optical fiber; 13) spectrometer and phototubes; 14) oscilloscope; 15) photodiode; 16) PC.*

Each single point is averaged over several tens of pump laser shots to get a better signal to noise ratio and all the procedures are controlled in real time from the PC by a LabView 7.0® routine.

Fig. 5.11 shows a typical P&P measurements of the variation of optical density (ΔOD) in time for a given probe wavelength (a) and at different probe wavelengths for a given time delay after the pump pulse (b). The differential optical density (ΔOD) is given by the difference between the optical density at every time (OD(*t*)) with the average optical density before the pump pulse ($\langle OD(t<0)\rangle$), normalized on $\langle OD(t<0)\rangle$. The time the pump pulse arrives on the sample is taken as *t=0*. An increase in absorbance after the pump pulse appears as a positive ΔOD signal, while a decrease in the absorbance or a luminescence signal appears as a negative ΔOD.

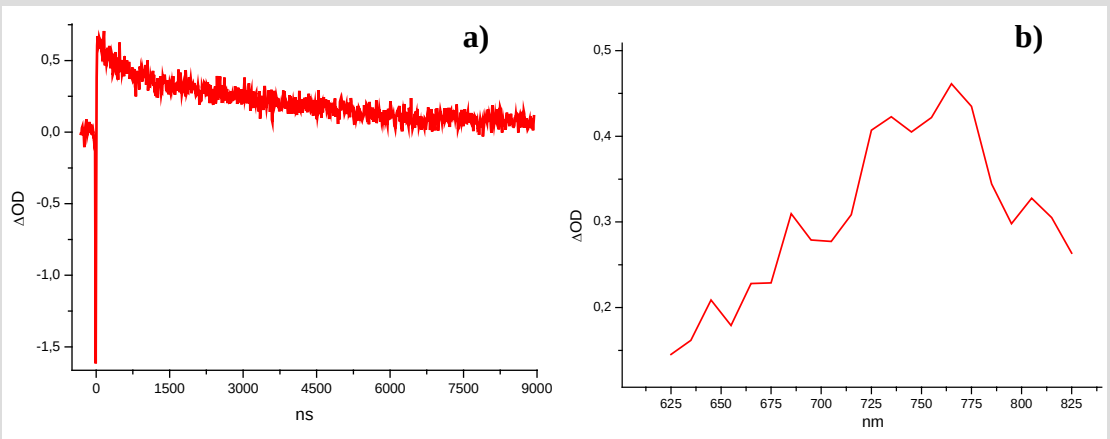

Figure 5.11 *Typical pump & probe trace at a given wavelength (a) and pump & probe spectrum at a given time (b) for a solution with long lifetime states (in the microseconds scale) having absorption cross section larger than the ground state (positive ΔOD – RSA behaviour).*

5.5 Multiphoton absorption properties of organic molecules.

The study of multiphoton absorption processes of organic molecules is necessary for understanding the correlation between their structure and their photophysical and photochemical behaviour. In the frame of the application for optical limiting, photodynamic therapy and electron or energy transfer, the classes of fullerenes, porphyrazines and porphyrins represents a reference point. C_{60} and its derivatives like fulleropyrrolidines have been applied in a gamut of photonic devices which are based on the RSA behaviour for optical limiting, on the intersystem crossing mechanism for the singlet oxygen production and on the extended π system for efficient electron transfer.[12, 13] Porphyrazines, porphyrins and their structural analogs like phthalocyanines, naphthalocyanines and anthracyanines are macrocyclic tetrapyrrolic

systems showing high symmetry, planarity and electronic delocalization.[14] Porphyrazines differ from porphyrins only for the presence of four *N* atoms instead of four *CH* groups in the macrocycle, with meso positions (see fig. 5.12). These systems usually coordinate a divalent metal atom (*Me*), but they can also exist as free ligands, with two *H* atoms replacing the metal, or can coordinate trivalent atoms together with a counteranion present in axial configuration. The typical UV-Vis spectrum of porphyrazines and porphyrins is composed by two intense absorption bands at high (about 350 nm) and low (about 700 nm) energies, called B band and Q band respectively.[14]

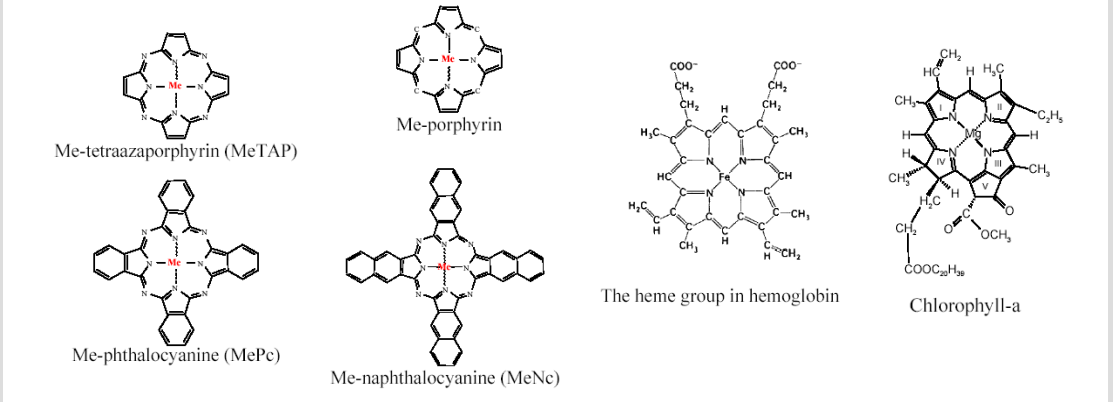

Figure 5.12 *The structure of porphyrins, porphyrazines (or tetraazaporphyrins), phthalocyanines, naphthalocyanines and two examples of porphyrins existing in nature: hemoglobin and chlorophyll A.*

As shown in Fig. 5.12, several tetrapyrrolic macrocycles exist in nature like clorophylls and the heme group in hemoglobin, which explains the high tolerability of porphyrazines and porphyrins in living organisms and their study as nontoxic photosensitizers for photodynamic therapy. Moreover the planar extended electronic structure of the macrocycle is suitable for charge and energy transfer and has been deeply investigated also in presence of fullerene as donor – acceptor charge transfer systems. In absence of hindering peripheral substituents, porphyrazines and porphyrins easily self assemble in J or H aggregates. Conversely, the presence of engineered functionalization of the peripheral corners of porphyrazines and porphyrins is the most common startegy for ensuring their solubility in common solvents, which is required for the investigation of nonlinear optical properties of isolated molecules.

Here the different multiphoton mechanisms of a series of organic molecules with innovative structures with respect to the ordinary class of fullerenes, porphyrazines and porphyrins have been investigated. The following results provides new unexpected

insights into the mechanisms of multiphoton absorptions and give useful indications on new strategies for the synthesis of innovative organic molecules with enhanced nonlinear optical performances, as well as for the coupling of these systems with nanostructured materials, with the aim of creating a new class of nanocomposites materials which combine the respective peculiarities.

Fullerene-(π-conjugated oligomer) dyad.[15] The past several years have seen a considerable interest in the development of photochemical molecular devices based on the combination of C_{60} with π-conjugated oligomers.[12] In particular, such hybrid systems have shown interesting excited state properties and have found applications in the field of solar energy conversion.[13] Less investigations exist about assemblies combining C_{60} and conjugated oligomers with strong multi-photon absorption (MPA) cross sections.[16] Such hybrid systems are however potentially interesting since they should be capable of generating singlet oxygen upon multi-photon absorption[17, 18] followed by energy transfer to the fullerene sensitizing unit.[19] This could broaden the applicability of C_{60} derivatives in photodynamic therapy[20] which is currently highly limited by both the weak linear and the low induced absorptions of fullerene-based sensitizers in the 650–750 nm region. In the present case we investigated the excited state properties of compound 1 (see Fig. 5.13), synthesized by assembling C_{60} with a new star-shaped MPA chromophore.

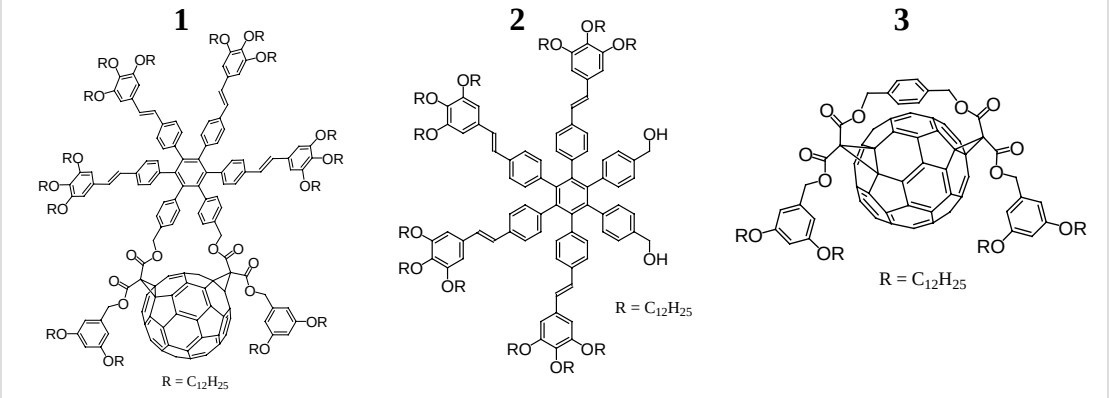

Figure 5.13 *The structure of compounds 1, 2 and 3.*

In fact, it has been shown that increased dimensionality and branched structures lead to highly effective multiphoton absorption.[21, 22] The preparation of compound 1 is reported in Ref. 15. The absorption spectrum of dyad 1 in CH_2Cl_2 is shown in Fig. 5.14, along with the profile obtained by summing the spectra of its component units 2 and 3. This comparison suggests substantial ground state interactions between the fullerene and π-

conjugated units in dyad 1, with the main absorption band of chromophore 2, centered around 335 nm, being reduced in intensity. The ground state interactions in dyad 1 may be explained by the close proximity of the two subunits as already observed for a bis(phenanthroline)Cu(I) derivative substituted with cyclic C_{60} bis-adduct moieties.[23]

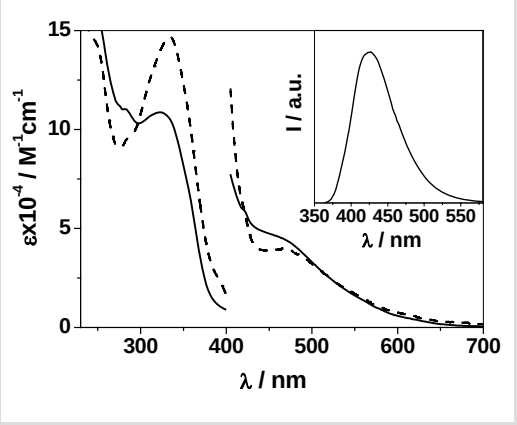

Figure 5.14 *A comparison of the absorption spectrum of the dyad* ***1*** *(—) in CH_2Cl_2 with that of the summation (--) of the absorption spectra of the reference compounds* ***2*** *and* ***4*** *in CH_2Cl_2 also. The inset shows the fluorescence spectrum of* ***2*** *in CH_2Cl_2.*

However, small conformational changes in the hexasubstituted benzene chromophore resulting from the cyclic structure involving two of its aromatic units may also explain, at least in part, the observed differences.

The fluorescence spectrum of 2 in CH_2Cl_2 is shown in Fig. 5.14. It displays a broad band with a maximum at 425 nm. The corresponding singlet lifetime was measured to be 1.5 ± 0.2 ns and the fluorescence quantum yield is 0.53 in CH_2Cl_2. Direct excitation of the star-shaped organic moiety in dyad 1 at 335 nm results in a 200-fold decrease of its emission intensity in toluene, CH_2Cl_2 and benzonitrile, when compared to 3 under the same conditions. Clear evidence on whether this process is followed by sensitization of the fullerene moiety in dyad 1 cannot be obtained because some residual emission from the appended fragment is still present above 650 nm, and this is enough to mask the weak fullerene fluorescence (ϕ=0.0004). Monitoring the luminescence of sensitized singlet oxygen allows us to indirectly evaluate the relative yield of formation of the lowest triplet excited state of C_{60}.[24] Fig. 5.15 shows the singlet oxygen emission spectra recorded for fullerene 3 compared to dyad 1 under the same

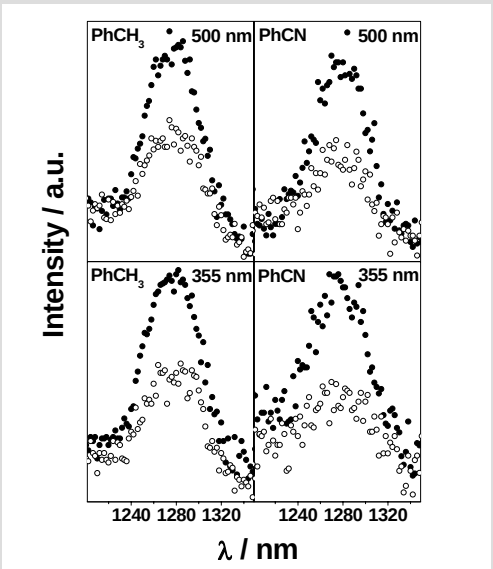

Figure 5.15 *Sensitized singlet oxygen luminescence of dyad* ***1*** *(○) and the fullerene reference* ***4*** *(●) in toluene (left) and benzonitrile (right) and while exciting at 500 nm (top) and 335 nm (bottom).*

conditions in toluene and benzonitrile and at two different excitation wavelengths (355 and 500 nm). These data provide the following information: (a) Dyad 1 is always a poorer sensitizer of singlet oxygen than fullerene 3; (b) irrespective of solvent polarity or excitation wavelength, the relative quantum yield of singlet oxygen of dyad 1 is the same, pointing to identical yields of fullerene triplet formation. The absence of any solvent effect on the yield of C_{60} triplet tends to discard any major role of electron transfer in the cascade of photoinduced processes. Furthermore, no C60 anion features were found in the NIR region down to 1200 nm, neither for 1 nor during bimolecular quenching experiments between 2 and 3 in toluene and benzonitrile, down to a 20 ns timescale. Therefore an occurrence of long-lived charge separated states is excluded. These data suggest that quenching of the star-shaped organic conjugated moiety is likely due to singlet–singlet energy transfer to the fullerene fragment, followed by intersystem crossing to generate the fullerene triplet, as observed for similar C_{60} arrays.[24] The lifetime of the quenched fluorescence could not be determined since it is shorter than the instrumental resolution (200 ps). However, from the fluorescence quenching data,[24] the rate constant of the energy transfer process can be estimated as larger than $1.3\ 10^{11}\ s^{-1}$ in all solvents.

Data in Fig. 5.15 suggest that the fullerene moiety in 1 has an inherently different yield of singlet oxygen sensitization, probably related to its own structure where the organic conjugated fragment is close to the carbon cage. This might lead to some protective effects towards oxygen quenching as previously found in bismethanofullerene dendrimers.[25] The transient absorption spectra of 1 and 3 (Fig. 5.16) compare well with triplet spectra of bismethanofullerenes reported earlier, however they are not fully superimposable to each other ($\Delta\lambda_{max}$ ca. 10 nm). This could be related to intramolecular interactions, as suggested above. Notably, the fullerene triplet lifetimes of dyad 1 (557 ns and 39 ms in air-equilibrated and air-free toluene solutions, respectively) are substantially longer than that of 3 (362 ns and 15 ms). This confirms that the triplet features of the fullerene are inherently different in 1 and 3 and protective effects of the

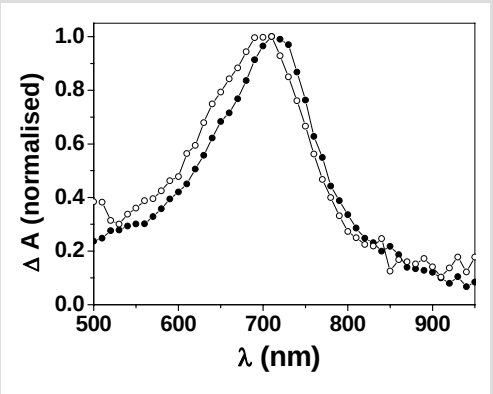

Figure 5.16 *Transient absorption spectra recorded at 530 μs following laser excitation at 355 nm in toluene of fullerene reference compound* ***2*** *(●) and dyad* ***3*** *(○).*

organic fragment toward quenching of O_2 (see triplet lifetime in air-equilibrated solutions) or solvent impurities (deaerated samples) could at least partly explain this trend.[25]

Fig. 5.17 shows the results of optical limiting measurements of benzonitrile solutions of the two separated moieties 2 and 3, and of dyad 1, using 9 ns pulses of a duplicated Nd : YAG at 532 nm. It is well known that fullerene is a reverse saturable absorption system with a greater absorption at high intensities due to the population of triplet states.[26] However, Fig. 5.17 shows that also 2 has a non linear behavior which should be considered in evaluating the behaviour of 1. A model which accounts for the non linear behaviour of 2 is a sequential three photon absorption in which, similarly to other cases,[27] a first one-photon transition populates an excited state of the molecule and then a two-photon absorption from this excited state occurs (ES-TPA). The fitting is reported on Fig. 5.17 and was obtained by solving coupled equations for the population dynamics of excited states.[11] We found a cross section for the ES-TPA, $\sigma^{(2)} = 1.58\ 10^{-43}$ cm^4 s ph^{-1} mol^{-1}, which is three to four order of magnitude larger than values found for ground state TPA, and is characteristic of excited states with very polarizable electronic states[27] (other fitting parameter values are reported in table 5.1).

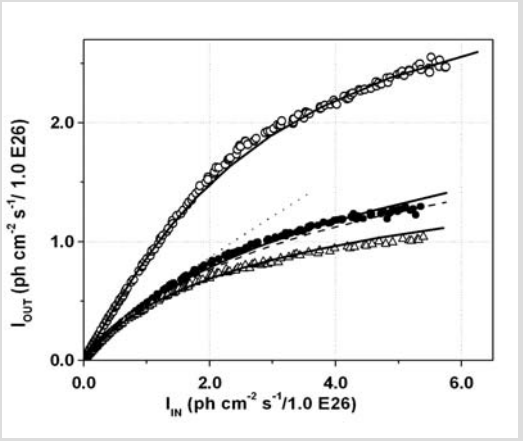

Table 5.1 *Values of the fitting parameters.*

Compound	2	3
ground state absorption $\sigma_{GS}^{(1)}$/ cm^2	$7.0\ 10^{-18}$	$8.9\ 10^{-18}$
lowest triplet state absorption $\sigma_{T1}^{(1)}$/ cm^2	$1.58\ 10^{-17}$	$1.80\ 10^{-17}$
first triplet state absorption $\sigma_{T2}^{(1)}$/ cm^2	$1.58\ 10^{-15}$	$2.0\ 10^{-15}$
relaxation first singlet state k_{S1}/ s^{-1}	$1.58\ 10^{9}$	$1.6\ 10^{9}$
intersystem crossing k_{IC}/ s^{-1}	$9.0\ 10^{8}$	$9.98\ 10^{8}$
relaxation first triplet state k_{T1}/ s^{-1}	$3.16\ 10^{11}$	$2.0\ 10^{11}$
relaxation second triplet state k_{T2}/ s^{-1}	$1.0\ 10^{13}$	$1.0\ 10^{13}$
relaxation lowest triplet state k_{T0}/ s^{-1}	$1.0\ 10^{5}$	$1.0\ 10^{5}$

Figure 5.17 *Optical limiting of* ***2*** *(open circle),* ***4*** *(full circle) and* ***1*** *(triangle) in benzonitrile solutions using 9 ns pulses at 532 nm. Straight lines starting from the axis origin would indicate a linear behaviour. Non linear absorptions are observed as deviations from straight lines. Fitting of the data are obtained with models for the excited state dynamic (see text).*

The non linear behaviour of 3 is characteristic of a fullerene derivative. In this case the fitting of the low intensity behaviour can be obtained with a four level system with two singlet states and two triplet states which absorb more than the singlet states.[28, 29] The best fitting, using this model, is reported as a dotted curve in Fig. 5.17. One finds that it fails to reproduce the large intensities data. The simplest model, which accounts for the

experimental data, must take into account that another one-photon transition can occur from the excited triplet state (values of the fitting are reported in Table 5.1). In this case, we obtain a good fitting which also accounts for the high intensity region (continuous line over full circles). By combining the separated non linear behaviour of 2 and 3, we are able to obtain an overall non linear response which is reported as a dashed line in Fig. 5.17. A small difference is found with respect to the fullerene behaviour, but the experimental data of 1 are not reproduced. This is another clear indication for an excited state interaction between the two moieties in 1. However the transient spectra (Fig.5.16) show that other excited states such as charge transfer are not involved in the process and that an energy transfer between singlet states occurs. Accordingly, the fitting of the experimental data of 1 can be obtained only with variation of the parameter values of the fullerene. The fitting is reported in Fig. 5.17 and the values of the fitting parameters in Table 5.1. In particular, one finds larger excited states absorption cross sections most probably due to the protective effect resulting from the large substituent on the fullerene sphere in 1, but the overall picture remains the same as deduced above.

Hence the combination of C_{60} with a MPA chromophore leads to improved optical limiting properties and owing to the intercomponent photoinduced energy transfer, the excited state deactivation dynamics is dominated by the fullerene chromophore. These findings pave the way towards the design of new efficient fullerene-based singlet oxygen sensitizer for photodynamic therapy applications.

Subphthalocyanine.[30] Subphthalocyanines (SubPcs)[31, 32] are conjugated complexes possessing special nonlinear optical (NLO) properties due to the simultaneous presence of an aromatic electronic structure,[33, 34] nonplanar skeleton[35] and a multipolar distribution of electrical charge.[36-38] Despite the many studies on the second- and third-order NLO properties of SubPcs, no evidence of their optical limiting (OL)[39] properties for ns pulses at 532 nm or any other wavelength in the visible has been reported so far. Different to SubPcs, phthalocyanines (Pcs) and naphthalocyanines (Ncs) are very well known for their remarkably strong OL of ns pulses in the visible range.[40, 41] This is due to their enhanced excited triplet state absorption,[40, 41] which generates the NLO effect of reverse saturable absorption (RSA).[42] In the case of SubPcs the effect of RSA could be produced at 532 nm if these afford excited electronic states with particularly high absorption cross-sections at this wavelength, say larger than 1 10^{-16} cm^2, since SubPcs generally display high linear absorption at 532 nm[37] (see Fig. 5.18). On the other hand,

the presence of a non-heavy central atom such as boron, and the bright fluorescence in the visible, are features that do not favor effective ISC in excited SubPcs.[43] Consequently, the excited triplet state of SubPcs would be populated with moderate yields and excited triplet state absorption would thus be comparatively weak.[37-39, 44-46] On the other hand, replacement of the axial ligand coordinated by central boron of SubPcs[47] with heavy atoms leads to an increase of the rate and yield of ISC.[37]

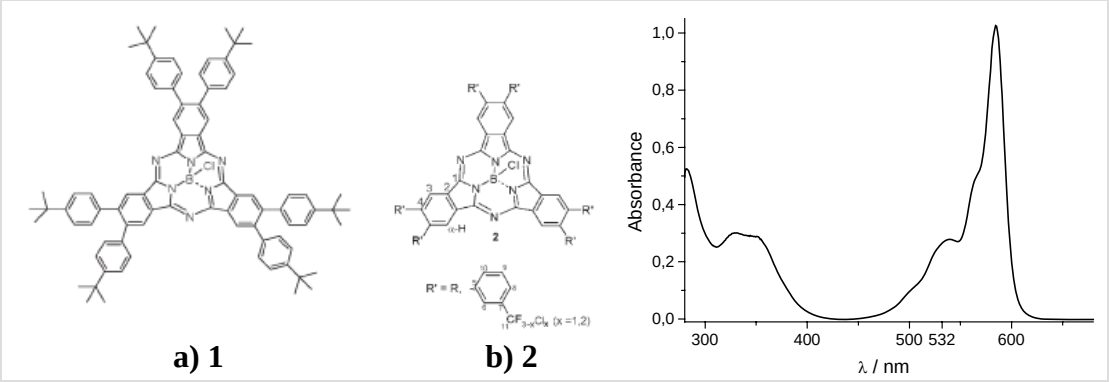

Figure 5.18 *Structure of $(tBuPh)_6$SubPcBCl (a) and $(CF_3Ph)_6$SubPcBCl (b) and linear optical spectrum of $3.5*10^{-5}$ M $(CF_{3-x}Cl_xPh)_6$SubPcBCl (2) solution in toluene (optical path 2mm).*

Despite the moderate yields of triplet state formation in SubPcs the lifetime of their excited triplet state is long enough[37] to allow the facile absorption of short-pulsed radiations such as those in the ns range. In particular, long-living excited states can be generated in SubPcs because of their generally high solubility which diminishes the probability of formation of molecular aggregates and, consequently, decreases the rate of relaxation of excited states.[48-50] Another advantage of highly soluble systems is the possibility of reaching high concentrations of absorber[48, 51] in the excited state with consequent generation of stronger optical effects.[52] In fact, the systems under investigation for OL studies are concentrated solutions of the photoactive molecular material[48, 51] in order to maximize the NLO effect[52] associated with such a material. In SubPcs high solubility is warranted by the cone-shaped structure of the ligand[31, 32] and the possible presence of bulky peripheral substituents[31, 32, 37, 38] such as p-tert-butylphenyl,[53, 54] m-trifluoromethylphenyl,[54] or m-trifluoromethylphenyloxy.[54] For this reason hexa(ptert-butylphenyl)subphthalocyaninato boron chloride and hexa(m-trifluoromethylphenyl)subphthalocyaninato boron chloride for OL studies [$(tBuPh)_6$SubPcBCl and $(CF_3Ph)_6$SubPcBCl in Fig. 5.18a and 5.18b, respectively) have been synthesized (cfr. Ref. 30). However, the resulting SubPc displayed poor photostability and the NLO properties could not be determined for $(tBuPh)_6$SubPcBCl.

To increase the photostability of a system the addition of substituents with electron-withdrawing (EW) character such as F,[55, 56] CF_3[55] and m-trifluoromethylphenyl is necessary.[57] Different to $(tBuPh)_6$SubPcBCl, SubPcs 2 with peripheral EW substituents, displayed enhanced photostability both in solution and in the solid state. This prompted us to evaluate the OL properties[44] of 2 at 532 nm since the verification of such a NLO effect requires the interaction of photochemically stable materials with high intensity radiations (in the order of 10^{10} W m^{-2}). Figs. 5.19a and 5.18 show the nonlinear transmitted intensity I_{out} at 532 nm and the linear absorption spectrum of a solution of 2 in toluene, respectively. Laser pulses with 9 ns time duration and a repetition rate of 2 Hz were used for the NLO measurements. This repetition rate is sufficiently low to avoid sample overheating and accumulating effects due to the possible slow relaxation processes of SubPcs excited states. The nonlinear variation (Fig. 5.19b) of the optical transmission of 2 at 532 nm vs. the incident intensity is obtained directly from the ratio I_{out}/I_{in} (Fig. 5.19a). The transmission is reported against input intensities on a logarithmic scale to give evidence to the data at low incident intensities which would not be otherwise appreciated from Fig. 5.19a. Fig. 5.19b indicates that $(CF_{3-x}Cl_xPh)_6$SubPcBCl 2 displays both effects of saturable absorption (SA) and RSA.[58] SA at 532 nm occurs below about 3 10^{25} photons cm^{-2} s^{-1}, i.e. below 1.12 10^{11} W m^{-2}, as indicated by the initial increase of transmittance with respect to the linear value (T_0 = 0.56).

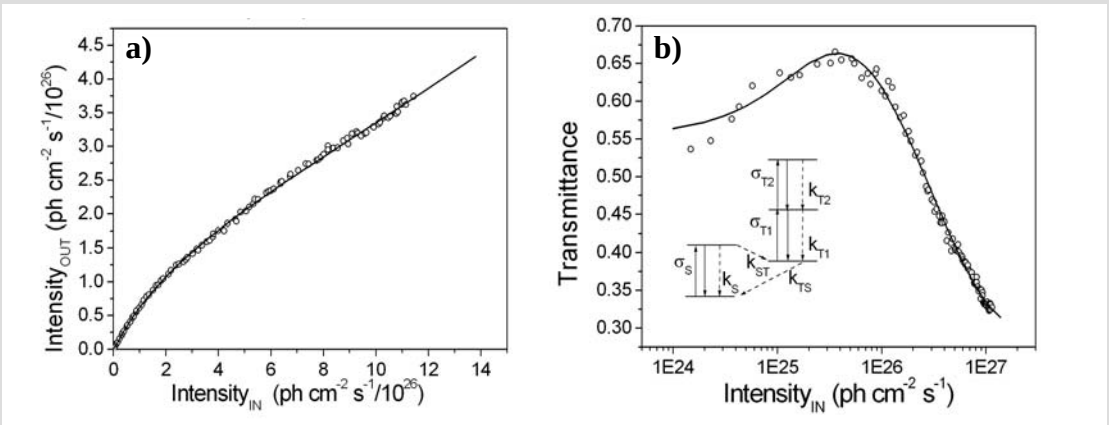

Figure 5.19 *a) Transmitted intensity vs. incident intensity at 532 nm for 3.5 10^{25} M $(CF_{3-x}Cl_xPh)_6$SubPcBCl (2) solution in toluene. Cuvette thickness: 2 mm. The continuous curve is the result of a calculation with the five level model (see text). b) Optical transmittance of 3.5 10^{25} M $(CF_{3-x}Cl_xPh)_6$SubPcBCl (2) solution in toluene with incident intensity at 532 nm. Errors of the transmittance values are estimated to be of the order of 0.1 at very low intensities, but 0.02 at intermediate intensities and 0.01 at higher intensities. The continuous curve is the result of a calculation based on the model shown in the inset, whereas the dashed curve refers to the same model but without the T_3 level (see text).*

For values of incident intensity higher than 4 10^{25} photons cm^{-2} s^{-1} SubPcs 2 start to behave as a reverse saturable absorber since transmittance decreases continuously until a minimum value of 0.32.

The present case is not the first one in which the same absorber displays both SA and RSA depending on the input intensity.[58] However, it is remarkable that SubPcs 2 could display also RSA at the present wavelength of analysis since linear absorption is very high (linear absorption cross-section σ_S for 2 is 1.4 10^{-16} cm^2 at 532 nm from Fig. 5.18).

A model which is able to account for the presented experimental data has to consider first that a strong absorption takes place at the pumping frequency (532 nm) and that SA is obtained when higher energy levels absorb less effectively than the ground state.

Since it is known that ISC is active for these molecular systems, and that the first singlet excited state lifetime is comparatively short with respect to ns pulses,[59] we have initially considered the presence of only one triplet state (four-level model).[60] A calculation of the variation of the optical transmission through this model could be done on the basis of the population dynamics of ground and excited states.[1] Solution of the kinetic equations was obtained according to Ehlert et al.[11] using a top-hat profile for the laser pulses, which is very similar to what is produced in correspondence of the focus in the actual laser beam. Fig. 5.19 shows the result of this type of calculation (dashed line). Although the modelled RSA starts at lower intensities than in the experiment, the calculation completely fails to reproduce the fast decreasing transmittance at higher intensities. The involvement of an excited singlet level for upper absorption did not produce a better fitting. We found that the simpler model which accounts for the experimental data has to consider an additional level in the triplet manifold (five-level model) (see inset of Fig. 5.19b). The calculation based on the five-level model gives a good fitting of the experimental data both at low (Fig. 5.19b), and higher intensities (Fig. 5.19a). The model considers three consecutive transitions, and the best fitting is obtained when the absorption cross-sections values are σ_S = 1.4 10^{-16}, σ_{T1} = 1.0 10^{-16} and σ_{T2} = 40 10^{-16} cm^2. Only σ_S has been experimentally determined from the linear optical spectrum (Fig. 5.18), whereas the other parameters have been obtained from the fitting. Rate constants of the reported fitting are k_S = 6.5 10^9 s^{-1}; k_{ST} = 0.25 10^9 s^{-1}; k_{T1} = 1.95 10^{11} s^{-1}; k_{T2} = 3 10^{12} s^{-1} and k_{TS} = 1.0 10^5 s^{-1}. As expected for this type of complexes, k_S and k_{ST} are comparable. Therefore, the RSA behaviour of SubPcs 2 is

due to 1 + 1 photon absorption from an excited state as recently observed in other systems.[27]

Hemiporphyrazine.[61, 62] For eye-protecting limiters,[39, 63] high transparency in the linear optical regime is generally desired and phthalocyanines (Pc) can afford that through the expansion of the inner ring into a naphthalocyanine[64] since such a transformation produces complexes with a wider range of high linear transmission in the UV-Vis by shifting the strong Q-band of Pcs towards NIR.[65] As an alternative strategy to Pc ring expansion in order to enlarge the high transmission window in the visible is represented by the hemiporphyrazine (Hp), i.e. a system with a lower extent of conjugation with respect to Pcs.

Similar to Pcs, Hps are tetraazadentate ligands which can coordinate a large variety of central atoms or divalent groups, but possess a reduced symmetry (C_{2v}) of the unsubstituted ligand with respect to the Pc ring (D_{4h}). The main effects of such structural features in Hps are the predominant absorption in the near UV (Fig. 5.20),[66-68] and fluorescent emission in the visible region[69-71] whereas Pcs emit in the NIR.[72-74] The combination of such linear optical features with the possible verification of reverse saturable absorption (RSA)[60] in the visible by Hps based systems would lead to the fulfilment of some of the most decisive conditions for the actual development of eyeprotecting limiters. In the present study [9,22-bis(dibutoxy)hemiporphyrazinato] chloroindium(III) [$(BuO)_2$HpInCl, **1**, fig. 5.20] was taken[75] since the presence of two alkoxy groups as peripheral substituent on the pyridine rings would impart solubility and processability to complex **1** (substituents on isoindoline moieties would produce the same effect of solubilization).[76] In addition, the presence of indium as central atom in $(BuO)_2$HpInCl (**1**) is expected to induce favourable effects[41, 48] on the mechanism of sequential multiphoton absorption in which efficiently pumped excited triplet states absorb photons more effectively than the ground state at the wavelength of irradiation[43] in the nonlinear optical regime. The strategy for the synthesis of $(BuO)_2$HpInCl (**1**) is reported in Ref. 61.

The solution of $(BuO)_2$HpInCl (**1**) with linear transmittance T_0 = 0.99 at 532 nm (ε = 218 L mol^{-1} cm^{-1} and σ_0 = 0.83 10^{-18} cm^2, being ε and σ_0 the ground state molar extinction coefficient and absorption cross-section, respectively) displays nonlinear optical behaviour at this wavelength starting at about 2.0 10^{25} photons cm^{-2} s^{-1} as the value of incoming photon flux (Fig. 5.21a). In correspondence of such a value the

transmittance of $(BuO)_2HpInCl$ (**1**) solution diminishes in a reversible fashion and shows a rapid decrease when incident intensity values get larger than 2.0 10^{26} photons cm^{-2} s^{-1} thus giving rise to the effect of RSA. Compound **1** displays an OL action against ns long pulses at 532 nm with the transmission of 29% of the total incident fluence (F_{in}) when it reaches the maximum value F_{in} = 3.5 J cm^{-2}.

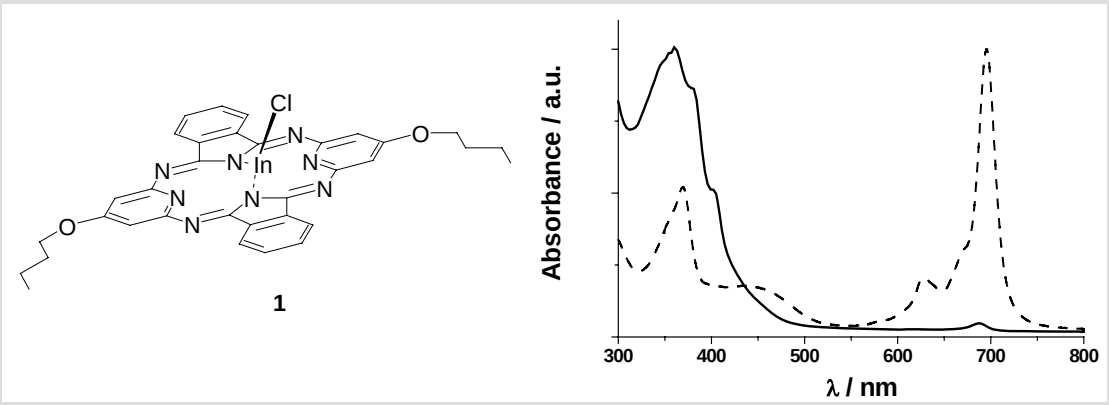

Figure 5.20 *9,22-bis-(dibutoxy) hemiporphyrazinato chloro indium (III) (**1**) for nonlinear optical transmission studies (left) and molar extinction coefficients (e) of 9,22-bis(dibutoxy)hemiporphyrazinato chloroindium(III) (1) (full line) and 2,3-octa-(2-ethyl-hexyloxy)-phthalocyaninato chloroindium(III) for comparison (dashed line) in the UV-visible. Solvent: toluene.*

This corresponds to F_{out} = 1.05 J cm^{-2} (F_{out} is the output fluence) at the minimum transmittance (T_{min}) displayed by **1**. The limiting threshold, which is defined as the fluence transmitted by the sample when T/T_0 = 0.5 (T and T_0 are the nonlinear and linear transmittance, respectively), is 1.5 J cm^{-2}. $(BuO)_2HpInCl$ (**1**) does not show any considerable variation of the linear UV-Vis spectrum after nonlinear transmission measurement, thus indicating that sample degradation does not take place after occurrence of this nonlinear optical effect. For the determination of the excited state spectrum of $(BuO)_2HpInCl$ (**1**) (Fig. 5.21b), pump and probe experiments were conducted on a **1** 10^{24} M solution of **1** in toluene pumping with the same nanosecond laser pulses at 532 nm used for recording the nonlinear transmission. In order to bring $(BuO)_2HpInCl$ (**1**) into a nonlinear optical regime the intensity of the pump radiation was set at 1.13 10^{26} photons cm^{-2} s^{-1}, corresponding to the intensity value at which the onset of larger nonlinear optical behavior of **1** is verified (Fig. 5.21a). Nanosecond long pulses at 532 nm pump complex **1** into a highly absorbing excited state in the range 400–650 nm with a maximum of absorption at about 500 nm similar to what is found for Pcs in a triplet excited state (Fig. 5.21b).[48] Moreover, we have found that the excited absorbing state shows a lifetime of about 500 ns, in the presence of oxygen which usually shortens it. This indicates that $(BuO)_2HpInCl$ (**1**) is one of the few examples of

Hps which possesses long living excited states and displays reverse saturable absorption.[77] These findings lead to the conclusion that also in the case of $(BuO)_2HpInCl$ (**1**) an intersystem crossing process operates for the generation of a triplet excited state of **1** which absorbs more effectively than in the ground state within the spectral range 400–650 nm. One should also observe that the nonlinear behaviour of $(BuO)_2HpInCl$ (**1**) is similar to that of Pcs, but the abrupt decrease of the nonlinear transmittance above 2.0 10^{26} photons cm^{-2} s^{-1} shows that an absorption process with more than one photon is active at higher intensities in the triplet manifold, since a smoother variation is expected when only one photon is absorbed by the triplet states. In fact, we have found that only the first part of the non linear transmission curve, up to 2.0 10^{26} photons cm^{-2} s^{-1}, can be fitted with a model which accounts for one-photon absorbed from the ground state and a second one from a triplet state (see Fig. 5.21a). The verification of these characteristics for $(BuO)_2HpInCl$ (**1**) discloses the use of this new class of complexes as photoactive materials with high potential for passive optical switching through nonlinear optical phenomena.[78, 79] This is mainly a consequence of the high linear transmission of $(BuO)_2HpInCl$ (**1**) in the visible range and the high nonlinear absorptivity in the same spectral range when **1** is irradiated with nanosecond laser pulses.

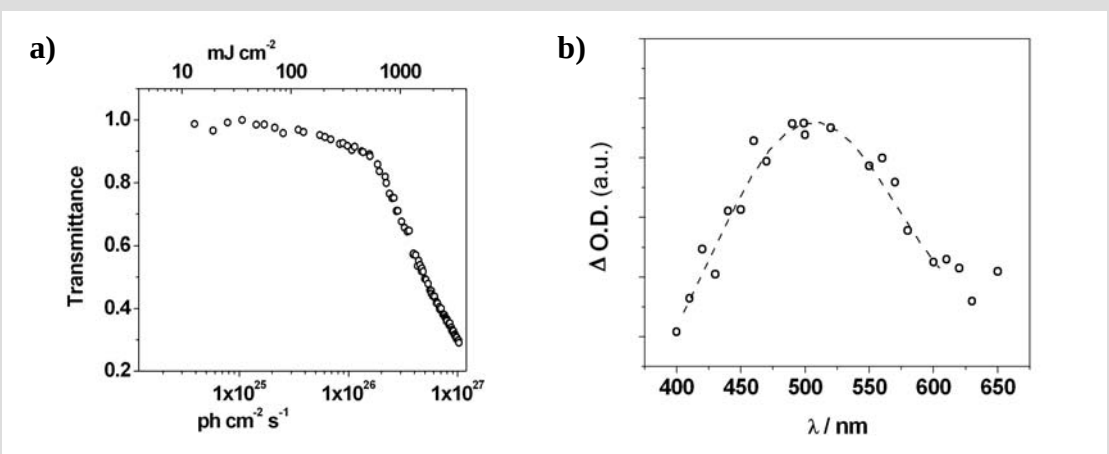

Figure 5.21 *a) Nonlinear transmittance of $1 \cdot 10^{-4}$ M toluene solution of $(BuO)_2HpInCl$ at 532 nm using 9 ns pulses. Linear transmittance of* ***1*** *at 532 nm: 0.97. b) Differential absorption spectrum of $1.0 \cdot 10^{-4}$ M $(BuO)_2HpInCl$ (**1**) in toluene determined with pump and probe experiments. For each wavelength points have been extracted from the temporal profiles of absorption of* ***1*** *at 100 ns after the laser pulse. Excitation of* ***1*** *was produced with laser pulses at 532 nm with 9 ns duration and incident intensity $1.13 \cdot 10^{26}$ photons cm^{-2} s^{-1}. Dashed line is an aid to the eye.*

Further modification of the structure for this type of molecules is expected to bring useful results for the realization of OL devices for the protection of eyes.[77]

Since the RSA dynamic depends on ligand structure,[65, 80, 81] irradiation conditions (laser wavelength[48] and pulse duration[82-84]) and in particular on the nature of central atom,[85, 86] which can favour an intersystem crossing toward the triplet state, we have focused our attention towards the nonlinear absorption properties of a series of various Hps which differ for the nature of the coordinating central atoms. In particular, we have considered the synthesis of metal-free 2(3), 15(16)-bis-(3,5-di-*tert*butyl-phenoxy)hemiporphyrazine [$(t\text{Bu}_2\text{PhO})_2\text{HpH}_2$, **2**],[67] 9,22-bis-(dihexyloxy)hemiporphyrazinato platinum [$(\text{HexO})_2\text{HpPt}$, **3**],[87] hemiporphyrazinato dichloro germanium (HpGeCl_2, **4**)[88] and 9,22-bis-(dibutoxy) hemiporphyrazinato lead [$(\text{BuO})_2\text{HpPb}$, **5**] (see Fig. 5.22), in order to determine the role of central atoms in the excited state dynamics. The multiphoton absorption properties of the complexes **1**- **5** and the dynamics of their excited states under irradiation have been recorded with ns laser pulses at 532 nm because it was shown that these long pulses can also explore multiphoton absorptions from excited states with very large cross sections.[27]

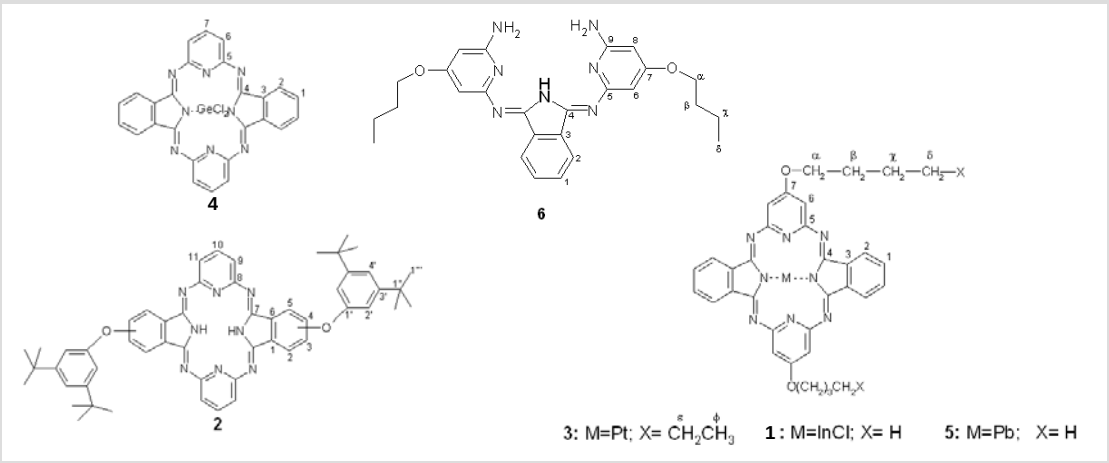

Figure 5.22 *9,22-bis-(dibutoxy) hemiporphyrazinato chloro indium [$(\text{BuO})_2\text{HpInCl}$, **1**], metal-free 2(3),15(16)-bis-(3,5-di-tertbutyl-phenoxy)hemiporphyrazine [$(t\text{Bu}_2\text{PhO})_2\text{HpH}_2$, **2**], 9,22-bis-(dihexyloxy) hemiporphyrazinato platinum [$(\text{HexO})_2\text{HpPt}$, **3**], Hemiporphyrazinato dichloro germanium (HpGeCl_2, **4**), 9,22-bis-(dibutoxy) hemiporphyrazinato lead [$(\text{BuO})_2\text{HpPb}$, **5**] and Bis-(6'-amino-4'-butoxy-2'-pyridylimino)-1,3-dihydroisoindoline (Pyr_2Ind, **6**).*

Beside the closed forms of Hps **1**-**5** the preparation of the open structure 1,3-bis-(6'-amino-4'-butoxy-2'-pyridylimino)-1,3-dihydroisoindoline (Pyr_2Ind, **6**) has been also considered (see Fig. 5.22)[89, 90] to verify how the conformational freedom, the reduction of the extent of π-electron conjugation and the absence of a central metal can influence the nonlinear absorption properties.

The strategy for the synthesis of Hps and of the open structure is reported in Ref. 62.

The values of the molar extinction coefficient (ε) in the UV-Vis spectral region for compounds **1**-**6** are presented in Figure 5.23.

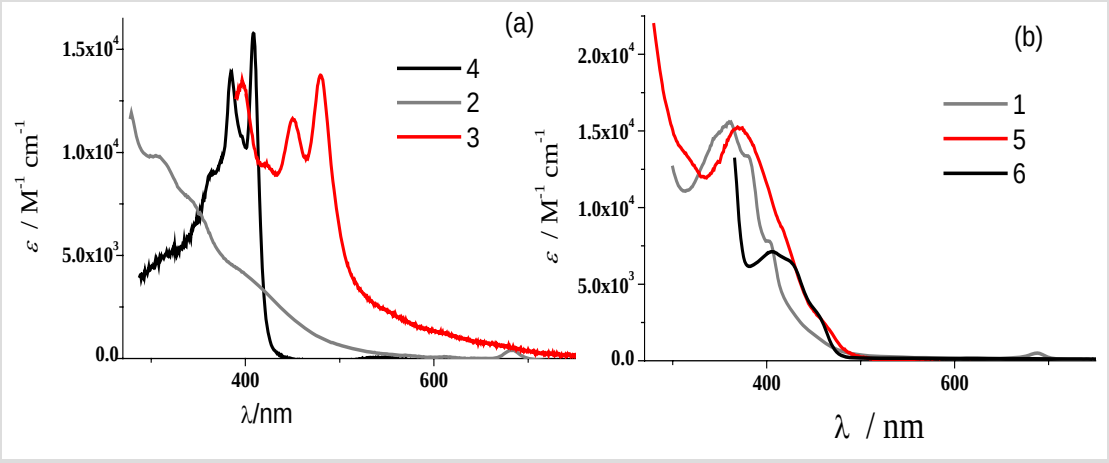

Figure 5.23 *Molar extinction coefficient (ε) values in the UV/vis range for the toluene solutions of (a) $HpGeCl_2$ (**4**), $(tBu_2PhO)_2HpH_2$ (**2**), $(HexO)_2HpPt$ (**3**), and (b) $(BuO)_2HpInCl$ (**1**), $(BuO)_2HpPb$ (**5**), Pyr_2Ind (**6**).*

Hps **1**-**5** and Pyr_2Ind (**6**) in toluene display moderate absorption being $\varepsilon < 2*10^4$ M^{-1} cm^{-1} in the near UV range (300-500 nm), and this feature imparts a yellowish colour to the solutions of these systems.[66, 69, 71-73] For wavelengths longer than 500 nm Hps and Pyr_2Ind spectra become practically flat with no relevant absorption (see Figure 5.23), the sole exception being $(HexO)_2HpPt$(**3**), which shows a tail of absorption between 510 and 720 nm and a bathochromic shift of its absorption bands with respect to the other Hps here considered.

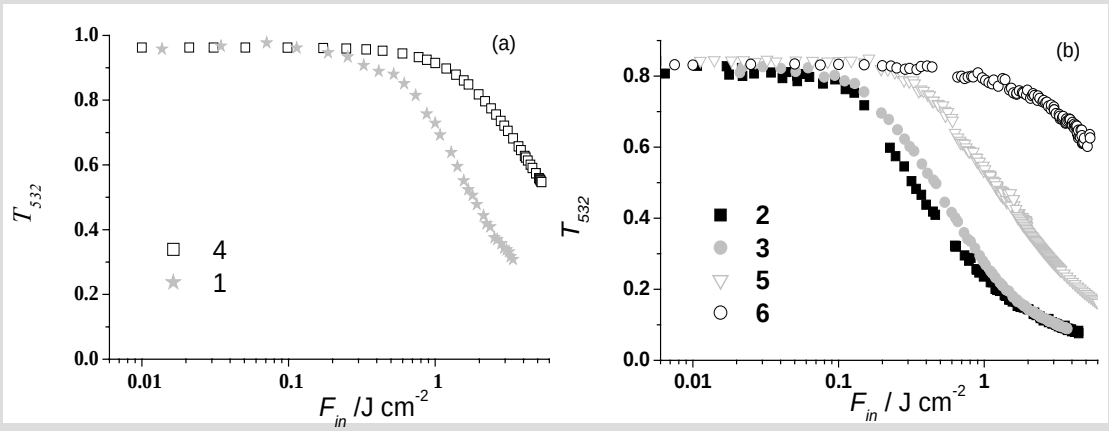

Figure 5.24 *Variations of the nonlinear transmission at 532 nm (T_{532}) for $(BuO)_2HpInCl$ (**1**), $HpGeCl_2$ (**4**) (a), and $(tBu_2PhO)_2HpH_2$ (**2**), $(HexO)_2HpPt$(**3**), $(BuO)_2HpPb$ (**5**) and Pyr_2Ind (**6**) (b) upon increase of incident fluence (F_{in}). Linear transmittance at 532 nm (T_0(532)) is 0.96 for complexes **1** and **4** and 0.83 for compounds **2**, **3**, **5** and **6**.*

The nonlinear optical properties of hemiporhyrazines **1**-**5** and the open structure Pyr_2Ind (**6**) have been determined using nanosecond laser pulses at 532 nm. The nonlinear

transmittance (T_{532}) for the toluene solutions of compounds **1-6** have been recorded as a function of the incident fluence (F_{in}) within the broad range $0 < F_{in} < 6$ J cm^{-2} (Figure 5.24).

For a direct comparison of the different nonlinear optical behaviors of Hps **1-5** and Pyr_2Ind (**6**) we have plotted in the same figure the data for those Hps solutions having the same value of linear transmittance [$T_0(532)$= 0.96 and 0.83 in the upper and lower graphs of Figure 5.24, respectively]. All species under investigation behave as reverse saturable absorbers at 532 nm for nanosecond laser pulses in the investigated fluence range. This implies that irradiation of compounds **1-6** induces the reversible formation of excited states or charge-transfer species derived from the ground states of **1-6**, which have larger absorption cross sections at 532 nm with respect to the ground state.[91]

In Table 5.2 the values of limiting threshold $F_{lim}(532)$, defined as the fluence value at which the nonlinear transmittance is half the value of the linear transmittance $T_0(532)$, and the values of molar extinction coefficient at 532 nm [$\varepsilon(532)$] are listed for compounds **1-6**. Data in Table 5.2 have been calculated for the experimental conditions which determined the nonlinear transmission profiles of Figure 5.24.

Compound	C /10^{-3} M	$T_0(532)$	$\varepsilon(532)$ M^{-1} cm^{-1}	$F_{lim}(532)$ J cm^{-2}
$(BuO)_2HpInCl$ (1)	0.1	0.99	218	1.85
$(tBu_2PhO)_2HpH_2$ (2)	3.5	0.84	108	0.45
$(HexO)_2HpPt$ (3)	0.4	0.82	1077	0.6
$HpGeCl_2$ (4)	0.3	0.96	295	> 5.4
$(BuO)_2HpPb$ (5)	0.96	0.84	762	1.65
Pyr_2Ind (6)	0.6	0.83	674	> 5.6

Table 5.2. *Values of molar concentration (C), linear transmittance at 532 nm ($T_0(532)$), molar extinction coefficient at 532 nm ($\varepsilon(532)$), and limiting threshold at 532 nm ($F_{lim}(532)$) for the toluene solutions of compounds **1-6** when they are irradiated with ns laser pulses (data taken from Figures 3 and 4). The values of $T_0(532)$ for the solutions of **1-6** are referred to air (blank), i.e. $T_0(532)air = 1$.*

For Hps **1-5** and the open derivative **6** the lowest values of $F_{lim}(532)$ are found around 0.5 J cm^{-2} and are associated to the nonlinear optical behavior of those hemiporphyrazinic complexes which reach trasmission saturation for $F_{in}(532) < 5$ J cm^{-2}, i.e. (tBu$_2$PhO)$_2$HpH$_2$ (**2**) and (HexO)$_2$HpPt (**3**) (Figure 5.24). The indium chloride complex **1** shows a value of $F_{lim}(532)$ = 1.85 J cm^{-2}, which is intermediate along the series of compounds **1-6** (Table 5.2).[61] In case of $HpGeCl_2$ (**4**) and PyrInd (**6**) $F_{lim}(532)$ could be only estimated because in the adopted experimental conditions the highest value of $F_{in}(532)$ did not permit to reach lower transmission levels because of the damage of cuvettes and focusing optics at larger fluences.

The value of the nonlinear optical parameter F_{lim} is related to the easiness with which a reverse saturable absorber becomes active. For optical power limiting purposes a lower value of F_{lim} means a better photoactive material.[48, 78] In this framework Hps **2** and **3** are the best examples among compounds **1-6**.

A comparison with the multiphoton absorption properties of similar molecules like phthalo- and naphthalocyanines or porphyrins, can be obtained considering that the nonlinear absorption of these systems derives from a one photon absorption from an excited state. Similarly, one can assume that the saturation of the nonlinear transmission (T_{min}), in particular in the case of the metal-free complex **2** and platinum hemiporphyrazine **3,** can derive from an effective one photon absorption from a completely populated excited state, although, below, we will find that the excited states dynamic of Hps is different. We can obtain a cross section for the effective one photon absorption simply by:[39]

$$\sigma'(\lambda) = \ln[1/T_{min}(\lambda)]/N\,l \qquad (5.39)$$

where N is the concentration of the molecules in solution (in cm^{-3}) and l the cell optical path (in cm).

In case of hemiporphyrazines **2** and **3** $N = 2.11*10^{18}$ cm^{-3} (**2**) and $2.41*10^{17}$ cm^{-3} (**3**), and since $T_{min}(532) = 0.08$ (**2**, **3**) (see Figures 5.28 and 5.29) and $l = 0.2$ cm, one finds $\sigma'(532) = 5.98*10^{-18}$ cm^2 (**2**) and $52.4*10^{-18}$ cm^2 (**3**). A figure of merit for comparing the multiphoton activity of molecules with a one photon excited state absorption, is obtained as the ratio $\kappa = \sigma'/\sigma_0$ where σ_0 is the ground state absorption cross-section at the chosen wavelength of analysis. In case of Hps **2** and **3** one obtains $\kappa = 14.9$ and 12.3, respectively, being $\sigma_0 = 0.4*10^{-18}$(**2**) and $4.3*10^{-18}$ (**3**) cm^2. One observes that the similarity of κ values indicates that inserting a coordinating central atom does not considerably affect the nonlinear behaviour of this type of complexes. A comparison of the κ values of Hps with those obtained for other classes of molecular nonlinear absorbers like phthalocyanines ($1 < \kappa < 34$),[39, 85] porphyrins ($2 < \kappa < 35$)[92-96] and also C_{60} ($\kappa < 5$)[39] at 532 nm, for ns pulses, indicates that Hps represent a very effective class of multiphoton absorber materials.

The knowledge of F_{lim} (Table 5.2) or κ for compounds **1-6** does not give any insight into the actual mechanism of their nonlinear absorption. As shown previously, the lower fluences nonlinear transmission behaviour of the complex $(BuO)_2HpInCl$ (**1**) at 532 nm has been simulated with a model which considered the absorption of one photon from

the ground state and the absorption of a second photon from an excited triplet state with absorption cross-section equal to $1.6*10^{-16}cm^2$. The activity of the excited triplet state in the nonlinear absorption process of **1** has been confirmed by a pump and probe experiment which determined a value longer than 100 ns for the lifetime of an absorbing excited state.[61] We also observed a well definite emission (see Figure 5.25), in the broad range 550-825 nm, with a lifetime faster than the resolution of the pump and probe experiments with ns pulses.

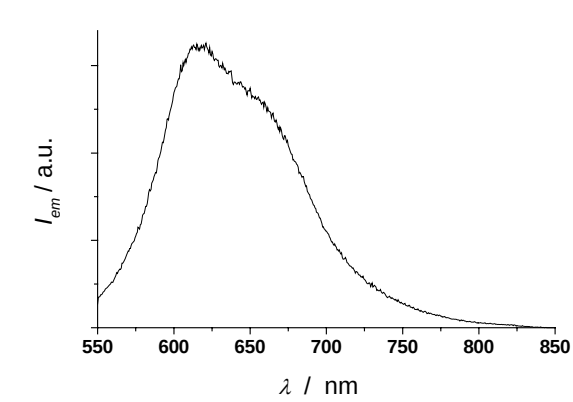

Figure 5.25 *Emission spectrum of $(BuO)_2HpInCl$ (**1**) in toluene. Excitation wavelength (λ_{exc}): 532 nm; concentration (C): $9.5*10^{-4}$ M.*

The model proposed previously proved to be valid for the fitting of the nonlinear transmission profile of $(BuO)_2HpInCl$ (**1**) when F_{in} < 0.9 J cm^{-2}, in correspondence of which complex **1** shows small variations of T_{532} (Figure 5.24). The same model could not fit the larger changes of T_{532} that occurred with $(BuO)_2HpInCl$ (**1**) when F_{in} >1 J cm^{-2}. Therefore, an extension of that model it is here proposed for the fitting of the nonlinear optical absorption within the whole range of applied incident fluences.

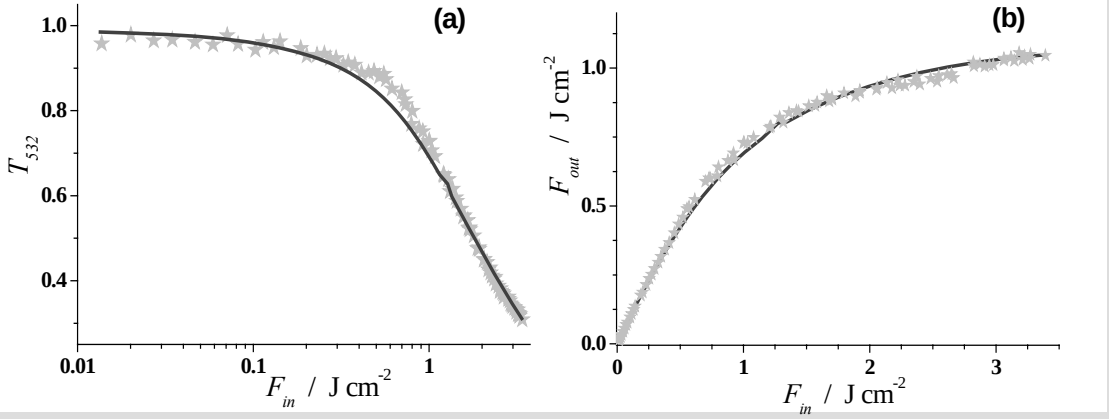

Figure 5.26 *Plots of (a) nonlinear transmission vs incident fluence (T_{532} vs F_{in}) and (b) transmitted fluence (F_{out}) vs F_{in} for $(BuO)_2HpInCl$ (**1**) at 532 nm. Fit of the experimental points has been created with the model of multiphoton absorption depicted in Figure 5.27.*

The nonlinear absorption of $(BuO)_2HpInCl$ (**1**) at 532 nm (Figure 5.26), has been fitted with a similar model which considers the absorption of one photon from the ground state, the absorption of one photon from the first excited triplet state and the successive

simultaneous absorption of two photons from the second excited triplet state (Figure 5.27). We report in Figure 5.26a-b the same data as transmittance T (= F_{out}/F_{in}) vs log(F_{in}) and F_{out} vs F_{in} since the first plot shows better the fitting of the experimental data in the low fluence regime whereas the second plot shows better the one at high fluence. One can see that both regimes are well fitted by the adopted model.

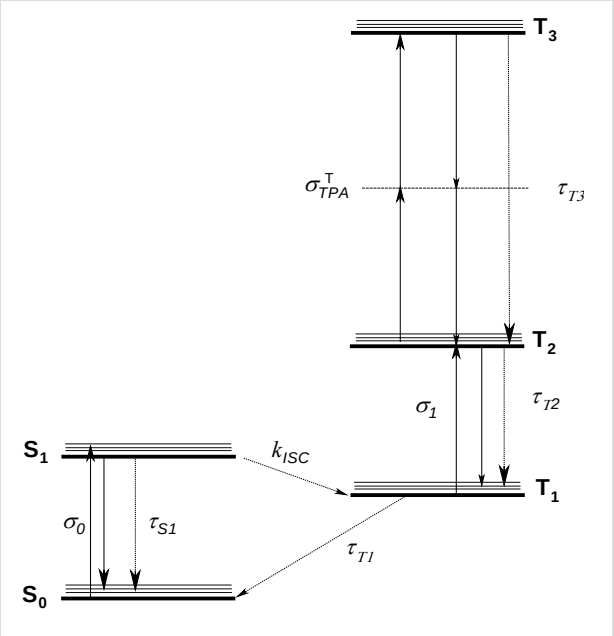

Figure 5.27 *Model for the excited state dynamics of $(BuO)_2HpInCl$ (**1**) with a two photon absorption from an excited triplet state.*

Fitting of the data required the optimization of σ_1, σ^T_{TPA}, the intersystem crossing k_{ISC} and the excited states lifetimes (see Figure 5.27). Fitting of the experimental curve of Figure 5.26 with $(BuO)_2HpInCl$ (**1**) has been achieved with the following values of free parameters: $\sigma_1 = 1.6*10^{-16}$ cm^2, $\sigma^T_{TPA} = 5.24*10^{-42}$ cm^4 s phot^{-1} mol^{-1}, $k_{ISC} = 3.0*10^9$ s^{-1}, $\tau_{S1} = 5.0*10^{-11}$ s, $\tau_{T1} = 2.0*10^{-6}$ s, $\tau_{T2} = 5.88*10^{-12}$ s, $\tau_{T3} = 5.55*10^{-14}$ s. The value of linear absorption cross section at 532 nm $\sigma_0(532) = 0.83*10^{-18}$ cm^2 was obtained from the linear spectrum (Figure 5.23).

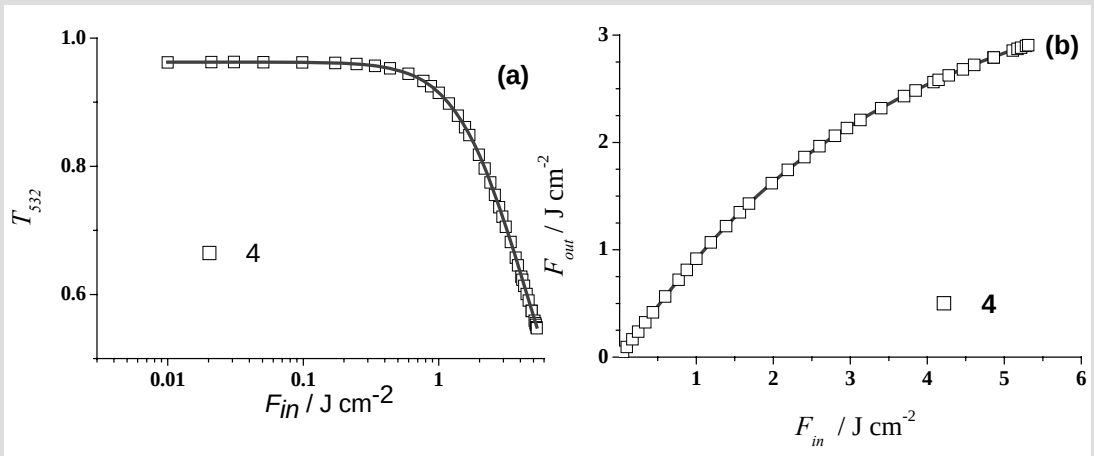

Figure 5.28 *Fitting of (a) T_{532} vs F_{in} and (b) F_{out} vs F_{in} for $HpGeCl_2$ (**4**) upon irradiation at 532 nm. Fit (continuous black line) has been generated with the multiphoton absorption model depicted in Figure 8 using the values of parameters reported in Table 5.3.*

One can observe that the absorption cross section for the simultaneous absorption of two photons from excited state, σ^{T}_{TPA}, has a very large value, which is four to five order of magnitude larger than corresponding values usually observed for two photon absorption processes from the ground state.

This is characteristic of nonlinear processes which start from excited states since, as recalled above, excited states are very polarizable states and, as a consequence of that, show very large optical responses.[27]

The profiles of nonlinear transmitted fluence for (*t*Bu$_2$PhO)$_2$HpH$_2$ (**2**), (HexO)$_2$HpPt (**3**), HpGeCl$_2$ (**4**), (BuO)$_2$HpPb (**5**) and PyrInd (**6**) (Figures 5.28 and 5.29) have been fitted with a more simple model which only includes the absorption of one photon from the ground state and the successive simultaneous two photon absorption from the first excited singlet state with no occurrence of intersystem crossing (Figure 5.30).

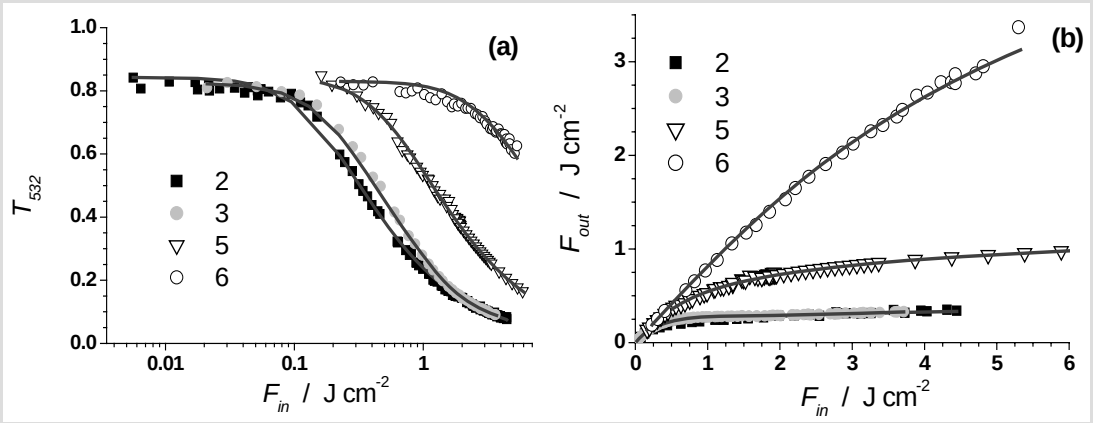

Figure 5.29 *Fitting of (a) T_{532} vs F_{in} and (b) F_{out} vs F_{in} for (tBu$_2$PhO)$_2$HpH$_2$ (**2**), (HexO)$_2$HpPt (**3**), (BuO)$_2$HpPb (**5**) and Pyr$_2$Ind (**6**) upon irradiation at 532 nm. Fit (continuous black lines) has been created with the multiphoton absorption model depicted in Figure 8 using the values of parameters reported in Table 5.3.*

Different from hemiporphyrazine **1**, the exclusion of any triplet state in the excited state dynamics of compounds **2**, **3**, **4**, **5** and **6** has been proved by means of pump and probe experiments which did not show any presence of long lived ($\tau > 10^{-8}$ s) excited states. The analysis of the nonlinear transmission curves of (*t*Bu$_2$PhO)$_2$HpH$_2$ (**2**), (HexO)$_2$HpPt (**3**), HpGeCl$_2$ (**4**), (BuO)$_2$HpPb (**5**) and PyrInd (**6**) has required, therefore, the evaluation of only three parameters: The simultaneous two-photon absorption cross-section for the transition between excited singlet states (σ^{S}_{TPA}), the lifetime of the first excited singlet state (τ_{S1}) and the lifetime of the second excited singlet state (τ_{S2}) (see Figure 5.30). Values of fitting parameters for (*t*Bu$_2$PhO)$_2$HpH$_2$ (**2**), (HexO)$_2$HpPt (**3**), HpGeCl$_2$ (**4**), (BuO)$_2$HpPb (**5**) and PyrInd (**6**) are listed in Table 5.3.

From the comparison of σ^{S}_{TPA} values in Table 2 it results that metal free (**2**), Pt (**3**), and Pb (**5**) Hps display the largest values (> $15*10^{-42}$ cm^4 s $phot^{-1}$ mol^{-1}) with respect to the unsubstituted $GeCl_2$ complex **4** and the open structure **6** (< $0.3*10^{-42}$ cm^4 s $phot^{-1}$ mol^{-1}). The different behaviour of the open structure can be understood as a consequence of the larger electronic polarizability for the cyclic complexes $(t Bu_2PhO)_2HpH_2$ (**2**), $(HexO)_2HpPt$ (**3**) and $(BuO)_2HpPb$ (**5**) in comparison to the acyclic form PyrInd (**6**) which possesses a lower extent of electronic conjugation. On the other hand $HpGeCl_2$ (**4**) lacks of any peripheral substituent and this structural feature might determine stronger interaction with other molecules.[97, 98] This phenomenon produces a faster decay of the first excited state (see Table 5.3) and, therefore, leads to a less efficient simultaneous two photon absorption from this state.

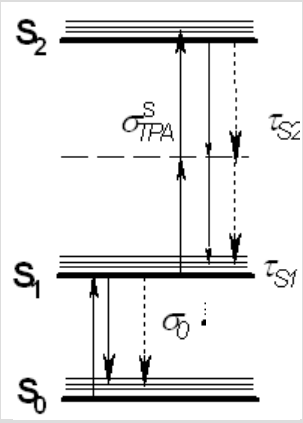

Table 5.3

Compound	σ_0(532nm) cm^2	σ^{S}_{TPA} (532nm) cm^4 s $phot^{-1}mol^{-1}$	τ_{S1}/s	τ_{S2}/s
$(tBu_2PhO)_2HpH_2$ (2)	$0.40*10^{-18}$	$45*10^{-42}$	$3.71*10^{-11}$	$7.9*10^{-13}$
$(HexO)_2HpPt$ (3)	$4.27*10^{-18}$	$25*10^{-42}$	$3.16*10^{-11}$	$2.5*10^{-13}$
$HpGeCl_2$ (4)	$1.05*10^{-18}$	$0.25*10^{-42}$	$0.13*10^{-11}$	$0.2*10^{-13}$
$(BuO)_2HpPb$ (5)	$2.90*10^{-18}$	$19*10^{-42}$	$0.67*10^{-11}$	$1.0*10^{-13}$
Pyr_2Ind (6)	$2.61*10^{-18}$	$0.1*10^{-42}$	$3.05*10^{-11}$	$0.2*10^{-13}$

Figure 5.30 *Model for the excited state dynamics of hemiporphyrazines* ***1-3***, ***5*** *and the open structure* ***6***. σ^{S}_{TPA} *and* τ_{S2} *denote the simultaneous two-photon absorption cross-section for the transition* $S_1 \rightarrow S_2$ *and the lifetime of the second excited singlet state* S_2, *respectively.* ***Table 5.3*** *Optimized values of* σ^{S}_{TPA}, τ_{S1} *and* τ_{S2} *for the fits of the NLO transmission curves at 532 nm generated by dichloro germanium (****1****), metal free (****2****), platinum (****3****), lead (****5****) hemiporphyrazines and the open structure* ***6***. *The mechanism of multiphoton absorption for compounds* ***1***, ***2***, ***3***, ***5*** *and* ***6*** *is depicted in Figure 5.30.*

The nonlinear transmission data of $(BuO)_2HpInCl$ (**1**) cannot be properly fitted both at high and low fluences with the simpler model valid for all other Hps, which does not include an intermediate long-lived excited state (Figure 5.30). This is in accord with the presence of an absorbing excited long-lived (triplet) state for $(BuO)_2HpInCl$ (**1**) as it was verified by means of a pump&probe experiment. The latter finding induced us to consider the model depicted in Figure 5.27, which includes the step of simultaneous two-photon absorption from the first excited triplet state of $(BuO)_2HpInCl$ (**1**). The proposed model was found appropriate for the description of the nonlinear optical behaviour of $(BuO)_2HpInCl$ (**1**) in the whole range of incident fluence.

The models describing the excited state dynamics and multiphoton absorption in Hps, therefore, are found to be substantially different from those of Pcs, their analogues and C_{60} which show, in the nanosecond time regime, a one-photon absorption from an excited triplet state. In case of Hps the simultaneous absorption of two photons from an excited state with very large cross sections renders these systems particularly interesting for photonic applications.

Pyrazinoporphyrazine.[99] Only a limited number of studies about excited state properties of porphyrazines and their OL behavior are present in the literature.[100, 101] This has led us to evaluate the OL properties of a pyrazinoporphyrazine macrocycle, the tetrakis-2,3-[5,6-di(2-pyridyl)pyrazino] porphyrazinato (monoaquo) - Mg(II), [Py8TPyzPzMg(H2O)] (**1**, Fig. 5.31), in DMSO at 532 nm and to measure its excited-state spectrum.

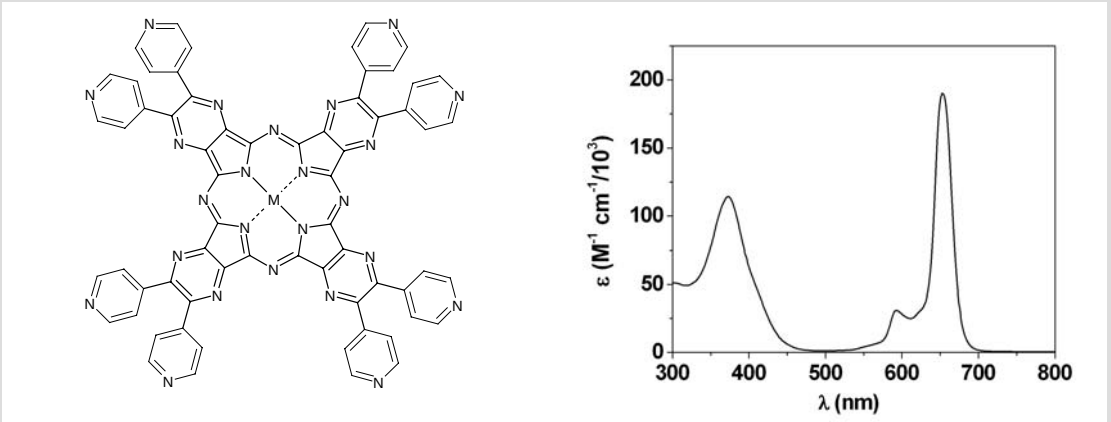

Figure 5.31 *Structure of [Py$_8$TPyzPzMg], (M = Mg) (**1**) and UV-Vis spectrum of **1** in DMSO.*

The excited-state absorption spectrum of **1** has been determined by exciting the macrocycle with nanosecond laser pulses at 532 nm, both at low and high intensities. We have found that the RSA mechanism, which is common for this type of macrocycle, is not the exclusive process responsible for the OL of **1** and that its one-electron reduced form has an important role in the observed nonlinear absorption behavior, particularly at high intensities. For the interpretation of the nonlinear transmission experimental data, a model will be presented that shows the importance of the excited states of both the neutral molecule and its reduced form.

The importance of the photoreduced state in determining the multiphoton absorption processes of porphyrazines was not reported, to our knowledge, in other studies, which shows the importance of the substituents of the porphyrazine skeleton in obtaining new nonlinear optical behaviors.

Complex **1** was synthesized as described elsewhere.[102] DMSO solutions of the complex (0.1 mM) were used for the OL experiments. Nonlinear transmission measurements (NLT) were carried out as usually with 9 ns (532 nm) pulses at 2 Hz in an open-aperture (collecting solid angle is 0.04 str) configuration. The pulse area on the sample was about 0.050 cm^2, and the fluence (F) of the incident beam was varied in the range 10 - 3000 mJ cm^{-2}, corresponding to 2.98 10^{24} - 8.93 10^{26} ph cm^{-2} s^{-1}. Linear optical spectra, recorded with a UV-Vis-NIR spectrometer (Varian Cary 5) before and after the nonlinear transmission measurements, showed the absence of detectable decomposition of the macrocyclic species during the experiments.

In the pump and probe experiments, the sample was excited at different fluences with the same pulses used for the NLT measurements. The white light of a Xe lamp was used as a probe in the range 400-600 nm, which is the spectral region where the excited state absorption of this kind of tetraazaporphyrin macrocycle is usually observed. A notch filter was used to remove the exciting laser line from the probe signal analyzed by the spectrometer. A total of 200-300 shots were averaged to minimize the signal to noise ratio.

We also produced the reduced form of the molecule by an electrochemical reduction using an EG&G model 273A potentiostat-galvanostat. Cyclic voltammetry and macroscale electrolysis experiments were performed with a classical three-electrode setup. Electrochemical experiments were performed in DMSO solutions containing 0.1 M tetrabutylammonium perchlorate as supporting electrolyte, using high purity argon to deoxygenate the solution. Cyclic voltammograms obtained on a saturated solution of the complex at a scan rate of 100 mV s^{-1} indicate a behavior similar to that previously observed with a pyridine solution.[10c] Exhaustive macroscale electrolysis was then performed, with stirring, on a 10 mL DMSO solution containing 2.3 mg of **1** at a potential of 100 mV more negative than the peak potential of the first reduction peak. Electrolysis was stopped when the measured current was less than 10% of the initial value.

The UV-Vis spectrum of the neutral porphyrazine complex **1** in DMSO (Fig. 5.31) closely resembles that normally observed for porphyrazine[14] and phthalocyanine macrocycles,[14] with a Q band in the 600-700 nm spectral region, accompanied by vibronic satellites at shorter wavelengths, and a B band in the near UV region (350-400 nm), both of which are due to π–π^* transitions.[14] The sharp and unsplit Q band is

indicative of a D_{4h} symmetry, as expected for the macrocycle with the central Mg(II). The narrow shape of the band also indicates that the complex is essentially in its monomeric form. This is an important aspect since aggregation phenomena, which can play an important role in OL behavior by modifying, in particular, excited state relaxations, have been frequently observed for the entire class of pyridinopyrazinoporphyrazines, either as freebase ligand[103] or metal derivatives,[102] depending on the particular species and solvent utilized.

The nonlinear transmission behavior of a 0.15 mM solution of **1** in DMSO with linear transmission T_0 = 87% at 532 nm (ε_{532} = 1.718 10^3 M^{-1} cm^{-1}) using 9 ns laser pulses is shown in Fig. 5.32. This figure shows the transmittance vs input fluence (F_{in}) in a logarithmic scale (or the corresponding intensities (I_{in}); Fig. 5.32a) and output fluences (F_{out}) vs F_{in} (or I_{in}; Fig. 5.32b), emphasizing, with the former, the low fluence region and, with the latter, that at high fluence.

As shown in Fig. 5.32a, nonlinear behavior is already observed at low incident fluences (20 mJ cm^{-2}). Two different slopes are found at low and high fluences, which are separated by a plateau in the 240-380 mJ cm^{-2} range. The solution is found to be stable up to fluences of about 2200 mJ cm^{-2}, as confirmed by the UV-Vis spectrum, which appears unchanged after the nonlinear optical measurements. This is a relevant aspect since other phthalocyanine analogues can undergo some decomposition under comparable experimental conditions of irradiation.[80]

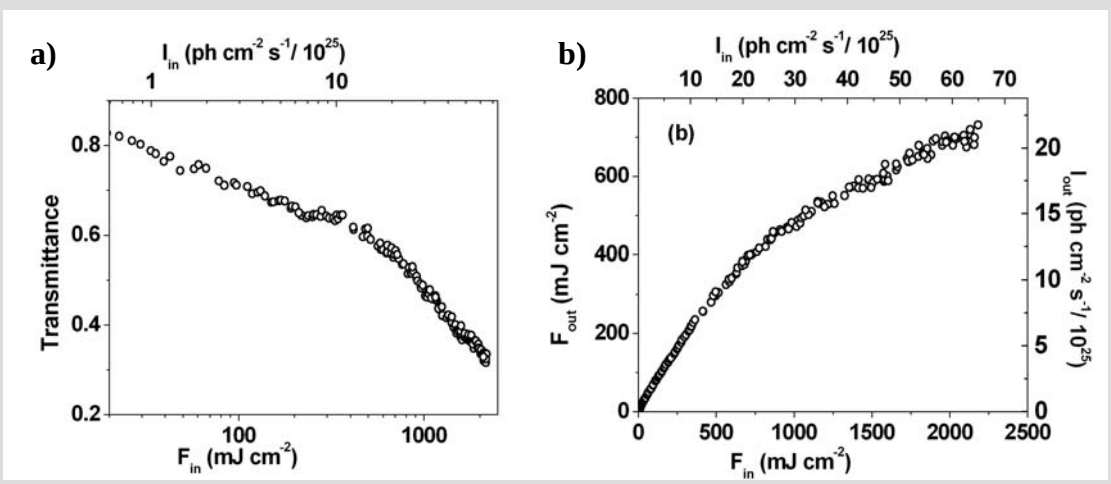

Figure 5.32 *Nonlinear optical transmission of a 0.15 mM solution of* ***1*** *in DMSO at 532 nm.*

The nonlinear transmission behavior of phthalocyanines usually derives from the absorption of an excited triplet state, which is populated by intersystem crossing from an excited singlet state. In these cases, the NLT curves are characterized by a low

nonlinear threshold and by a smooth decrease in transmittance against fluence. The experimental data reported in Fig. 5.32 show a low NL threshold, but as pointed out before, one cannot see a smooth behaviour. For this reason, we measured pump and probe spectra to characterize the spectrum of the excited states involved in the nonlinear behaviour. Pump and probe experiments were performed on a DMSO solution of **1**, probing at different wavelengths and pumping with various fluences at 532 nm.

The excited-state spectra obtained with an incident fluence of 200 mJ cm^{-2} are reported in Fig. 5.33a. They are characterized by two main absorption peaks located at about 450 and 560 nm, whereas photobleaching can be observed in the spectral range below 410 nm and above 590 nm. The structure of the spectrum does not evolve with time and is found to be different from that which is usually observed for the transient spectrum of phthalocyanines, which shows one main peak at about 500 nm that is due to the absorption of the triplet state. Two typical temporal traces of the transient optical absorption of **1** at 450 and 500 nm, following excitation at 532 nm, are reported in Fig. 5.33b. One observes, after the pulse, a transient absorption that lasts several tens of microseconds. In Fig. 5.33a, one can also see that the spectrum is very similar at 0.5 μs and at 80 μs after the pulse.

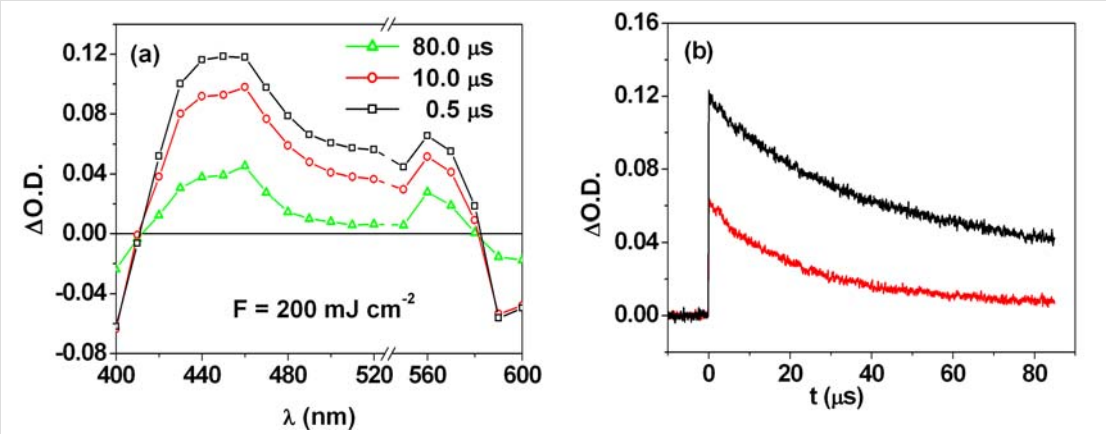

Figure 5.33 *(a) Transient excited spectra of* ***1*** *at F = 200 mJcm^{-2} after 0.5 µs (squares, black line), 10 µs (circles, red line) and 80 µs (triangles, green line) from the excitation pulse. (b) Temporal traces of the optical absorption of 1 in DMSO at 450 nm (black line) and 500 nm (red line) following photoexcitation at 532 nm.*

The influence of the laser beam fluences on the excited-state absorption of **1** was studied performing pump and probe experiments at low (30 mJ cm^{-2}) and high (400 mJ cm^{-2}) fluences, where the two regimes of the NLT data can be better recognized. Furthermore, we analyzed the temporal traces immediately after excitation at 532 nm to

obtain a more clear view of the evolution of the excited spectra absorption. Fig. 5.34 reports excited-state spectra of **1** at 25 and 100 ns after the excitation pulse.

At higher fluences, two absorption maxima at about 450 and 560 nm can be observed, as seen in Fig. 5.33; however, in this case, a larger relative intensity of the 560 nm peak with respect to that of the peak at 450 nm is observed. A quite different behavior is observed at low fluences (Fig. 5.34b). Immediately after the excitation pulse (25 ns), the two absorption peaks previously observed at larger fluences are not present. Rather, the spectrum shows a broad absorption with a maximum at about 470 nm. However, at 100 ns after excitation, the spectrum becomes more similar to that found at higher fluences with two peaks at about 450 and 560 nm.

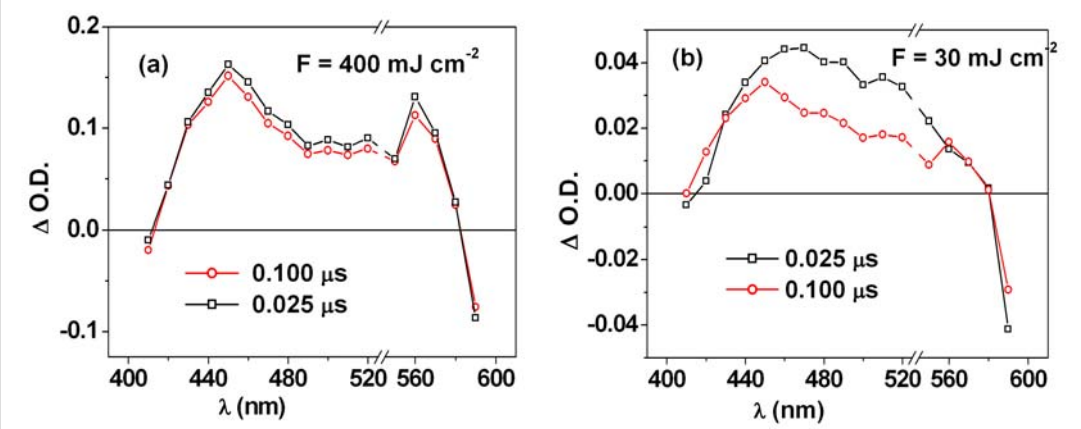

Figure 5.34 *Transient excited spectra of* ***1*** *obtained at (a) F = 400 mJ cm^{-2} and (b) F = 30 mJ cm^{-2} after 25 ns (squares, black line) and 100 ns (circles, red line) from the excitation pulse.*

The above data clearly suggest that two species are present in the observed processes: one that is widely prevalent at low fluences and a second that is mostly present at higher fluences. While the spectrum at low fluences strongly resembles that of the triplet species commonly seen for phthalocyanines, the spectrum observed at high fluences must be assigned to the radical anion ([Py8TPyzPzMg(H2O)]$^{\bullet-}$), as unequivocally indicated by spectroelectrochemical measurements, which show that, in the spectral region between 400 and 600 nm, the monoanion has two characteristic bands with maxima at 454 and 566 nm.[103]

A multiphoton absorption based on a reverse saturable absorption (RSA) mechanism that involves triplet excited states is known to be the active process for structures such as porphyrins, phthalocyanines, and porphyrazines.[40, 41, 48, 80, 100] Our pump and probe data suggest that this is also the case for the present species, [Py8TPyzPzMg(H2O)] (**1**),

at low fluences. However, at high fluences, a charged molecular system, namely, the monoanion [Py8TPyzPzMg(H2O)] $^{\bullet-}$, is the widely dominant species.

To interpret the above data, we developed a model which accounts both for the presence of the triplet state of **1** at low fluences and for that of the monoanion at higher fluences.

A different oxidation state, induced by a photoexcitation process, was already observed in other cases, and usually this state is generated from a long-lived state like a triplet state.[104, 105] Since the presence of a triplet state, in our case, is observed at low fluences, our model must take into account an intersystem crossing from an excited singlet state to a triplet manifold and the formation of the monoanion from the triplet state. However, if we consider that the monoanion is formed from the lowest state of the triplet manifold, we are not able to fit the experimental data. The situation is different if we consider that the monoanion is produced when the molecule is in the first excited state of the triplet manifold.

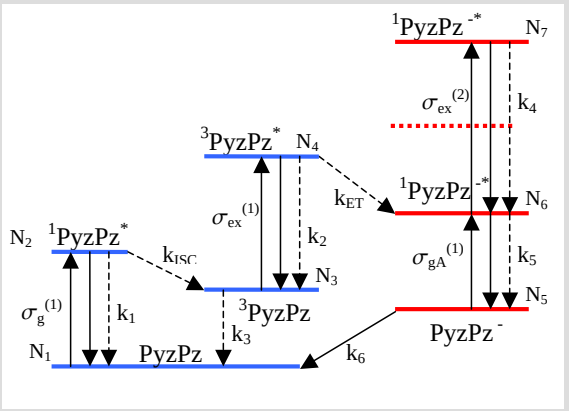

Figure 5.35 *Schematic energy level diagram for triplet absorption and photoinduced electron transfer (ET) process of [Py$_8$TPyzPzMg(H$_2$O)] upon 532 nm excitation.*

$\sigma_g^{(1)}$ [cm^2]	6.57 10^{-18}	k_{ET} [s^{-1}]	3.02 10^8
k_1 [s^{-1}]	1.49 10^9	τ_{ET} [ns]	3.3
τ_1 [ns]	0.67	$\sigma_{ex}^{(2)}$[cm^{4}ph^{-1}mol^{-1}]	6.25 10^{-42}
k_{isc} [s^{-1}]	8.00 10^9	k_4 [s^{-1}]	1.50 10^{12}
τ_{ISC} [ns]	0.12	τ_4 [ps]	0.66
$\sigma_{ex}^{(1)}$ [cm^2]	3.60 10^{-17}	$\sigma_{gA}^{(1)}$ [cm^2]	4.74 10^{-17}
k_3 [s^{-1}]	5.00 10^5	k_5 [s^{-1}]	1.00 10^{11}
τ_3 [µs]	2.0	τ_5 [ps]	10
k_2 [s^{-1}]	1.10 10^{10}	k_6 [s^{-1}]	3.30 10^4
τ_2 [ps]	90	τ_6 [µs]	30

Table 5.4*. Values of the fitting parameters for nonlinear absorptions of* ***1****.*

Fig. 5.35 shows the energy level diagram and the relevant parameters for the dynamics. In this case, we find a good fit of the experimental data by taking into account a two-photon absorption for the monoanion since a one-photon excitation does not produce the steep variation in the transmittance at high fluences, as found in the experimental data. Fig. 5.36 shows the fit obtained by using the values of the fitting parameters that are reported in Table 5.4. The fitting results are quite good at both low and high fluences as shown in Fig. 5.36. One finds that the important excited state absorption at low intensities is the triplet-state absorption (RSA process), whereas at high intensities the two-photon absorption (TPA process) of the monoanion is the relevant process.

One should note that the cross section for the two-photon absorption from the excited state ($\sigma_{ex}(2)$) of the monoanion is very large, since it is four to five orders of magnitude larger than that usually observed for this type of nonlinear absorption when the initial state is a ground state. However, cross sections with such large values are known to be possible for excited states since they are very polarizable.[27]

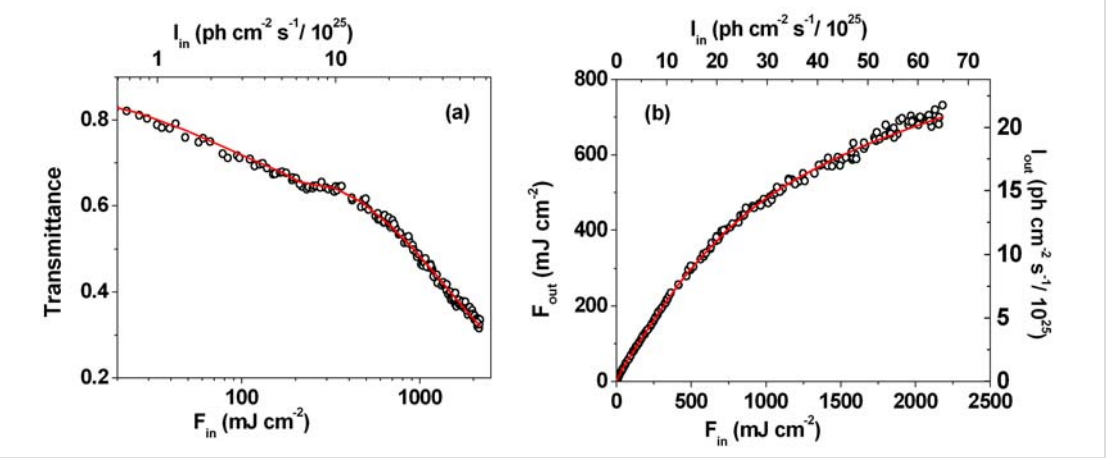

Figure 5.36 *Fitting of the experimental nonlinear transmission data of 0.15 mM DMSO solution of* ***1*** *(continuous red lines)*

The behavior of the monoanion, obtained by an electrochemical reduction at controlled potential in DMSO, was also examined by NLT measurements. The NLT experimental data of this solution at 532 nm are presented in Fig. 5.37.

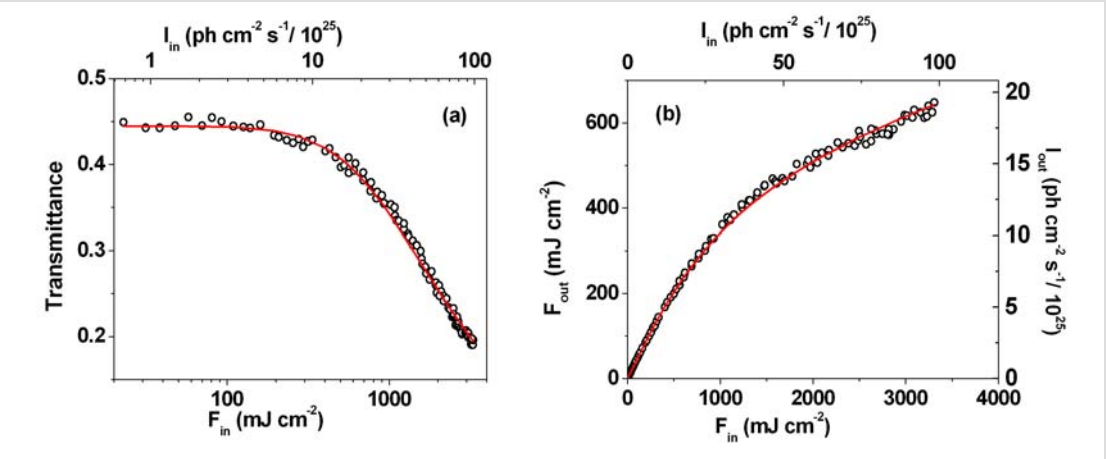

Figure 5.37 *Nonlinear optical transmission measurement of a solution of the monoanion of* ***1*** *at 532 nm.*

The fit of the curve can be obtained by a simple two-photon absorption from the first excited state using the same levels for the radical anion reported in Fig. 5.35. The values of the fitting parameters are reported in Table 5.5, where one can note the same value for the two-photon absorption cross section (σ_{ex}) 6.25 10^{-42} cm^4 ph^{-1} mol^{-1}) and very similar parameters for the other processes. This result is of further support to the model

proposed here (Fig. 5.35) for the dynamics of the neutral molecule. In many experiments reported in the literature, the concentration of the solutions used for the measurements is high and the linear transmission at 532 nm is low. In this situation, it is difficult to observe the processes which are activated at high intensities because of the prevalence of those activated at low intensities. We have observed this situation in the present case.

$\sigma_{gA}^{(1)}$ [cm^2]	3.87 10^{-17}	$\sigma_{ex}^{(2)}$ [cm^{4}ph^{-1}mol^{-1}]	6.25 10^{-42}
k_5 [s^{-1}]	2.00 10^{11}	k_4 [s^{-1}]	1.5 10^{12}
τ_5 [ns]	0.5	τ [ps]	0.66

Table 5.5 *Values of the fitting parameters for the nonlinear absorption process of the monoanion.*

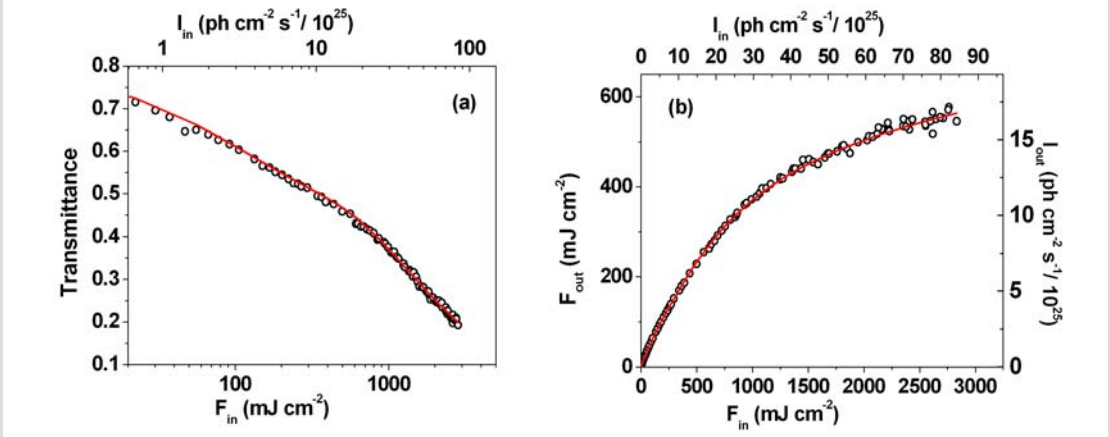

Figure 5.38 *Nonlinear optical transmission at 532 nm of a solution of* ***1*** *in DMSO with a linear transmittance of T = 75%.*

In Fig. 5.38, we report the NLT of a concentrated solution of complex **1** with a linear transmission of T_0 = 75% at 532 nm. In this case, the plateau observed for the low-concentration solution is not present and the most important contribution to the nonlinear absorption of **1** comes from the triplet excited state absorption. In fact, a good fit can be obtained by using the same parameters reported in Table 5.4, changing only the concentration of the solution. One can see that, by increasing the concentration, the contribution from the monoanion is reduced to the very high-intensity region above 900-1000 mJ cm^{-2}. This shows that, at high concentrations, the RSA mechanism is the most important process responsible for the observed nonlinear response of **1**, in line with the expectation for this kind of molecule; however, the presence of the monoanion must be considered for a more complete description of its nonlinear behavior, particularly at higher intensities. The results obtained with [Py8TPyzPzMg(H2O)] suggest a way to modify the tetrapyrrolic system, which shows nonlinear absorption properties depending not only on the triplet excited states but also on charged states.

This can be particularly interesting in the nanosecond time regime for which long-lived excited states are important.

Functionalized distyrylbenzene analogs.[106] Nonlinear otpical molecular switches represent key components for the control and processing of information for future technology. It has been shown that the functionalized distyrylbenzene (DSB) derivative 1 reported in Fig. 5.39 exhibits the switching of its multiphoton absorption properties upon Zn^{2+} complexation.[107] This result encouraged the preparation and study of chromophores 2 and 3 in which a styryl(vinylpyridyl)benzene (SVPB) structure is part of a tris(2-pyridylmethyl)amine-based receptor (TPMA), known for its Zn^{2+} binding characteristics and whose coordination chemistry has been studied in great detail.[108-111]

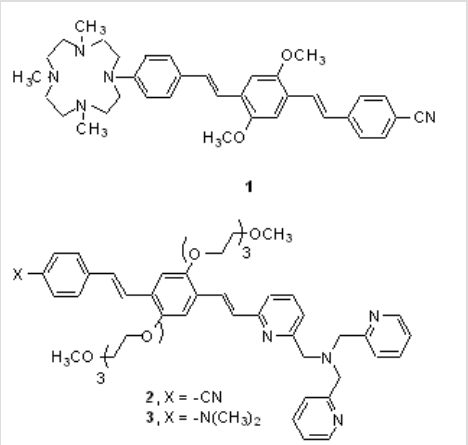

Figure 5.39 *Molecular structures of compounds* ***1, 2*** *and* ***3****.*

We have found that, upon complexation with Zn^{2+}, 2 and 3 change their linear absorption, as in the case of 1, thus allowing a control of their multiphoton absorption properties. It is worth noting that a variation in the linear absorption translates into a different excited state population and, therefore, into a different sequential multiphoton absorption. In the case of 2 and 3, a higher NL transmission was recorded in the absence of Zn^{2+}. In DSB 1, instead, the same variation was found in the presence of Zn^{2+}. The effect that we observe for 2 and 3 is also opposite to that reported by Pond and coworkers[112] in which a lower TPA activity is observed upon Mg^{2+} complexation.

The results presented herein could also be of interest in view of understanding the mechanism of NL absorption changes induced by ion complexation in the frame of bio-imaging,[112-116] although other important factors, such as protonation equilibria or solvent effects,[117] should be considered.

Compounds 2 and 3 (Fig. 5.39), have an electron-donor amine or an electron-acceptor cyano substituent located at position 4 of the side benzene ring of the SVPB structure. It is reasonable to assume that complexation with Zn^{2+} induces a higher localization of the electrons of the TPMA receptor and, in particular, of the π electrons of the pyridine moiety which is part of the SVPB structure, thus making this pyridine ring a stronger acceptor. This change should, at least partially, affect the intramolecular charge

distribution of the molecules both in their ground and excited states and could be useful for obtaining a variation of their NLO activity. In this connection, Pond and coworkers have demonstrated in a recent publication[112] that a similar design scheme can be employed for the development of NL molecular sensors for use in two-photon laser scanning applications.

SVPBs 2 and 3 were synthesized as reported in Ref. 106. Solutions of metal complexes 2-Zn^{2+} and 3-Zn^{2+} for spectrophotometric measurements were prepared in CH_3CN by mixing SVBP 2 or 3 with 2 equiv. of $Zn(ClO_4)_2$ hexahydrate at room temperature. The absorption spectra of CH_3CN solutions of 2 and of 2-Zn^{2+} are reported in Fig. 5.40a. The corresponding spectra of 3 and 3-Zn^{2+} are shown in Fig. 5.40b.

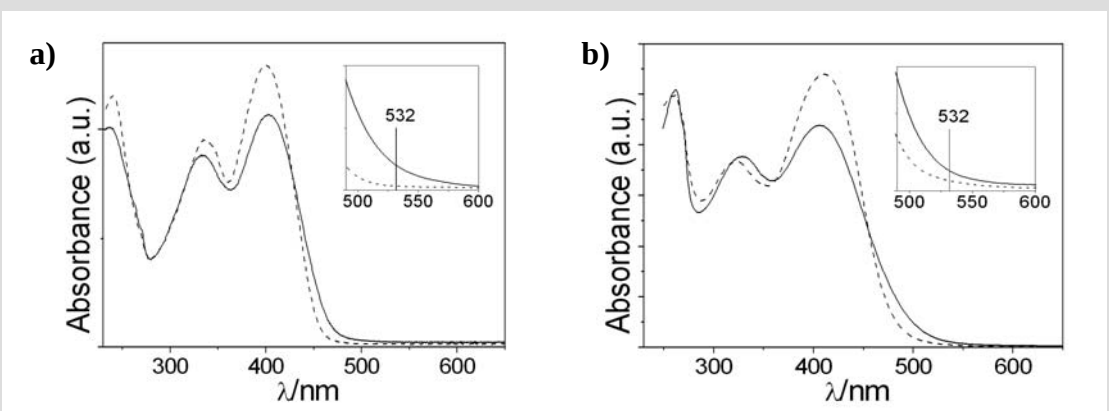

Figure 5.40 *a) Absorption spectra of 2 (dashed line) and 2-Zn^{2+} (continuous line) 1.21×10^{-3} M in CH_3CN. Inset shows an expanded part of the spectrum around 532 nm. b) Absorption spectra of 3 (dashed line) and 3-Zn^{2+} (continuous line) 1.26×10^{-3} M in CH_3CN. Inset shows an expanded part of the spectrum around 532 nm.*

The spectra of 2 and 3 show that a variation of the linear absorption follows the formation of the Zn^{2+} complex, as it is clear in the low energy part of the spectrum around 400 nm, where 2-Zn^{2+} and 3-Zn^{2+} have a weaker absorption than their uncomplexed counterpart. This can be ascribed to a reduced number of backbone π electrons as a consequence of the participation of the SVPB pyridyl ring to Zn^{2+} complexation. A similar effect was also observed earlier for a DSB-based receptor for Mg^{2+}.[112] However, it is interesting to note that a stronger absorption of the Zn^{2+} complexes is present in the wing of the 400 nm band toward longer wavelengths and that, therefore, at 532 nm 2-Zn^{2+} and 3-Zn^{2+} absorb slightly more than 2 and 3. This condition is fundamental for obtaining a variation of sequential multiphoton absorption[107] because a stronger linear absorption makes it possible to populate the first excited state easier, from which further absorptions may occur.

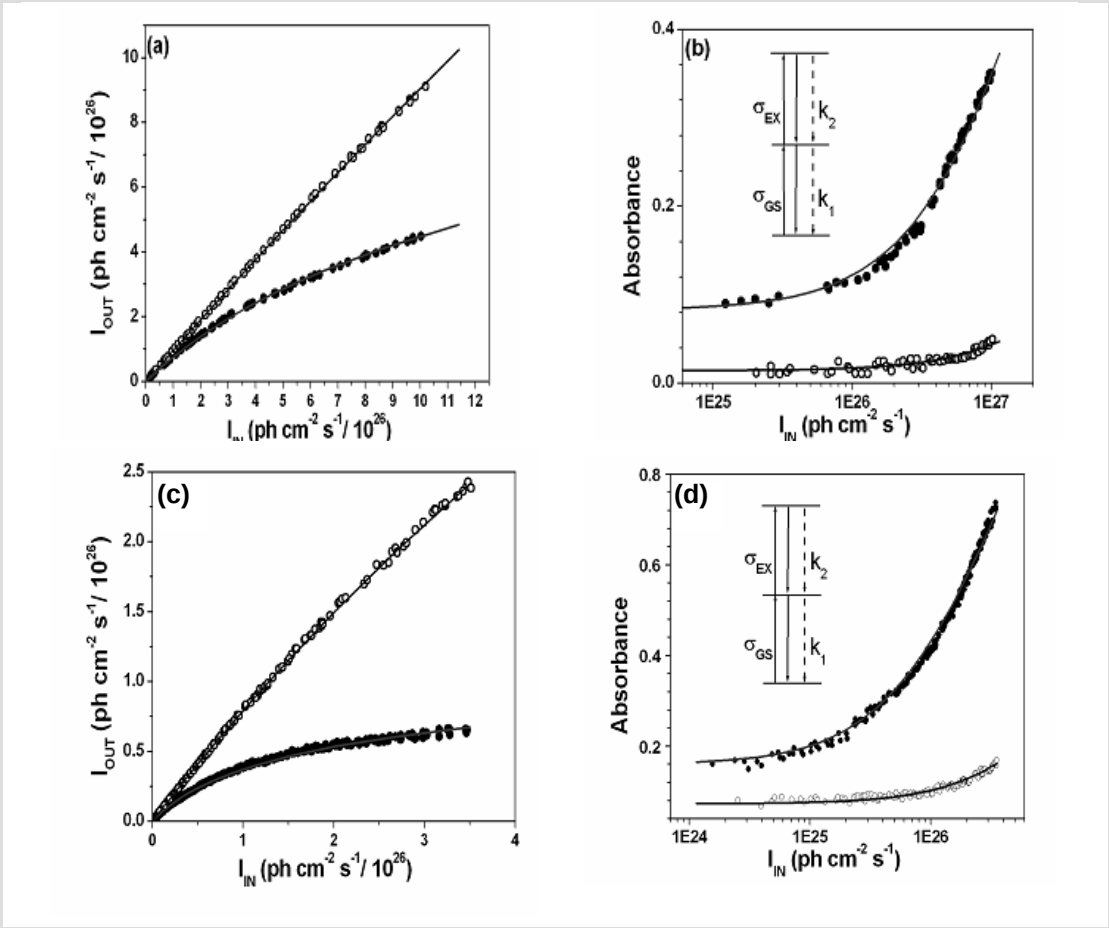

Figure 5.41 *a-b) NL absorption at 532 nm of 2 (○) and of 2-Zn^{2+} (●) 1.21×10^{-3} M in CH_3CN. Solid lines are the results of model calculations (see text) whereas the inset shows the model parameters (absorption cross sections σ_{GS} and σ_{EX} and decay rates k_1 and k_2), whose values are reported in Table 5.4. (a) Recorded output intensities versus input intensities; (b) same data as in (a) but plotting the NL absorption as a function of input intensities in a logarithmic scale. c-d) Corresponding data of a-b) but for 3 (○) and 3-Zn^{2+} (●) with a concentration of 1.23×10^{-3} M in CH_3CN.*

NL absorption measurements at 532 nm of 2, 3, 2-Zn^{2+} and 3-Zn^{2+} are shown in Fig. 5.41a and 5.41c, respectively, where a lower output intensity is determined by an intensity dependent absorption. One finds that the NL absorption is very important only for 2-Zn^{2+} and 3-Zn^{2+}, whereas the almost linear behaviour of 2 and 3 confirms their poor NL activity. This shows that an enhancement of the NL absorption can be obtained upon complexation. Fig. 5.41b and 5.41d report the same experimental data of Fig. 5.41a and 5.41c, respectively, but directly showing the absorption as a function of input intensities in a logarithmic scale. These plots allow a better inspection of the low intensity part of the data and are useful for controlling the model fitting at these intensities as well. One also finds that 3-Zn^{2+} displays a larger non-linearity than 2-Zn^{2+}, pointing out the important role of the functional groups in the SVPB structure.

Explanation of the observed results could be provided by considering the excited state population dynamics of the molecules. In fact, the interaction between light and matter can be described within a density matrix approach, and when the laser pulse duration is longer than the relaxation processes, as in the present case (see below), one can use the diagonal part of the density matrix, which corresponds to the populations of the states of the system.[1] Solutions of the rate equation for the dynamics of these populations can be obtained according to Ehlert et al.[11] The model that has been used for the experimental data description is reported in the inset of Fig. 5.41b. The first excitation to be considered is in fact related to the linear absorption, with an absorption cross section σ_{GS}, which depends on the linear optical susceptibility, usually larger than higher-order susceptibilities. After the first one-photon excitation, a one- or two-photon absorption from the excited state can occur.[27] We have found that a one-photon absorption, with an absorption cross section σ_{EX}, is sufficient for fitting the experimental data. Four parameters (see inset of Fig. 5.41b and Table 5.4) are needed for the fitting. Among them, σ_{GS} is determined from the experimental linear absorption spectrum, whereas the decay time for the second excited state ($\tau_2 = k_2^{-1}$) can be considered very fast (of the order of ps) as it is usually observed for organic molecules.[118] These values and those of the other two parameters (σ_{EX} and the decay rate for the first excited state k_1) that are obtained from the fitting of the experimental data, are reported in Table 5.4.

	σ_{GS}/cm^2	σ_{EX}/cm^2	k_1/s^{-1}	k_2/s^{-1}
2	2.2×10^{-19}	1.6×10^{-16}	5.0×10^{10}	1.0×10^{13}
2-Zn^{2+}	1.3×10^{-18}	4.0×10^{-16}	5.0×10^{10}	1.0×10^{13}
3	1.1×10^{-18}	5.5×10^{-17}	8.0×10^{9}	1.0×10^{12}
3-Zn^{2+}	2.4×10^{-18}	3.7×10^{-16}	8.0×10^{9}	1.0×10^{12}

Table 5.4 *Parameters for the model of the excited states dynamics.*

It is worth noting that fitting of the data strongly depends on the variation of the cross section for the one-photon excitation from the ground state, which is experimentally evaluated from the UV-Vis spectra. This shows the importance of the population of the first excited state from which the second one-photon absorption starts. Good fittings have been obtained both in the high (Fig. 5.41a and 5.41c) and in the low (Fig. 5.41b and 5.41d) intensity regions, indicating that the TPA model gives a good description of the excited states dynamics that contribute to the NLO properties of the investigated molecules.

5.6 Optical limiting properties of AuNP:Zinc phthalocyanines blend.[119]

Nanostructured materials provide a wide range of powerful tools to science and technology. If, on one hand, the "nano" size implies that such materials can have interesting functional properties, on the other hand it also implies that they have high surface/interface energy due to the large number of surface/interface atoms, which represents a limitation to practical applications.[120] Nonlinear optical applications of metal nanoparticles represent an example of such pros and cons, since AuNP and AgNP have large polarizability, i.e. huge nonlinear optical properties, but undergo to a fast and irreversible damaging.[44, 121-131]

Gold and silver nanoparticles are well known as excellent optical limiters with nanosecond, picosecond and femtosecond laser pulses, exploiting a mechanism to date not completely understood.[44, 132-144] The most part of investigations on metal nanoparticles pointed out the free carriers multiphoton absorption processes,[44, 127, 135, 137, 138, 141, 142, 144] the particles fragmentation due to electrons photoejection[128, 142, 145, 146] and, interparticle electronic coupling in particles aggregates,[136, 137, 147, 148] as possible optical limiting (OL) mechanisms. Nonlinear scattering was conjectured at the origin of the strong optical limiting of gold and silver nanoparticles in few cases.[133, 138-140] However the main part of nonlinear spectroscopy studies on metal nanoparticles did not found differences between open aperture and closed aperture measurements, which excluded nonlinear scattering as the prevalent mechanism for optical limiting of metal nanoparticles.[44, 127, 135-138, 141, 142, 144, 147, 148]

Independent on the mechanism, all the previous investigations on optical limiting properties of gold and silver nanoparticles pointed out the following aspects: *i*) the OL performances are amongst the best ones ever measured; *ii*) big nanoparticles are better optical limiters than small ones *iii*) nanoparticles loose limiting efficiency after few laser pulses due to their fragmentation, that is more rapid and has a lower threshold when particles size is big; *iv*) nanoparticles have good optical limiting performances for wavelengths resonant with the surface plasmon absorption as well as with the interband transitions.

In case of gold nanoparticles, a large number of papers exist about various nonlinear optical properties (cfr. paragraph 2.16) or about charge transfer processes in organic molecules blended with gold nanoparticles like fullerenes,[5, 7, 128, 149-151] porphyrins and fullerenes,[152] β-carotene[153] or Er^{3+} ions,[154] while few authors considered optical limiting

of gold nanoparticles in presence of organic chromophores with multiphoton absorption properties. For instance it has been reported that gold nanoparticles conjugated to a fullero-pyrrolidine by a disulphur bridge showed better optical limiting preformances than the isolated metal nanoparticles, with laser pulses at 532 nm (9 ns), which was compatible with an energy transfer from the AuNP to the fullerenes of about 60%.[9] An enhancement of optical limiting has been found also for AuNP conjugated to fullerenes – pyridine derivatives.[155, 156]

Here we report of a gold nanoparticles (AuNP) and zinc phthalocyanines (Pc) solution in tetrahydrofuran (THF) that joins both the high optical limiting performances of AuNP and the extremely long durability under laser irradiation of common organic optical limiters. As a consequence of their interaction, the OL properties of the AuNP-Pc blend are remarkably better than for AuNP or Pc alone. We found that the origin of these enhanced OL performances resides in the ability of the gold nanoparticles in the AuNP-Pc blend to self – heal during the laser pulse irradiation. This finding is interesting since, in general, the structural instability of nanostructured materials upon their utilisation can be surmounted by reducing the interface energy or by designing a nanomaterial able to self heal or to regenerate during the usage itself.[157-160] In our case the AuNP-Pc blend represents a rare example of a functional nanomaterials that self – heals during the use itself, exploiting a promising mechanism able of opening new ways to photonics and nanotechnology.

The optical limiting (OL) and nonlinear transmittance (NLT) measurements were carried out with 9 ns pulses of a Nd:YAG laser (Quantel YG980E) at its duplicated frequency (532 nm) at 1 Hz. Measurements of the incident and transmitted energies were recorded pulse by pulse with a pyroelectric detector (Scientech SPHD25) and a calibrated photodiode. A half-wave plate and a cube polarizer were used for controlling the pulse energies. Glass cuvettes with 2 mm optical path length were used for the THF solutions. The laser beam diameter on the sample was in the order of 2.5 mm. Associated linear optical spectra were recorded before and after the NLO transmission measurements. UV-Vis spectra were recorded with a Varian Cary 5 spectrometer in 2 mm optical path quartz cells.

Gold nanoparticles were obtained by laser ablation synthesis in liquid solution (LASiS), as previously reported.[161-164] The laser ablation was carried out with Nd:YAG Quantel YG981E laser pulses at 1064 nm (9 ns) focused with a 10 cm focus lens on a gold plate

placed at the bottom of a cell containing THF. Since no ligands are needed by LASiS to obtain stable particles in THF up to several days, no chemicals were present in solution. Particles were obtained with pulses of about 10 J/cm^2 at a 10 Hz repetition. The target was a plate of 99.9% gold and we used spectroscopic grade THF.

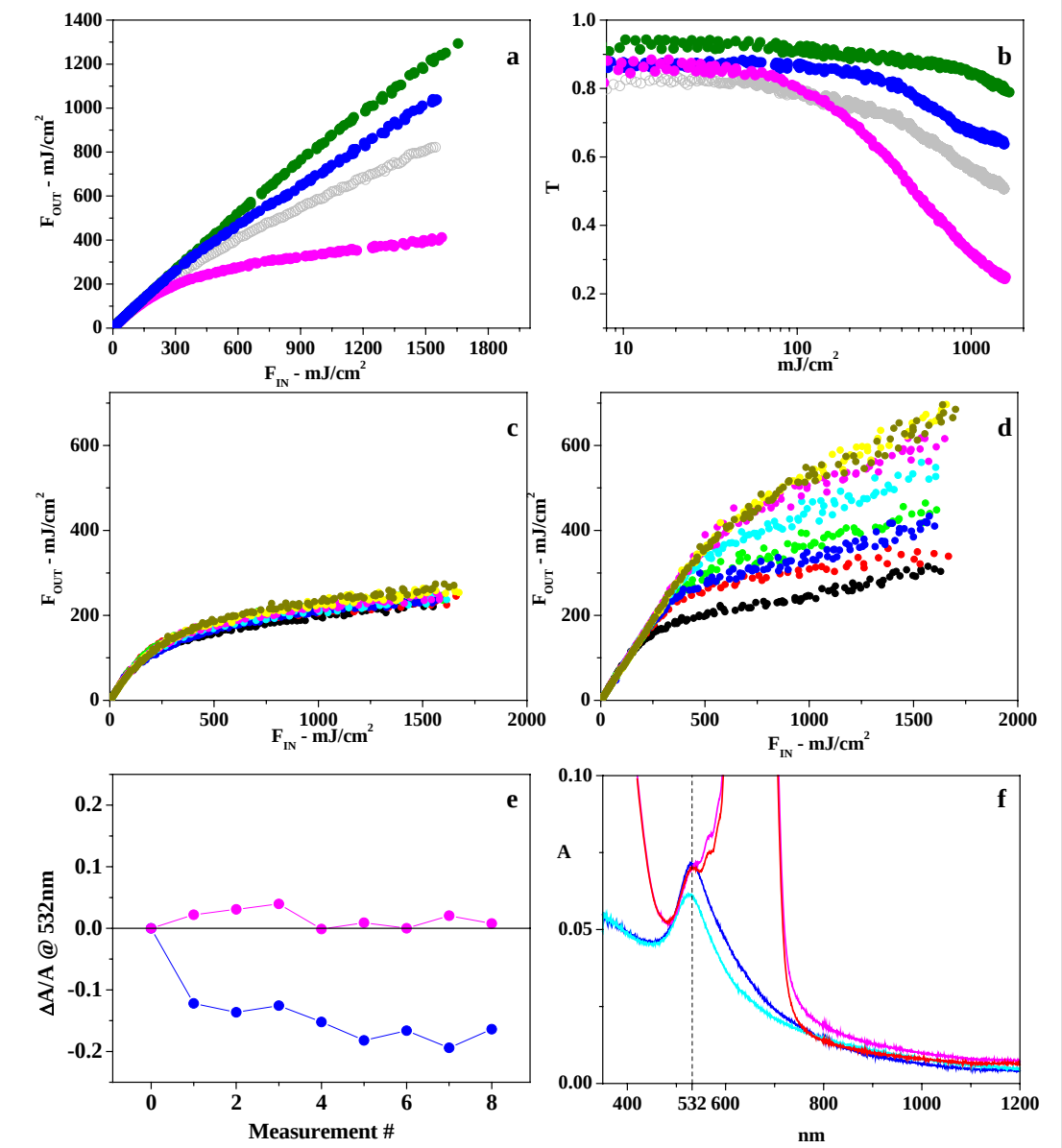

Figure 5.42 *a-b) Optical Limiting and Non Linear Transmittance curves with 532 nm - 9 ns laser pulses for Pc (green circles), AuNP (blue circles) and the AuNP-Pc blend (violet circles). Grey open circles correspond to the sum of the optical limiting contributes of Pc plus AuNP solutions. Linear transmittance at 532 nm equal to 85% for both AuNP and AuNP-Pc solutions and to 99% for Pc solution; Pc concentration of 3.1 10^{-5} M, gold particles concentration of 4 10^{-10} M and average radius of 8 nm estimated by Mie – Gans fitting model. c-d) Optical Limiting curves obtained for 8 consecutive measurements on the same AuNP-Pc (c) and AuNP (b) solutions. The colour sequence is: black = #1, red = #2, blue = #3, green = #4, cyan = #5, violet = #6, yellow = #7, brown = #8. e) Differential linear absorbance at 532 nm of the AuNP-Pc (violet) and AuNP (blue) solutions of fig.1c-d compared to the OL measurement number. f) UV – vis spectra before and after the 8 OL measurements for AuNP (blue and cyan lines respectively) and for AuNP-Pc (violet and red line respectively).*

The Zinc phthalocyanine was synthesized as described in Ref. 119. The AuNP-Pc blend was obtained mixing the AuNP solution with the Pc solution in THF and performing the measurements within one hour after the mixing.

Fig. 5.42a-b report the OL and NLT results for three different solutions: AuNP-Pc blend (violet circles), bare AuNP (blue circles) with the same linear transmittance of the blend and Pc (green circles) with the same concentration as in the blend. The good OL of the blend is evident, despite the linear transmittance of the solution was only 85% at 532 nm, and it is remarkably better than the sum of the two single contributes of bare AuNP and Pc (grey circles).

In Fig. 5.42c and 5.42d we compared 8 consecutive cycles of OL carried out on 0.8 ml of the AuNP-Pc blend and of bare AuNP respectively, continuously recirculating the same solution in the cell during all the 8 measurements. In this case the good durability of the AuNP-Pc blend is self – evident, as well as the fast degradation of the optical limiting performances for bare AuNP. This behaviour is directly correlated with the linear absorbance at 532 nm after each OL run, because the AuNP-Pc blend maintains almost the same value while the AuNP solution undergoes to a progressive reduction of the absorption, as shown in Fig. 5.42e. In the UV – Vis spectra of Fig. 5.42f, relative to the solutions before and after the 8 OL cycles, one can see that the AuNP spectrum underwent to remarkable changes, while the blend spectrum underwent only minor alterations.

The zinc phthalocyanines are known to be very good optical limiters exploiting a reverse saturable absorber mechanism,[41] hence we made pump and probe (P&P) measurements to check the role of the Pc excited states absorptions on the enhanced performances of the AuNP-Pc blend. In the pump and probe experiments, the samples were excited at a fluence of 225 mJ/cm^2 with the same 9 ns pulses of a Nd:YAG laser at 532 nm used for the OL measurements. The white light of a W lamp was used as a probe. A digital oscilloscope (1 GHz, Le Croy LC564A) recorded the transient signals observed with a Jobin Yvon Horiba TRIAX 320 spectrometer, equipped with a Hamamatsu phototube (R2257), in the range 400 - 850 nm. The spectral region where the excited state absorption of the Zinc phtalocyanine is usually observed is comprised between 400 and 600 nm, while the fluorescence signal of the B band of the Pc is comprised in the 625 - 825 nm region. The fluorescence signal was corrected for the response curve of the experimental set up. A notch filter was used to remove the

exciting laser line from the probe signal analyzed by the spectrometer. A total of 50-75 shots have been averaged to minimize the signal to noise ratio and the irradiated solution was replaced for each point.

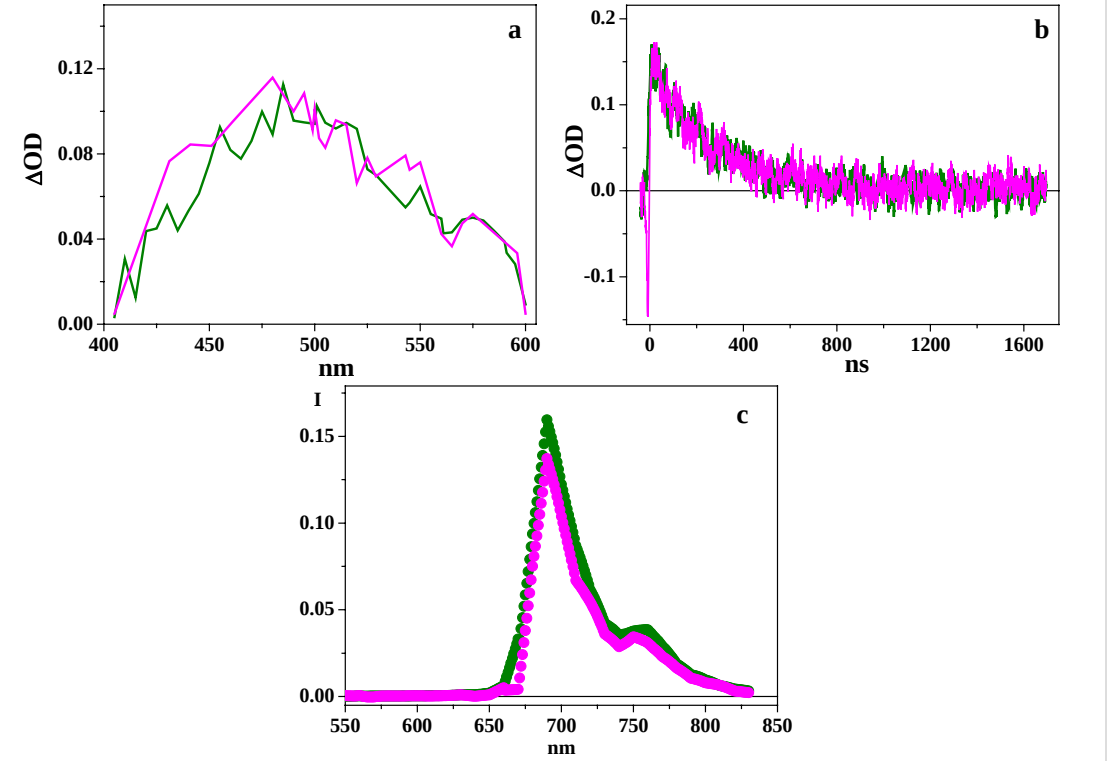

Figure 5.43 *P&P measurements at a fluence of 225 mJ/cm^2 and 532 nm on the same AuNP-Pc (violet line) and Pc (green line) solutions as in figure 1. a) P&P spectrum in the region of excited state absorption of the Zinc phtalocyanine collected after 100 ns after the pump laser pulse. b) P&P trace at 500 nm. c) The fluorescence emission spectra of the B band of the Pc for AuNP-Pc (violet circles) and Pc (green circles) collected at 0 ns after the pump laser pulse.*

P&P spectra of the first Pc triplet excited state do not show any difference between the molecule alone and the AuNP-Pc blend (Fig. 5.43a-b). Also the Pc fluorescence signal obtained by P&P measurements does not indicate an increase in the population of singlet excited states of the phthalocyanine that are responsible for the fluorescence emission (Fig. 5.43c). These results stress out that the nonlinear spectroscopic behaviour of the Pc is essentially independent on the presence of AuNP. This means that the OL enhancement in the case of AuNP-Pc blend is not originated by energy transfer or light harvesting from the AuNP to the zinc phthalocyanine, despite the major light absorber at 532 nm are the gold nanoparticles.

This finding is fully supported by the OL measurements of fig. 5.42c-d, carried out on 0.8 ml of solution of AuNP-Pc and AuNP while recirculating them in the cell. In the case of the first run, concerning not yet irradiated solutions, we found that the optical

limiting contribution of the bare AuNP joined to the contribution of the Pc alone are exactly matching the result of the AuNP-Pc blend (Fig. 5.44), while in the following runs the OL performances of the bare AuNP solution undergo to a sensible worsening and the two contributes do not match anymore (Fig. 5.42c-d).

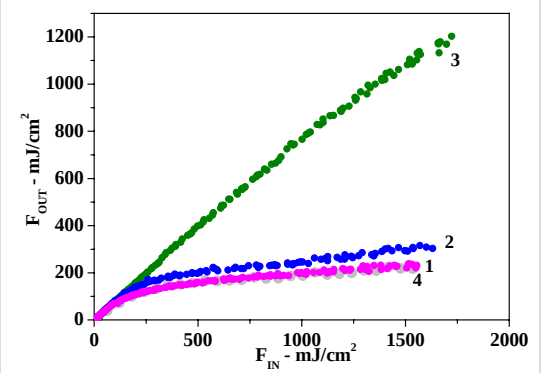

Figure 5.44 *OL measurements carried out on not irradiated 0.8 ml of AuNP-Pc blend (violet circles - 1), of bare AuNP (blue circles - 2) and bare Pc (green circles - 3) continuously recirculating the same solution amount in the cell during all the measurement. Grey circles (4) correspond to the sum of the optical limiting contributes of Pc plus AuNP solutions and overlap very well with the AuNP-Pc blend curve.*

The remarkable difference between OL properties of the AuNP-Pc blend, bare AuNP (with the same linear transmittance at 532 nm) and bare Pc (with the same concentration as in the blend) can be further inspected in the experiment reported in Fig. 5.45a, concerning the non linear transmittance signal for a sequence of 250 laser pulses at a fixed fluence of 1100 mJ/cm^2, while recirculating 0.8 ml of solution in the optical cell. Due to the low Pc concentration, one can clearly see that the Pc optical limiting at 532 nm is poor compared to bare AuNP and AuNP-Pc and that both AuNP and AuNP-Pc initially have the same transmittance at 1100 mJ/cm^2. However, while for bare AuNP the performances are progressively degraded by laser irradiation, for the AuNP-Pc blend only a minor degradation after 250 laser pulses was observed.

We also used a sequence of 532 nm laser pulses at a fixed fluence of 1100 mJ/cm^2 to study the role of Pc concentration on the blend. We found that the performances after 350 shots are entirely retained for an AuNP:Pc ratio above 1:2000 (fig. 5.45b) and that the preservation effect is still present even for an AuNP:Pc ratio as low as 1:500. As found for ordinary OL measurements, also in this case the preservation of the OL performances is tied with the preservation of AuNP size and, then, of the linear absorbance at 532 nm (fig. 5.46c). Moreover, the comparison of the UV-Vis spectra before and after the measurements show that the Pc amount in solution was partially reduced during the irradiation process (fig. 5.46a-b).

TEM measurements performed on the AuNP solution before irradiation (Fig. 5.45c) and on the solutions irradiated with 250 pulses of bare AuNP (fig. 5.45d) and of AuNP-Pc (fig 5.45e) evidenced remarkable differences in the particles size distributions. Samples

for TEM analysis were prepared by depositing some gold colloid drops on a copper grid covered with a holey carbon film and drying them at room temperature. TEM images were collected at 300 kV with a JEOL JEM 3010 microscope equipped with a Gatan multiscan CCD camera, model 794.

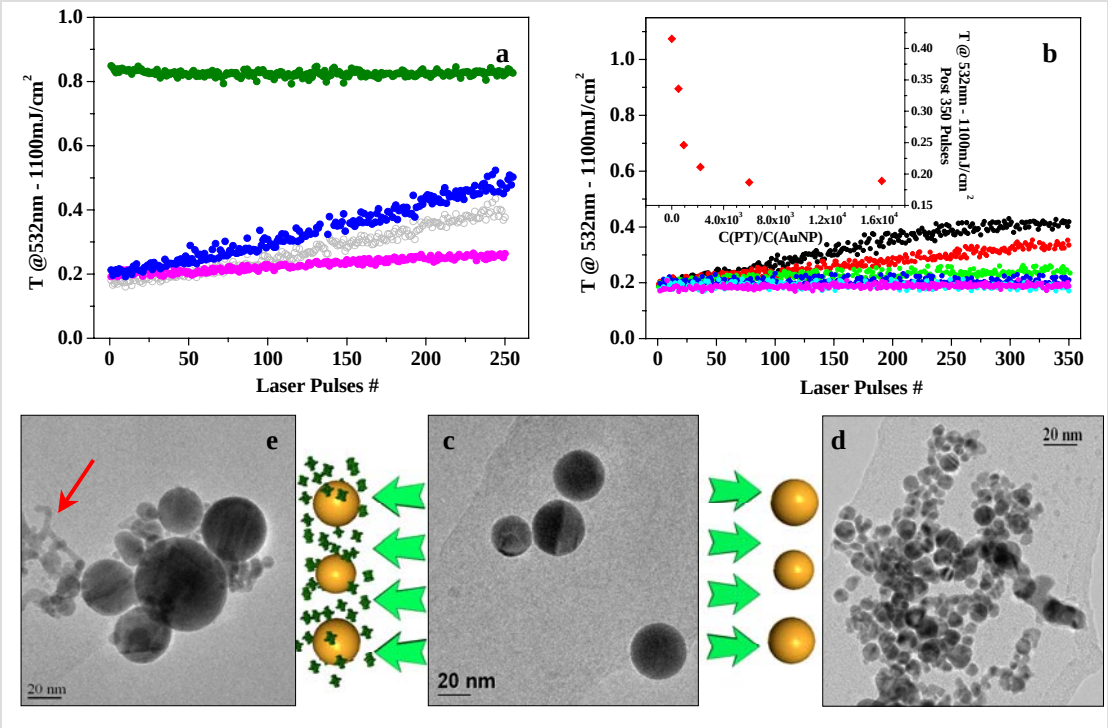

Figure 5.45 *a) Non Linear Transmittance at 532 nm for 250 consecutive laser pulses with fluence 1100 mJ/cm^2 on the same solutions as in figure 1: Pc (green circles), AuNP (blue circles) and the AuNP-Pc blend (violet circles). Grey open circles correspond to the sum of the optical limiting contributes of Pc plus AuNP solutions. b) Non Linear Transmittance at 532 nm for 350 consecutive laser pulses with fluence 1100 mJ/cm^2 on gold nanoparticles solutions with increasing AuNP:Pc ratio: black circles = 1:0, red circles = 1:515, green circles = 1:927, blue circles = 1:2214, cyan circles = 1: 5974, violet circles = 1: 16222. Inset: Non Linear Transmittance values after 350 pulses for the different AuNP:Pc ratios. Representative TEM images of the AuNP before (c) the measurement at 532 nm for 250 consecutive laser pulses with fluence 1100 mJ/cm^2 and after it in case of bare AuNP (d) and of the AuNP-Pc blend (e). The red arrow in (e) indicates some AuNP partially melted with irregular shape.*

In absence of Pc, the AuNP size is readily reduced by laser irradiation with respect to non irradiated samples. In presence of Pc the average size is smaller than for non irradiated samples, but the amount of big nanoparticles is significant and also AuNP aggregates with irregular shape are frequent, probably due to partial melting (arrow in fig. 5.45e). This finding is confirmed by the radii corresponding to the average volume of particles, that is 11 nm before irradiation, 9 nm after irradiation of the AuNP-Pc blend and only 4 nm after irradiation of the bare AuNP solution. It is worth to point out as the difference in the average volume has dramatic effects on the nonlinear optical properties of AuNP solutions if one considers three main factors: *i*) the well known

predominant contribute of big nanoparticles to optical limiting; [44, 132-144] *ii*) the linear dependence of the extinction cross section on the volume of AuNP, meaning that big nanoparticles contribute is dominating in the UV - Vis absorption spectra; [161-163, 165-168] *iii*) the maximum in the linear absorption cross section at 532 nm for volume units of AuNP when the radius is about 20 nm, due to the best compromise between SPA intensity and surface damping effects.[161, 165-170]

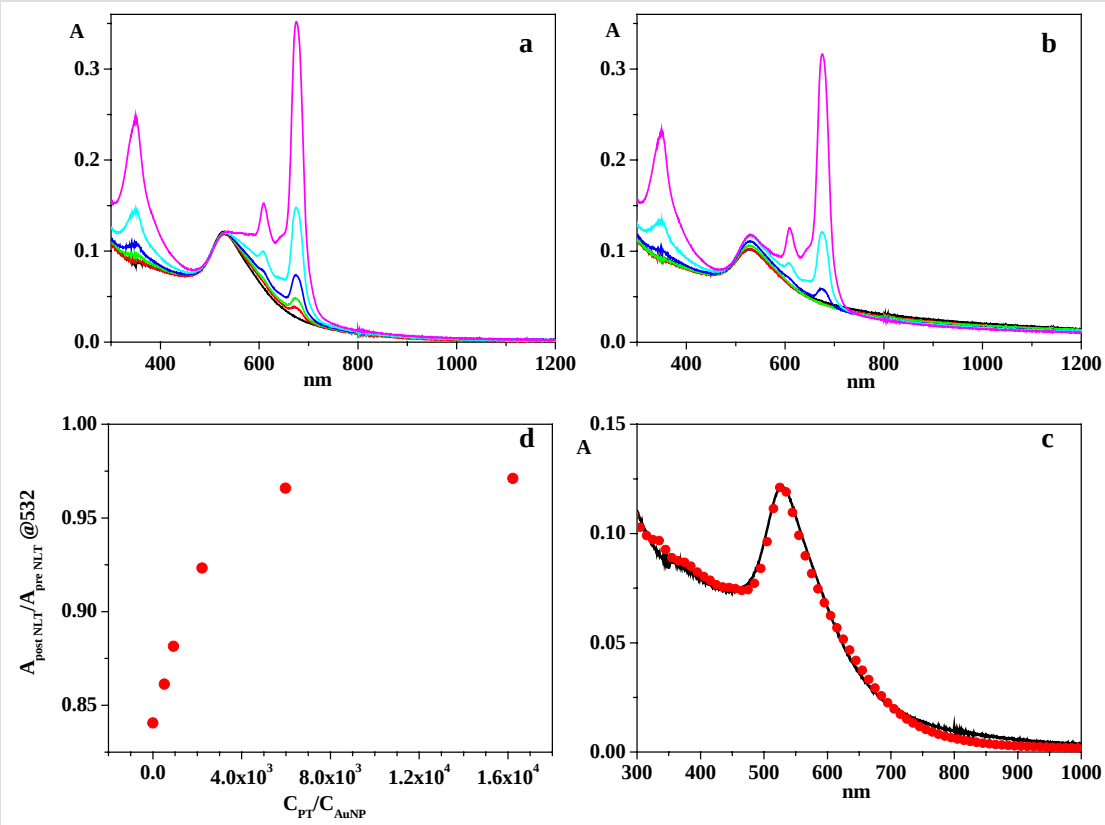

Figure 5.46 *a – b) UV – vis spectra before (left) and after (right) 350 laser pulses at 532 nm and 1100 mJ/cm^2 on AuNP-Pc solutions with increasing Pc amount from 0 to 1.1 10^{-5}M. AuNP concentration of 7 10^{-10} M and average radius of 8 nm estimated by the Mie – Gans fitting model (c). d) Ratio of the linear absorbance at 532 nm after and before the measurements for increasing Pc amount.*

The size histograms referred to the gold atoms percentage (fig. 5.47a) confirms that the main part of Au atoms is located in particles with bigger radii when considering the AuNP-Pc irradiated blend and in particles with small radii when considering the irradiated bare AuNP. More in details, histograms of Fig. 5.47a stress out that the percentage of big particles (R > 15 nm) in the irradiated AuNP-Pc blend is larger than before irradiation, which is an indication of particles growth during the irradiation process.

To go further insight the mechanism of AuNP-Pc optical limiting, we irradiated with 600 consecutives laser pulses at 532 nm and 1100 mJ/cm^2 four solutions containing

AuNP with size bigger than in the previous experiments (average radius of 19 nm, estimated by Mie – Gans fitting model, instead of 9 nm). We used solutions with linear transmittance at 532 nm comparable to that of the experiments shown in Fig. 5.45, then in reason of the larger size of AuNP, they presented a lower concentration of particles and contained AuNP having a less efficient thermal energy dissipation. [161, 165-168]

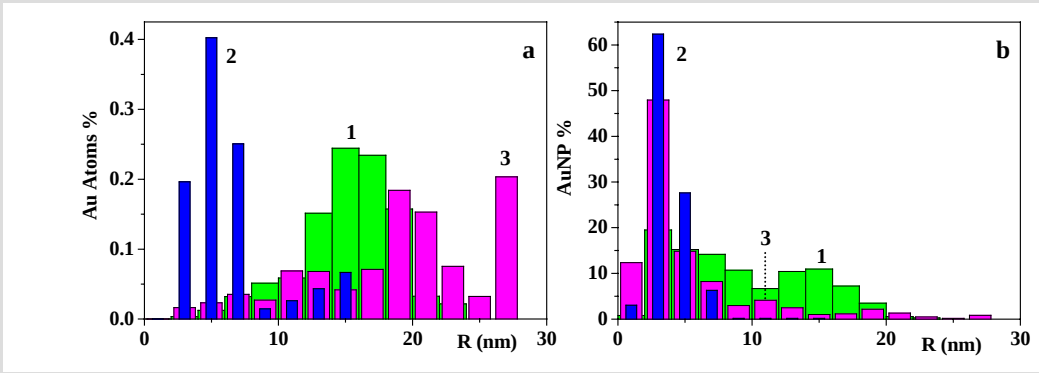

Figure 5.47 *a) TEM histograms of gold atoms versus AuNP radii before (green - 1) and after the irradiation with 250 pulses at 532 nm and 1100 mJ/cm^2 for bare AuNP (blue - 2) and the AuNP-Pc blend (violet - 3). b) Same histograms referred to AuNP number instead of gold atoms. Average radii of 9 ± 5 nm, 4 ± 1 nm and 5 ± 5 nm respectively. Average volumes corresponding to a radius of 11nm, 4 nm and 9 nm respectively.*

All these things are effective in obtaining a strong and fast particles fragmentation.[161, 165-168] We carried out the measurements on 4 different samples: bare Pc solution, bare AuNP solution, AuNP-Pc blend and finally a bare AuNP solution to which, after irradiation with 400 pulses on the total of 600, we added the Pc in the same amount as that of the AuNP-Pc blend. Fig. 5.48a shows that the result for the Pc, AuNP and AuNP-Pc solutions are similar to what observed in fig. 5.45a, except for the presence of a plateaux after about 300 shots and a faster degradation of the OL performances. The plateaux indicates that a dynamic equilibrium in the particles fragmentation process is reached. The faster degradation of the OL performances is due to the higher fragmentation efficiency of big AuNP previously discussed. In the case of the bare AuNP solution to which we added the Pc after 400 pulses, we found that the OL performances became the same of the blend in few tens of laser pulses after the Pc addition (fig 5.45a). Furthermore the UV-Vis of this solution after 600 shots is almost identical to the AuNP-Pc blend spectrum (after subtraction of the Pc contribute, fig. 5.49a). Also the average diameter, estimated with the Mie – Gans fitting model, is of 6 nm instead of 4 nm, as estimated for bare AuNP (fig. 5.49b).

The systematic occurrence of AuNP with average size larger in the AuNP-Pc blend than in the bare AuNP solutions after laser irradiation experiments, and the TEM findings of

a relevant percentage of AuNP with size larger than before irradiation are strong indications that the Pc plays a role in the aggregation and regrowth of gold particles during the OL measurements.

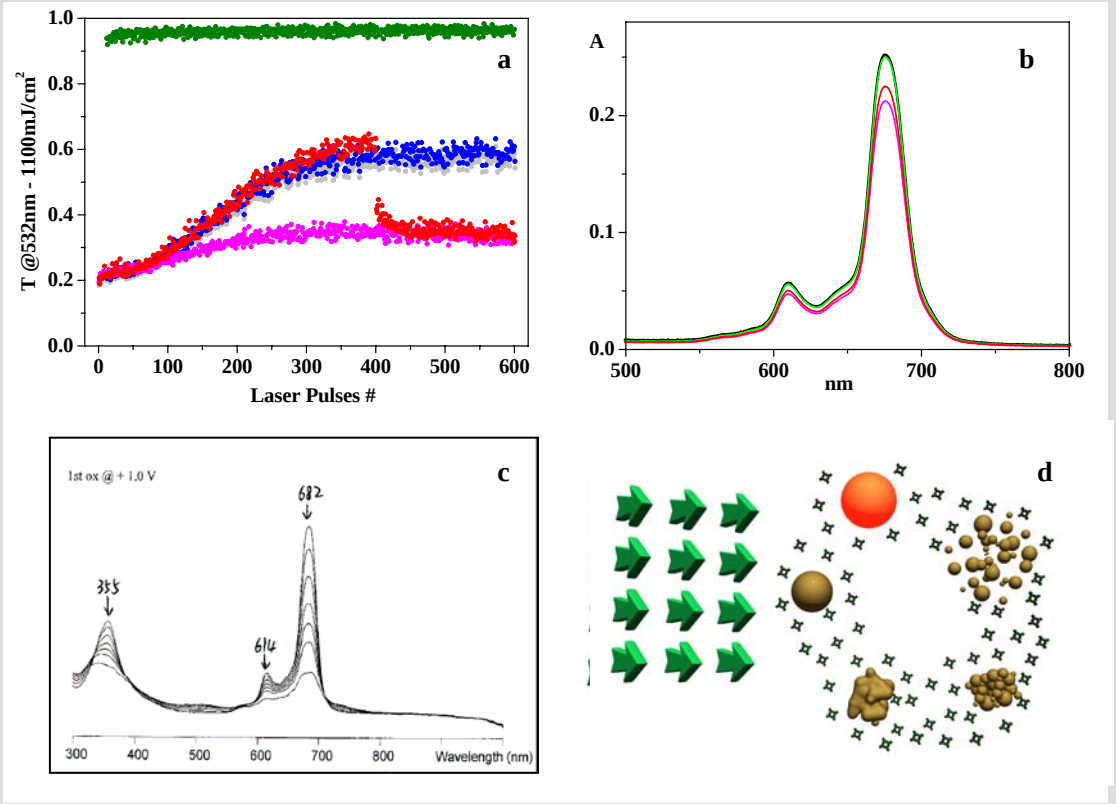

Figure 5.48 *a) NLT at 532 nm for 600 consecutive laser pulses with fluence 1100 mJ/cm^2 for bare Pc in THF (green circles), bare AuNP (blue circles), the AuNP-Pc blend (violet circles) and a bare AuNP solution to which after 400 shots we added the same amount of Pc present in the blend (red circles). Grey circles correspond to the sum of the optical limiting contributes of Pc plus AuNP solutions. Linear transmittance at 532 nm equal to 80% for both AuNP and AuNP-Pc solutions and to 99% for Pc solution; Pc concentration of 9 10^{-6} M, gold particles concentration of 5 10^{-11} M and average radius of 19 nm estimated by Mie – Gans fitting model. b) The Pc UV – vis spectra or contribute to the overall spectra before irradiation (black line, equal for bare Pc and AuNP-Pc blend), and after 600 pulses for bare Pc (green line), for the AuNP-Pc blend (violet line) and for the AuNP solutions to which we added the Pc after 400 pulses (red line). d) Spectroelectrochemical measurements of the first oxidation observed at +1.0 V on a Pc solution, in which one can observe the same decrease of the overall absorption spectrum as after the NLT measurements. d) Self – Healing mechanism at the base of the durable OL properties of the AuNP-Pc blend. From left in clockwise order: AuNP absorb photons; AuNP heat up over explosion treshold; AuNP fragment in several smaller particles positively charged; some of the positive charges are acquired in an oxidation reaction of Pc molecules, promoting the aggregation of particles; the aggregates is progressively melted until the formation of a new spherical AuNP.*

Ageing experiments carried out on not irradiated AuNP-Pc and bare AuNP solutions confirmed this aggregation trend in presence of the Pc (Fig. 5.50a). In the ageing experiments we mixed two identical as synthesized AuNP solutions with a Pc solution and, as a reference, with an equal volume of pure THF. The AuNP:Pc ratio was about 1:5000. We stored the two solutions in the dark at room temperature and collected UV –

Vis spectra each day for a week. Also dynamic light scattering (DLS) and Z – spectroscopy measurements evidenced the role of Pc in producing aggregates of AuNP (Fig. 5.50b) and in decreasing the charge of gold particles obtained by laser ablation in THF, which resulted positively charged (Fig. 5.50c). Gold nanoparticles obtained by LASiS without stabilizing agents are stable due to the presence of a net surface charge, like all the colloidal systems. For DLS and Z-spectroscopy measurements we used a Spectra Physics Nicomp 380 instrument (Particle Sizing Systems, Santa Barbara, CA, USA) equipped with a 633 nm He – Ne laser.

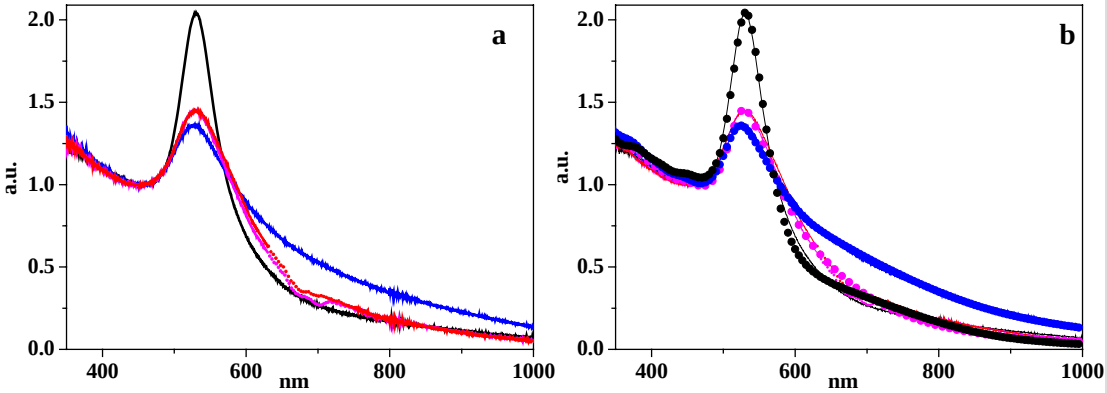

Figure 5.49 *a) AuNP UV – Vis spectra before irradiation (black line) and after irradiation for bare AuNP (blue line), AuNP-PT blend (violet line) and the bare AuNP solutions to which we added the PT after 400 pulses (red line). All spectra were normalized at 450 nm to enhance the difference in the SPA and, where needed, the PT contribute was subtracted. b) Mie – Gans fittings (circles) of the 4 spectra indicate an average radius of 19 nm before irradiation, of 3 nm for both the AuNP solutions containing PT at the end of the measurements and of 2 nm for bare AuNP.*

Since the Pc is a non-ionic molecule, the aggregation of AuNP and the coincident decrease of their Z-potential suggests that an oxidation mechanism of the pyrrolic ring by draining positive charges from the colloidal gold particles occurred. This statement is supported by the decrease of Pc linear absorption contribution to the UV-Vis spectra of the AuNP-Pc blend before and after all the OL measurements. For instance, in the experiment of Fig. 5.48a, we found that the Pc contribution to the UV – Vis spectra of the free Pc before and after 600 laser shots is almost the same, while for the AuNP-Pc blend one can clearly see a decrease of the B band at 675 nm (violet line in fig. 5.48b). The entity of this decrease depends on the number of laser shots, since when the Pc is added after 400 shots we found a lower degradation (red line in fig. 5.48b). The spectroelectrochemical measurements performed on the Zn phthalocyanines (Fig. 5.48c) show that the decrease of Pc absorption after laser irradiation in presence of AuNP is compatible with the oxidation of the molecule. In fact, as one can see in Fig.

5.48c, the first oxidation of the molecule at +1.0 *V* produced the quenching of both the Q and the B absorption bands.

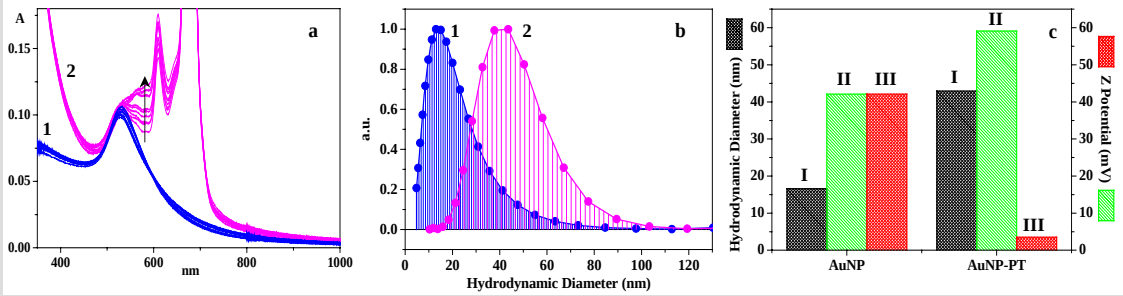

Figure 5.50 *a) Ageing of AuNP (blue lines - 1) and AuNP-Pc (violet line - 2) solutions on a time frame of a week. b) Hydrodynamic diameter distribution measured by DLS for bare AuNP (average: 16.6 nm) and for the AuNP-Pc blend (average: 42.9 nm). c) Histogram comparing the hydrodinamic diameter (black - I) and the Z Potential (green - II) for bare AuNP (16.6 nm and +42.1 mV) and for AuNP-Pc (42.9 nm and + 59.1 mV). If one considers the Z Potential divided for the number of particles with diameter 16.6 nm in an aggregate of 42.9 nm (17 AuNP), the value for AuNP-Pc goes from + 59.1 mV to + 3.5 mV/AuNP (red - III).*

In this frame one can suggest an overall mechanism for the enhanced optical limiting properties based on a self – healing process of AuNP when coupled to Pc, which represents a new and promising alternative to tandem or concentration gradient methods used for the protection of optical limiting devices from irreversible damaging.[44, 52] This example of a functional nanomaterials able to self heal simply using it, based on a mechanism that does not mimic biological systems, as often hypothesized for nanosistems,[157, 158] can open a new pathway to obtain functional nanodevices with enhanced durability. In the first step of the self healing mechanism, AuNP irradiated with 532 nm and 9 ns laser pulses show strong optical limitation but also fragment in smaller particles. In absence of Pc, these particles repulse each other due to the high surface charge as characteristic for colloidal systems, while in presence of the Pc a redox mechanism can occur that produces the Pc oxidation, the decrease of AuNP surface charge and, then, to AuNP aggregation (Fig. 5.48d). The absence of any ligands or stabilizing agents allowed by LASiS in THF is helpful for the process to occur, since it avoids that small particles are stabilized after their formation or that the interaction between nanoparticles and Pc is obstructed by ligands as reported by Hirsch et al.[171] After the aggregation, further absorption of laser light causes melting of the clusters and the formation of a new spherical nanoparticle, ready to limit light with higher efficiency than smaller particles or aggregates. In fact it is well known in literature and confirmed by present measurements that smaller particles have worse optical limiting properties[44, 132-144] and better thermal dissipation efficiency[161, 165-168] than big nanoparticles, due to

the higher surface to volume ratio, in particular with nanosecond laser pulses. Also aggregates of small particles with low density like those shown in fig 5.45e have a surface to volume ratio higher than spheres with equal volume, and they possess a better thermal dissipation efficiency. The surface to volume ratio and the irregular shape imply also that the 532 nm linear absorption cross section of aggregates is usually smaller than that of spherical nanoparticles with equivalent volume. This has been confirmed by the experimental spectra of non irradiated bare AuNP, after the irradiation with 300 laser pulses at 532 nm and 1100 mJ/cm^2 and after the addition of Pc in solution (fig. 5.51).

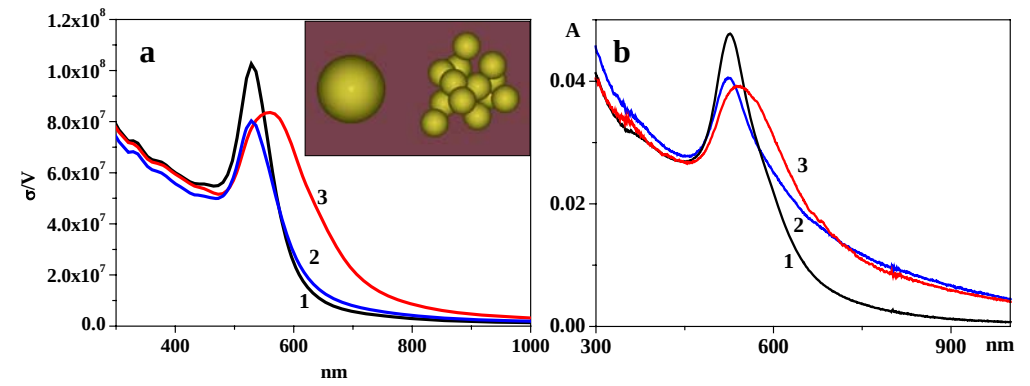

Figure 5.51 *a) DDA simulations for a gold sphere of radius 9.1 nm (black), 3.8 nm (blue) and for a cluster formed from 14 touching AuNP (red) of 3.8 nm average radius, random arranged in the space but having the same overall volume of a 9.1 nm particle. Inset shows the 14 AuNP aggregate shape. b) Experimental UV – vis spectra of AuNP before (black) and after 250 laser pulses at 532 nm and 1100 mJ/cm^2 without (blue) and with (red) the addition of Pc at the end of the irradiation experiment.*

We used a Discrete Dipole Approximation (DDA) code to perform the calculation of the extinction cross section of a single AuNP before irradiation, after irradiation and after promoting the aggregation with Pc to form a cluster of 14 AuNP, using the data obtained from TEM and DLS for the calculations. Calculations of the extinction cross sections of AuNP by DDA were carried out using the free DDSCAT 6.1 code of Draine and Flatau.[172] For simple spheres before and after irradiation we used 27000 dipoles and a radius of 9.1 nm and 3.8 nm respectively, as obtained from TEM analysis. For the particles aggregate after the addition of Pc, we considered a cluster formed of 14 touching AuNP of 3.8 nm average radius, randomly arranged in the space but having the same overall volume of a 9.1 nm particle (inset of Fig. 5.51a). We used 295000 dipoles for the aggregate and we made an average over 11 random orientations and 2 ortogonal polarization directions. For the AuNP dielectric constant we used the Johnson and Christy values corrected for the size as done with the Mie – Gans fitting model.

Calculations were made in THF as dielectric environment and were checked for convergence increasing the dipole numbers until no appreciable changes were observed. Also in this case the comparison between experimental and calculated spectra is good and confirms that the aggregation process occurred after Pc addition and that the final 532 nm linear absorbance of the aggregate is lower than the original big nanoparticle.

Experiments of fig. 5.45b showed that the best results were obtained for AuNP:Pc ratio higher than 1:2000. In this case the mechanism proposed in fig. 5.48d is more efficient due to the large amount of Pc in solution, but we can not exclude that there is also a tandem effect between the Pc and AuNP, i.e. the contribute to optical limiting of the Pc becomes important and is able to exert a protection effect on the AuNP, further reducing the fragmentation. However the tandem mechanism alone can not account for the observation made by TEM that the blend after irradiation contains AuNP bigger than before irradiation, nor for the enhanced OL durability for AuNP:Pc ratio lower than 1:2000, where the Pc optical limiting is negligible, nor for the complete overlap between OL curves for AuNP-Pc and bare AuNP plus bare Pc shown in fig. 5.44, because the OL contribute of AuNP in the blend should be different under the protection effect of optical limiting by the Pc.

References.

1. Mentzel, R., *Photonics*. Springer Berlin, 2001.
2. DeRosa, M. C.; Crutchley, R. J., *Coord. Chem. Rev.* **2002,** 233/234, 351-371.
3. Konan, Y. N.; Gurny, R.; Allemann, E., *J. Photochem. Photob. B* **2002,** 66, 89–106.
4. Gust, D.; Moore, T. A.; Moore, A. L., *Acc. Chem. Res.* **1993,** 26, 198.
5. Sudeep, P. K.; Ipe, B. I.; Thomas, K. G.; George, M. V.; Barazzouk, S.; Hotchandani, S.; Kamat, P. V., *Nano Lett.* **2002,** 2, 29-35.
6. Eckert, J. F.; Nicoud, J. F.; Nierengarten, J. F.; Liu, S. G.; Echegoyen, L.; Barigelletti, F.; Armaroli, N.; Ouali, L.; Krasnikov, V.; Hadziioannou, G., *J. Am. Chem. Soc.* **2000,** 122, 7467-7479.
7. Thomas, K. G.; Kamat, P. V., *Acc. Chem. Res.* **2003,** 36, 888-898.
8. Hasobe, T.; Imahori, H.; Kamat, P. V.; Ahn, T. K.; Kim, S. K.; Kim, D.; Fujimoto, A.; Hirakawa, T.; Fukuzumi, S., *J. Am. Chem. Soc.* **2005,** 127, 1216–1228.
9. Amendola, V.; Mattei, G.; Cusan, C.; Prato, M.; Meneghetti, M., *Synthetic Metals* **2005,** 155, 283 – 286.
10. Boyd, R. W., *Nonlinear Optics*. Academic Press: San Diego, 1992.
11. Ehlert, J.; Stiel, H.; Teuchner, K., *Computer Physics Communications* **2000,** 124, 330-339.
12. Segura, J. L.; Martın, N.; Guldi, D. M., *Chem. Soc. Rev.* **2005,** 34, 31.
13. Nierengarten, J.-F., *Sol. Energy Mater. Sol. Cells* **2004,** 83, 187.
14. Kadish, K.; Smith, K.; Guilard, R., *The Porphyrin Handbook*. Academic Press: New York, 2003.
15. Figueira-Duarte, T. M.; Clifford, J.; Amendola, V.; Gegout, A.; Olivier, J.; Cardinali, F.; Meneghetti, M.; Armaroli, N.; Nierengarten, J.-F., *Chem. Commun.* **2006,** 19, 2054-2056.
16. Chiang, L. Y.; Padmawar, P. A.; Canteenwala, T.; Tan, L.-S.; He, G. S.; Kannan, R.; Vaia, R.; Lin, T.-C.; Zheng, Q.; Prasad, P. N., *Chem. Commun.* **2002**, 1854.
17. Dichtel, W. R.; Serin, J. M.; Eder, C.; Frechet, J. M. J.; Matuszewski, M.; Tan, L.-S.; Ohulchanskyy, T. Y.; Prasad, P. N., *J. Am. Chem. Soc.* **2004,** 126, 5380.
18. Bhawalkar, J. D.; Kumar, N. D.; Zhao, C. F.; Prasad, P. N., *J. Clin. Med. Surg.* **1997,** 37, 510.
19. Guldi, D. M.; Martin, N., *Fullerenes: From Synthesis to Optoelectronic Devices*. Kluwer Academic Publishers: Dordrecht, 2002.
20. DaRos, T.; Prato, M., *Chem. Commun.* **1999**, 663.
21. Brunel, J.; Mongin, O.; Jutand, A.; Ledoux, I.; Zyss, J.; Blanchard-Desce, M., *Chem. Mater.* **2003,** 15, 4139.
22. Mongin, O.; Brunel, J.; Porre`s, L.; Blanchard-Desce, M., *Tetrahedron Lett.* **2003,** 44, 2813.
23. Rio, Y.; Enderlin, G.; Bourgogne, C.; Nierengarten, J.-F.; Gisselbrecht, J.-P.; Gross, M.; Accorsi, G.; Armaroli, N., *Inorg. Chem.* **2003,** 42, 8783.
24. Gutierrez-Nava, M.; Accorsi, G.; Masson, P.; Armaroli, N.; Nierengarten, J.-F., *Chem. Eur. J.* **2004,** 10, 5076.
25. Y. Rio, G. A.; Nierengarten, H.; Bourgogne, C.; Strub, J.-M.; Dorsselaer, A. V.; Armaroli, N.; Nierengarten, J.-F., *Tetrahedron* **2003,** 59, 3833.
26. Tutt, L. W.; Kost, A., *Nature* **1992,** 356, 225.
27. Schiccheri, N.; Meneghetti, M., *J. Phys. Chem. A* **2005,** 109, 4643.
28. McLean, D. G.; Sutherland, R. L.; Brandt, M. C.; Brandelik, D. M.; Fleitz, P. A.; Pottenger, T., *Opt. Lett.* **1993,** 18, 858.
29. Signorini, R.; Zerbetto, M.; Meneghetti, M.; Bozio, R.; Maggini, M.; Faveri, C. D.; Prato, M.; Scorrano, G., *Chem. Commun.* **1996,** 1996, 1891.
30. Dini, D.; Vagin, S.; Hanack, M.; Amendola, V.; Meneghetti, M., *Chem. Commun.* **2005**, 3796-3798.
31. Zyskowski, C. D.; Kennedy, V. O., *J. Porphyrins Phthalocyanines* **2000,** 4, 707–712.
32. Claessens, C. G.; Gonzalez-Rodriguez, D.; Rey, B. D.; Torres, T.; Mark, G.; Schuchmann, H. P.; Sonntag, C. V.; MacDonald, J. G.; Nohr, R. S., *Eur. J. Org. Chem.* **2003**, 2547–2551.
33. Ferro, V. R.; Poveda, L. A.; R.H.Gonzalez-Conte; Vega, J. M. G. D. L.; Torres, T.; Rey, B. D., *J. Porphyrins Phthalocyanines* **2000,** 4, 610–619.
34. Claessens, C. G.; Torres, T., *Chem. Commun.* **2004**, 1298–1299.
35. Kietaibl, H., *Monatsh. Chem.* **1972,** 103, 405–418.
36. Rauschnabel, J.; Hanack, M., *Tetrahedron Lett.* **1995,** 36, 1629–1632.
37. Rey, B. D.; Keller, U.; Torres, T.; Rojo, G.; Agullo-Lopez, F.; Nonell, S.; Marti, C.; Brasselet, S.; Ledoux, I.; Zyss, J., *J. Am. Chem. Soc.* **1998,** 120, 12808–12817.
38. Claessens, C. G.; Gonzalez-Rodriguez, D.; Torres, T., *Chem. Rev.* **2002,** 102, 835–853.

39. Nalwa, H. S.; Miyata, S., *Nonlinear Optics of Organic Molecules and Polymers*. CRC: Boca Raton, 1997; p 841–860.
40. Shirk, J. S.; Pong, R. G. S.; Bartoli, F. J.; Snow, A. W., *Appl. Phys. Lett.* **1993,** 63, 1880–1882.
41. Perry, J. W.; Mansour, K.; Lee, I. Y. S.; L.Wu, X.; Bedworth, P. V.; Chen, C. T.; D. Ng; S.R.Marder; Miles, P.; Wada, T.; Tian, M.; Sasabe, H., *Science* **1996,** 273, 1533–1536.
42. Blau, W.; Byrne, H.; Dennis, W. M.; Kelly, J. M., *Opt. Commun.* **1985,** 56, 25–29.
43. Lower, S. K.; El-Sayed, M. A., *Chem. Rev.* **1966,** 66, 199–241.
44. Sun, Y. P.; Riggs, J. E., *Int. Rev. Phys. Chem.* **1999,** 18, 43–90.
45. Dini, D.; Barthel, M.; Hanack, M., *Eur. J. Org. Chem.* **2001**, 3759–3769.
46. Chen, Y.; Dini, D.; Hanack, M.; Fujitsuka, M.; Ito, O., *Chem. Commun.* **2004,** 2004, 340–341.
47. Ferro, V. R.; Vega, J. M. D. L.; Claessens, C. G.; Poveda, L. A.; Gonzalez-Jonte, R. H., *J. Porphyrins Phthalocyanines* **2001,** 5, 491–499.
48. Shirk, J. S.; Flom, S. R.; Pong, R. G. S.; Heckmann, H.; Hanack, M., *J. Phys. Chem. A* **2000,** 104, 1438–1449.
49. Barthel, M.; Dini, D.; Vagin, S.; Hanack, M., *Eur. J. Org. Chem.* **2002**, 3756–3762.
50. Maya, E. M.; Snow, A. W.; Shirk, J. S.; Pong, R. G. S.; Flom, S. R.; Roberts, G. L., *J. Mater. Chem.* **2003,** 13, 1603–1613.
51. Hanack, M.; Schneider, T.; Barthel, M.; Shirk, J. S.; Flom, S. R.; Pong, R. G. S., *Coord. Chem. Rev.* **2001,** 219–221, 235–258.
52. Xia, T.; Hagan, D. J.; Dogariu, A.; Said, A. A.; Stryland, E. W. V., *Appl. Opt.* **1997,** 36, 4110–4122.
53. Sugimori, T.; Torikata, M.; Nojima, J.; Tominaka, S.; Tobikawa, K.; Handa, M.; Kasuga, K., *Inorg. Chem. Commun.* **2002,** 5, 1031–1033.
54. Vagin, S.; Hanack, M., *Eur. J. Org. Chem.* **2004**, 600–606.
55. Dini, D.; Yang, G. Y.; Hanack, M., *J. Chem. Phys.* **2004,** 119, 4857–4864.
56. Yang, G. Y.; Hanack, M.; Lee, Y. W.; Chen, Y.; Lee, M. K. Y.; Dini, D., *Chem. Eur. J.* **2003,** 9, 2758–2762.
57. Vagin, S.; Barthel, M.; Dini, D.; Hanack, M., *Inorg. Chem.* **2003,** 42, 2683–2694.
58. Giuliano, C. R.; Hess, L. D., *Appl. Phys. Lett.* **1968,** 12, 292–294.
59. Kipp, R. A.; Simon, J. A.; Beggs, M.; Ensley, H. E.; Schmehl, R. H., *J. Phys. Chem. A* **1998,** 102, 5659–5664.
60. Giuliano, C. R.; Hess, L. D., *J. Quantum Electron.* **1967,** 3, 358–367.
61. Dini, D.; Calvete, M. J. F.; Hanack, M.; Amendola, V.; Meneghetti, M., *Chem. Commun.* **2006**, 2394-2396.
62. Dini, D.; Calvete, M. J. F.; Hanack, M.; Amendola, V.; Meneghetti, M., *Submitted*.
63. Leznoff, C. C.; Lever, A. B. P., In *Phthalocyanines: Properties and Applications*, VCH Publishers: New York, 1996.
64. Schneider, T.; Heckmann, H.; Barthel, M.; Hanack, M., *Eur. J. Org. Chem.* **2001**, 3055–3065.
65. Shirk, J. S.; Flom, S. R.; Lindle, J. R.; Bartoli, F. J.; Snow, A. W.; Boyle, M. E., *MRS Proc.* **1994,** 328, 661–666.
66. Bossa, M.; Cervone, E.; Garzillo, C.; Re, G. D., *J. Mol. Struct.* **1995,** 342, 73–86.
67. Bossa, M.; Cervone, E.; Garzillo, C.; Peluso, A., *J. Mol. Struct.* **1997,** 390, 101–107.
68. Bossa, M.; Grella, I.; Nota, P.; Cervone, E., *J. Mol. Struct.* **1990,** 69, 267–271.
69. Altucci, C.; Borrelli, R.; Lisio, C. D.; Riccardis, F. D.; Persico, V.; Porzio, A.; Peluso, A., *Chem. Phys. Lett.* **2002,** 354, 160–164.
70. Ruf, M.; Durfee, W. S.; Pierpont, C. G., *Chem. Commun.* **2004**, 1022–1023.
71. Persico, V.; Carotenuto, M.; Peluso, A., *J. Phys. Chem. A* **2004,** 108, 3926–3931.
72. Eastwood, D.; Edwards, L.; Gouterman, M.; Steinfeld, J. I., *J. Mol. Spectrosc.* **1966,** 20, 381–390.
73. Bajema, L.; Gouterman, M.; Meyer, B., *J. Mol. Spectrosc.* **1968,** 27, 225–235.
74. Dini, D.; Hanack, M.; Egelhaaf, H. J.; Sancho-Garcia, J. C.; Cornil, J., *J. Phys. Chem. B* **2005,** 109, 5425–5432.
75. Haberroth, K.; M.Rack; D.Ruff; Hanack, M., *Chem. Ber.* **1995,** 128, 417–421.
76. Fernandez-Lazaro, F.; Torres, T.; Hauschel, B.; Hanack, M., *Chem. Rev.* **1998,** 98, 563–575.
77. Torre, G. D. L.; Gray, D.; Blau, W.; Torres, T., *Synth. Met.* **2001,** 121, 1481–1482.
78. Tutt, L. W.; Boggess, T. F., *Prog. Quantum Electron.* **1993,** 17, 299–338.
79. Khoo, I. C.; Diaz, A.; Ding, J., *J. Opt. Soc. Am. B* **2004,** 21, 1234–1240.
80. Dini, D.; Barthel, M.; Shneider, T.; Ottmar, M.; Verma, S.; Hanack, M., *Solid State Ionics* **2003,** 165, 289.

81. Dini, D.; Calvete, M. J. F.; Hanack, M.; Pong, R. G. S.; Flom, S. R.; Shirk, J. S., *J. Phys. Chem. B* **2006,** 110.
82. Lepkowicz, R. S.; Cirloganu, C. M.; Fu, J.; Przhonska, O. V.; Hagan, D. J.; Van Stryland, E. W.; Bondar, M. V.; Slominsky, Y. L.; Kachkovski, A. D., *J. Opt. Soc. Am. B* **2005,** 22, 2664-2685.
83. Lin, T. C.; He, G. S.; Zheng, Q.; Prasad, P. N., *J. Mat. Chem.* **2006,** 16, 2490-2498.
84. Baev, A.; Rubio-Pons, O.; Gel'mukhanov, F.; Agren, H., *J. Phys. Chem. A* **2004,** 108, 7406-7416.
85. O'Flaherty, S. M.; Hold, S. V.; Cook, M. J.; Torres, T.; Chen, Y.; Hanack, M.; Blau, W. J., *Adv. Mat.* **2003,** 15, 19-32.
86. Ford, W. E.; Rodgers, M. A. J.; Schechtman, L. A.; Sounik, J. R.; Rihter, B. D.; Kenney, M. E., *Inorg. Chem.* **1992,** 31, 3371-3377.
87. Igarashi, T.; Watanabe, K.; Ichijima, S.; Ise, T., *WO 2004099339 A1 20041118* **PCT Int. Appl. 2004**.
88. Esposito, J. N.; Sutton, L. E.; Kenney, M. E., *Inorg. Chem.* **1967,** 6, 1116-1120.
89. Hanack, M.; Hauschel, B.; Stihler, P.; Rack, M.; Linssen, T., *Mat. Res. Soc. Symp. Proc.* **1996,** 413, 465-470.
90. Anderson, O. P.; La Cour, A.; Dodd, A.; Garrett, A. D.; Wicholas, M., *Inorg. Chem.* **2003,** 42, 122-127.
91. Dini, D.; Hanack, M.; Ji, W.; Chen, W., *Mol. Cryst. Liq. Cryst.* **2005,** 431, 559-574.
92. McEwan, K. J.; Bourhill, G.; Robertson, J. M.; Anderson, H. L., *J. Nonlin. Opt. Phys. Mat.* **2000,** 9, 451-468.
93. McEwan, K. J.; Robertson, J. M.; Anderson, H. L., *Mat. Res. Soc. Symp. Proc.* **2000,** 597, 395-406.
94. McEwan, K. J.; Fleitz, P. A.; Rogers, J. E.; Slagle, J. E.; McLean, D. G.; Akdas, H.; Katterle, M.; Blake, I. M.; Anderson, H. L., *Adv. Mat.* **2004,** 16, 1933-1935.
95. Krivokapic, A.; Anderson, H. L.; Bourhill, G.; Ives, R.; Clark, S.; McEwan, K. J., *Adv. Mat.* **2001,** 13, 652-656.
96. McEwan, K. J.; Lewis, K.; Yang, G. Y.; Chng, L. L.; Lee, Y. W.; Lau, W. P.; Lai, K. S., *Adv. Funct. Mat.* **2003,** 13, 863-867.
97. Calvete, M. J. F.; Dini, D.; Flom, S. R.; Hanack, M.; Pong, R. G. S.; Shirk, J. S., *Eur. J. Org. Chem.* **2005**, 3499-3509.
98. Maya, E. M.; Snow, A. R.; Shirk, J. S.; Pong, R. G. S.; Flom, S. R.; Roberts, G. L., *J. Mat. Chem.* **2003,** 13, 1603-1613.
99. Villano, M.; Amendola, V.; Sandona', G.; Donzello, M. P.; Ercolani, C.; Meneghetti, M., *J. Phys. Chem. B* **2006,** 110, 24354-24360.
100. Dini, D.; Hanack, M.; Meneghetti, M., *J. Phys. Chem. B* **2005,** 109, 12691.
101. Hwang, L. C.; Tsai, C. Y.; Tiao, C. J.; Wen, T. C., *Opt. Quantum Electron.* **2000,** 32, 641.
102. Donzello, M. P.; Ou, Z.; Monacelli, F.; Ricciardi, G.; Rizzoli, C.; Ercolani, C.; Kadish, K. M., *Inorg. Chem.* **2004,** 43, 8626.
103. Donzello, M. P.; Ou, Z.; Dini, D.; Meneghetti, M.; Ercolani, C.; Kadish, K. M., *Inorg. Chem.* **2004,** 43, 8637.
104. Abramczyk, H.; Szymczyk, I.; Waliszewska, G.; Lebioda, A., *J. Phys. Chem. A* **2004,** 108, 264.
105. Zeng, H.-P.; Wang, T.; Sandanayaka, A. S. D.; Araki, Y.; Ito, O., *Phys. Chem. A* **2005,** 109, 4713.
106. Fabbrini, G.; Ricco´, R.; Menna, E.; Maggini, M.; Amendola, V.; Garbin, M.; Villano, M.; Meneghetti, M., *Phys. Chem. Chem. Phys.* **2007,** 9, 616-621.
107. Fabbrini, G.; Menna, E.; Maggini, M.; Canazza, A.; Marcolongo, G.; Meneghetti, M., *J. Am. Chem. Soc.* **2004,** 126, 6238–6239.
108. Zahn, S.; Canary, J. W., *J. Am. Chem. Soc.* **2002,** 124, 9204–9211.
109. Mareque-Rivas, J. C.; Prabaharan, R.; Rosales, R. T. M. d., *Chem. Commun.* **2004**, 76–77.
110. Ogo, S.; Yamahara, R.; Roach, M.; Suenobu, T.; Aki, M.; Ogura, T.; Kitagawa, T.; Masuda, H.; Fukuzumi, S.; Watanabe, Y., *Inorg. Chem.* **2002,** 41, 5513–5520.
111. Zahn, S.; Canary, J. W., *Science* **2000,** 288, 1404–1407.
112. Pond, S. J. K.; Tsutsumi, O.; Rumi, M.; Kwon, O.; Zojer, E.; Bredas, J. L.; Marder, S. R.; Perry, J. W., *J. Am. Chem. Soc.* **2004,** 126, 9291–9306.
113. Fahrni, C. J.; O'Halloran, T. V., *J. Am. Chem. Soc.* **1999,** 121, 11448–11458.
114. Taki, M.; Wolford, J. L.; O'Halloran, T. V., *Journal of the American Chemical Society* **2004,** 126, (3), 712-713.

115. Charier, S.; Ruel, O.; Baudin, J.-B.; Alcor, D.; Allemand, J.-F.; Meglio, A.; Jullien, L., TPA_bio. *Angew. Chem. Int. Ed.* **2004,** 43, 4785-4788.
116. Cahalan, M. D.; Parker, I.; Wei, S. H.; Miller, M. J., TPA_immune. *Nature Rev. Immunol.* **2002,** 2, 872-880.
117. Woo, H. Y.; Liu, B.; Kohler, B.; Korystov, D.; Mikhailovsky, A.; Bazan, G. C., *Journal of the American Chemical Society* **2005,** 127, (42), 14721-14729.
118. Gel'mukhanov, F.; Baev, A.; Macak, P.; Luo, Y.; Agren, H., *Journal Of The Optical Society Of America B-Optical Physics* **2002,** 19, (5), 937-945.
119. Amendola, V.; Dini, D.; Polizzi, S.; Hanack, M.; Kadish, K.; Meneghetti, M., *In preparation*.
120. Schmid, G., *Nanoparticles*. Wiley - VCH: Weinheim, 2004.
121. Gonella, F.; Mazzoldi, P., *Handbook of Nanostructured Materials and Nanotechnology*. Academic Press: San Diego, 2000.
122. Tanaka, K., *J. Mat. Sci.* **2005,** 16, 633– 643.
123. Hu, M.-S.; Chen, H.-L.; Shen, C.-H.; Hong, L.-S.; Huang, B.-R.; Chen, K.-H.; Chen, L.-C., *Nat. Mater.* **2006,** 5, 102-106.
124. Lepeshkin, N. N.; Schweinsberg, A.; Piredda, G.; Bennink, R. S.; Boyd, R. W., *Phys. Rev. Lett.* **2004,** 93, 123902.
125. Morandi, V.; Marbelli, F.; Amendola, V.; Meneghetti, M.; Comoretto, D., *Adv. Funct. Mater.* **2007,** 17, 2770.
126. Gu, J.-L.; Shi, J.-L.; You, G.-J.; Xiong, L.-M.; Qian, S.-X.; Hua, Z.-L.; Chen, H.-R., *Adv. Mater.* **2005,** 17, 557 – 560.
127. Tom, R. T.; Nair, A. S.; Singh, N.; Aslam, M.; Nagendra, C. L.; Philip, R.; Vijayamohanan, K.; Pradeep, T., *Langmuir* **2003,** 19, 3439-3445.
128. Kamat, P. V., *J. Phys. Chem. B* **2002,** 106, 7729-7744.
129. Bozhevolnyi, S. I.; Beermann, J.; Coello, V., *Phys. Rev. Lett.* **2003,** 90, 197403.
130. Lippitz, M.; Dijk, M. A. v.; Orrit, M., *Nano Lett.* **2005,** 5, 799-802.
131. Jin, R.; Jureller, J. E.; Kim, H. Y.; Scherer, N. F., *J. Am. Chem. Soc.* **2005,** 127, 12482-12483.
132. Zhang, H.; Zelmon, D. E.; Deng, L.; Liu, H.-K.; Teo, B. K., *J. Am. Chem. Soc.* **2001,** 123, 11300-11301.
133. Ispasoiu, R. G.; Balogh, L.; Varnavski, O. P.; Tomalia, D. A.; Theodore Goodson, I., *J. Am. Chem. Soc.* **2000,** 122, 11005-11006.
134. Porel, S.; Singh, S.; Harsha, S. S.; Rao, D. N.; Radhakrishnan, T. P., *Chem. Mater.* **2005,** 17, 9-12.
135. Martin, R. B.; Meziani, M. J.; Pathak, P.; Riggs, J. E.; Cook, D. E.; Perera, S.; Sun, Y.-P., *Opt. Mater.* **2007,** 29, 788–793.
136. Wang, G.; Sun, W., *J. Phys. Chem. B* **2006,** 42, 20901 -20905.
137. Sun, W.; Dai, Q.; Worden, J. G.; Huo, Q., *J. Phys. Chem. B* **2005,** 109, 20854-20857.
138. West, R.; Wang, Y.; III, T. G., *J. Phys. Chem. B* **2003,** 107, 3419-3426.
139. Francois, L.; Mostafavi, M.; Belloni, J.; Delouis, J.-F.; Delaire, J.; Feneyrou, P., *J. Phys. Chem. B* **2000,** 104, 6133-6137.
140. Francois, J.; Mostafavi, L. M.; Belloni, J.; Delaire, J., *Phys. Chem. Chem. Phys.* **2001,** 3, 4965-4971.
141. Elim, H. I.; Yang, J.; Lee, J.-Y.; Mi, J.; Jib, W., *Appl. Phys. Lett.* **2006,** 88, 083107.
142. Unnikrishnan, K. P.; Nampoori, V. P. N.; Ramakrishnan, V.; Umadevi, M.; Vallabhan, C. P. G., *J. Phys. D* **2003,** 36, 1242–1245.
143. Philip, R.; Kumar, G. R.; Sandhyarani, N.; Pradeep, T., *Phys. Rev. B* **2000,** 62, 13160 - 13166.
144. Thomas, J.; Anija, M.; Cyriac, J.; Pradeep, T.; Philip, R., *Chem. Phys. Lett.* **2005,** 403, 308–313.
145. Kamat, P. V.; Flumiani, M.; Hartland, G. V., *J. Phys. Chem. B* **1998,** 102, 3123-3128.
146. Chandrasekharan, N.; Kamat, P. V.; Hu, J.; II, G. J., *J. Phys. Chem. B* **2000,** 104, 11103-11109.
147. Ramakrishna, G.; Dai, Q.; Zou, J.; Huo, Q.; III, T. G., *J. Am. Chem. Soc.* **2007,** 129, 1848 -1849.
148. Jain, P. K.; Qian, W.; El-Sayed, M. A., *J. Phys. Chem. B* **2006,** 110, 136 -142.
149. Pramod, P.; Sudeep, P. K.; Thomas, K. G.; Kamat, P. V., *J. Phys. Chem. B* **2006,** 110, 20737-20741.
150. Barazzouk, S.; Kamat, P. V.; Hotchandani, S., *J. Phys. Chem. B* **2005,** 109, 716-723.
151. Hasobe, T.; Imahori, H.; Kamat, P. V.; Ahn, T. K.; Kim, S. K.; Kim, D.; Fujimoto, A.; Hirakawa, T.; Fukuzumi, S., *J. Am. Chem. Soc.* **2005,** 127, 1216-1228.
152. Imahori, H.; Fukuzumi, S., *Adv. Funct. Mater.* **2004,** 14, 525-536.
153. Yakuphanoglu, F.; Aydin, M. E.; Kiliçoglu, T., *J. Phys. Chem. B* **2006** 110, 9782-9784.
154. Trave, E.; Mattei, G.; Mazzoldi, P.; Pellegrini, G.; Scian, C.; Maurizio, C.; Battaglin, G., *Appl. Phys. Lett.* **2006,** 89, 151121.

155. Fang, H.; Du, C.; Qu, S.; Li, Y.; Song, Y.; Li, H.; Liu, H.; Zhu, D., *Chem. Phys. Lett.* **2002,** 364, 290-296.
156. Qu, S.; Song, Y.; Du, C.; Wang, Y.; Gao, Y.; Liu, S.; Li, Y.; Zhu, D., *Opt. Commun.* **2001,** 196, 317-323.
157. Drexler, K. E., *Nanosystems: molecular machinery, manufacturing, and computation*. Wiley: 1992.
158. Toohey, K. S.; Sottos, N. R.; Lewis, J. A.; Moore, J. S.; White, S. R., *Nat. Mater.* **2007,** 6, 581-585.
159. White, S. R.; Sottos, N. R.; Geubelle, P. H.; Moore, J. S.; Kessler, M. R.; Sriram, S. R.; Brown, E. N.; Viswanathan, S., *Nature* **2001,** 409, 794-797.
160. Shchukin, D. G.; Mçhwald, H., *Small* **2007,** 6, 926 – 943.
161. Amendola, V.; Meneghetti, M., *J. Mater. Chem.* **2007,** 17, 4705–4710.
162. Amendola, V.; Polizzi, S.; Meneghetti, M., *J. Phys. Chem. B* **2006,** 110, (14), 7232-7237.
163. Amendola, V.; Polizzi, S.; Meneghetti, M., *Langmuir* **2007,** 23, (12), 6766-6770.
164. Amendola, V.; Rizzi, G. A.; Polizzi, S.; Meneghetti, M., *J. Phys. Chem. B* **2005,** 109, (49), 23125-23128.
165. Link, S.; El-Sayed, M. A., *Int. Rev. Phys. Chem.* **2000,** 19, 409-453.
166. Link, S.; Burda, C.; Nikoobakht, B.; El-Sayed, M. A., *J. Phys. Chem. B* **2000,** 104, 6152-6163.
167. Takami, A.; Kurita, H.; Koda, S., *J. Phys. Chem. B* **1999,** 103, 1226–1232.
168. Kurita, H.; Takami, A.; Koda, S., *Appl. Phys. Lett.* **1998,** 72, 789-791.
169. Kreibig, U.; Vollmer, M., *Optical Properties of Metal Clusters*. Springer Verlag: Berlin, 1995.
170. Berciaud, S.; Cognet, L.; Tamarat, P.; Lounis, B., *Nano Lett.* **2005,** 5, 515-518.
171. Hirsch, T.; Shaporenko, A.; Mirsky, V. M.; Zharnikov, M., *Langmuir* **2007,** 23, 4373-7.
172. Draine, B. T.; Flatau, P. T., *Source code DDSCAT 6.0 http://www.astro.princeton.edu/_draine/DDSCAT.html*.

Chapter 6

Optical doping and optical switching of AuNP infiltrated opals

The final aim of photonics consists in providing alternatives to electronics for faster information technologies and computing. This goal requires a sophisticated control over photons manipulation. Currently, photonic crystals are structures which allow good perspectives for a control of photons interactions giving access to a large series of linear and nonlinear optical effects useful for obtaining both active or passive photonic devices.

The family of photonic crystals is rather heterogeneous from the point of view of materials, structure and applications. Materials include dielectrics (namely insulators), semiconductors and even metals, while the structure can be developed in one, two or three dimensions and can also host engineered defects. Applications range from passive or active devices for optical communications to sensing.

Merging metal nanostructures with ordinary photonic crystals offers a further degree of freedom for photons manipulation. Here we will discuss how the insertion of gold nanoparticles in a polystyrene opal, which is one of the simplest type of photonic crystals, dramatically affected linear and nonlinear optical properties of the crystal.

6.1 Overview on photonic crystals.[1]

Photonic crystals can be described as materials bearing a periodic variation of the dielectric constant on a size scale of the order of the electromagnetic wavelength to be controlled, which, usually, is in the visible or near infrared spectral region. An array of close packed polystyrene spheres with a uniform size of the order of the visible wavelength represents the most common example of photonic crystals. According to the Bragg law, a lattice made of dielectric spheres with size of hundreds of nanometers can diffract visible light like a lattice made of atoms diffracts X rays. This means that the dispersion relation of photons frequency versus its wavevector shows a band splitting which corresponds to an interval of frequencies which is not allowed in the photonic crystal. This interval is known as photonic bandgap. Photons having frequency and wavevector in the photonic bandgap cannot propagate through the photonic crystal.

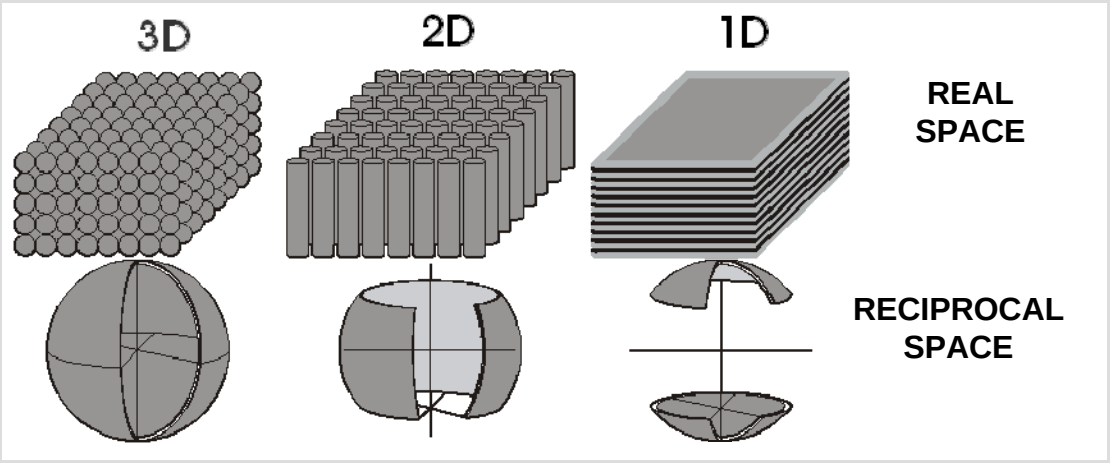

Figure 6.1 *Real space representation of a photonic crystal and reciprocal space regions for which propagation is shielded. From http://www.icmm.csic.es/cefe/pbgs.htm.*

A wide variety of methods have been used to fabricate photonic crystals. Self assembly methods are efficient for three-dimensional crystals made of colloidal particles (opals). These particles can be insulators like silica or polystyrene spheres or semiconductor materials and the self assembly process usually take place during sedimentation or vertical deposition. Due to the low refraction index difference between SiO_2 or polystyrene and air, such structures do not show a full photonic bandgap, i.e. the photon

density of states does not go to zero in the bandgap, which is defined as *pseudogap*. One can obtain a photonic crystal with a full bandgap by filling the voids between colloidal particles with high refraction index materials (like semiconductors or metals) and, then, dissolving the spheres. Such a structure is called inverse opal because air replaces colloidal spheres and the material replaces air in the voids. Lithographic methods like two photon lithography or electron beam lithography are used for obtaining complex or engineered three- and two-dimensional photonic structures, while etching methods are versatile and fast for obtaining two-dimensional photonic crystals.[1]

The photonic band structure of a photonic crystal defines its optical properties, such as transmission, reflection and their angular dependence and related properties like photons group velocity and refractive index dispersion. The photonic band can be calculated from first principles using two families of methods: time domain techniques, like the FDTD method discussed in paragraph *2.8*, and frequency domain techniques, where the following photon eigenvalues equation is solved to obtain the allowed photon states and their energies:[1]

$$\left\{\nabla\times\frac{1}{\varepsilon(\omega,r)}\nabla\times\right\}B(\omega,r)=\left(\frac{\omega}{c}\right)^2 B(\omega,r) \qquad (6.1)$$

where $\varepsilon(\omega,r)$ is the medium dielectric constant dependent on the position r and the photon frequency ω, $B(\omega,r)$ is the displacement vector of the magnetic field and c is the light speed.

The periodic modulation of dielectric constant originates unusual photonic band structures and optical properties in photonic crystals with respect to ordinary materials, and many practical applications become possible.

The presence of a photonic band gap makes photonic crystals suitable for narrow band filters or for sensors. Sensor applications exploit the dependence of the band gap position on the dielectric periodicity, which can be modulated in presence of the target analytes. In materials with appreciable optical Kerr susceptibility, the band gap position can be shifted also by using the optical Kerr effect, which describes a variation of the refractive index as a function of the intensity of the electromagnetic light. This effect can be used, in particular, for ultrafast optical switching applications.

Near the photonic band gap, the low frequency modes concentrate their energy in the high refractive index regions, whereas the high frequency modes concentrate in the low

refractive index material. This kind of local field enhancement can be exploited for improving nonlinear optical effects.

The presence of a photonic band gap originates strong modification of photons group velocity inside the crystal, in general with very low values for frequencies close to the gap. This feature can be used to enhance optical interactions that require longer time to manifest. Another phenomenon due to the anomalous group velocity dispersion is the superprism effect, which originates dispersion of various wavelength components over a much wider angle than in a normal prism and a large variation of angle of refraction in response to small variations of the angle of incidence. The anomalous refraction index dispersion is not related to any absorption, contrary to ordinary materials, therefore no loss are involved. This is very important to achieve phase matching for efficient nonlinear frequency conversion like third harmonic generation.

A point defect in a photonic crystal can behave like an optical cavity, originating defect modes not allowed in the perfect crystal band gap, in close analogy to defects in semiconductor crystals. Defects cavity in photonic crystals can join high quality factors, high selectivity of wavelengths and large enhancement of the resonant electromagnetic field within the cavity. If a point defect in a photonic crystal behave as an optical cavity, defects on a line can act as waveguides. Joining point and linear defects, namely microcavities and waveguides, represents the starting point for obtaining photonic crystal based optical circuitry. Waveguides obtained by linear defects in photonic crystals have the peculiar property of allowing sharp bending angles, up to 90°, without significant losses. The concept of lines of defects for the efficient confinement of photons, is also exploited in photonic crystal optical fibers. These fibers have a periodic modulation of refraction index in the clad and a normal dielectric medium or even air in the core. Photonic crystal optical fibers allow enhanced control over group velocity dispersion, birefringence and modal shape and excellent loss performances can be obtained by using an air core. Due to the flexibility in the design of photonic bandgap, photonic crystal optical fibers can guide light in a range between 500 and 1700 nm, overcoming the limitation of conventional fibers which works only with 1550 nm light.[1] This variety of active and passive devices provides the opportunity for a relatively dense integration of emitter, receiver, amplifier, transmitter and routers on the same photonic crystal platform, i.e. a photonic chip.[1]

6.2 Synthesis of opals infiltrated with gold nanoparticles.[2, 3]

Even though several papers have been published on opaline photonic crystals,[4] opals and inverse opals are still interesting since provide a useful playground for photonic bandgap engineering. This can be done both by introducing engineered linear and planar defects into the opal structure or by infiltration of sphere interstices with photoactive materials. Among active nanomaterials suitable for opal infiltration, gold nanoparticles appear to be very stimulating due their optical properties.

The infiltration process of polystyrene opals is not as simple as for silica ones due to the different wettability and solubility properties of these two materials. For this reason, we directly grew AuNP infiltrated polystyrene opals of different sphere diameters.

Infiltrated opals were grown from commercial polystyrene monodisperse microspheres (260 and 300 nm diameters) water suspension 10% in volume (Duke Scientific; refractive index, n_{PS} = 1.59; standard deviation < 5 %).

AuNP were prepared by laser ablation at 1064 nm of a gold metal plate in water using sodium dodecyl sulfate as surfactant as described in Chapter 3.

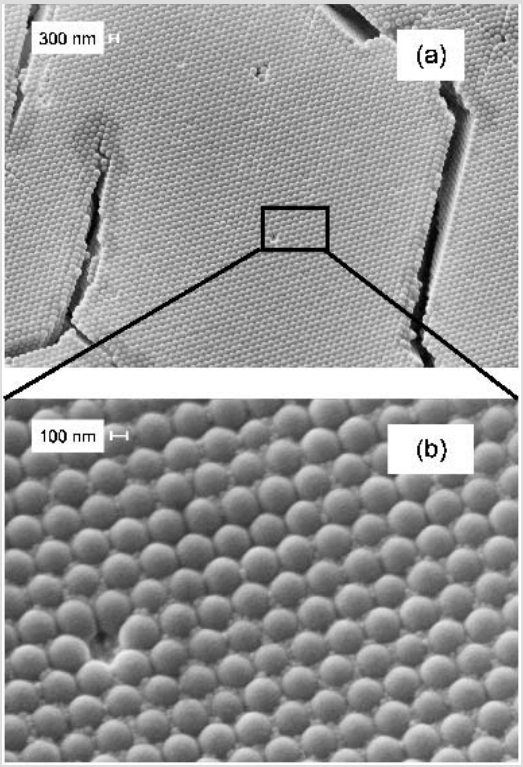

Figure 6.2 *SEM images of AuNP high load infiltrated opal surface at different magnification. Sphere diameter 260 nm.*

Microspheres suspension were mixed with AuNP water dispersion according to Tessier et al.[5] The relative ratio of AuNP and microspheres were determined as follows: From the Mie-Gans fitting of the AuNP suspension absorption spectrum, we determined the AuNP concentration as well as their shape (cfr. Chapter 3). We found that 90% of AuNP in water suspension have a spherical shape with average radius 10 nm and a concentration of about 1×10^{12} cm^{-3}. We then calculated the number of AuNP in order to have about two AuNP for one PS microsphere (high loading, HL). Additionally, we also considered numbers of AuNP 10 and 100 times lower (medium loading, ML; low loading, LL, respectively). We did not use higher AuNP loading being aware that AuNP

coalescence may take place, thus giving rise to bulk gold. For these three cases, we mixed together the correspondent volumes of AuNP and microspheres suspensions. In order to have a suitable sample thickness, we properly diluted these mixtures with distilled water, and then we grew opals films having different degrees of infiltration (AuNP doping) by using the meniscus technique.[6]

The surface and cross section images of opal films have been recorded with a Leica-Stereoscan 440 (LEO Electron Microscopy Ltd.) electronic microscope operating at 20 kV. Samples were made conductive by deposition of a thin gold layer.

Figure 6.2a shows typical SEM images of opals with the highest degree of AuNP loading (HL). The surface is fractured in several different plates of about 100 micrometer size. A magnification of this image (Fig. 1b) shows that between PS microsphere some material is infiltrated. For lower AuNP loading, infiltrated material can be hardly observed. The thickness of these films is not uniform along the whole sample. However, on the dimension of few plates (larger than the spot dimension for optical investigation) thickness is uniform.

6.3 Linear optical properties of opals doped with gold nanoparticles.[2, 3]

Polarized reflectance and transmittance spectra has been measured in the 8000–32000 cm^{-1} spectral range by means of a Fourier-transform spectrophotometer Bruker IFS66 with 8 cm^{-1} spectral resolution. The light of a Xe arc-lamp was collimated and then focused to a spot of 100 μm diameter on the sample surface. The sample was placed on a homemade θ–2θ goniometer that allows the incidence angle to be varied between 5° and 80°, with an angular resolution of 1° determined by the angular divergence of the incident light cone. The two arms of the reflectometer can be rotated around its axis in order to result collinear and then to measure the intensity of the incident light. This allows for the determination of the absolute reflectance without using a reference mirror. Sample visualization and precise allocation of the light spot on the surface was achieved by an optical microscope mounted on the goniometer.

Reflectance spectra of opals with different degree of AuNP doping are reported in Figure 6.3 and there compared with those of bare ones both for 260 and 300 nm spheres. 260 nm bare opals (Fig. 6.3a) show the typical reflectance peak (Bragg peak) due to backward diffraction of incident light by the photonic crystal at 17305 cm^{-1} (578

nm) as well as a well pronounced interference fringes pattern due to reflection from the backside of the sample.

The spectral position of the Bragg reflectance peak bathochromically shifts upon increasing the AuNP doping. In particular for LL, ML and HL 260 nm opals the peak is observed at 16601 (602), 15843 (631), 15571 cm^{-1} (642 nm), respectively. One can note that, for 260 nm LL samples, the spectral position of the Bragg peak is quite sensitive (from 602 to 590 nm) to the position of the probing spot on the sample surface due to the inhomogeneous dispersion of AuNP in the interstices. Inhomogeneity is reduced upon increasing the doping level. Furthermore, for all samples, reflectance spectra show interference fringes (both below and above the energy of the Bragg peak) for all AuNP doping levels, thus confirming the good optical quality of opals grown from mixed suspensions of microspheres and nanoparticles.

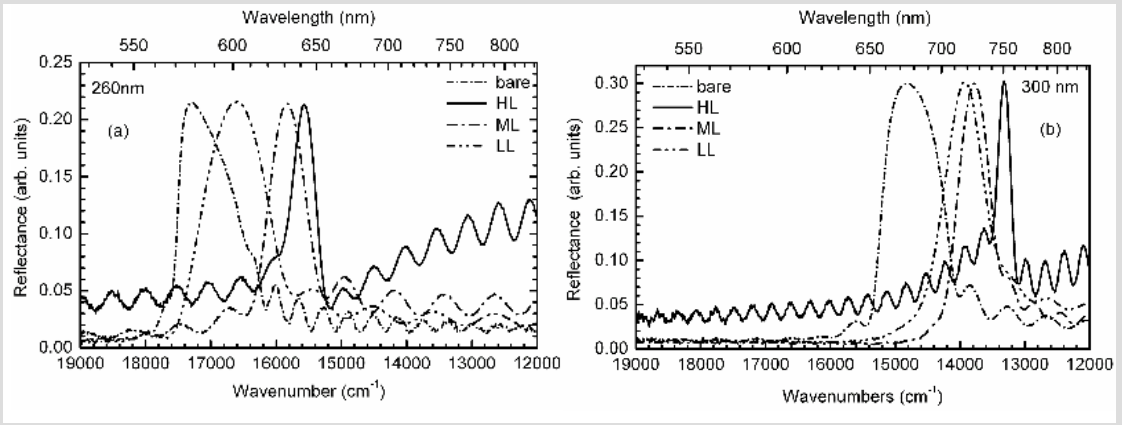

Figure 6.3 *Comparison of the normalized reflectance spectra for 260 (a) and 300 nm (b) bare and AuNP infiltrated opals at different loading recorded with incidence angle 5°.*

Similar results are observed for opals having different sphere diameters (300 nm, Fig. 6.3b), although spectrally shifted according to the scaling laws of photonic crystals.[7] Indeed the Bragg peak for bare, LL, ML and HL doping samples is observed at 14813 (675), 13922 (718), 13783 (725), and 13320 cm^{-1} (751 nm), respectively.

Also in this case, for LL samples the inhomogeneous distribution of AuNP affect the spectra being the Bragg peak detected between 695 and 720 nm. Finally, one also finds that in reflectance spectra, the spectroscopic features assigned to AuNP surface plasmon resonance are not detected whereas they can be observed in transmittance.

From the spectra reported in Figure 6.3 as well as from the images in Figure 6.2, we can conclude that infiltration took place. In order to understand the nature of the material infiltrated between the PS spheres, we dissolved one of samples with toluene (solvent

for PS) and we recorded the electronic absorption spectra in different zones (Fig. 6.4). The typical absorbance spectrum for dissolved infiltrated opals (solid solution of AuNP blended in PS) shows a band at about 530 nm and a structured shoulder between 600 and 700 nm (Fig. 6.4a, full line). In Figure 6.4b one can see that water AuNP suspensions show absorption of spherical nanoparticles at 520 nm, while alcohol suspensions, where aggregation of the nanoparticles occurs, show bands at 535 nm for spherical particles and at 700 nm for spherical particles aggregated in a spheroidal form (Fig. 6.4b). The spectral features observed for dissolved opals therefore indicates that AuNP preserve their nature inside opals, with some contributions also from spheroidal particles.

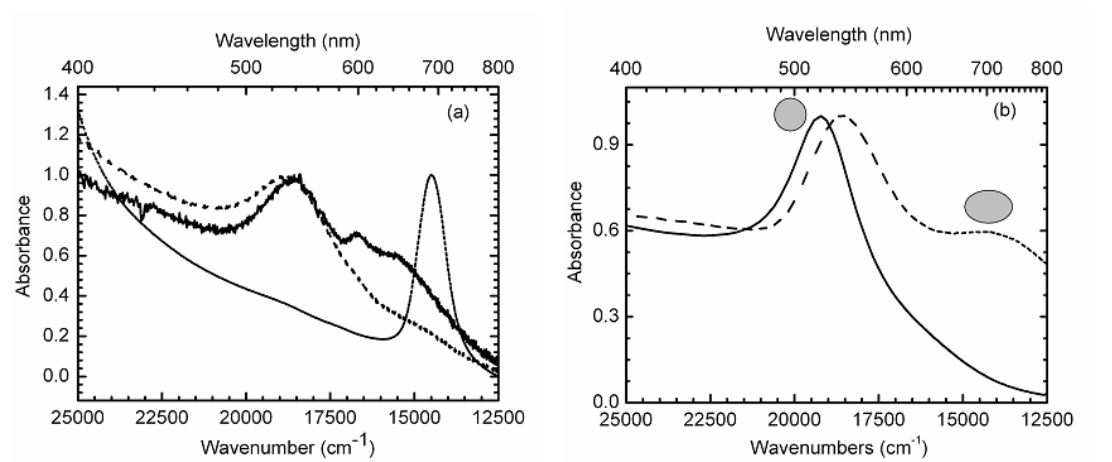

Figure 6.4 *Absorbance spectra of AuNP infiltrated opals (a) and AuNP suspensions (b). In panel (a): dissolved opal as grown (full line); dissolved opal after P&P measurements (dashed line); 300 nm LL AuNP opal (dotted line). Panel (b): AuNP water (full line) and alcohol (dashed line) suspensions. The circle and ellipse indicate typical absorption of spherical and spheroidal AuNP.*

SEM images (Fig. 6.2) and spectral features reported in Figure 6.3, unambiguously indicate that doping of opals with AuNP strongly modifies the optical properties of the PC and creates a new nanocomposite material. This finding is further supported by reflectance measurements recorded at different incidence angle (Fig. 6.5) for 300 nm samples.

Due to the dispersion of the photonic bands, the Bragg peak shifts towards higher energies and no additional features appear for high incidence angles (> 45°) as instead observed for bare opals.[8] Moreover, we notice that infiltration removes all polarization dependence on both dispersion and full width half maximum (FWHM) of the reflectance peak, as instead predicted and observed for bare opals.[9, 10] This effect can be

explained with a reduction of the symmetry of the doped photonic crystal due to the random arrangement of the AuNP inside the interstices between the spheres.

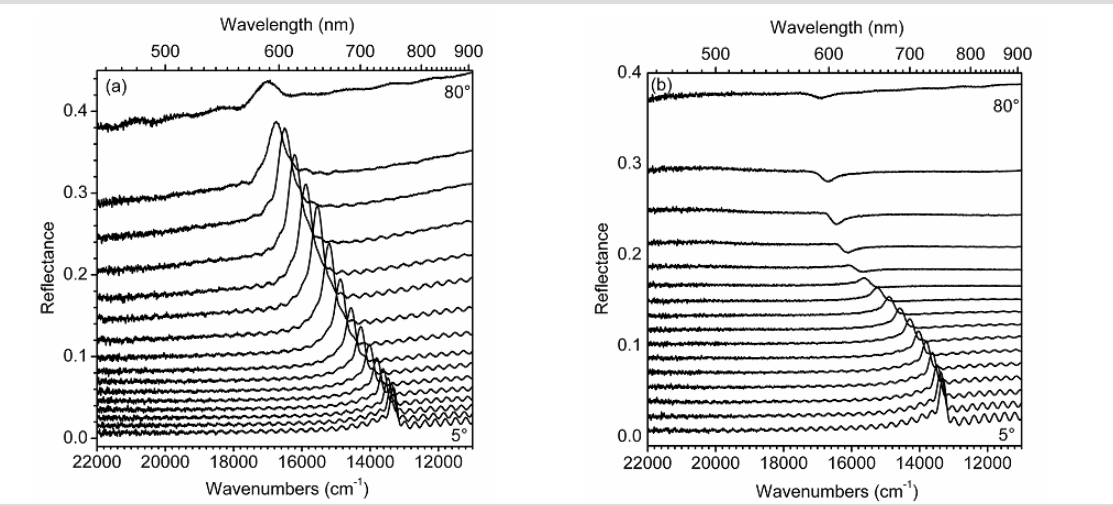

Figure 6.5 *Reflectance spectra of a HL AuNP infiltrated 300 nm opal film as a function of the incidence angle recorded every 5° and properly offset for TE (a) and TM (b) polarization.*

Similar considerations hold also for 260 nm samples except for the different spectral region, according to the scaling law of photonic crystals.[7] Interesting to notice is that our infiltration procedure does not change the cell length for both bare and doped opals as instead observed for opals grown by AuNP grafted microspheres,[11-14] thus allowing an easier assignment of the effect of doping on the optical properties of PCs. Moreover, the metallic shell around microspheres deeply affect both the dielectric contrast of the PC and AuNP plasmon resonance (strongly reduced plasmon oscillator strength with resonance shifted toward NIR) thus making complicate to achieve spectral overlap between photonic stop band and AuNP absorption.

The dispersion of the Bragg peak (k_{Bragg}) contains a lot of information, which may be extracted by the very simple Bragg–Snell formula:[15]

$$m\lambda_{Bragg} = 2D\sqrt{n_{eff}^2 - sin^2\,\theta} \qquad (6.2)$$

where m is the diffraction order, D is the interplanar spacing in the (1,1,1) direction which is perpendicular to the surface, θ is the incidence angle measured off from the normal, and n_{eff} is the effective refractive index ($n_{eff}^2 = \varepsilon_{eff}$, effective dielectric constant) obtained by the Lorentz–Lorenz formula for the effective medium:

$$\frac{\varepsilon_{eff} - 1}{\varepsilon_{eff} + 2} = f_{PS}\frac{\varepsilon_{PS} - 1}{\varepsilon_{PS} + 2} + (1 - f_{PS})\frac{\varepsilon_i - 1}{\varepsilon_i + 2} \qquad (6.3)$$

where ε_{PS} = 1.592 is the dielectric constant of polystyrene sphere, ε_i is the dielectric constant of the interstices (ε_i = 1 for bare opals), and f_{PS} is the fraction of the unitary cell filled with microspheres (0.74 for a close packed Face Centred Cubic (FCC) crystal). Since AuNP doping is very low, it is reasonable to assume it does not modify the FCC close packed structure. Then we assume f_{PS} = 0.74 and $D = a(2/3)^{0.5}$ (a sphere diameter) as for bare opals.

By fitting the dispersion of reflectance peak as a function of the incidence angle with equation *6.2*, we get n_{eff} and then, from equation *6.3*, the refractive index of voids where few AuNP were inserted (n_i). The fitting procedure has been repeated for TE and TM polarization, for all samples having different AuNP loading level and, within the same sample, on different surface positions. For HL samples we obtained n_{eff} = 1.52 (1.54) for 260 (300) nm opals. These values indicate that a relevant variation of n_{eff} upon infiltration took place (about 8–9%) with respect to the case of bare opal (n_{eff} = 1.41). From equation *6.3* the dielectric constant of interstices can be estimated as 1.33 (1.40) for 260 (300) nm HL opals. Another interesting property of AuNP doped opals is the dramatic reduction of the Bragg peak FWHM. It can be interpreted as the effect of the reduction of the dielectric contrast between microspheres and interstices, where the presence of few AuNP modifies ε_i of more than 30% with respect to the case of bare opals (ε_i = 1). The high sensitivity of the photonic band structure upon partial infiltration of interstices with highly polarizable materials envisage their use not only for photonics but also for sensing.[16] The dependence of the FWHM on the AuNP doping level can be understood recalling the expression for the stop band width (W) for a 1D photonic crystal:[17]

$$W = \frac{4}{\pi} E_{Bragg} \frac{|n_i - n_{PS}|}{n_i + n_{PS}} \qquad (6.4)$$

Here E_{Bragg} is the spectral position of the Bragg peak, theoretically provided by the Bragg-Snell law, n_i is the refractive index of the infiltrated voids, which can be derived from equation *6.3* (n_{eff} was previously deduced from the fitting with equation *6.2* of the reflectivity peak

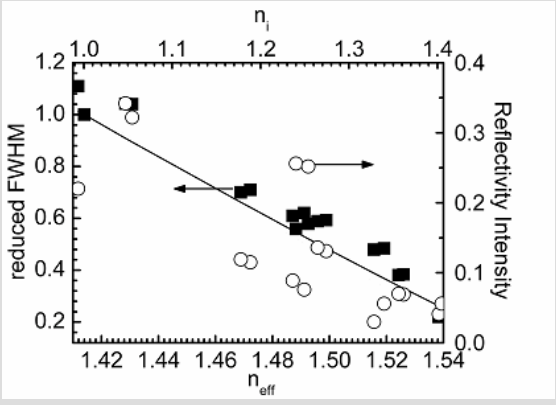

Figure 6.6 *Reduced full width half maximum and absolute reflectance intensity of the Bragg peak as a function of n_{eff} or n_i for AuNP doped opals having different sphere diameters. Reduced FWHM: full line (theory); full squares (experimental data). Reflectance intensity: open circles.*

dispersion upon changing the incidence angle). Even though equation *6.4* cannot be directly used to determine the FWHM of infiltrated opals, since they posses a much more complicated photonic structure with respect to a 1D PC, it is interesting to analyze the reduced FWHM, i.e., the FWHM for infiltrated opals divided by that measured for a bare one. The reduced FWHM as a function of n_{eff} or n_i for all our samples is reported in Figure 6.6. Both n_{eff} and n_i are representative of the AuNP doping level, through Equation *6.3*. A very good agreement between experimental and theoretical data is achieved.

An additional optical effect related to the infiltration process concerns the intensity of the reflectance peak. The increase of n_i upon increasing the doping level reduces the dielectric contrast with respect to polystyrene spheres. This implies a reduction of light diffraction efficiency by the sphere planes along the [111] direction thus decreasing the intensity of the Bragg peak. An additional effect of doping with strongly absorbing media is light scattering due to AuNP, which increases upon increasing their loading. Photons scattered in all directions reduces the signal detected in specular reflectance and transmittance configurations. In order to verify these behaviours, we also reported in Figure 6.6 the absolute reflectivity intensity measured at the Bragg peak for our samples. Even though these samples have different thickness, which gives rise to different interference pattern and then reflectivity intensity, a clear trend of intensity reduction upon increasing doping occurs.

All spectral properties (peak positions, FWHM, dispersion upon changing the incidence angle) can be well understood by modelling the material with equations 6.2–6.4 and show that AuNP doped opals are a new kind of photonic crystal with completely different dielectric properties with respect to bare ones. One should also note that this composite material retains a remarkable optical quality as testified by the pronounced interference pattern which can be observed for energies both below and above the stop band indicating a homogeneous thickness over the probed area.

6.4 Light localization effects in opals doped with gold nanoparticles.[18]

Figure 6.7 reports the transmittance (T) spectra recorded for the same samples of Fig. 6.3 and in the same spot area used for R measurements. For 260 nm bare opals the T minimum is detected at 17105 cm^{-1} (585 nm) while for LL opals at 16717 cm^{-1} (598 nm), in agreement with above findings observed in R spectra. For ML opals the shape

of the T spectrum is modified into a broad background band (15000-21000 cm^{-1}) with a weak dip at about 15872 cm^{-1} (630 nm). This weak dip occurs almost at the same wavelength of the peak of the R spectrum for the same sample (Fig. 6.3a).

If the AuNP doping level is further increased (HL samples), the background becomes more pronounced and broader (21000-12000 cm^{-1}) and the weak dip becomes a sigmoidal structure whose center (indicated by an arrow in Fig. 6.7a) is located at 15580 cm^{-1} (642 nm). The broad T background is very similar to the absorption spectrum of aggregated AuNP as observed both in solutions and in AuNP doped opals after solubilization of the PS microspheres. We point out that this effect was not observed in the R spectra thus suggesting its origin being due to an absorption process by AuNP.

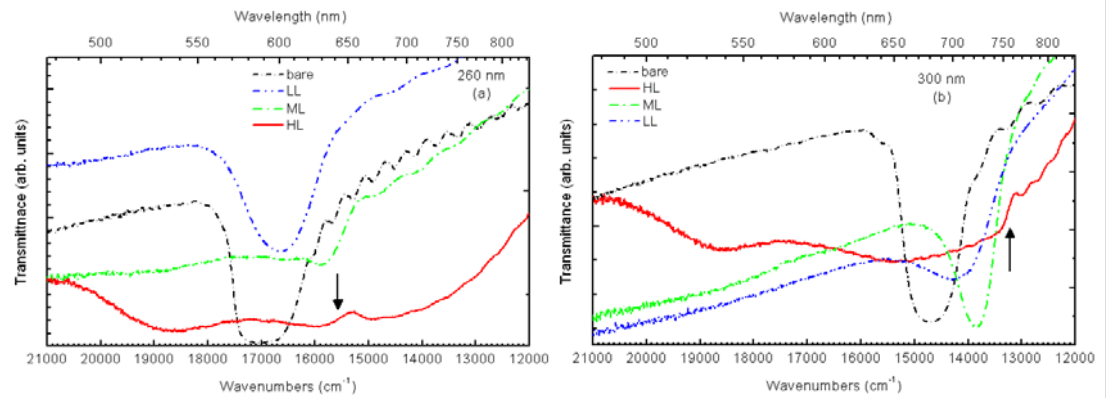

Figure 6.7 *Normal incidence transmittance spectra for 260 (a) and 300 nm (b) bare and different NpAu doped opals.*

More puzzling is instead the origin of the sigmoidal structure, since we notice that the center of this feature matches the Bragg peak of the corresponding R spectrum thus suggesting some correlation with the photonic pseudogap, that will be discussed later.

The T spectra recorded for 300 nm samples (Fig. 6.7b) have similar behaviour to those described for 260 nm opals except for the bathochromic shift associated with the scaling laws of PCs. For bare, LL, and ML opals the minima are detected at 14721 (679), 14229 (703), and 13870 cm^{-1} (721 nm) respectively and favourably compare to the spectral position of the Bragg peak in the R spectra for correspondent samples.

For the 300 nm HL opals, again a double minima (18644 cm^{-1} - 536 nm, 15317 cm^{-1} - 653 nm) broad background absorption is observed and the sigmoidal structure is overlapped to the steep part of the T spectrum at about 13222 cm^{-1} (756 nm), thus giving it a pronounced step-like character.

Notice again that its center is located at the same wavelength of the Bragg peak in the R spectra. The energy shift of the stop band observed in the R and T spectra can be related to the concentration of AuNP inside the opal interstices. As a matter of fact, the infiltration of AuNP modifies the PC dielectric contrast, increasing the effective refractive index (n_{eff}) of the structure. The spectral position of the observed sigmoidal structure also appears to follow such a dependence, with respect either to the doping level and to the PS sphere diameter.

An explanation for the unusual lineshape of the sigmoidal feature observed in T spectra is possible taking into account the effect of AuNP absorption joined to the localization of the electromagnetic field close to the band gap (Fig. 6.8). This can be qualitatively understood by observing that this structure is found only in the T spectra and not in R ones and, therefore, it can be directly probed only by light travelling through the sample. In the R spectra the main contribution to the measured signal comes instead from the sample surface, which is weakly affected by bulk absorption.

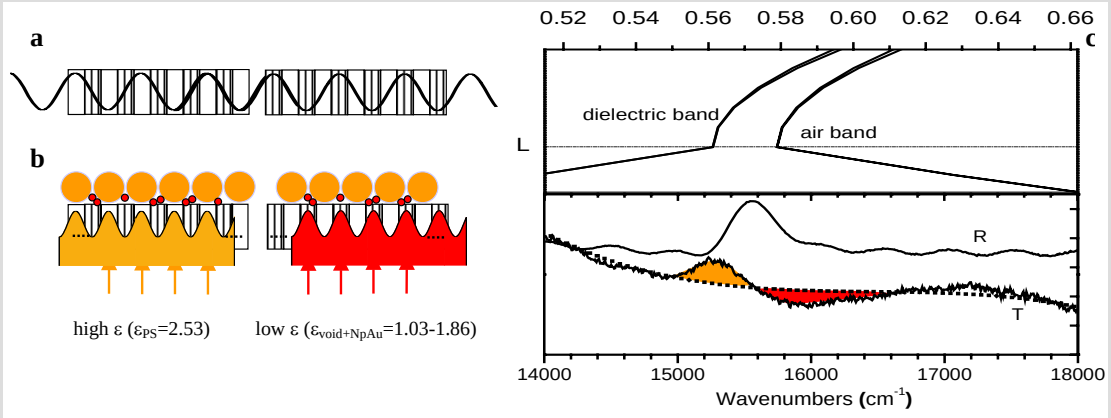

Figure 6.8 *Sketch of electric field localization in the high (low) dielectric constant materials for a one dimensional photonic crystal when photon frequency approaches dielectric (air) bands (left and right, respectively), at the photonic gap (a). Same sketch for the energy of the electromagnetic field (b). Yellow balls represent PS NS (ε_{PS}=2.53) while red dots correspond to AuNP ($\varepsilon_{void+NpAu}$=1.03-1.86 depending on the doping level). Comparison of the calculated photonic band structure of a HL infiltrated opal with R and T measured spectra (c). Yellow (red) dashed area indicates reduction (increase) of absorption due to PS NS (AuNP).*

At the pseudogap in the L point of the Brillouin zone, the photonic bands are almost flat (see Fig. 6.8c), thus making the effective refractive index divergent and then slowing down to zero the group velocity of the light, i.e. generating a stationary wave. In this conditions, the electromagnetic field in the air band, namely the high energy photonic band, is mainly localized in the low dielectric constant material (Fig. 6.8a), whereas the electromagnetic field of the dielectric band, the low energy photonic band, results to be mainly localized in the high dielectric constant material.[7] In the present case the high

dielectric constant material is represented by the PS spheres (n_{PS}=1.59, ε_{PS}=2.53) and the low dielectric constant material by the voids infiltrated with the AuNP particles since we have found above that their dielectric constant is in the range 1.03-1.86. Therefore, one can predict that a lower absorption is operating in the dielectric band since the electromagnetic field is localized where the transparent PS spheres are present. On the contrary, a larger absorption can be found for the air band since in this case the electromagnetic field is localized where the absorbing AuNP are present.

This explains (see Fig. 6.8c) the structure of the sigmoidal feature which reflects a higher absorption (red area), with respect to the background, at higher frequency and a lower absorption (yellow area) at lower frequency.

At best of our knowledge, this is the first evidence of the effect of light localization in the transmittance spectra of opals photonic crystal infiltrated with absorbing materials. This result is particularly stimulating since this effect might be further exploited with infiltrating materials possessing large nonlinear optical or lasing properties. In this case, light localization in the spatial region where active material is infiltrated might allow to reduce optical thresholds to activate harmonic generation, switching effects or lasing. A possible strategy to obtain such nanophotonics systems can be the simple functionalization of gold nanoparticles with non linear active molecules.

6.5 Optical switching properties of opals doped with gold nanoparticles.[2]

Photoinduced optical switching is an important property of materials, which may open the way to interesting applications. In order to test our new photonic crystals to this end, we measured the variation of their transmission properties upon laser photoexcitation. Previous findings in this field have been obtained for silicon-opal composite and bare polystyrene opals.[19, 20] In the first case, very weak switching properties (of the order of 10^{-3}) were achieved in the femtosecond time regime due to the photoinduced change of silicon optical properties. In the second report, the optical switching was driven by the nonlinear optical Kerr response in polystyrene. In this case, only a shift of the stop band edge was detected by using picosecond laser pulses.[20] No detailed spectral properties during the photoexcitation process were shown. Here, we report nanosecond pump and probe (P&P) measurements over a spectral range covering the stop band with the aim of characterizing optical switching effects on AuNP doped opals driven by the

photoexcitation of AuNP plasmon, which may be enhanced by light localization as already observed in 2D and 3D PC.[21, 22]

We performed P&P measurements on the LL AuNP doped 300 nm opals to avoid spectral overlap between the surface plasmon absorption band of AuNP and the stop band of 260 nm opals.

The pump and probe (P&P) experiments were carried out with a 1 GHz digital oscilloscope (LeCroy LC564A) to record the transient signals detected by a Jobin-Yvon Horiba TRIAX 320 spectrometer equipped with an Hamamatsu phototube (R2257). 9 ns pulses at 532 nm and at 10 Hz from a doubled Nd:YAG laser (Quantel YG980E) were used as a pump source and a stabilized W lamp as a probe. We used a low pass filters and a notch filter to cut off the laser radiation from that analysed by the spectrometer. The probe radiation, with a 2.5 mm spot size, crossed the pump radiation with a diameter 3.5 mm on the sample. Pulse energies were measured with a Scientech SPHD25 pyroelectric detector. The measurements performed on the interval between 620 and 750 nm were obtained with 150–200 accumulation for each point. Linear optical spectra before and after the P&P measurements have been recorded with a Varian Cary 5 UV-Vis spectrophotometer.

Notice also that a photoluminescence (PL) is observed from our AuNP doped opals and, since it could be interpreted as an increased transmission of the sample, it was subtracted from the P&P signal for the proper understanding of the data. The photophysical origin of PL, observed both for AuNP in solutions and inside opals, is currently under investigation. Interband transitions have been proposed to explain single- and multi-photon excited PL from roughened gold surfaces.[22] A similar mechanism may be active in our system too.

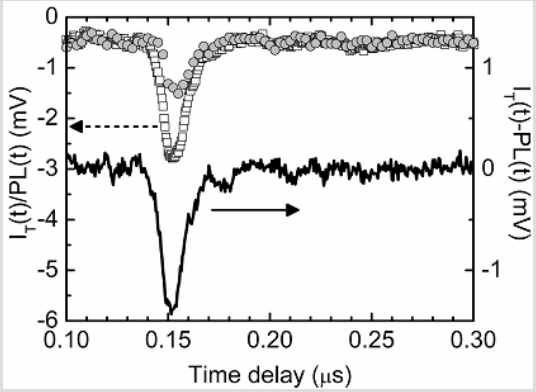

Figure 6.9 *Time evolution of the P&P signals (I_T, open squares; PL, circles; and their difference, full line) as detected in a LL AuNp doped 300 nm opal at 682 nm.*

The subtraction of the photoluminescence signal (*PL*) from the transmitted light (I_T) is done as following. First, we remember that the transmission spectrum of the sample is obtained by dividing I_T with the intensity of the probing beam I_0, separately measured. Then, *PL* is subtracted from I_T and the corrected transmission spectrum (T) is

obtained by $T = (I_T - PL)/I_0$. Notice that the *PL* spectrum is almost structureless at the photonic stop band. Moreover its intensity is almost one half of the I_T signal during pumping. When pump & probe are time delayed, the point-to-point correction procedure provide a very weakly noisy flat background. These findings indicate that PL subtraction is possible and is not responsible for spectral features observed in $\Delta T/T$ spectrum.

Figure 6.9 shows the time traces for the intensity of transmitted light through the sample (I_T), the PL signal and their difference ($I_T - PL$) for AuNP doped 300 nm opals at 682 nm upon photoexcitation with 9 ns pulses at 532 nm and using 32 mJ cm^{-2} fluence. One can see that the PL signal is only a fraction of the I_T one and that the corrected transmittance ($I_T - PL$) shows a remarkable variation only during pump pulse while a low noise level is observed when pump and probe are delayed. These facts show that the observed variation is not an artifact due to PL, it is reversible, and it can be interpreted as an optical switching process. The same measurements on bare opals do not show any particular variation of the corrected transmittance even during the laser pulse. These findings unambiguously show that resonant photoexcitation of AuNP strongly modify the optical response of the photonic crystal.

In order to better understand this result, P&P and PL measurements have been repeated for several probe wavelengths in the spectral region of the photonic stop band (620–750 nm). The absorbance spectra with and without the presence of the laser excitation are reported in Figure 6.10 for bare (a) and AuNP doped opals (b). For bare opals, the absorbance spectrum does not change, within the experimental noise, indicating that the photoexcitation does not alter the optical properties of the photonic crystal.

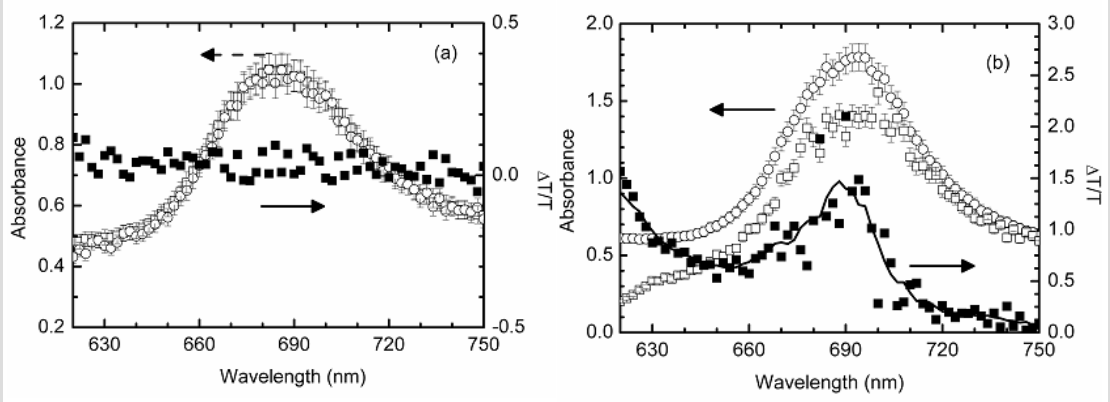

Figure 6.10 *Absorbance and ΔT/T spectra for bare (a) and AuNp infiltrated (b) opal films. Open circle (square) absorbance spectrum detected without (with) laser pump pulse; full square, ΔT/T spectra; full line is a guide for eyes obtained by 5 point smoothing of the ΔT/T data. Error bares (about 5%) for absorption measurements are also shown.*

This is particularly evident in the spectrum of the variation of transmission upon photoexcitation, $\Delta T/T$ ($\Delta T/T = (T^* - T)/T$), where T^* (T) is the corrected transmission spectra recorded during (about 200 ns after) photoexcitation also reported in Figure 6.10. This result compares favourably with previous findings, showing that at the fluence used for these experiments (32 mJ cm^{-2}), no optical switching signal is expected for polystyrene opals.[20]

Very different is the situation for AuNP doped opals (Fig. 6.10b), whose absorbance spectra are strongly modified by the photoexcitation. In particular, in the $\Delta T/T$ spectrum, two main effects are observed: A change in the background and a modification of the transmission window within the stop band.

Let's first discuss the $\Delta T/T$ background. The background change is particularly evident in the high energy part of the spectrum, where aggregated AuNP absorb (see Fig. 6.4b), thus suggesting a modification of the AuNP structure upon photoexcitation. In order to better understand this effect, we compared the absorption spectra of dissolved opals (i.e., without the effect of the photonic crystal) before and after a long and repeated series of P&P measurements (see Fig. 6.4a). As outlined before, the absorption spectrum of dissolved AuNP doped opals shows a relevant contribution of aggregated AuNP. On the other hand, after several thousands repeated series of P&P measurements, the absorption spectra of dissolved doped opals show a remarkable reduction of the spectral features assigned to aggregated nanoparticles (around 650–700 nm), thus indicating a structural change towards spherical ones (absorption peak at 520 nm). These data show that disaggregation of AuNP during ns photoexcitation takes place and that the corresponding modification of absorbance is responsible for the broad $\Delta T/T$ background.

We turn now our attention to the $\Delta T/T$ spectrum in the stop band spectral region. There, the increase of transmittance (about 150%) is exactly overlapped to the photonic stop band and it is detected only for AuNP doped opals, thus indicating the fundamental role of AuNP inside the photonic cavity to achieve the optical switching effect. We suggest that this effect is due to the confinement of the electromagnetic field within the photonic crystal joined to the response of AuNP surface plasmon, resonantly excited at 532 nm. The prominent $\Delta T/T$ signal within the stop band cannot be due to the variation of linear absorption of AuNP caused by their disaggregation. Indeed, absorption of AuNP in that

spectral region is structureless (see comparison with PC absorbance in Fig. 6.4a) and then only the background may be modified.

We also considered the possibility that the observed variation within the stop bandgap could be due to thermal effects. Our experience on photoinduced absorption of highly polarizable systems like conjugated polymers and organic materials (absorption coefficient 10^4–10^5 cm^{-1})[23] shows that thermal effects may be important even though they usually are of the order of few percents and possess long time responses whereas the observed switching effect seems to be too large (150%) and fast to be explained only on this basis.

At present, the understanding of the dependence of the optical switching effect on pump fluence is prevented by the relatively poor stability of AuNP doped opals after several P&P scans recorded at different pumping fluence with nanosecond pulses. However, the origin of the optical switching effect has to be found in the fast complex NLO response of the AuNP (cfr. paragraphs *2.16* and *5.6*) confined within the photonic crystal. For this reason, we are undertaking new experiments with shorter pulses to better understand the NLO response of AuNP doped opals.

References

1. Prasad, P. N., *Nanophotonics*. Wiley: 2004.
2. Morandi, V.; Marbelli, F.; Amendola, V.; Meneghetti, M.; Comoretto, D., *Adv. Funct. Mater.* **2007,** 17, 2770.
3. Comoretto, D.; Morandi, V.; Marabelli, F.; Amendola, V.; Meneghetti, M., *Proceedings of SPIE* **2006,** 6182, 61820D.
4. López, C., *Adv. Mater.* **2003,** 15, 1679.
5. Tessier, P. M.; Velev, O. D.; Kalambur, A. T.; Lenhoff, A. M.; J. F. Rabolt; Kaler, E. W., *Adv. Mater.* **2001,** 13, 396.
6. Jiang, P.; Bertone, J. F.; Hwang, K. S.; Colvin, V. L., *Chem. Mater.* **1999,** 11, 2132.
7. Joannopulos, J. D.; Meade, R. D.; N.Win, J., *Photonic Crystals: Molding the Flow of the Light*. Princeton University Press: Princeton 1995.
8. Pavarini, E.; Andreani, L. C.; Soci, C.; Galli, M.; Marabelli, F.; Comoretto, D., *Phys. Rev. B* **2005,** 72, 045102.
9. Galisteo-Lopez, J. F.; Lopez-Tejeira, F.; Rubio, S.; Lopez, C.; Sanchez-Dehesa, J., *Appl. Phys. Lett.* **2003,** 82, 4068.
10. Lopez-Tejeira, F.; Ochiai, T.; Sakoda, K.; Sanchez-Dehesa, J., *Phys. Rev. B* **2002,** 65, 195110.
11. Miclea, P. T.; Susha, A. S.; Liang, Z.; Caruso, F.; Torres, C. M. S.; Romanov, S. G., *Appl. Phys. Lett.* **2004,** 84, 3960.
12. Romanov, S. G.; Susha, A. S.; Torres, C. M. S.; Liang, Z.; Caruso, F., *J. Appl. Phys.* **2005,** 97, 086103.
13. Wang, D.; Salgueirño-Maceira, V.; Liz-Marzán, L. M.; Caruso, F., *Adv. Mater.* **2002,** 14, 908.
14. Wang, D.; Li, J.; Chan, C. T.; Salgueirño-Maceira, V.; Liz-Marzán, L. M.; Romanov, S.; Caruso, F., *Small* **2005,** 1, 122.
15. Vos, W. L.; Sprik, R.; Blaaderen, A. v.; Imhof, A.; Lagendijk, A.; Wegdam, G. H., *Phys. Rev. B* **1996,** 53, 16231.
16. Busch, K.; Lölkes, S.; Wehrspohn, R. B.; Föll, H., *Photonic Crystals: Advances in Design, Fabrication, and Characterization*. Wiley: Weinheim, 2004.
17. Haroche, S., *Fundamental Systems in Quantum Optics* Elsevier: Amsterdam, 1992.
18. Morandi, V.; Marbelli, F.; Amendola, V.; Meneghetti, M.; Comoretto, D., Submitted.
19. Mazurenko, D. A.; Kerst, R.; Dijkhuis, J. L.; Akimov, A. V.; Golubev, V. G.; Kurdyukov, D. A.; Pevtsov, A. B.; Selkin, A. V., *Phys. Rev. Lett.* **2003,** 91, 213903.
20. Hu, X.; Zhang, Q.; Liu, Y.; Cheng, B.; Zhang, D., *Appl. Phys. Lett.* **2003,** 83, 2518.
21. Markowicz, P. P.; Tiryaki, H.; Pudavar, H.; Prasad, P. N.; Lepeshkin, N. N.; Boyd, R. W., *Phys. Rev. Lett.* **2004,** 92, 083903.
22. Malvezzi, A. M.; Vecchi, G.; Patrini, M.; Guizzetti, G.; Andreani, L. C.; Romanato, F.; Businaro, L.; Fabrizio, E. D.; Passaseo, A.; Vittorio, M. D., *Phys. Rev. B* **2003,** 68, 161306R.
23. Comoretto, D.; Ottonelli, M.; Musso, G. F.; Dellepiane, G.; Soci, C.; Marabelli, F., *Phys. Rev. B* **2004,** 69, 115215.

Chapter 7

Controlled cell uptake of AuNP for photothermal therapy

The contribution of nanotechnology to medicine and biology is continuously growing. The reason consists in the size scale of nanomaterials, which is comparable to many common biomolecules.[1, 2] Hence the synthesis of hybrid materials is facilitated and chemical and physical interactions on the same scale of biological processes are possible. The introduction of nanostructures in biology is the natural evolution of bioconjugate chemistry, which is based on the combination of biomolecules with other functionalities usually coming from organic and inorganic chemistry.[1] For the same reason, main applications of nanomaterials in biomedicine recalls those of several bioconjugate molecules, as labelling or drug delivery. Indeed nanobiotechnology, ranging abroad physics, chemistry, engineering and biomedicine, shows larger multidisciplinarity than bioconjugate chemistry, as proved by the unprecedented

versatility for diagnosis and therapy.[2, 3] This explains why cancer research is devoting particular attentions to nanotechnology.[4] To date, significant progress in cancer biology has not been translated into equivalent advances in cancer therapy.

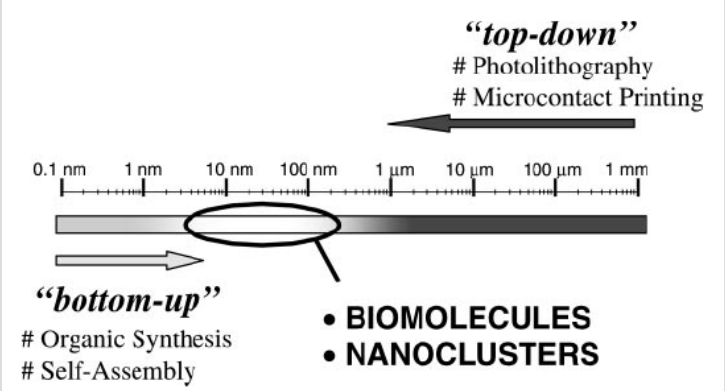

Figure 7.1 *Both biomolecules and metal or semiconductor colloidal nanoparticles have a characteristic size in the range of 1 – 100 nm. From Ref. 2.*

The main obstacle consists of selectively administering therapeutic drugs without collateral effects. Selectivity is a general drawback in medicine and biology, since only 1-10 parts every 10^5 of intravenously administered drugs as well as contrast agents reach their targets.[4] Nanotechnology provides new pathways for overcoming these obstacles, because of its peculiarities in sensing and delivery. The ability of early detection and diagnostics of cancer is strongly bound to the ability of nanoengineered surfaces in joining both enhanced sensitivity and multiplexed detection of a broad range of biomolecules in real time.[4] The ability of designing multifunctional vectors on the nanoscale is a key objective for selective cancer therapy and imaging. In particular these multifunctional nanovectors are addressed in avoiding biobarriers and improving biomarker based targeting. From this point of view, the perspective is bright, since combining 100 selected drugs with 100 different nanovectors and 100 biorecognition markers one would obtain 10^6 targeted agents.[4]

On the other side, nanomaterials pose severe concerns about their own impact on living organisms. A meaningful point is that nanovectors fall in three branches of regulations according to Food and Drugs Administration, which are drugs, medical devices and biological agents.[4, 5] The research on nanomaterials which enter the body accidentally or deliberately is still at the beginning and there are no standards for assessing their immunotoxicity.[5] To date only general issue exist, which indicates that nanoparticles actually interact with the immune system in a way largely determined by their surface chemistry.[5-7] The stimulatory or anti-stimulatory action is typically due to binding of proteins in the blood, which influence the nanoparticles uptake by immune system cells and the interaction with other blood components.[5-7] Some data indicates that the size on

a scale of tens of nanometers and the shape (i.e. spherical or spheroidal) affect the cell uptake of nanoparticles (endocytosis) as well as their subsequent discharge (exocytosis).[6, 7] Hence the surface and the shape of nanomaterials can be engineered to minimize side effects on biochemical and cellular components. In case of "intrinsically" toxic nanomaterials, like semiconductor quantum dots used as fluorescent labels, surface engineering is not resolutive for their use *in vivo*.[8, 9] On the contrary, gold nanoparticles are intrinsically biocompatible and noncytotoxic, their surface chemistry is easy, their size can be controlled with high precision as well as their absorption and scattering properties, which are mainly determined by size and shape.[9] Bioconjugation of gold particles is facilitated since several proteins bear thiols in their cysteine residues, otherwise thiol groups can be incorporated by chemical means or genetic engineering.[2] Therefore AuNP can be used as nanovectors, biolabels and even as therapeutic agents for various diseases.

In this chapter we present a new efficient strategy for controlling cell uptake of gold nanoparticles conjugated to a thermoresponsive polymer. Though the uptake mechanism itself is of seminal importance for nanobiotechnology, we also exploited the controlled cell loading with AuNP as a first step toward the application in clinic of metal nanoparticles for photothermal therapy.

7.1 Photothermal therapy.

Therapies for most forms of cancer concerns surgical tumor removal, chemotherapy, and radiation therapy. Unfortunately surgery is limited to accessible tumors, while chemotherapy and radiotherapy have remarkable side effects.[9] These drawbacks can be avoided by photothermal therapy, which offers a gentler alternative for cancer treatment by using optical heating for ablation of tumors. Photothermal therapy requires that strong photoabsorbers are located selectively in the tumor region to reduce nonspecific injury to adjacent healthy tissue.[9]

Gold nanostructures are particularly suitable for this purposes due to their plasmonic properties. For instance the absorption cross-section of Au nanoparticles (σ_{abs} ~ 2.9 10^{-15} m^2 for 40 nm spheres with an absorption band around 530 nm) is five orders of magnitude larger than that of indocyanine green (σ_{abs} ~ 1.7 x 10^{-20} m^2 around 800 nm), a dye used in earlier demonstrations of laser photothermal tumor therapy, thus promising effective photothermal therapy at much lower irradiation energy.[9] The SPR

absorption of Au nanoparticles is followed by the rapid conversion (~1 ps) of the absorbed light into heat.[9]

El-Sayed and its group recently showed by *in vitro* experiments that some carcinoma cells which overexpress a protein called EGFR can be efficiently immunotargeted using 40 nm Au nanoparticles conjugated to anti-EGFR antibodies.[10] Another approach, paved by Halas group, consists of *in vitro* monocytes uptake of nanoparticles and the subsequent *in vivo* recruitment of these monocytes in the inner tumor tissue.[11] These strategies are suitable for intravascular injection, which virtually offer the possibility of striking every cancer cell in the organism. Besides, selection of a plasmonic nanoparticle configuration with optimum plasmon absorption as well as scattering makes a dual imaging/therapy approach possible.[9]

Therapy and imaging with visible light is suitable for *in vitro* studies and *in vivo* applications for surface type cancers, while in vivo applications to deeper tissues requires plasmon features in the near infrared region of the spectra. The biological NIR window is around 900 nm, where hemoglobin and water have the highest transmittance.[9] Three types of gold nanostructures have plasmon features in this range, which are nanorods,[9] silica@gold (core@shell) spheres[11] and gold nanocages.[12]

In general, the temperature increase due to the transformation of electromagnetic radiation into heat depends on the absorption cross section as well as on the particle radius. In particular the temperature increase on the surface of a gold particle is given by:[13]

$$\Delta T_{max}(I_0) = R_{NP}^2 \frac{1}{3k_m} Re\left[i\omega \frac{1-\varepsilon_{Au}(\omega)}{8\pi} \left| \frac{3\varepsilon_0}{2\varepsilon_0+\varepsilon_m} \right|^2 \right] \frac{8\pi}{c\sqrt{\varepsilon_0}} I_0(\omega) \qquad (7.1)$$

where R_{NP} is the particle radius, ε_{Au} is the gold dielectric constant, k_m and ε_m are the matrix thermal conductivity and dielectric constant respectively, ε_0 is the vacuum dielectric permittivity, c is the light speed and I_0 is the incident light intensity. The dependence on the second power of the particle radius is due to the balance between the heat generation rate, which depends on the particle volume, and the heat dissipation rate, which depends on R_{NP}^{-1}.[13]

Equation *7.1* holds for steady state conditions, which are readily reached since AuNP requires few picoseconds to dissipate the energy of each absorbed photon to the surrounding medium.

7.2 Conjugation of gold nanoparticles with pNIPAm.

Polymers that can respond to external stimuli are of great interest in medicine, especially as controlled drug release vehicles, as well as cell adhesion mediators or controllers of enzyme function and gene expression. The functions of living cells are regulated by macromolecules that respond to changes in local environment and stimuli responsive polymers exploits the same principle. The key parameter defining the responsive behaviour of the polymers is a non-linear response to an external signal, which usually consists of pH, temperature or light.[14] As in nature, the overall response of the polymer is usually due to multiple co-operative interactions such as loss of H-bonding, which induce a large structural change in the material although individually small, when summed over the whole polymer.[14]

The most studied synthetic responsive polymer is poly(N-isopropylacrylamide) (pNIPAm), which undergoes a coil–globule transition in water at 32°C, changing from a hydrophilic state below this temperature to a hydrophobic state above it.[14] When the temperature reach a critical point, the phase transition arises from the entropic gain as water molecules associated with the side-chain isopropyl moieties are released into the aqueous phase. The temperature at which this occurs (the lower critical solution temperature or LCST) corresponds to the region in the phase diagram at which the enthalpic contribution of water hydrogen-bonded to the polymer chain becomes less than the entropic gain of the system as a whole and thus is largely dependent on the hydrogen-bonding capabilities of the constituent monomer units.

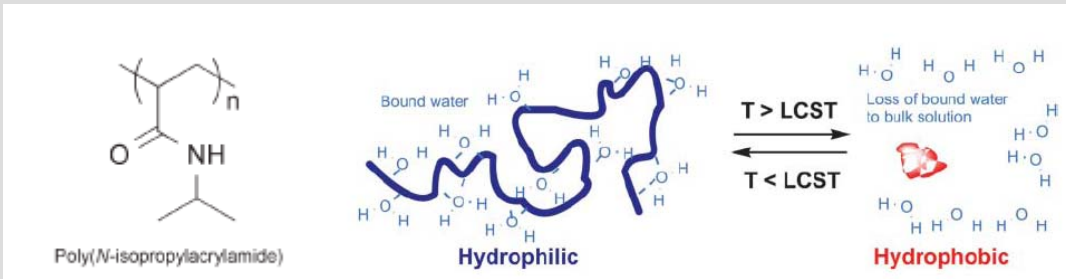

Figure 7.2 *Sructure of poly(N-isopropylacrylamide) and sketch of pNIPAm idrofilic – idrophobic transition around the LCST. From Ref. 14.*

The LCST of a given polymer can be tailored as desired by variation in hydrophilic or hydrophobic co-monomer amount.[14] The fact that the LCST of pNIPAm homopolymer lies close to body temperature and can be increased above and below 37 °C by

incorporation of co-monomer units renders pNIPAm-based materials particularly suitable for biomedical applications.

In the present case a carboxyl-terminated poly(N-isopropylacrylamide-co-acrylamide (pNIPAm-co-Am-COOH) were prepared via free-radical polymerisations using the protocols in Ref. 15. Further derivatization of pNIPAm-co-Am-COOH with cysteine via an intermediate NHS ester yielded a thiol-terminated responsive polymer for reaction with the gold particles as reported in Ref. 16.

Gold nanoparticles in water were obtained by laser ablation synthesis in liquid solution (LASiS), as previously reported.[15] Laser ablation was obtained with Nd:YAG (Quantel YG981E) laser pulses at 1064 nm (9 ns) focused with a 10 cm focus lens on a 99.9% pure gold plate placed at the bottom of a cell containing bidistilled water. Pulses of 10 J cm^{-2} at a 10 Hz repetition rate for 90 min were employed.

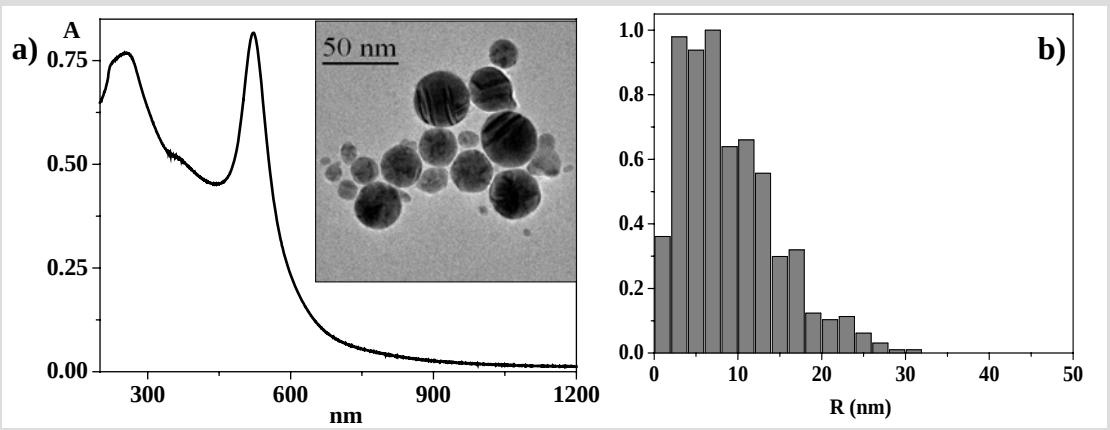

Figure 7.3 *UV – vis spectrum and TEM image of AuNP synthesized by LASiS (a) and size particles distribution of the synthesized AuNP based on 360 particles observed in TEM images (b).*

Gold nanoparticles were characterized both by UV-Vis spectroscopy using a Varian Cary 5 spectrometer in 2 mm optical path quartz cells, and by transmission electron microscopy collecting images at 300 kV with a JEOL JEM 3010 microscope equipped with a Gatan Multiscan CCD Camera model 794TEM. The samples for TEM analysis were prepared by evaporating gold nanoparticles suspension on a copper grid covered with an amorphous carbon holey film. Gold nanoparticles concentration was estimated by the Mie – Gans model fitting of UV – Vis spectra, as previously reported.[15] The distribution of the nanoparticles obtained with TEM images show that gold nanoparticles have an average diameter <d> of 18 nm with a standard deviation of 11 nm (Fig. 7.3). Assuming a spherical shape for AuNP and considering the TEM measured size distribution, we calculated an average surface area for single AuNP

(proportional to $<d^2>$) of 1408 nm^2 and an average volume for single AuNP (proportional to $<d^3>$) of 7352 nm^3.

Functionalization of AuNP with pNIPAm-co-Am-SH was confirmed both by the SPA red shift after the polymer addition ($\Delta\lambda$= 3 nm) and by salt induced aggregation experiments (Fig. 7.3). Fig 7.3b reports the UV – vis spectra of an aqueous solutions of bare gold nanoparticles (0.9 nM), of gold nanoparticles (0.9 nM) : pNIPAm-co-Am-SH with ratio 1:5400 and of gold nanoparticles (0.9 nM) : not thiolated pNIPAm-co-Am with ratio 1:5400, to which 50 mM KCl have been added.

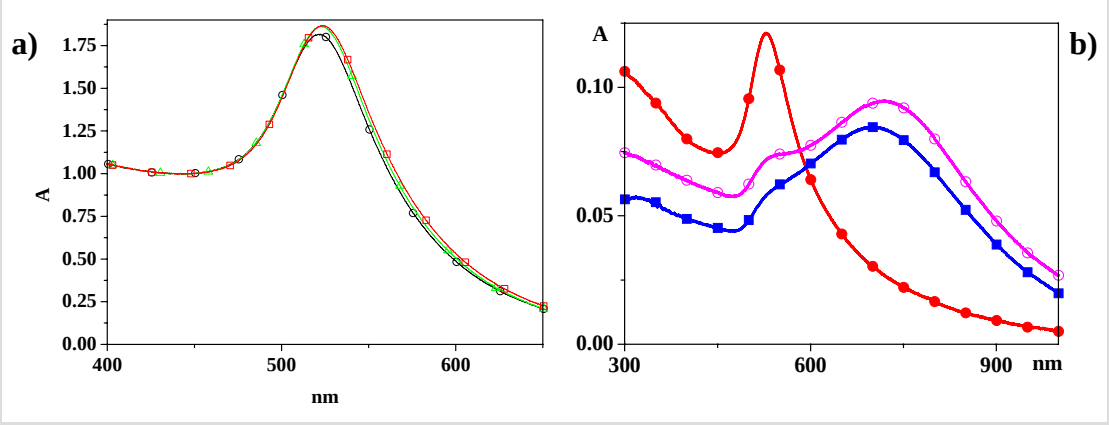

Figure 7.4 *a) SPA shift upon addition of pNIPAm: as synthesized AuNP (black circles – 521.5 nm), AuNP conjugated with thiolated pNIPAm (red circles – 524.0 nm) and AuNP conjugated to not thiolated pNIPAm (green circles – 523.0 nm). b) UV-Vis spectrum of pNIPAM-co-Am-SH functionalized AuNPs (red circles, not aggregated), not thiolated pNIPAM-co-Am decorated AuNPs (violet open circles, aggregated) and bare AuNPs (blue squares, aggregated) after KCl addition.*

It is well known that AuNP aggregate in presence of a salt if they are not well protected and Fig. 7.4b shows that only the spectrum of AuNP functionalized with pNIPAm-co-Am-SH is unaffected by the presence of the salt, while the spectra of non functionalized AuNP or that of nanoparticles in presence of the polymer without the thiol group, shows broad absorption bands due to the significant aggregation of gold nanoparticles.

The 3 nm red shift in the SPA maximum after the addition of the thiolated polymer indicated that the AuNP dielectric environment changed due to the presence of the polymer on their surface, while the salt induced aggregation experiment indicates that the functionalization of AuNP by the polymer is stable and involved the S – Au bound and not the simple physisorption of the polymer chain on the particle surface, as in presence of the not thiolated polymer.

The number of pNIPAm-co-Am-SH chains for single AuNP was measured in two different ways. In the first one, increasing amount of pNIPAm-co-Am-SH (46.3, 139, 278, 741 μg) were added to 3 ml of 1.90 nM gold nanoparticles in water. The mixtures

were maintained under mild stirring overnight at room temperature. The suspensions were centrifuged at 14000 rpm for 5 minutes to obtain the gold nanoparticle sedimentation and the supernatant was lyophilized and re-dissolved in 1 ml of water. The polymer present in the supernatant, corresponding to the polymer which did not functionalize the gold nanoparticles, was determined by iodine titration.[16].

Figure 7.5a shows that the number of polymer chains linked to the AuNP surface increased up to 3000-3800 pNIPAM-co-Am-SH chains/particle. Considering spherical nanoparticles with average surface area of 1408 nm^2, as deduced by the AuNP size distribution measured by TEM, the maximal polymer functionalization was found to correspond to about 1.75 chains/nm^2, which is in fair agreement with data reported in the literature for 20 kDa pNIPAM-co-Am-SH AuNP functionalization.[17, 18] Therefore, a 5400:1 polymer/particles molar ratio can be used to guarantee maximal polymer functionalization. Removal of unbound polymer was efficiently carried out by gel filtration chromatography, as reported in Ref. 19.

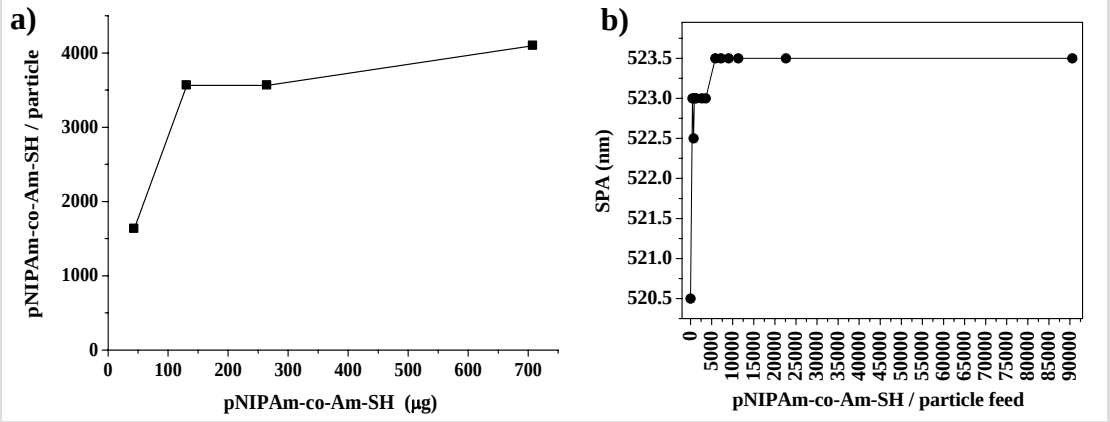

Figure 7.5 *Degree of functionalization of AuNP by pNIPAm-co-Am-SH. a) determination of the number of polymer chains linked on the gold nanoparticles surface at increasing polymer / particle ratio as described in pNIPAm-co-Am-SH functionalization studies of Materials and Methods section. Experiment was performed 4 times for each concentration ratio. b) correlation between the SPA maximum wavelength and the pNIPAm-co-Am-SH:AuNP ratio.*

A parallel functionalization study was carried out by UV – Vis spectroscopy monitoring the gold nanoparticles surface plasmon absorption red shift which depends on the nanoparticles environment according to the Mie theory.[20] An increasing pNIPAm-co-Am-SH molar excess (from 460:1 to 89700:1) was added to 0.52 nM AuNP solutions and the UV – Vis spectra were recorded after 48 hours.

Fig. 7.5b shows that the red shift reach a maximum between 4100:1 and 5400:1 polymer chain/ particles which agree with above result.

We monitored the LCST of the pNIPAm:AuNP conjugate by photon correlation spectroscopy (PCS) analysis. Dynamic light scattering analysis was carried out using a SpectraPhysics Nicomp 380 instrument (Particle Sizing Systems, Santa Barbara, CA, USA). Naked and pNIPAm-co-Am-SH functionalized nanoparticle samples (0.37 nM) in RPMI medium (cfr. Ref. 21 for details) added of 10% heat-inactivated foetal calf serum were filtered through a 0.45 μm cut-off filter, thermostated for 30 min at 34 °C or 40 °C, namely 3°C below and 3°C above the LCST, and analysed.

The LCST of pNIPAM-co-Am-SH in foetal calf serum added RPMI was found to be 37°C by PCS measurements. The analysis of the experimental data show that the particle size of the naked AuNP was in the range 10-13.5 nm both at 34 and at 40°C indicating that the nanoparticles did not undergo aggregation. At 34°C, the functionalized AuNP showed the same size of the naked counterparts, but at 40°C the data showed that the mean diameter size increased to 47-66 nm, revealing that an aggregation occurred as deduced from the UV-Vis spectra.

UV-Vis spectra were recorded to monitor the spectral changes related to the phase transition of the thermosensitive polymer coated on the nanoparticles in comparison to the constituent moieties. With this aim we prepared water suspensions of *i*) bare gold nanoparticles (13.4 nM), *ii*) gold nanoparticles (13.4 nM) and pNIPAm-co-Am-SH with ratio 1:4100, *iii*) bare pNIPAm-co-Am-SH (54.6 μM). All the solutions were thermostated for 30 minutes at stepwise increasing temperature of 1 °C from 20 to 75°C and were spectrophotometrically analyzed in the wavelength range of 300-1200 nm in 1 cm optical path quartz cells. We also evaluated the influence of the foetal calf serum on the transition and for this reason we studied a solution of gold nanoparticles (2.4 nM) and pNIPAm-co-Am-SH with ratio 1:4100 added of 10% foetal calf serum. The solution was thermostated for 30 minutes at stepwise increasing temperatures of 1 °C from 20 to 40°C and spectrophotometrically analyzed at 600 nm wavelength in 1 cm optical path quartz cells. The same solution was kept at 40°C for 1000 min and spectrophotometrically monitored at 600 nm wavelength in various time intervals. All solutions were incubated for 24 hours before the analysis.

Fig. 7.6 shows the UV – Vis spectra for the solutions *i*), *ii*) and *iii*) in a temperature range of 20 – 75 °C and the relative LCST curves obtained by monitoring the absorbance values at 600 nm. Naked AuNP absorption does not show any dependence on the temperature in the explored interval and, as a consequence of the lower

sensitivity of UV – Vis spectrometry with respect to the PCS, the hydrophobic transition of bare pNIPAM-co-Am-SH is observed only between 43°C and 46 °C. On the contrary AuNP functionalized with pNIPAM-co-Am-SH allowed the earlier recognition of the hydrophobic transition between 37°C and 40°C. In this case the polymer transition determined also a variation of the SPA absorption of the AuNP which became an optical nanoprobe of the LCST. However, a variation of the solubility of the functionalized AuNP after the LCST was not observed. The solubility changed dramatically when the same experiment was carried out in presence of KCl or of foetal calf serum added RPMI. In this case the salt effectively screened the surface charge of colloidal particles and produced a reversible strong aggregation of the functionalized AuNP.

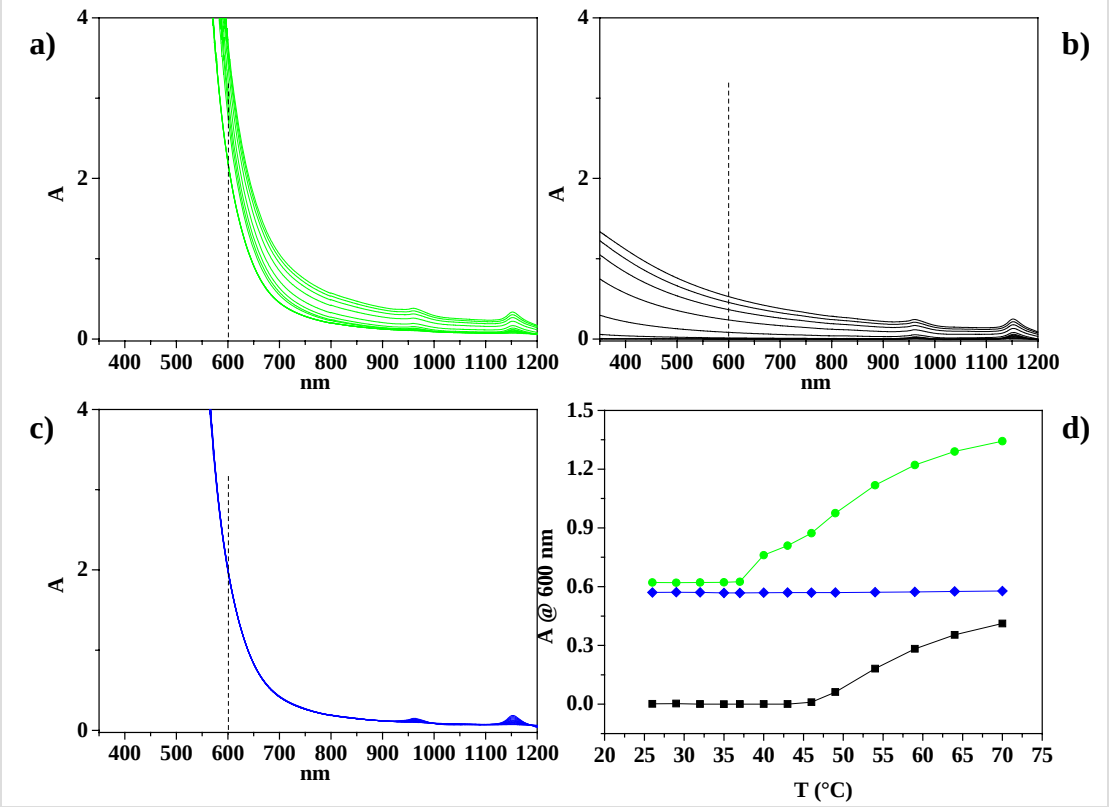

Figure 7.6 *UV – vis of aqueous solutions of pNIPAM-co-Am-SH functionalized gold nanoparticles (a, green lines), bare pNIPAM-co-Am-SH (b, black lines) and bare AuNP (c, blue lines at increasing temperature from 25 to 70°C. Part d reports the absorbance at 600 nm for the three solutions versus temperature (green circles: a; black squares: b; blue diamonds: c).*

Figure 7.7a shows the LCST of functionalized AuNP in foetal calf serum added RPMI. When monitoring at increasing time the absorbance value at 600 nm and 40°C, one observes, after aggregation, a continuous precipitation of AuNP. The variation of the absorption spectrum is reported in Fig. 7.7b where a solution of gold nanoparticles (13.4

nM) : pNIPAm-co-Am-SH with ratio 1:4100 in presence of 32 mM KCl was used since it produces the same effect of the serum added RPMI but it does not absorb in the visible range. One finds that, after the LCST, AuNP underwent fast and extended aggregation, as one can deduce from the broad absorption in the near infrared, and particles precipitated in few minutes. Therefore, the presence of serum or KCl reveals the presence of the LCST not only with the onset of a strong spectral variation but also with the precipitation of the functionalized nanoparticles.

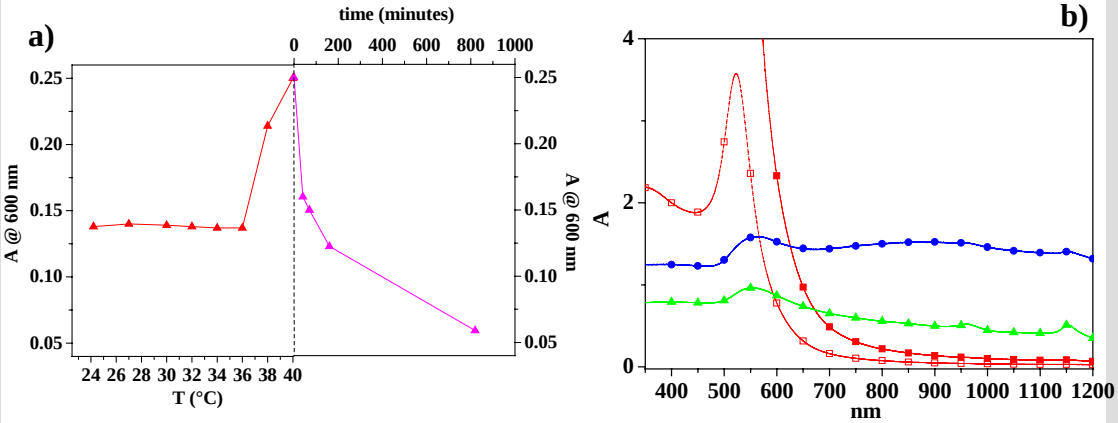

Figure 7.7 *a) LCST of pNIPAM-co-Am-SH functionalized gold nanoparticles in foetal calf serum added RPMI and AuNP precipitation kinetic at 40°C measured by monitoring the absorbance at 600 nm versus temperature and time. b) UV-Vis spectra of pNIPAM-co-Am-SH functionalized AuNPs in 32 mM KCl solution at 25°C (red squares), after incubation for 20 min at 40°C (blue circles) and after incubation for 40 min at 40 °C (green triangles). The dashed red line corresponds to the spectrum at 25°C scaled by 1/3.*

7.3 Temperature controlled cell uptake of gold nanoparticles.

The combination of functional properties in the AuNP:pNIPAm conjugate, such as switchable associative behaviour and surface plasmon absorption, renders these materials attractive for many applications, with the ability to target selectively diseased cells, via localized heating followed by specific nanothermolysis, as a key first step towards use in the clinic. We used a co-polymer based on pNIPAm that would exhibit a phase transition at or close to body temperature when conjugated to gold particles, with the specific aim of targeting tumour cells via a combined surface-property switching and plasmon heating response. Thermal abnormalities are present in several disease states, and a specific correlation has been shown between the degree of angiogenesis in cancerous tissue and hyperthermia, with the mean temperature in malignant cancer tissues being ~ 1.5 °C higher as compared to normal tissue.[21] It is also well-known that lipophilic species pass through cell membranes more easily than hydrophilic chain-

extended polymers. Therefore, the design criteria for the thermosensitive polymers in this study included an LCST close to the disease tissue temperature, such that the change in the polymer coating from a hydrophilic to lipophilic state would take place at the tumour site, but not in normal tissue. We also aimed for the polymers to be sufficiently hydrophilic below LCST so as to exhibit properties desirable in a drug delivery application, i.e. such as prolonged residence in the circulation, reduced opsonization, and enhanced tumor localization by the EPR effect[22].

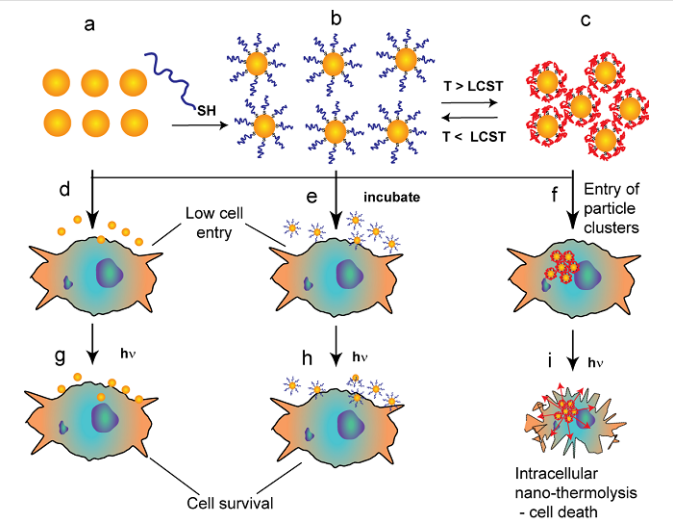

Figure 7.8 *Schematic of selective cancer cell death via plasmon induced thermolysis of responsive polymer coated gold nanoparticles. In (a) gold nanoparticles are reacted with a thiol-terminated polymer to generate stable conjugated colloids (b). Increase of temperature above the LCST of the polymer coating results in reversible association of the nanoconjugates. Incubation of the 3 different particle 'types', i.e. naked gold nanoparticles (e), polymer-gold conjugates with chain-extended polymer coat (e) and chain-collapsed polymer coat (f) results in differential levels of cell entry. Exposure to laser pulses (g, h, i) causes localised heating and cell death only for the self-associated polymer-gold nanoconjugate clusters (i).*

The concepts behind the nanoconjugate materials are shown schematically in Fig. 7.8.

In vitro studies aimed at quantifying temperature controlled cell uptake of gold nanoparticles were undertaken by incubating gold nanoparticles with human breast adenocarcinoma (MCF7) cells for 18 hours at 34 and 40°C. MCF7 cell line was cultured as reported in Ref. 16. It's reported in literature that 6 hours are required to reach equilibrium of gold nanoparticles uptake for mammalian cells.[7]

Preliminary studies demonstrated that under these conditions the cell viability was maintained and that gold nanoparticles obtained by LASiS are devoid of biological toxicity while commercial AuNP display toxicity due to the presence of stabilizers and preservatives.

The gold content into the cells was determined by inductively coupled plasma atomic emission spectroscopy (ICP-AES). Samples prepared as reported in Ref. 16, were analyzed by ICP-AES on the Spectroflame Modula spectrometer equipped with an ultrasonic nebulizer, Model USN-100 from Spectro Analytical (Klev, Germany). The

content of gold in each sample was referred to a calibration curve obtained by diluting gold stock solutions with 1% HCl-water solution.[23] After incubation, cells were washed several time in order to remove particles non associated to cells. Amount of gold was normalized per cell number in each sample.

The number of gold atoms determined by ICP-AES was converted in number of gold nanoparticles, as suggested by Chitrani et al.,[7] on the basis of the average volume per particle, obtained from the TEM measurements, and the unit cell of gold.

The conjugation of the thermosensitive polymer pNIPAM-co-Am was found to modify dramatically the nanoparticle interaction with cells. The experiments performed with MCF7 human cancer cells showed that the naked nanoparticles can be fairly taken up by the cells according to a temperature independent mechanism. On the contrary, the cell up-take of pNIPAM-co-Am-SH functionalized gold nanoparticles depended strictly on the LCST of the conjugated polymer.

Figure 7.9a shows that about 6100 and 6400 naked AuNP are up-taken per cell after incubation at 34°C and at 40°C, respectively. In the case of functionalized nanoparticles, the cell up-take was negligible at 34°C (140 nanoparticles/cell), while about 12000 particles/cell were found when incubation was performed at 40°C. The ratio of functionalized nanoparticles uptake at 40° C versus that at 34°C was 88 whereas in the case of naked nanoparticles it was 1.06.

Number of naked gold nanoparticles per cell as determined by ICP-AES analysis is in good agreement with data reported in the literature though the experiment was performed with nanoparticles obtained by standard solution techniques and with a different mammalian cell line.[7] Gold nanoparticles are supposed to penetrate mammalian cells by cell uptake induced by a non specific absorption of serum proteins on the nanoparticles surface.[7] In the case of naked nanoparticles, considering they are up-taken by the cells we can infer that serum proteins adsorb to the gold surface regardless the temperature of incubation (34 and 40°C). Considering pNIPAM-co-Am-SH functionalized gold nanoparticles, serum proteins may adsorb on the metal surface at temperature above the LCST which guarantees effective particles uptake as demonstrated by ICP-AES analysis. On the contrary, pNIPAM-co-Am-SH does not allow serum protein to adsorb on particles surface when the polymer is in the extended hydrophilic conformation below the LCST and guarantee for stealth properties of the surface toward both the serum protein and the cell membrane.[7]

In order to visualize the presence and position of gold nanoparticles within cells, TEM analysis was performed on MCF7 cell samples incubated with particles suspension in foetal calf serum supplemented RPMI medium at 40°C for 18 hours. Cells were washed and detached by trypsin treatment and the pellet collected and embedded in epoxidic resin for TEM analysis with a Tecnai G2 transmission electron microscope (FEI, Oregon- USA), as reported in Ref. 16.

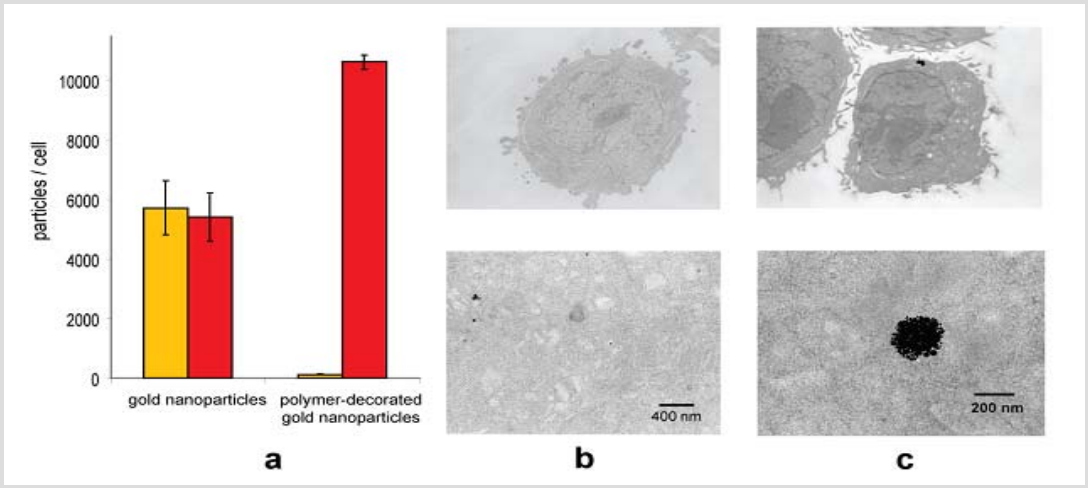

Figure 7.9 *Cell uptake and nanothermolysis of Au and polymer-conjugated Au nanoparticles. The uptake of particles by MCF7 cell lines is shown in (a) with orange bars expressing number of nanoparticles per cells on samples incubated at 34 °C and red bars express number of nanoparticles per cell on samples incubated at 40°C. Transmission Electron Micrographs depict MCF7 cells following incubation with naked gold nanoparticles (b) and polymer decorated gold nanoparticles (c) at 40°C. The overall uptake can be deduced from the upper images, while the relative distributions of particles in the cellular compartments is indicated in the lower images: clusters of polymer decorated gold nanoparticles are clearly visible in both the upper and lower panels of 2c.*

When cells were incubated with naked nanoparticles at 40°C, diffused single or small cluster nanoparticles composed of very few particle units disposed in a “bunch shape” were observed (Fig. 7.9b). Similar results were obtained with cells incubated with naked nanoparticles at 34°C. The particle clusters were spread into the citoplasmic compartment, seldom associated with nuclear membrane but never inside the nucleus. When cells were incubated with functionalized AuNP at 40°C very few citosolic clusters composed of many particles were observed (Fig. 7.9c). The cluster dimension was 200-400 nm and neither small aggregation nor single particles were detected.

TEM pictures show particles dispersed on the citosolic compartment and the nuclear compartment is devoid of particles.

Nanoparticle clusters confirm the cell uptake of polymer functionalized colloids at 40°C in agreement with aggregation found by UV – Vis and PCS analysis. It is noteworthy

that PCS analysis was performed at lower particles concentration and for reduced time with respect to the in vitro test.

7.4 Laser induced cell thermolysis.

Being this colloidal system intended for laser activated nano-thermolysis, in the present study we have evaluated whether, besides controlled cell penetration of gold nanoparticles, a differentiation on cell damage could be achieved by naked or pNIPAM-co-Am-SH functionalized AuNP.

MCF7 cells were seeded in a 24 wells plate at a density of 15 x 10^3 cells per well and grown for 24 hours at 37°C. The medium was then replaced with fresh complete medium containing 0.62 nM naked or pNIPAm-co-Am-SH functionalized nanoparticles and incubated at 34 or 40°C for 18 hours. Wells were irradiated at 532 nm for two minutes with 240 laser pulses having a low fluence of 19 mJ/cm^2. Afterwards, the medium was replaced with fresh medium and cells grown for further 24 hours at 37°C and then treated as reported in Ref. 16. The cell viability was expressed as percent of the samples/reference absorbance ratio. The reference was constituted by plain medium.

Viability test revealed that only functionalized AuNP provoked cell damage and decreased the biological viability of cell samples treated at 40°C. Cells incubated with naked gold nanoparticles at 34°C and 40°C did not show significant cell viability decrease as compared to the plain cells. Also, no photothermal response was detected for cell samples pre-incubated with polymer functionalized AuNP at 34 °C. On the contrary, 27% cell viability decrease was obtained in the case of cells pre-incubated with functionalized AuNP at 40 °C (Fig. 7.10). As assessed by ICP-AES analysis pNIPAM-co-Am decorated nanoparticles do not undergo cell uptake in samples treated at temperature below the LCST. Despite

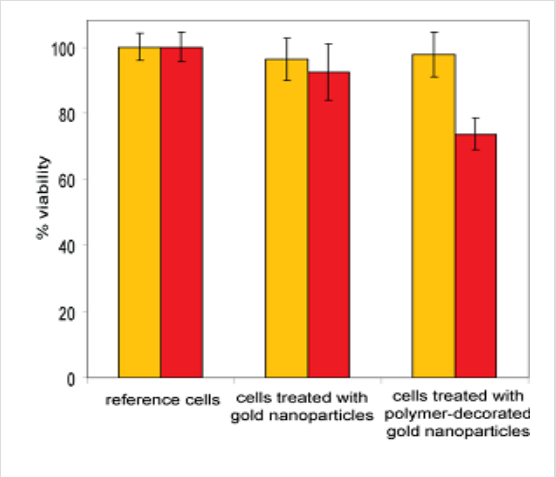

Figure 7.10 *The effect of laser pulses on cell viability is shown: yellow bars depict reference cells or cells incubated with particles at 34 °C and red bars refer to the same cells but incubated at 40°C. Significant cell kill (> 20 % loss in cell viability) is observed for MCF7 cells incubated with thermoresponsive polymer decorated gold nanoparticles above theor phase transition temperature.*

naked gold nanoparticles do penetrate cell treated both at 34 and 40°C, they do not induce viability decrease after samples laser irradiation.

It is reported in the literature that laser activated nano-thermolysis is efficient when gold nanoparticles are associated in clusters with diameter of more than 300 nm.[24] Clusters of gold nanoparticles can be heated by laser light and produce microbubbles with adequate dimension to provoke cell damage. By a consequence of these findings, we observed a biological photothermal response only on cell samples incubated with functionalized nanoparticles at 40 °C which were solely to show big particle clusters by TEM analysis.

According to Cortie et al.,[25] the cell damage is correlated to the heat absorbed by:

$$Q = \iint I(\lambda,t)\sigma_{abs}(\lambda)dtd\lambda \qquad (7.2)$$

where Q is the absorbed heat, I is the incident laser intensity at wavelength λ in the time t and σ_{abs} is the absorption cross section. We performed DDA calculations to obtain reliable absorption cross section values at 532 nm for the two case of a single isolated AuNP and of an AuNP aggregate. For a single AuNP having a diameter of 20 nm σ_{abs} = 5.31 10^{-16} m^2, while for an aggregate of 50 AuNP with average diameter of 20 nm σ_{abs} = 1.38 10^{-14} m^2, that is 26 folds larger than for the isolated AuNP. Details of calculation are reported in Fig. 7.11. Consequently, the heat absorbed for a single laser pulse at 532 nm and with fluence of 19 mJ/cm^2 is 1.0 10^{-13} J and 26.2 10^{-13} J for the isolated 10 nm AuNP and for the 50 AuNP aggregate respectively. Considering particles uptake for each cell as reported in Fig. 7.9, one can estimate an absorbed heat for single cell and for single laser pulse of 6.2 10^{-10} J – 6.5 10^{-10} J in case of cells treated with gold nanoparticles and of 7.3 10^{-12} J – 6.3 10^{-10} J in case of cells treated with polymer-decorated gold nanoparticles at 34°C and 40°C respectively. This figures point out as the overall heat absorbed by each cell is not a decisive factor for cell photothermolysis, while the difference in the heat absorbed by each isolated nanostructure is the only parameter which can account for the difference in cell mortality upon irradiation. This happened despite DDA calculations indicate that AuNP aggregates have lower absorption cross section for unit volume than isolated gold nanoparticles (see Fig.7.11).

Cell viability decrease on those samples highlights the biological relevance to have metal colloidal systems which undergo controlled self aggregation and cluster formation and can be taken up by cells. The data obtained in our study confirm that the

performance of gold nanoparticles intended for laser ablation can be strongly improved by thermosensitive polymer decoration.

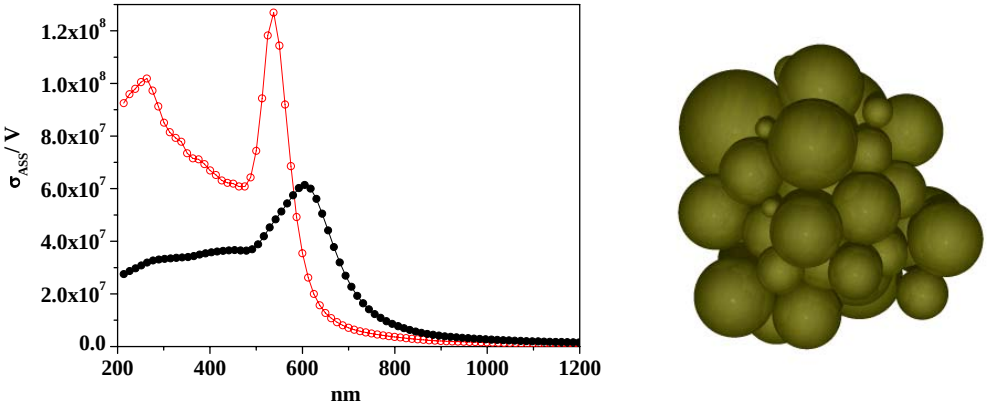

Figure 7.11 *Absorption contribute to the extinction cross sections calculated by DDSCAT for an isolated AuNP with diameter of 20 (red hollow circles) and for an aggregate of 50 non touching AuNP with average diameter of 20 nm (black filled circles – aggregate shown on the right) and same size distribution as shown in Fig. 7.3b. Matrix refraction index n=1.5. 20000 dipoles have been utilised for the isolated AuNP and 2073600 dipoles have been utilised for the aggregate.*

References.

1. West, J. L.; Halas, N., *Current Opinion in Biotechnology* **2000,** 11, 215 - 217.
2. Niemeyer, C. M., *Angew. Chem. Int. Ed.* **2001,** 40, 4128-4158.
3. Prasad, P. N., *Nanophotonics*. Wiley: 2004.
4. Ferrari, M., *Nat. Reviews* **2005,** 5, 161-171.
5. Dobrovolskaia, M. A.; McNeil, S. E., *Nat. Nanotech.* **2007,** 2, 469 - 478
6. Chithrani, B. D.; Chan, W. C. W., *Nano Letters* **2007,** 7, 1542 - 1550.
7. Chithrani, B. D.; Ghazani, A. A.; Chan, W. C. W., *Nano Letters* **2006,** 6, (4), 662-668.
8. Derfus, A. M.; Chan, W. C. W.; Bhatia, S. N., *Nano Letters* **2004,** 4, 11-18.
9. Jain, P. K.; El-Sayed, I. H.; El-Sayed, M. A., *Nano Today* **2007,** 2, 18-29.
10. Huang, X. H.; El-Sayed, I. H.; Qian, W.; El-Sayed, M. A., *Journal of the American Chemical Society* **2006,** 128, (6), 2115-2120.
11. Choi, M.-R.; Stanton-Maxey, K. J.; Stanley, J. K.; Levin, C. S.; Bardhan, R.; Akin, D.; Badve, S.; Sturgis, J.; Robinson, J. P.; Bashir, R.; Halas, N. J.; Clare, S. E., *Nano Letters* **2007,** 7, 10.1021/nl072209h
12. Skrabalak, S. E.; Chen, J.; Au, L.; Lu, X.; Li, X.; Xia, Y., *Adv. Mater.* **2007,** 19, 3177 – 3184.
13. Govorov, A. O.; Richardson, H. H., *Nano Today* **2007,** 2, 30-38.
14. Alarcon, C. d. l. H.; Pennadam, S.; Alexander, C., *Chem. Soc. Rev.* **2005,** 34, 276-285.
15. Amendola, V.; Polizzi, S.; Meneghetti, M., *Journal of Physical Chemistry B* **2006,** 110, (14), 7232-7237.
16. Sims, G. E. C.; Snape, T. J., *Analytical Biochemistry* **1980,** 107, (1), 60-63.
17. Raula, J.; Shan, J.; Nuopponen, M.; Niskanen, A.; Jiang, H.; Kauppinen, E. I.; Tenhu, H., *Langmuir* **2003,** 19, (8), 3499-3504.
18. Shan, J.; Nuopponen, M.; Jiang, H.; Kauppinen, E.; Tenhu, H., *MACROMOLECULES* **2003,** 36, (12), 4526-4533.
19. Salmaso, S.; Caliceti, P.; Amendola, V.; Meneghetti, M.; Pasparakis, G.; Cameron, A., *Submitted*.
20. Nath, N.; Chilkoti, A., *Anal. Chem.* **2004,** 76, 5370–5378.
21. Stefanadis, C.; Chrysochoou, C.; Markou, D.; Petraki, K.; Panagiotakos, D. B.; Fasoulakis, C.; Kyriakidis, A.; Papadimitriou, C.; Toutouzas, P. K., *Journal of Clinical Oncology* **2001,** 19, (3), 676-681.
22. Maeda, H.; Wu, J.; Sawa, T.; Matsumura, Y.; Hori, K., Tumor Vascular Permeability and the Epr Effect in Macromolecular Therapeutics: a Review. *Journal of Controlled Release* **2000,** 65, (1-2), 271-284.
23. Dinoto, V.; Ni, D.; Via, L. D.; Scomazzon, F.; Vidali, M., *Analyst* **1995,** 120, 1669-1673.
24. Lapotko, D. O.; Lukianova, E.; Oraevsky, A. A., *Lasers In Surgery And Medicine* **2006,** 38, (6), 631-642.
25. Harris, N.; Ford, M. J.; Cortie, M. B., *J. Phys. Chem. B* **2006,** 110, 10701-10707.

Conclusions

As shown in this thesis, new interesting advances about the synthesis and the photonic properties of gold and silver nanoparticles have been possible, mainly exploiting the interaction of nanoseconds laser pulses with matter.

LASiS provided an easily and reproducible synthetic approach for metal nanostructures, which are highly available for further functionalization and bioconjugation. In some specific cases, also metal - graphite nanocomposites can be obtained in one step by choosing the appropriate solvent. A chemical free laser based size manipulation technique has been presented, which allows the efficient bioconjugation of gold nanoparticles of selected size, preserving all the advantages of the LASiS approach. Due to the characteristic surface plasmon absorption, a simple method based on the fitting of UV-Vis spectra was conceived, which gives useful informations about metal nanoparticles without the need for TEM analysis.

Chemical reduction synthesis of silver particles stabilized by thiophenol molecules originated nanostructured composites with innovative absorption and fluorescence behaviours. This finding represents a novelty in nanotechnolgy and it has the potential of initiating a new research topic about the interactions of oligoatomic metal cores with shells made by organic molecules with delocalized electronic structures.

The plasmonic and metallic properties of metal nanoparticles obtained by the above recalled synthetic approaches opened the way to the study of several nanophotonic applications.

The charge transfer between gold particles and zinc phthalocyanines, in synergy with 532 nm laser pulses, originated a mechanism of self healing for gold nanoparticles. This process allowed a durable and efficient optical limiting and indicated that metal nanoparticles and organic molecules can interact in interesting ways.

The bandgap energy in a opal crystal has been manipulated by controlling the doping amount of gold nanoparticles. The presence of an highly polarizable and absorbing material as gold nanoparticles in the spacing between the opal spheres allowed the observation of electromagnetic field localization effects and the optical switching of the bandgap by irradiation with 532 nm – 9 ns pulses.

The surface functionalization of gold particles with a thermo responsive polymer has been exploited for the temperature switched cell uptake of these particles. The combination of this property with the plasmon induced laser heating of gold nanoparticles designed a new strategy for the photothermal therapy of cancerous tissues.

The intimate nature of this thesis, which design a transversal path through the synthesis and the application of metal nanoparticles in nanophotonics and biophotonics, is that of a seminal work for lightening new approaches to these disciplines. Hence each of the discussed topics is still available for further investigations and developments.

Appendix A

Extinction cross sections of metal nanostructures calculated by DDSCAT 6.1

Credits:
Draine, B.T., & Flatau, P.J.
Discrete Dipole Approximation Code DDSCAT (Version 6.1), 2004
http://arxiv.org/abs/astro-ph/0409262

Gold Sphere

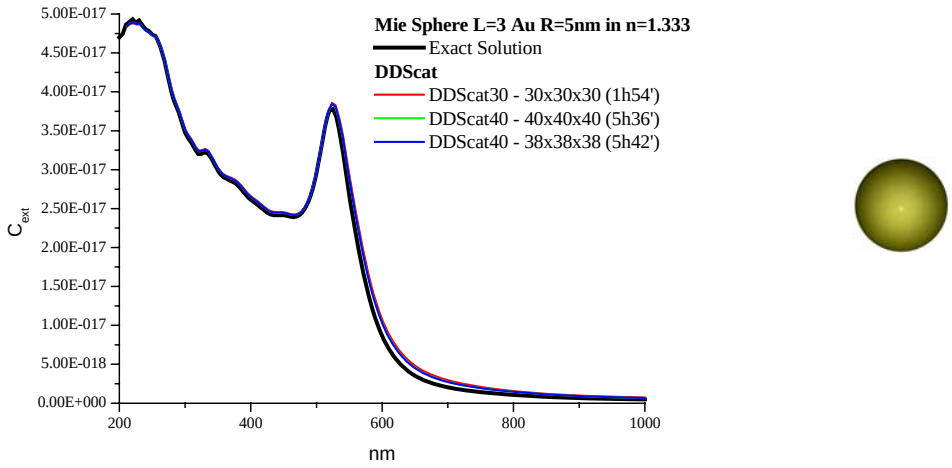

Gold – Silica Core@Shell Spheres

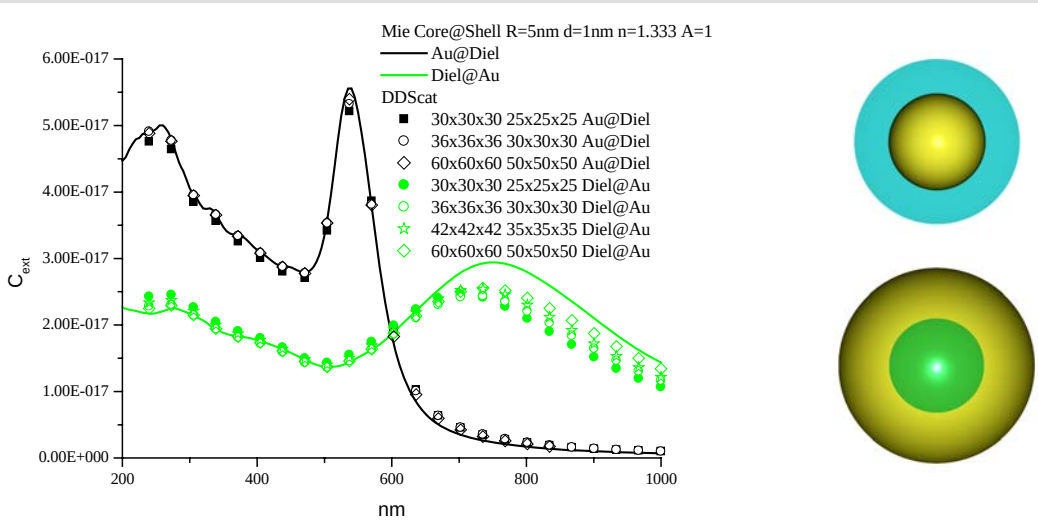

Silver Slab

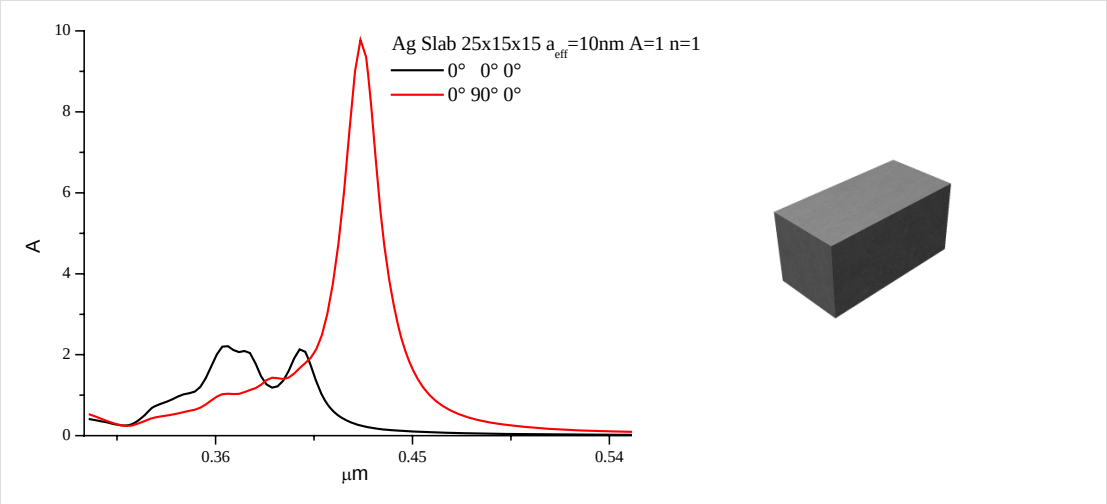

Silver Cubes

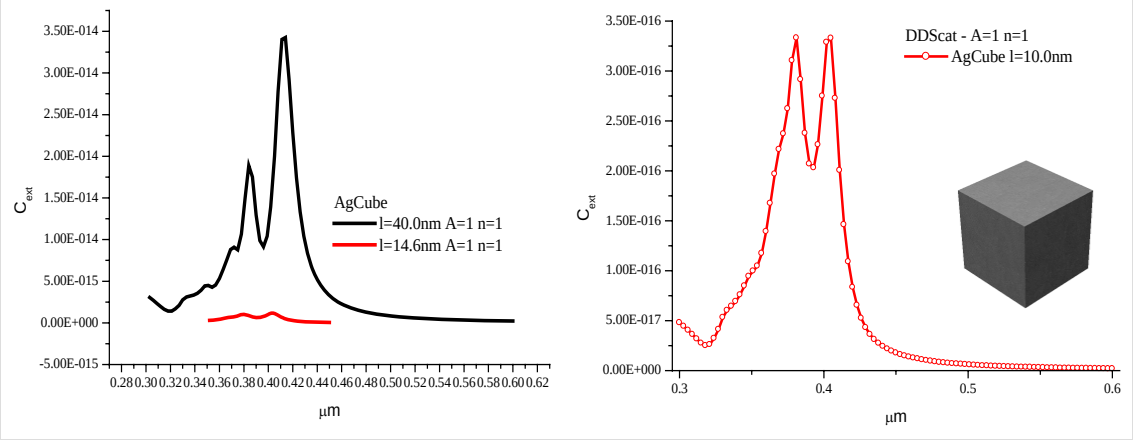

Silver and Silver@Dielectric Cubes

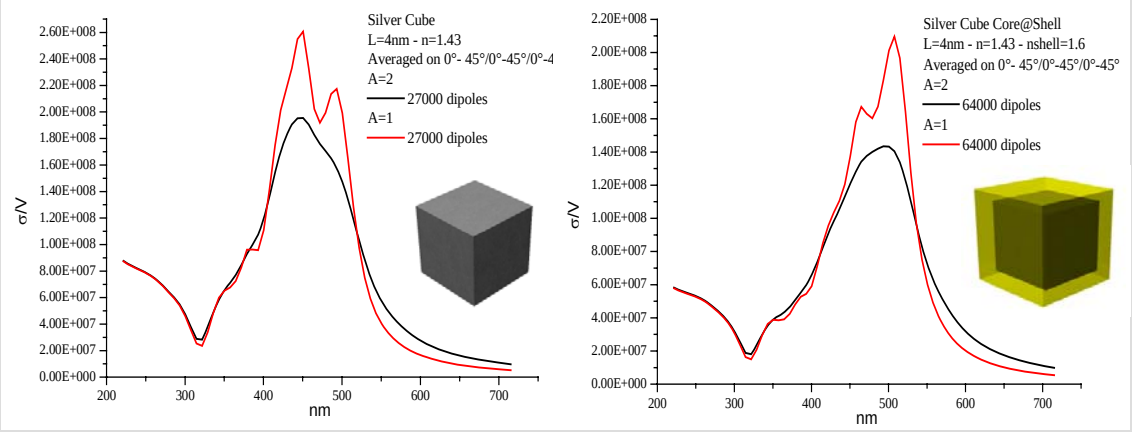

Silver and Silver@Dielectric Cubes

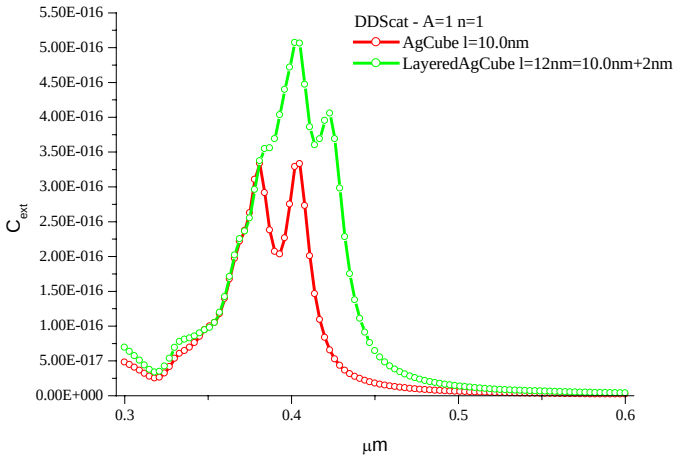

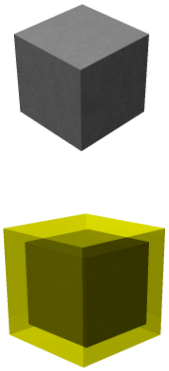

Two Silver@Dielectric Cubes

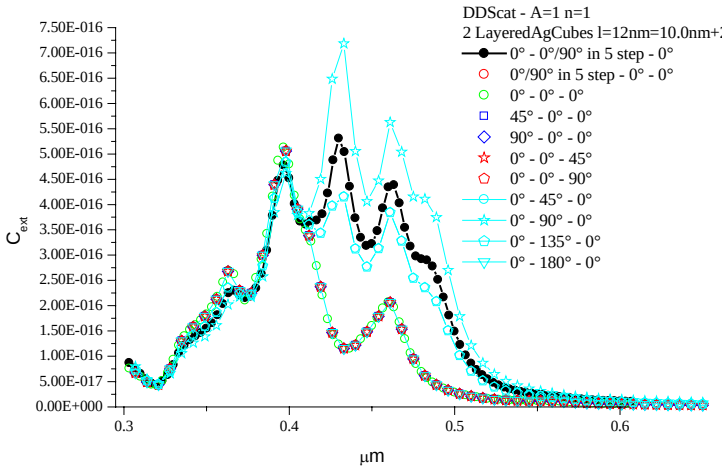

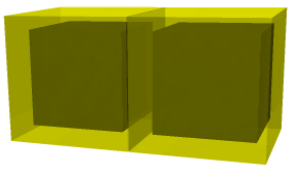

Two and Four Silver@Dielectric Cubes

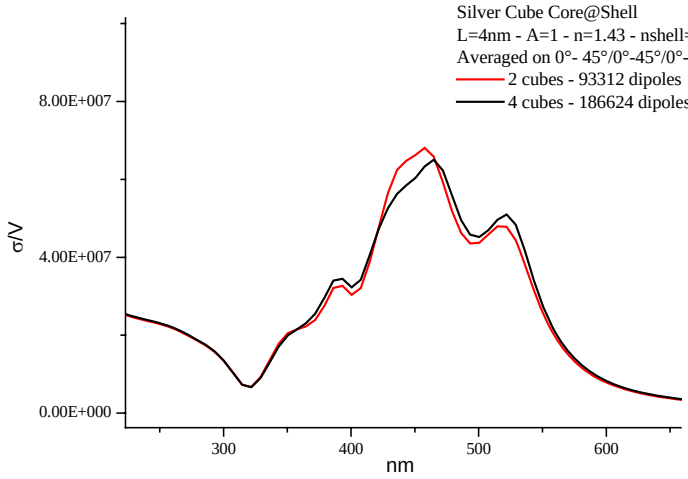

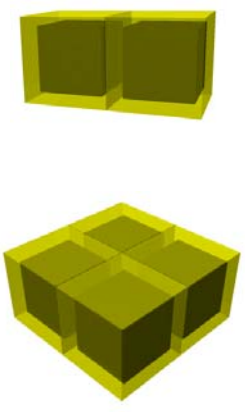

Hollow Silver Cube

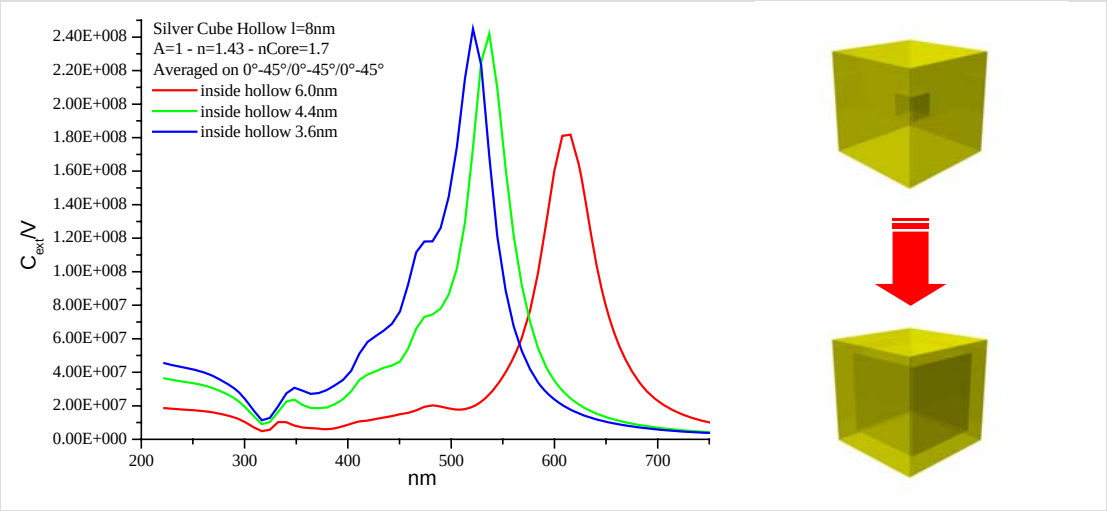

Silver Prism

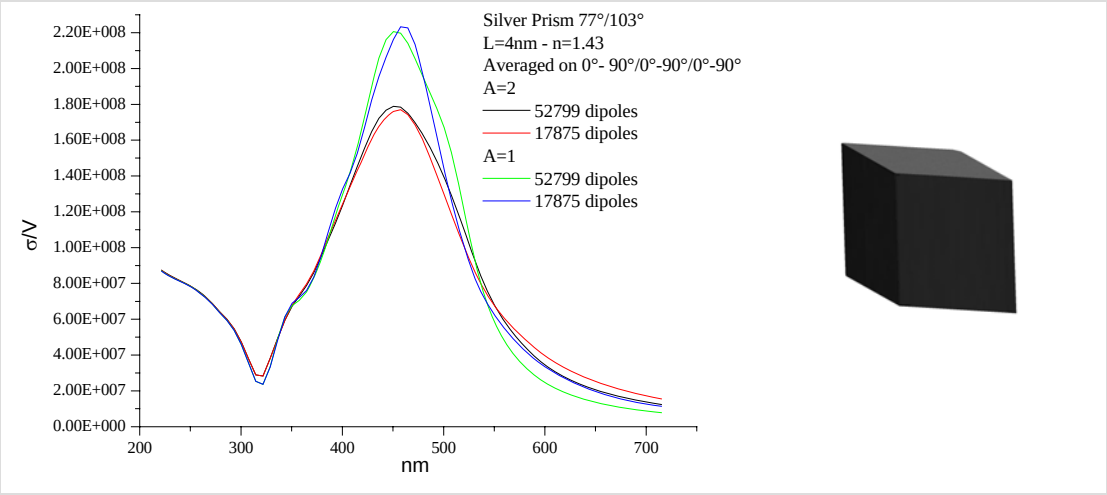

Silver@Dielectric Prism

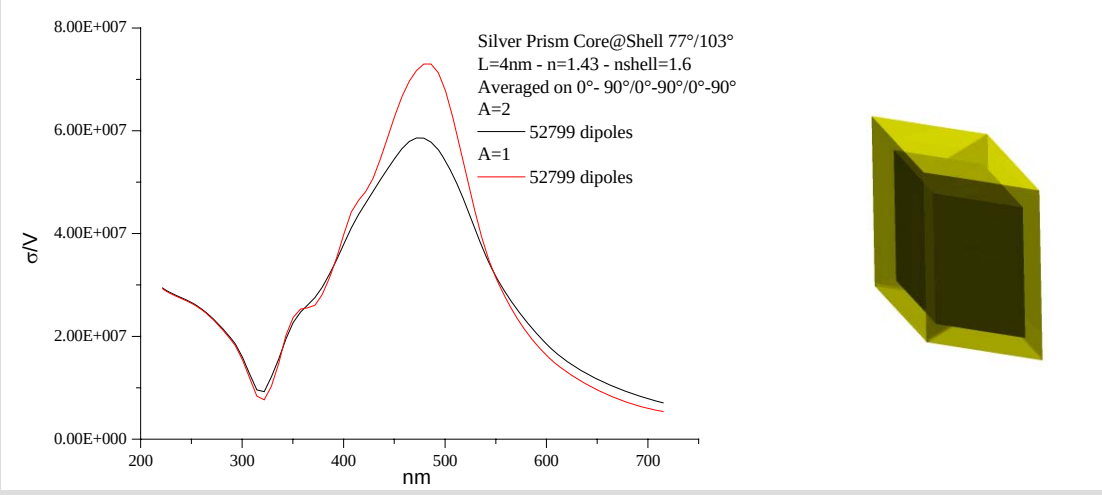

Two Silver@Dielectric Prisms

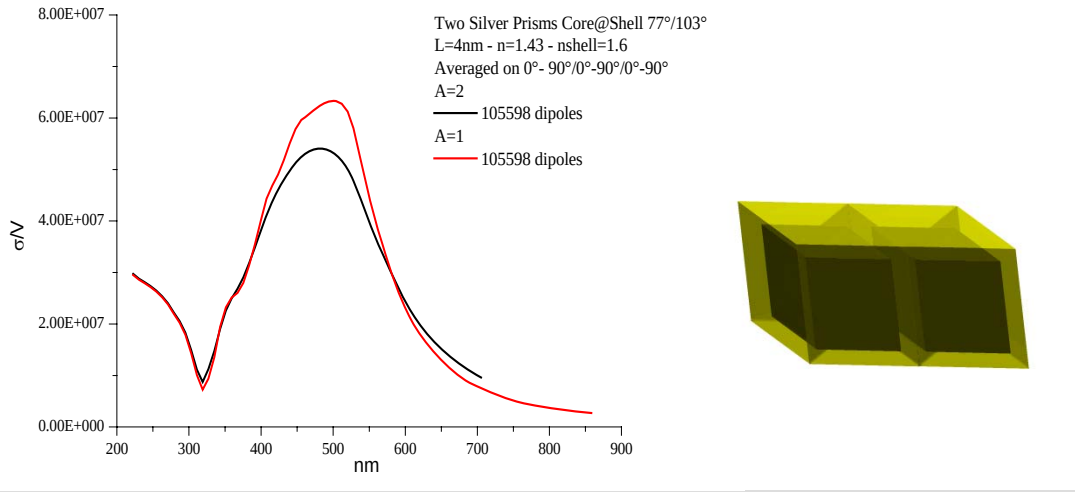

Silver@Dielectric Tilted Prisms

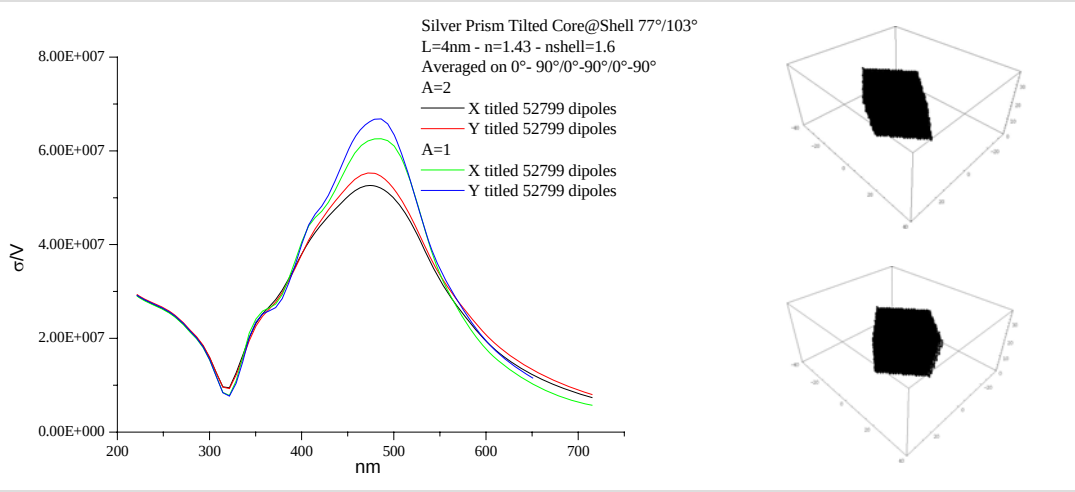

Silver@Dielectric Tilted Prism

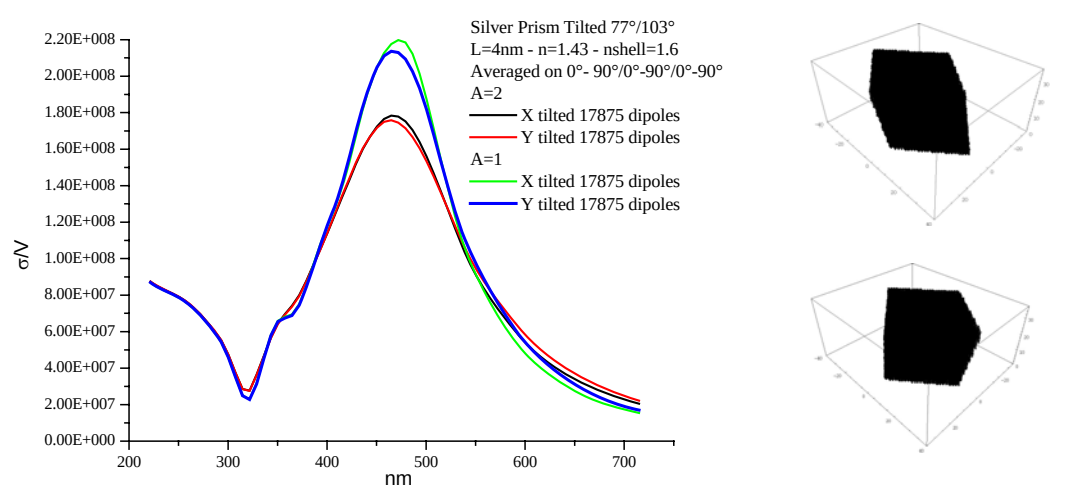

Silver@Dielectric Prisms

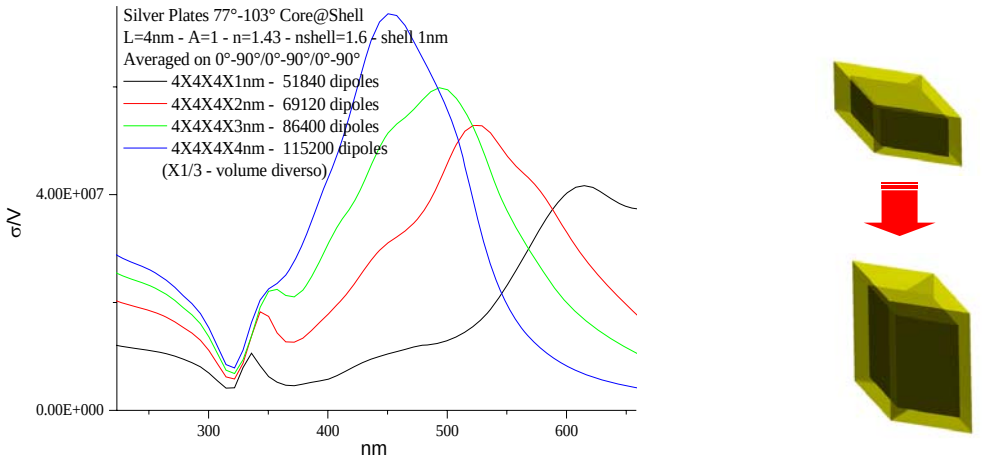

Silver@Dielectric Triangular Prisms

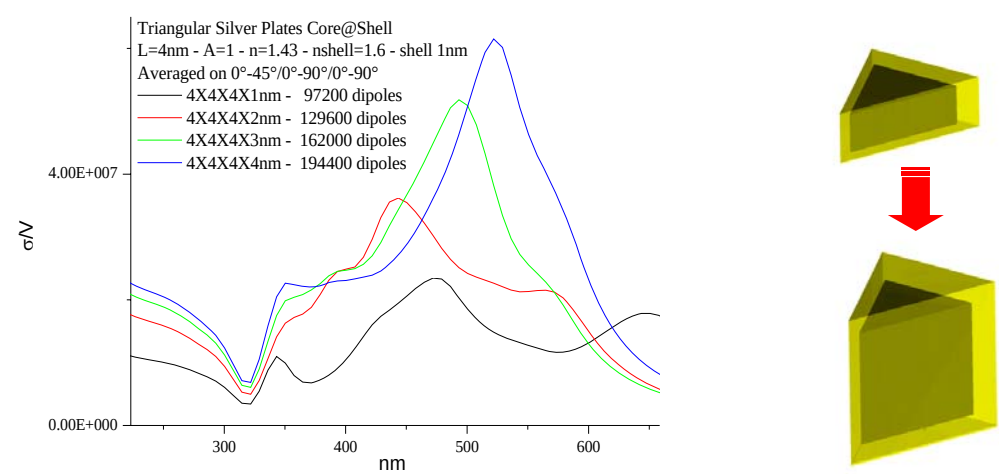

Silver@Dielectric Square Plates

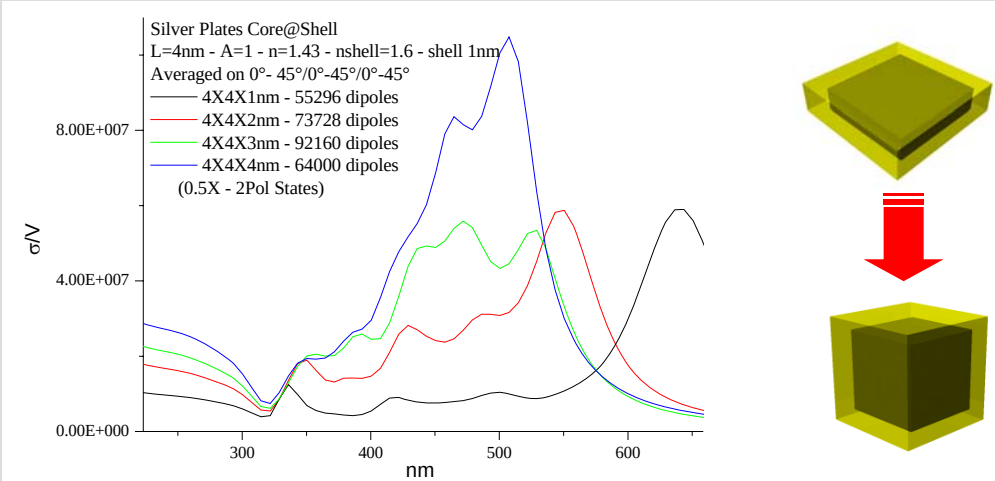

Two Stacked Silver@Dielectric Square Plates

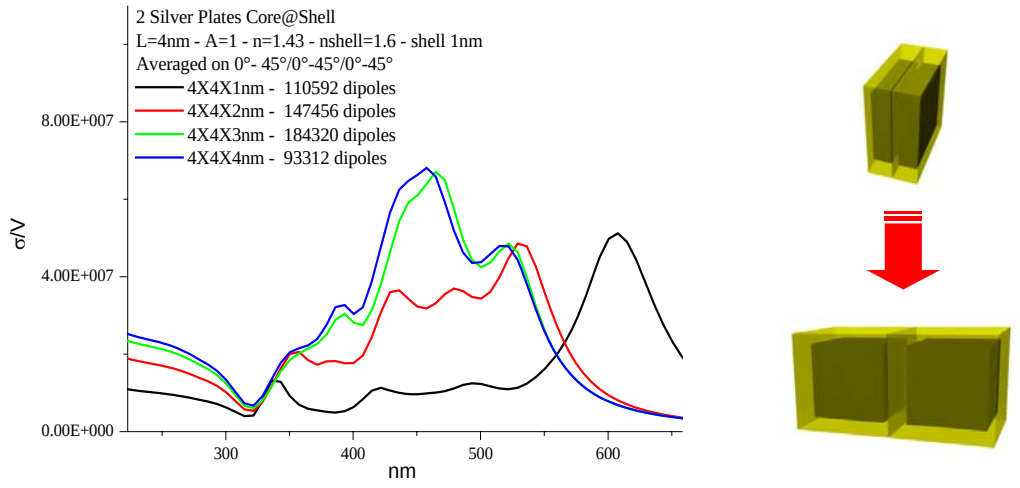

Silver Cylinders

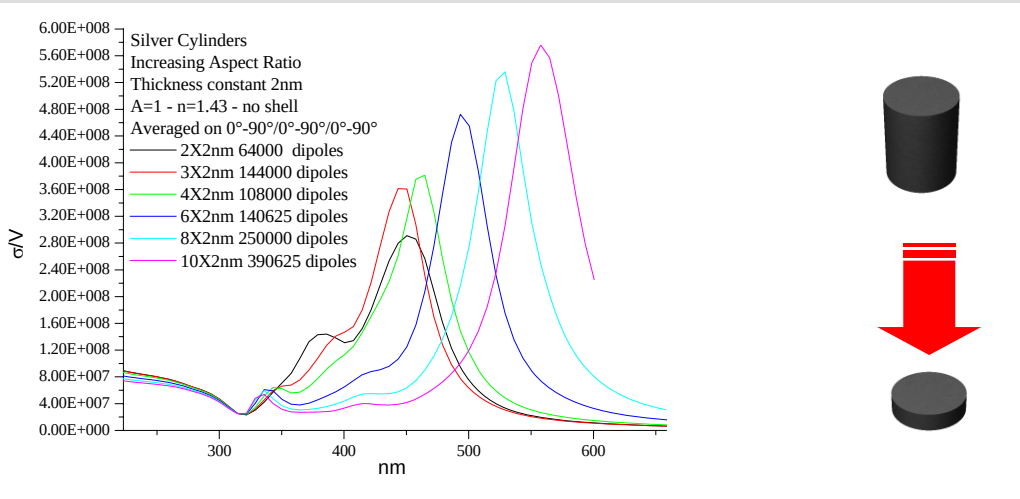

Silver Cylinders

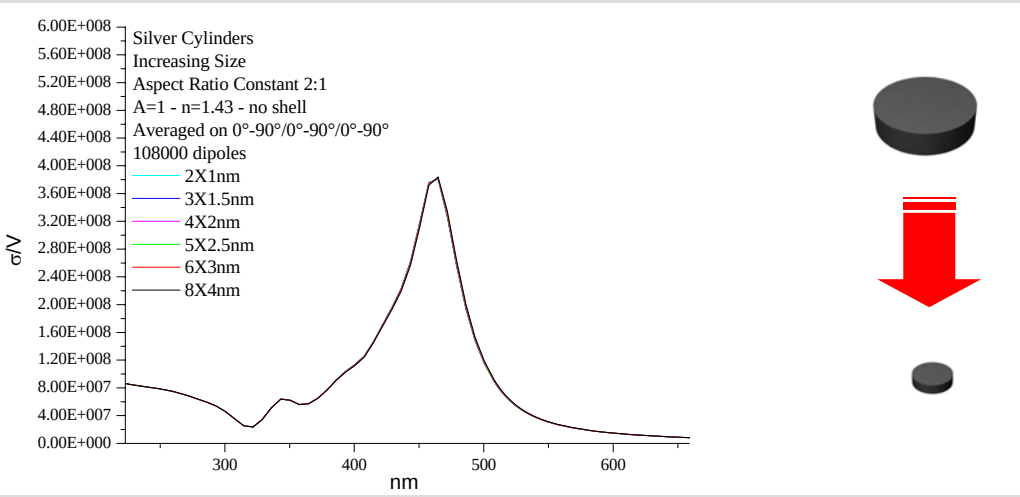

Silver@Dielectric Cylinders

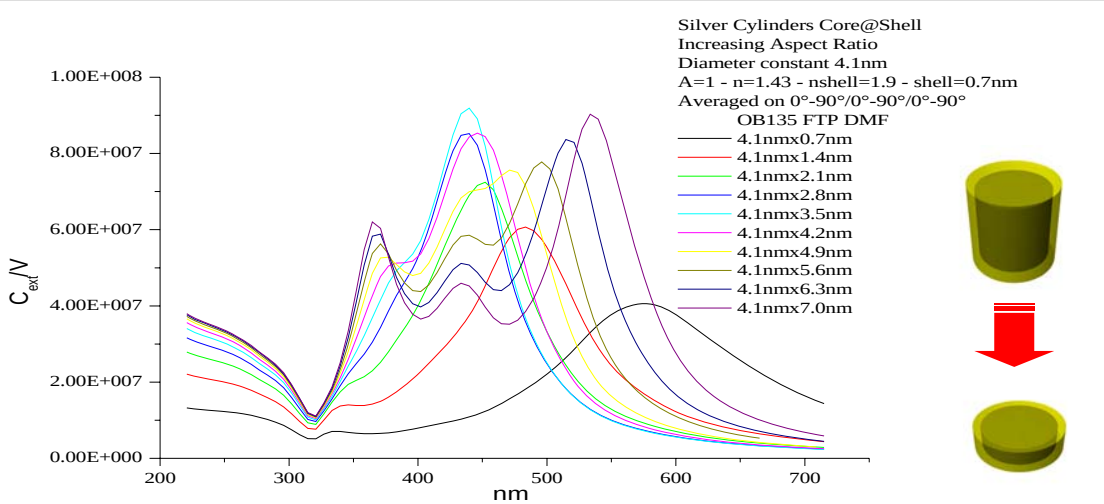

Silver@Dielectric Cylinders

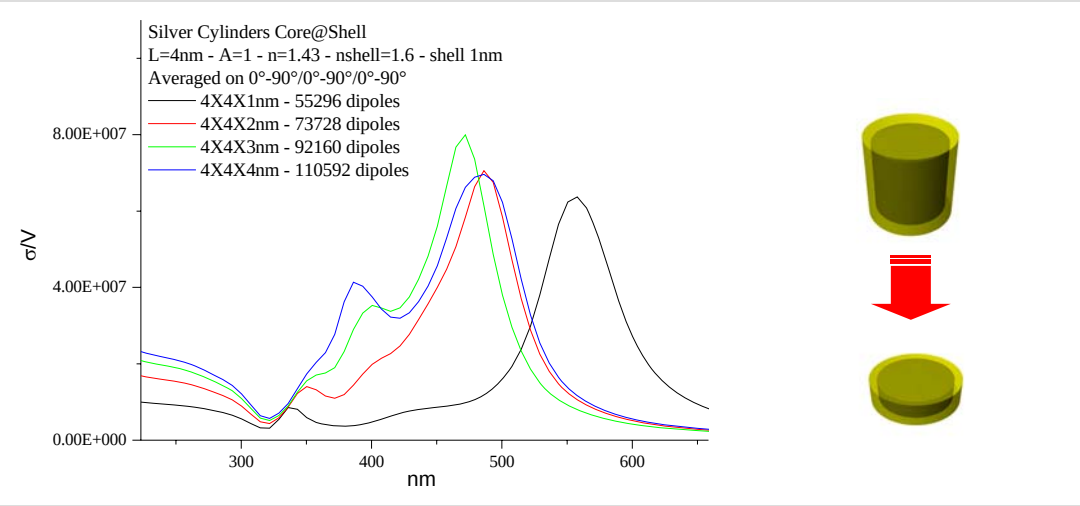

Simple Assemblies of Silver@Dielectric Spheres

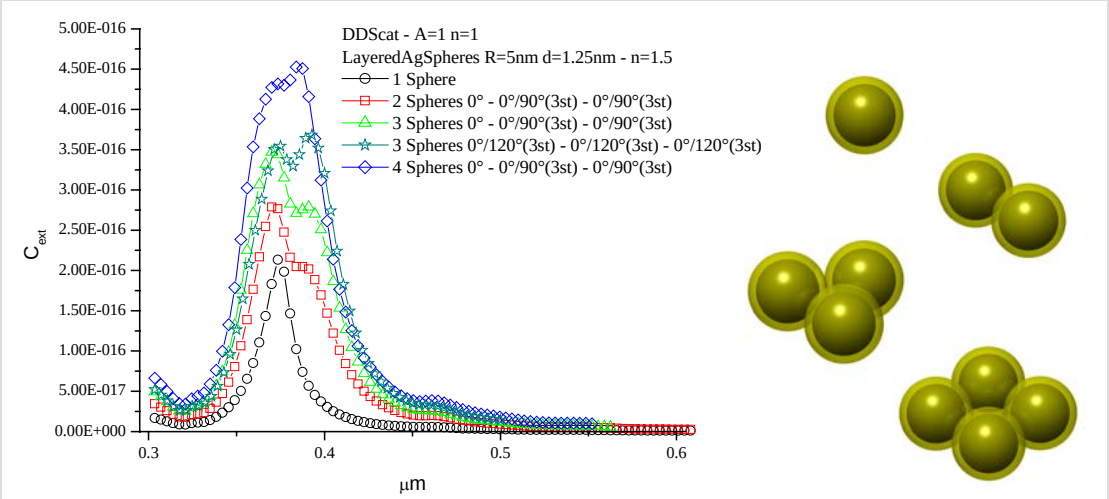

Chains of Silver@Dielectric Spheres

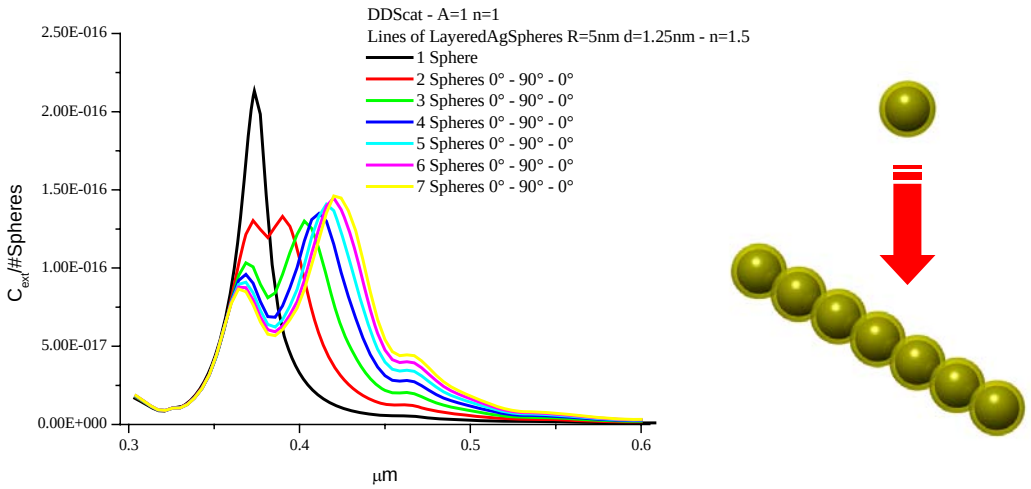

Chains of Gold@Dielectric Spheres

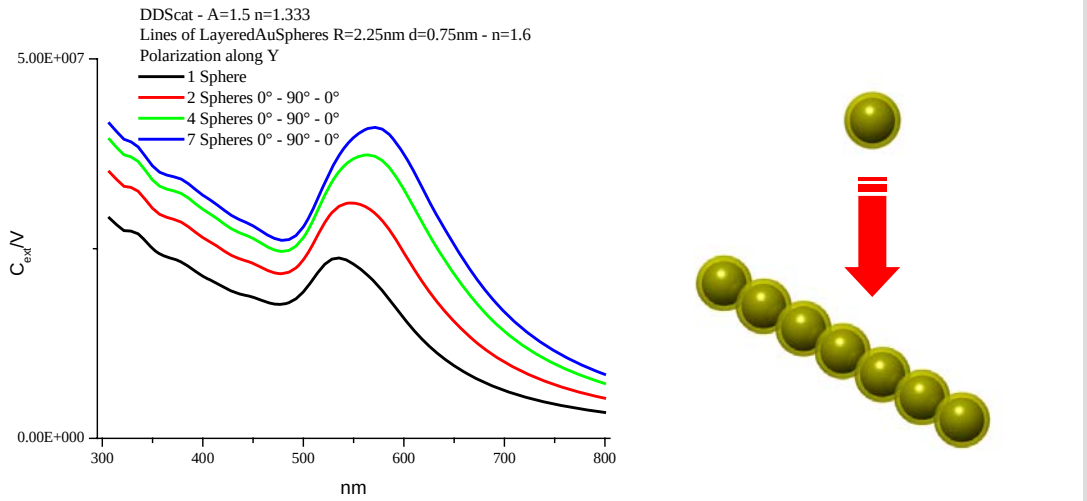

50 Gold Nanoparticles in a Compact Spherical Aggregate

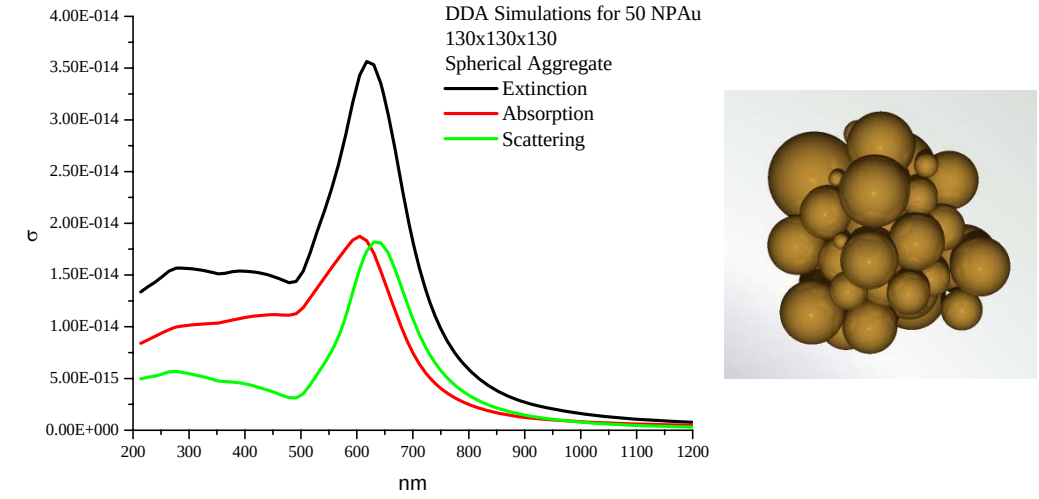

50 Gold Nanoparticles in a Compact Spheroidal Aggregate

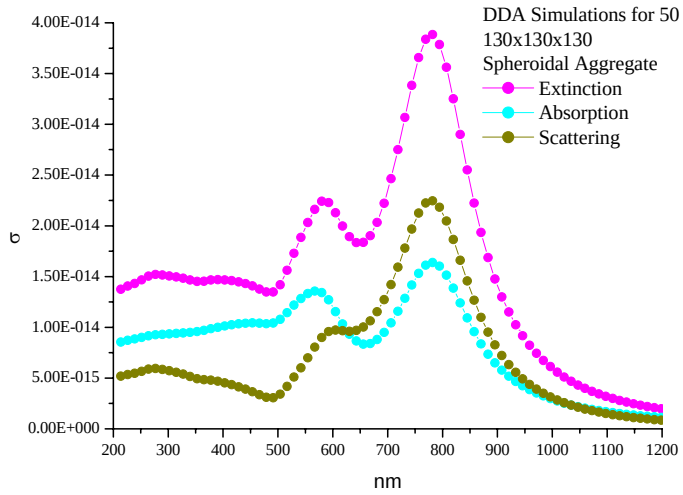

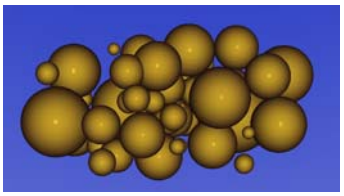

Appendix B

List of scientific publications

The work of this PhD thesis originated the following scientific publications:

2005

Papers:

- ***V. Amendola**, G. A. Rizzi, S. Polizzi, M. Meneghetti; **"Synthesis of Gold Nanoparticles by Laser Ablation in Toluene: Quenching and Recovery of the Surface Plasmon Absorption"**; Journal of Physical Chemistry B 2005, 109, 23125 – 23128.*
- ***V. Amendola**, G. Mattei, C. Cusan, M. Prato, M. Meneghetti; **"Fullerene non linear excited state absorption induced by gold nanoparticles light harvesting"**; Synthetic Metals 155 (2005) 283 – 286.*
- *D. Dini, S. Vagin, M. Hanack, **V. Amendola**, Moreno Meneghetti; **"Nonlinear optical effects related to saturable and reverse saturable absorption by subphthalocyanines at 532 nm"**; Chemical Communication (2005) 3796 – 3798.*

Conferences:

- *M. Meneghetti, **V. Amendola**, G. Mattei, C. Cusan, M. Prato; **"Fullerene non linear excited state absorption induced by gold nanoparticles light harvesting"**; Optical Probes 2005 (January 4 – 8, 2005; Bangalore, India).*
- *M. Meneghetti, **V. Amendola**, N. Schiccheri, G. Marcolongo, M. Prato, G. Fabbrini, M. Maggini; "**Enhancement of multiphoton absorption properties of molecular systems"**; European Conference on Molecular Electronics (June 29 – July 2, 2005; Bologna, Italy) and Conferenza Nazionale della Divisione di Chimica Fisica della Società Chimica Italiana (June 20 – 24, 2005; Siena,Italy).*

2006

Papers:

- ***V. Amendola**, S. Polizzi, M. Meneghetti; **"Laser Ablation Synthesis of Gold Nanoparticles in Organic Solvents"**; Journal of Physical Chemistry B 2006, 110, 7232 – 7237.*
- *D. Dini, M. J. F. Calvete, M. Hanack, **V. Amendola**, M. Meneghetti; **"Demonstration of the optical limiting effect for an hemiporphyrazine"**; Chemical Communication 2006, 2394 – 2396.*
- *M. Villano, **V. Amendola**, G. Sandonà, M. P. Donzello, C. Ercolani, M. Meneghetti; **"Excited States Dynamic and Nonlinear Absorption of a Pyrazinoporphyrazine Macrocycle Carrying Externally Appended Pyridine Rings"**; Journal of Physical Chemistry B 2006, 110, 24354 – 24360.*
- *T. M. Figueira-Duarte, J. Clifford, **V. Amendola**, A. Gegout, J. Olivier, F. Cardinali, M. Meneghetti, N. Armaroli, J. F. Nierengarten; **"Synthesis and excited state properties of a [60]fullerene derivative bearing a star-shaped multi-photon absorption chromophore"**; Chemical Communication 2006, 19, 2054 – 2056.*
- *D. Comoretto, V. Morandi, F. Marabelli, **V. Amendola**, M. Meneghetti; **"Optical effects in artificial opals infiltrated with gold nanoparticles"**; Proceedings of SPIE 2006, 6182, 61820D.*

Conferences:

- ***V. Amendola,** S. Polizzi, M. Meneghetti, **"Laser Ablation: an Easy Route to Obtain Gold and Silver Nanomaterials"**; NanoItaly 2006 (May 22 – 24, 2006; Trieste, Italy).*

- *M. Meneghetti,* ***V. Amendola****, N. Schiccheri, M. Villano, M.P. Donzello, C. Ercolani, D. Dini, M. Hanack;* ***"Excited states two photon absorption of molecular systems"****; The International Conference on Science and Technology of Synthetic Metals 2006 (July 2 – 7, 2006; Dublin, Ireland).*
- *D. Comoretto, V. Morandi, F. Marabelli,* ***V. Amendola****, M. Meneghetti;* ***"Spectroscopic Properties of Artificial Opals Infiltrated with Gold Nanoparticles"****; Material Research Society - Fall Meeting 2005 (November 28 – December 2, 2006; Boston, USA).*

2007

Papers:

- ***V. Amendola****, M. Meneghetti;* ***"Controlled size manipulation of free gold nanoparticles by laser irradiation and their facile bioconjugation"****; Journal of Material Chemistry 2007, 17, 4705-4710.*
- ***V. Amendola****, S. Polizzi, M. Meneghetti;* ***"Free Silver Nanoparticles Synthesized by Laser Ablation in Organic Solvents and Their Easy Functionalization"****; Langmuir 2007, 23, 6766 – 6770.*
- *V. Morandi, F. Marabelli,* ***V. Amendola****, M. Meneghetti, D. Comoretto;* ***"Colloidal Photonic Crystals Doped With Gold Nanoparticles: Spectroscopy & Optical Switching Properties"****; Advanced Functional Materials 2007, 17, 2779–2786.*
- *G. Fabbrini, R. Riccò, E. Menna, M. Maggini,* ***V. Amendola****, M. Garbin, M. Villano, M. Meneghetti;* ***"Sequential multiphoton absorption enhancement induced by zinc complexation in functionalized distyrylbenzene analogs";*** *Physical Chemistry Chemical Physics, 2007, 9, 616 – 621.*

Conferences:

- ***V. Amendola****, M. Meneghetti; "****Free metal nanoparticles obtained by laser ablation in water and organic solvents: Size manipulation, easy functionalization and bioconjugation"****; ACS Fall Meeting (Boston, USA, August 19-23, 2007).*
- *M. Meneghetti, G. Marcolongo, G. Ruaro,* ***V. Amendola****, J. Alfonsi, M. Gobbo;* ***"Aminoacid Functionalization and Raman Characterization of DWNT"****; APS March Meeting (Denver, USA, March 5-9, 2007).*

Submitted/In preparation

Papers:

- *V. Morandi, F. Marabelli,* ***V. Amendola****, M. Meneghetti, D. Comoretto;* ***"Light Localization Effect On The Optical Properties Of Opals Doped With Gold Nanoparticles"****; Submitted*
- *S. Salmaso, P. Caliceti,* ***V. Amendola****, M. Meneghetti, G. Pasparakis, A. Cameron; "****Temperature Selective Cell Targeting and Plasmon Induced Thermolysis via Responsive Polymer Coated Gold Nanoparticles"****; Submitted.*
- *D. Dini, M.J.F. Calvete, M. Hanack,* ***V. Amendola****, M. Meneghetti; "****Large excited states two photon absorptions found in multiphoton absorptions of hemiporphyrazines with different central atoms"****; Submitted.*
- ***V. Amendola****, D. Dini, S. Polizzi, M. Hanack, K. Kadish, M. Meneghetti; "****Self – Healing Blend of Gold Nanoparticles and Zinc Phthalocyanines for Efficient Optical Limiting"****; In preparation.*
- ***V. Amendola****, M. Meneghetti; "****Sizing of gold nanoparticles by Mie model fitting of UV-Vis spectra"****; In preparation.*

In primo luogo ringrazio di cuore i miei genitori ed i miei nonni.
Per avermi aiutato a riempire il sacchetto del tempo,
ringrazio i miei amici e le sorridenti onde del mare.

Ringrazio Moreno per la sua straordinaria e costante attività di advisor e per avermi offerto l'opportunità di un'attività di ricerca dinamica e policromatica.

Ringrazio Francesco per l'opportunità di lavorare nel suo gruppo e la Fondazione Aldo Gini e la mia Scuola di Dottorato per il sostegno economico durante questa esperienza.

I'm really grateful to Osman because he trusted in me though all the difficulties of our project.

Ringrazio tutte le persone, molte, che hanno contribuito positivamente al mio lavoro, in qualsiasi forma.
I'm grateful to all the people, many, that helped me for my PhD thesis.